

UNIVERSITY OF CALIFORNIA

Los Angeles

Dissecting the Baryon Cycle  
at the Peak of Cosmic Star Formation  
with Hubble Space Telescope Slitless Spectroscopy

A dissertation submitted in partial satisfaction  
of the requirements for the degree  
Doctor of Philosophy in Astronomy and Astrophysics

by

Xin Wang

2019

© Copyright by

Xin Wang

2019

ABSTRACT OF THE DISSERTATION

Dissecting the Baryon Cycle  
at the Peak of Cosmic Star Formation  
with Hubble Space Telescope Slitless Spectroscopy

by

Xin Wang

Doctor of Philosophy in Astronomy and Astrophysics

University of California, Los Angeles, 2019

Professor Tommaso L. Treu, Chair

To explore the chemo-structural properties of galaxies and understand quantitatively the cycling of baryons at the peak epoch of cosmic star formation, I developed a highly effective method for sub-kiloparsec scale spatially resolved spectroscopy of strongly lensed galaxies using space-based wide-field slitless grism data. Applying this method to the deep Hubble Space Telescope near-infrared grism data, I obtained precise gas-phase metallicity maps of a large sample of star-forming galaxies at  $1.2 \lesssim z \lesssim 2.3$ , over half of which reside in the dwarf mass regime. My work presents the first statistically representative sample of high-redshift dwarf galaxies with their metallicity spatial distribution measured with sufficient resolution. These metallicity maps reveal a variety of baryonic physics, such as efficient radial mixing from tidal torques, rapid accretion of low-metallicity gas, and various feedback processes which can significantly influence the chemo-structural properties of dwarf galaxies. In particular, we find two galaxies at  $z \sim 2$  displaying strongly inverted metallicity radial gradients, suggesting that powerful galactic winds triggered by central starbursts carry the bulk of stellar nucleosynthesis yields to the outskirts. I also observe an intriguing correlation between stellar mass and metallicity gradient, consistent with the “down-sizing” galaxy formation picture that more massive galaxies are more evolved into a later phase of disk growth, where they experience more coherent mass assembly at all radii and thus show shallower metallicity gradients. My method can also be readily applied to data from future space missions employing grism instruments, e.g., JWST, Euclid, WFIRST, CSST.

The dissertation of Xin Wang is approved.

Omer M. Blaes

Matthew A. Malkan

Alice E. Shapley

Tommaso L. Treu, Committee Chair

University of California, Los Angeles

2019

*To my wife Dr. Xiao-Lei Meng  
who have nourished and sustained me  
with her illuminating love  
especially during the darkest hours*

## TABLE OF CONTENTS

<b>1</b>	<b>Introduction</b>	<b>1</b>
1.1	What is the baryon cycle and why is it important?	1
1.2	How can we observe the baryon cycle at the peak of cosmic star formation?	1
1.3	Dissertation Overview	6
<b>2</b>	<b>Mass Reconstruction of the Lensing Cluster Abell 2744 from HFF Imaging and GLASS Spectroscopy</b>	<b>10</b>
2.1	Introduction	10
2.2	Data	12
2.2.1	The Grism Lens-Amplified Survey from Space	12
2.2.2	Hubble Frontier Fields	13
2.2.3	<i>Spitzer</i> Frontier Fields	14
2.3	GLASS Observation and Data Reduction	14
2.4	Identification of Multiple Images	18
2.4.1	Imaging Data: Identification and Photometric Redshifts	18
2.4.2	Targeted GLASS Spectroscopy	22
2.4.3	Blind Search in GLASS Data	25
2.5	Gravitational Lens Model	31
2.5.1	Comparison with Previous Work	34
2.6	The Spatial Distribution of Stellar and Dark Matter	35
2.6.1	Stellar Mass Map	35
2.6.2	Stellar to Total Mass Ratio	39
2.7	Conclusions	40

<b>3 Sub-kiloparsec Resolution Gas-phase Metallicity Maps at Cosmic Noon behind the Hubble Frontier Fields cluster MACS1149.6+2223 . . . . .</b>	<b>56</b>
3.1 Introduction . . . . .	56
3.2 Spectroscopic Data and Sample Selection . . . . .	59
3.2.1 Hubble Space Telescope Grism Spectroscopy . . . . .	59
3.2.2 Sample Selection . . . . .	63
3.3 Photometry and Lens Models from the <i>HFF</i> . . . . .	65
3.4 Analysis Procedures . . . . .	69
3.4.1 Spectral Energy Distribution Fitting . . . . .	69
3.4.2 Source Plane Morphology . . . . .	69
3.4.3 Emission Line Maps from Grism Spectra . . . . .	70
3.4.4 Line-flux-based Bayesian Inference of Metallicity . . . . .	74
3.5 Global Demographic Properties . . . . .	77
3.6 Spatially Resolved Analysis . . . . .	85
3.6.1 Gas-phase Metallicity Maps at Sub-kpc Resolution . . . . .	87
3.6.2 Notes on Individual Galaxies . . . . .	98
3.7 Summary and Discussion . . . . .	104
3.7.1 Summary . . . . .	104
3.7.2 Interpretation of Flat/steep Metallicity Gradients at High Redshifts . . . . .	106
3.A Emission line kinematics from ground-based IFU observations . . . . .	108
3.2 Emission line flux measurements from <i>HST</i> grisms . . . . .	110
<b>4 Discovery of Strongly Inverted Metallicity Gradients in Dwarf Galaxies at <math>z \sim 2</math> . . . . .</b>	<b>115</b>
4.1 Introduction . . . . .	115
4.2 Data and Galaxy Sample . . . . .	117

4.2.1	<i>HST</i> Grism Slitless Spectroscopy	117
4.2.2	Grism Data Reduction	117
4.2.3	<i>HST</i> Imaging: Estimating $M_*$ from SED Fitting	118
4.2.4	Two Dwarf Galaxies with Strongly Inverted Metallicity Gradients	119
4.3	Methods and Results	120
4.3.1	Radial Metallicity Gradients	122
4.3.2	SFR, Stellar Population Age, and Gas Fraction	125
4.3.3	Spatially Resolved Gaseous Outflows	131
4.4	Summary and Discussion	134
4.A	Gas kinematics from <i>Keck OSIRIS</i> observations	136
4.B	Extracting and fitting 1D and 2D <i>HST</i> grism spectra	137

## LIST OF FIGURES

1.1	Onset of baryon cycling in the local Universe: M82. . . . .	2
1.2	The rise and fall of the cosmic average star-formation rate density. . . . .	3
1.3	The relationship among the effective radius, star-formation rate and stellar mass for galaxies at $z \sim 2$ . . . . .	5
1.4	State-of-the-art data reduction techniques for <i>HST</i> WFC3/IR slitless spectroscopy. . . .	7
2.1	The color composite image of Abell 2744 based on the HFF and GLASS imaging. . . .	16
2.2	The GLASS G102 and G141 grism pointings of Abell 2744 at two distinct P.A.s. . . .	17
2.3	All multiple images discovered to date in Abell 2744. . . . .	19
2.4	Flow chart describing our procedure for assigning photometric redshifts to multiple image systems. . . . .	23
2.5	Emission line detection results on object ID #00963 (arc 6.1). . . . .	26
2.6	Same as Figure 2.5, except that object ID #00523 (arc 6.2) is shown. . . . .	27
2.7	Same as Figure 2.5, except that object ID #00433 (arc 6.3) is shown. . . . .	28
2.8	Same as Figure 2.5, except that object ID #00336 (arc 1.3) is shown. . . . .	29
2.9	Same as Figure 2.8, except that object ID #00888 (arc 56.1) is shown. . . . .	30
2.10	Comparison between the spectroscopic and photometric redshifts. . . . .	32
2.11	Convergence and magnification of our lens model. . . . .	33
2.12	Surface mass density profile of our lens model. . . . .	36
2.13	Cumulative source plane area versus magnification at $z = 9$ . . . . .	37
2.14	Comparison of the redshifts estimates. . . . .	38
2.15	Stellar mass surface density and stellar to total mass ratio. . . . .	40
3.1	Color composite image of MACS1149.6+2223 from the full-depth 7-filter <i>HFF</i> photometry. . . . .	61

3.2	Zoom-in color composite stamps of our metallicity gradient sample. . . . .	66
3.3	Multi-perspective view of the SN Refsdal host galaxy multiple image 1.3, i.e., ID 04504 in our sample. . . . .	67
3.4	Multi-perspective view of our metallicity gradient sample. . . . .	71
3.5	Marginalized 1D and 2D constraints from our Bayesian parameter inference. . . . .	78
3.6	Mass excitation diagnostic diagram. . . . .	80
3.7	Star formation rate as a function of stellar mass for emission-line galaxies. . . . .	82
3.8	The mass-metallicity relation at $z \sim 1.8$ . . . . .	84
3.9	Offset from the fundamental metallicity relation. . . . .	86
3.10	Sub-kpc resolution metallicity maps and radial gradients. . . . .	89
3.11	Spatially resolved BPT diagrams. . . . .	92
3.12	Evolution of metallicity gradients with redshift. . . . .	93
3.13	Observed metallicity gradients as a function of $M_*$ . . . . .	99
3.14	Velocity fields derived from integral field spectra. . . . .	111
3.15	The <i>HST</i> grism spectra for one exemplary source in our sample ID 03746. . . . .	113
3.16	Same as Figure 3.15, except that source ID 02389 is shown. . . . .	114
4.1	Two star-forming dwarf galaxies at $z \sim 2$ displaying unusually strong inverted metallicity gradients . . . . .	120
4.2	The diagnostic diagrams for our sources. . . . .	123
4.3	Metallicity maps and radial gradient measurements of the two galaxies. . . . .	126
4.4	Maps of SFR surface density, average stellar population age, and gas fraction for our galaxies, derived from our spatially resolved analysis of stellar continuum and nebular emission. . . . .	129
4.5	Gas fraction and metallicity estimated in different radial annuli. . . . .	130
4.6	First ever maps of gaseous outflow rates at $z \sim 2$ . . . . .	131



## LIST OF TABLES

2.1	Multiply lensed arc systems identified in the Abell 2744 field . . . . .	43
2.1	Multiply lensed arc systems identified in the Abell 2744 field . . . . .	44
2.1	Multiply lensed arc systems identified in the Abell 2744 field . . . . .	45
2.1	Multiply lensed arc systems identified in the Abell 2744 field . . . . .	46
2.1	Multiply lensed arc systems identified in the Abell 2744 field . . . . .	47
2.1	Multiply lensed arc systems identified in the Abell 2744 field . . . . .	48
2.2	Emission line detection results on multiply and singly lensed sources . . . . .	49
2.2	Emission line detection results on multiply and singly lensed sources . . . . .	50
2.2	Emission line detection results on multiply and singly lensed sources . . . . .	51
2.2	Emission line detection results on multiply and singly lensed sources . . . . .	52
2.2	Emission line detection results on multiply and singly lensed sources . . . . .	53
2.2	Emission line detection results on multiply and singly lensed sources . . . . .	54
2.2	Emission line detection results on multiply and singly lensed sources . . . . .	55
3.1	Properties of the grism spectroscopic data used in this work . . . . .	60
3.2	Global demographic properties of the metallicity gradient sample analyzed in this work	64
3.3	Sampling parameters and their prior information. . . . .	74
3.4	Coefficients for the EL flux ratio diagnostics used in our Bayesian inference. . . . .	79
3.5	Gas-phase metallicity gradients measured by two different methods. . . . .	87
3.6	Measured velocity dispersions using ground-based IFU data. . . . .	109
3.7	Measured emission line fluxes . . . . .	112
4.1	Measured quantities of the two dwarf galaxies . . . . .	121

## ACKNOWLEDGMENTS

First of all, I should thank my advisor Tommaso Treu, for his guidance, patience, and in particular his generous financial support throughout the entire course of my PhD studies. His ruthless pragmatism educated me of the urgency of publishing to avoid being replaced by collaborators. I would also like to acknowledge my external advisor, Tucker Jones, who have helped me grow scientifically. A significant portion of my PhD research is “prototyped” in his seminal work and I have been following his footsteps ever since to have finally climbed over this monumental mountain called Doctor of Philosophy.

I am also greatly indebted to Louis Abramson. Tommaso and Tucker *had* to deal with me, but for some reasons Louis *chose* to. His profound understanding of galaxy evolution combined with his eloquent arguments has always made our discussions highly beneficial and enlightening to me. An enormous thank you also goes to Takahiro Morishita. He was my inspiration, as we face similar situations doing research abroad. Being in a foreign country, where the speaking language does not resemble at all our mother tongues, we can only earn respect through hard work, wholehearted dedication, and unique expertise. In a way, Takahiro showed me a path and I am so proud that I have found the courage to follow it.

I would never take for granted the ample opportunities of close collaborations with experts in the field, who have helped transform me into a confident and resourceful astronomer. First and foremost, I would say millions of thank you to Gabe Brammer, for giving me the precious chance to come to STScI to receive face-to-face hands-on training on grism data reduction from him, and answering me numerous questions on astronomical data analysis in general. “Learning from Achilles himself; kings would kill for the honor.” I am sincerely grateful for having the great opportunity to collaborate with and learn from Emanuele Daddi. He played a crucial role in helping develop the inverted gradient discovery paper, and really expanded my horizon on the physics of galaxy evolution. I cannot thank Keren Sharon enough for her help and advice, as well as giving me the awesome chance to visit UMich. She is the one who redeemed my faith in gravitational lensing for galaxy clusters, by teaching me Lenstool step-by-step, which now has become an indispensable part in my skill set. Matt Malkan is greatly appreciated for his pivotal

help in securing a postdoc position for me at Caltech/IPAC starting this summer, and for allowing me to join the WISPs collaboration. I acknowledge Kasper Schmidt and Kuang-Han Huang, who initiated me on Python programming.

I would also like to thank Omer Blaes, Matt Malkan, Alice Shapley and Tommaso Treu for serving on my dissertation committee.

My deep gratitude also goes to all my fellow graduate students at both UCSB and UCLA, in particular, Suoqing Ji, Xinnan Du, and Ryan Sanders. Suoqing started graduate school at UCSB in the same year as I did, and has given me some great tips in transitioning to US life. Becoming close friends with Suoqing is one of the few things that made my days at UCSB not a total failure. Xinnan helped me a great deal with my transfer from UCSB to UCLA. Without her invaluable help, I could not have won the prestigious Chinese Government Award for Outstanding Graduate Student Abroad. Ryan served as my graduate student mentor for over a year, and set up an excellent role model for me. I sincerely thank him for proof-reading my proposals/papers numerous times. Also acknowledged are the Treu group members whom I have been sharing pizzas with: Alessandro Sonnenfeld, Simon Birrer, Peter Williams, Anowar Shajib, Daniel Gilman, Xuheng Ding, Lilan Yang.

I would also like to appreciate the kindness and assistance from local people when I visited their institutes. First of all, Prof. Shude Mao is wholeheartedly acknowledged for giving me multiple opportunities of lengthy visits to THCA. Bravo on the recently founded Department of Astronomy. I am also truly grateful to the help and financial support from Prof. Le Zhang for my visit to SJTU, Prof. Xu Kong for my visit to USTC, Prof. Yu Gao for my visit to PMO, Prof. Gongbo Zhao for my visit to NAOC. Furthermore, thank you also goes to Jessie Hirtenstein at UC Davis, Raymond Simons, Alaina Henry and Ivelina Momcheva at STScI, Yuan-Sen Ting at IAS, Jacqueline van Gorkom at Columbia, Xiangcheng Ma at Caltech/UC Berkeley, Zheng Cai and Song Huang at UCSC. Since my college day one, I have been living in the giant shadow shaded by Song; his fanatic passion for astronomy is extremely contagious and has always spurred me onto greater effort in pursuit of astronomical achievements. My special gratitude to Hui Li, whos is also a Nanjing University alumnus. He provided tremendous help to me when I visited Ann Arbor as well as Boston. Congratulations to his recent achievement on the Hubble fellowship. Last but not

the least, the professors at Nanjing University, i.e., Profs. Zhiyuan Li, Yong Shi, Qiu-Sheng Gu, Yong Feng Huang, Jilin Zhou, etc., are cordially acknowledged for my several trips back to my Alma Mater.

## VITA

2006	Graduated, Yaohua High School, Tianjin, China
2010	Bachelor of Science in Astronomy, Summa Cum Laude, Department of Astronomy, Nanjing University, Jiangsu Province, China
2013	Master of Science in Astrophysics, School of Astronomy and Space Sciences, Nanjing University, Jiangsu Province, China
2015	Master of Arts in Physics, Physics Department, University of California, Santa Barbara, California, USA
2018	Dissertation Year Fellowship, University of California, Los Angeles, California, USA

## PUBLICATIONS

**Wang, X.**, Huang, Y. F., & Kong, S. W. On the Afterglow from the Receding Jet of Gamma-Ray Bursts. 2009, *Astron. Astrophys.*, 505, 1213 ([arXiv:0903.3119](#))

**Wang, X.**, Huang, Y. F., & Kong, S. W. Constraint on the Counter-jet Emission in GRB Afterglows from GRB 980703. 2010, *Sci. China-Phys. Mech. Astron.*, 53 (Suppl.1), 259

Meng, X.-L., Zhang, T.-J., Zhan, H., & **Wang, X.** Morphology of Galaxy Clusters: A Cosmological Model-Independent Test of the Cosmic Distance-Duality Relation. 2012, *Astrophys. J.*, 745, 98 ([arXiv:1104.2833](#))

**Wang, X.**, Meng, X.-L. et al. Observational Constraints on Cosmic Neutrinos and Dark Energy Revisited. 2012, *J. Cosmol. Astropart. Phys.*, 11, 018 ([arXiv:1210.2136](#))

**Wang, X.**, Meng, X.-L., Huang, Y. F., & Zhang, T.-J. Testing X-ray Measurements of Galaxy Cluster Gas Mass Fraction Using the Cosmic Distance-Duality Relation and Type Ia Supernovae. 2013, *RAA*, 13, 1013 ([arXiv:1305.2077](#))

Schmidt, K. B., Treu, T., Brammer, G. B., Bradac, M., **Wang, X.** et al. Through the Looking GLASS: HST Spectroscopy of Faint Galaxies Lensed by the Frontier Fields Cluster MACSJ0717.5+3745. 2014, *Astrophys. J. Letters*, 782L, 36 ([arXiv:1401.0532](#))

Jones, T., **Wang, X.** et al. The Grism Lens-Amplified Survey from Space (GLASS) II. Gas-Phase Metallicity and Radial Gradients in an Interacting System At  $z \sim 2$ . 2015, *Astron. J.*, 149, 107 ([arXiv:1410.0967](#))

**Wang, X.** et al. The Grism Lens-Amplified Survey from Space (GLASS) IV. Mass reconstruction of the lensing cluster Abell 2744 from frontier field imaging and GLASS spectroscopy. 2015, *Astrophys. J.*, 811, 29 ([arXiv:1504.02405](#))

Rodney, S., ..., **Wang, X.**, et al. Illuminating a Dark Lens : A Type Ia Supernova Magnified by the Frontier Fields Galaxy Cluster Abell 2744. 2015, *Astrophys. J.*, 811, 70 ([arXiv:1505.06211](#))

Treu, T., Schmidt, K. B., Brammer, G. B., Vulcani, B., **Wang, X.** et al. The Grism Lens-Amplified Survey from Space (GLASS). I. Survey Overview and First Data Release. 2015, *Astrophys. J.*, 812, 114 ([arXiv:1509.00475](#))

Schmidt, K. B., ..., **Wang, X.** The Grism Lens-Amplified Survey from Space (GLASS). III. A census of Ly $\alpha$  Emission at  $z \gtrsim 7$  from HST Spectroscopy. 2016, *Astrophys. J.*, 818, 38 ([arXiv:1511.04205](#))

Hoag, A., ..., **Wang, X.** et al. The Grism Lens-Amplified Survey from Space (GLASS). VI. Comparing the Mass and Light in MACSJ0416.1-2403 using Frontier Field imaging and GLASS spectroscopy. 2016, *Astrophys. J.*, 831, 182 ([arXiv:1603.00505](#))

Huang, K., ..., **Wang, X.** Detection of Lyman-Alpha Emission From a Triple Imaged z=6.85 Galaxy Behind MACS J2129.4-0741. 2016, *Astrophys. J. Letters*, 823L, 14 ([arXiv:1605.05771](#))

Morishita, T., ..., **Wang, X.**, et al. The Grism Lens-Amplified Survey from Space (GLASS). IX. The dual origin of low-mass cluster galaxies as revealed by new structural analyses. 2017, *Astrophys. J.*, 835, 254 ([arXiv:1607.00384](#))

Vulcani, B., ..., **Wang, X.** The Grism lens-amplified survey from space (GLASS). VIII. The influence of the cluster properties on Halpha emitter galaxies at  $0.3 < z < 0.7$ . 2017, *Astrophys. J.*, 837, 126 ([arXiv:1610.04615](#))

**Wang, X.** et al. The Grism Lens-Amplified Survey from Space (GLASS) X. Sub-kiloparsec resolution gas-phase metallicity maps at cosmic noon behind the Hubble Frontier Fields cluster MACS1149.6+2223. 2017, *Astrophys. J.*, 837, 89 ([arXiv:1610.07558](#))

Morishita, T., Abramson, L. E., Treu, T., Schmidt, K. B., Vulcani, B., **Wang, X.** Characterizing Intracluster Light in the Hubble Frontier Fields. 2017, *Astrophys. J.*, 846, 139 ([arXiv:1610.08503](#))

Schmidt, K. B., ..., **Wang, X.** The Grism Lens-Amplified Survey from Space (GLASS). XI. Detection of CIV in Multiple Images of  $z = 6.11$  Ly $\alpha$  Emitter Behind RXCJ2248.7-4431. 2017, *Astrophys. J.*, 839, 17 ([arXiv:1702.04731](#))

Williams, P. R., ..., **Wang, X.** Discovery of three strongly lensed quasars in the Sloan Digital Sky Survey. 2018, *MNRAS*, 477L, 70 ([arXiv:1706.01506](#))

Kelly, P. L., ..., **Wang, X.** et al. An individual star at redshift 1.5 galaxy-cluster lens. 2018, *Nature Astronomy*, 2, 334 ([arXiv:1706.10279](#))

Abramson, L. E., ..., **Wang, X.** et al. The Grism Lens-Amplified Survey from Space (GLASS). XII. Spatially Resolved Galaxy Star Formation Histories and True Evolutionary Paths at  $z > 1$ . 2018, *Astron. J.*, 156, 29 ([arXiv:1710.00843](#))

Morishita, T., Abramson, L. E., Treu, T., **Wang, X.** et al. Metal Deficiency in Two Massive Dead Galaxies at  $z \sim 2$ . 2018, *Astrophys. J. Letters*, 856L, 4 ([arXiv:1803.01852](#))

Strait, V., ..., **Wang, X.** et al. Mass and Light of Abell 370: A Strong and Weak Lensing Analysis. 2018, *Astrophys. J.* accepted ([arXiv:1805.08789](#))

Quinn, E., ..., **Wang, X.** et al. Mass Modeling of Frontier Fields Cluster MACS J1149.5+2223 Using Strong and Weak Lensing. 2018, *Astrophys. J.*, 859, 1 ([arXiv:1806.00698](#))

**Wang, X.** et al. Discovery of Strongly inverted metallicity gradients in Dwarf Galaxies at  $z \sim 2$ . 2018, *Astrophys. J.* in press ([arXiv:1808.08800](#))

Hirtenstein, J., Jones, T., **Wang, X.** et al. The OSIRIS Lens-Amplified Survey (OLAS) I: Dynamical Effects of Stellar Feedback in Low Mass Galaxies at  $z \sim 2$ . 2018, *Astrophys. J.* in press, ([arXiv:1811.11768](#))

# CHAPTER 1

## Introduction

### 1.1 What is the baryon cycle and why is it important?

Baryon cycle is the cycling of the cosmic baryon budget through star formation and gas flows. Galaxies grow by getting their fuel from the intergalactic medium (gas inflows), converting it into stars (star formation), and returning energy/material to their surroundings (gas outflows). Figure 1.1 presents a vivid example of this complex phenomenon in the local Universe. While we have developed a concordance cosmological framework of the  $\Lambda$  cold dark matter ( $\Lambda$ CDM) hierarchical structure formation (see e.g. Aghanim et al., 2018, and references therein), we still lack a quantitative and coherent understanding of these baryonic processes, without which the formation and evolution of galaxies, e.g., our Milky Way (MW), cannot be characterized in detail.

### 1.2 How can we observe the baryon cycle at the peak of cosmic star formation?

The integral field spectroscopy (IFS) has expanded our vision of galaxies from integrated spectroscopic quantities extracted from small subregions through single slits/fibres to panoramic 2-dimensional (2D) views across their full surfaces, allowing for spatial variations of physical properties. This facilitates several large ground-based surveys, e.g., MaGNA (Bundy et al., 2015; Law et al., 2015), SAMI (Green et al., 2018; Medling et al., 2018), CALIFA (Sanchez et al., 2016), to capture the dynamic signatures of the baryon cycle in action. Yet the requirement of sufficient sampling, i.e., on sub-kiloparsec (sub-kpc) scale, to accurately map interesting kinematic features and spatial structures have limited the focus of such surveys to nearby galaxies ( $z \lesssim 0.03$ ). However,

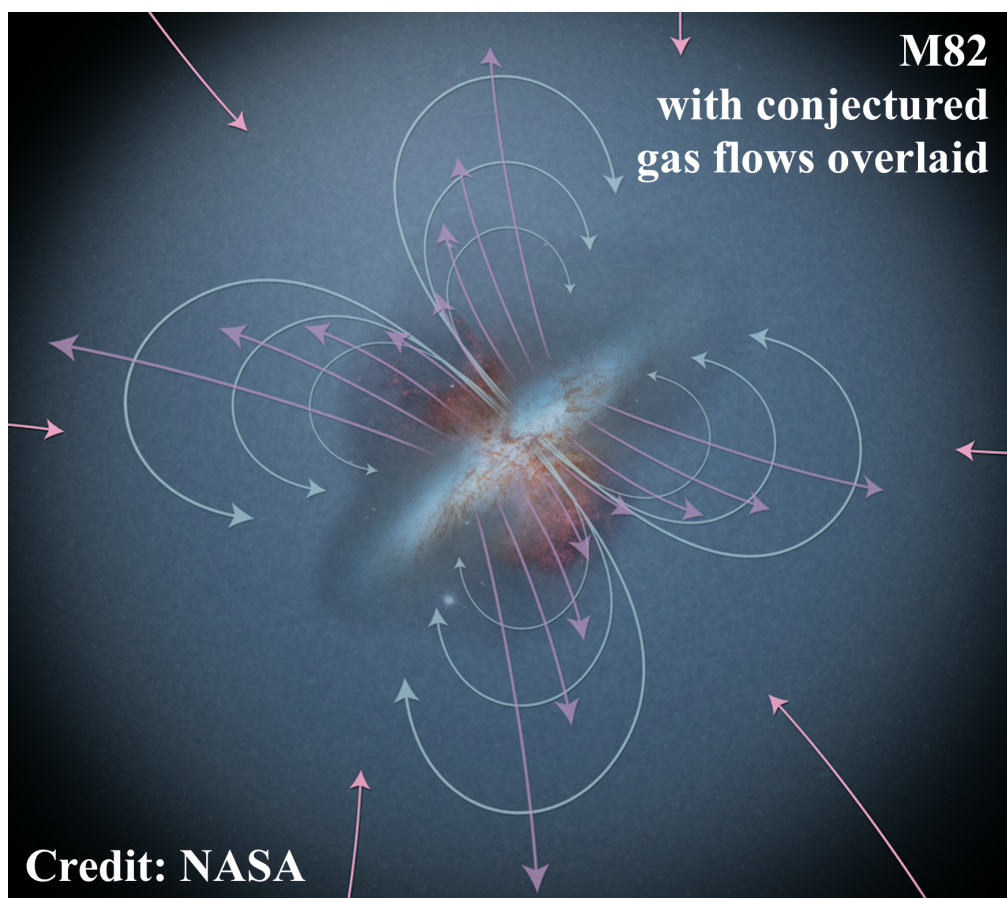


Figure 1.1 Onset of baryon cycling in the local Universe: the Messier 82 galaxy. Overlaid are the conjectured movements of gas in and around this galaxy undergoing active star formation.

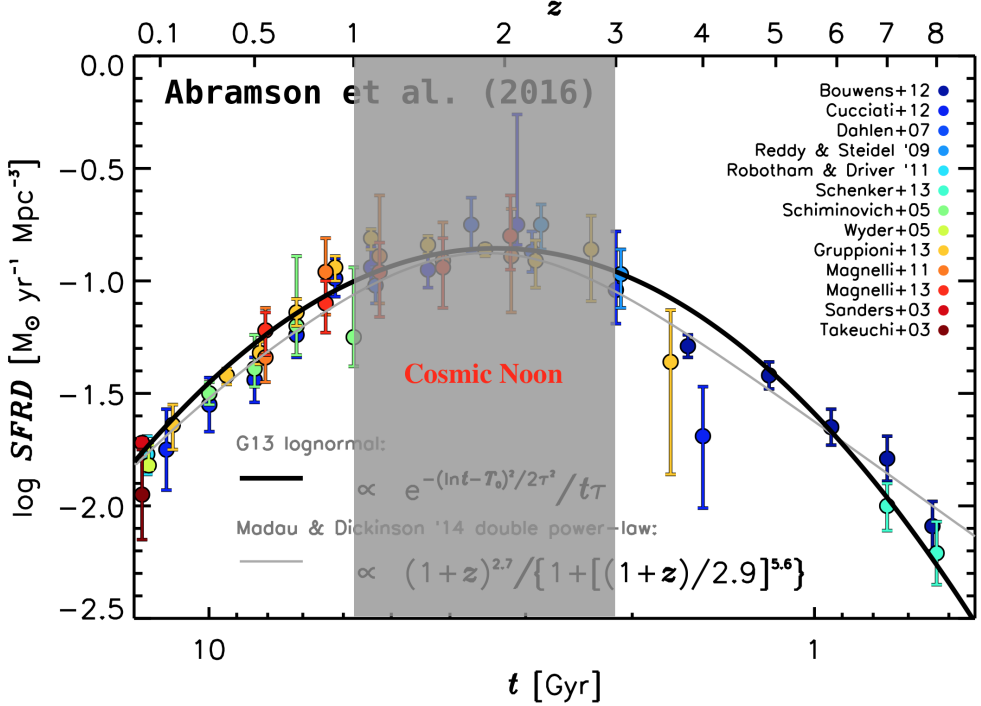


Figure 1.2 The rise and fall of the cosmic average star-formation rate density. The grey shaded region marks the peak epoch of cosmic star formation, usually coined the “cosmic noon”. At the cosmic noon, our Universe assembled roughly one half of its present day stellar mass using less than one third of its age. Figure credit: Abramson et al. (2016).

the local Universe is only the downhill of cosmic star formation, and the true climax of baryonic mass assembly and chemical enrichment happens at the epoch of  $1 \lesssim z \lesssim 3$ , as shown in Figure 1.2 (see e.g., Madau & Dickinson, 2014; Abramson et al., 2016, and references there in).

Numerical hydrodynamic simulations are by design capable of reproducing realistic galaxies at this epoch, by modeling various baryonic processes as sub-grid prescriptions (Davé et al., 2017; Hopkins et al., 2017; Pillepich et al., 2019). The vast majority of observational programs targetting cosmic-noon galaxies only measure their integrated spectroscopic quantities through single slits. Albeit offering great insight on the physics of galaxy formation and evolution at a population level, this kind of integrated spectroscopy lacks the ability to dissect the baryon cycle in individual systems. Ground-based IFS is no longer capable of probing the necessarily fine details at sub-kpc scale, ascribed to the atmospheric beam smearing effect and the intrinsically small size of high- $z$

galaxies. As displayed in Figure 1.3, the half-light radius of a typical  $L_*$  galaxy at  $z \sim 2$  is  $\sim 2.5\text{kpc}$ . In comparison, the optimal median seeing of  $\sim 0.^{\prime\prime}6$  is equivalent to a physical size of  $\sim 5\text{kpc}$ , resulting in the vast majority of  $z \sim 2$  star-forming galaxies unresolved. The assistance of adaptive optics (AO) can mitigate this problem, yet is challenging due to several reasons: low Strehl ratio and throughput, dearth of tip/tilt stars, narrow field of view with limited multiplexing capability, etc. Therefore, we need a more effective approach for sub-kpc scale spatially resolved spectroscopy of cosmic noon sources to compare statistically with theoretical results of cosmological zoom-in simulations, to shed light upon the cycling of baryons.

In my dissertation, I took a different route. The native resolution of the wide-field camera three (WFC3) onboard the Hubble Space Telescope (*HST*) is  $\sim 0.^{\prime\prime}13$ , equivalent to a spatial scale of  $\sim 1\text{kpc}$  at  $z \sim 2$  (cf. Figure 1.3), already matching the spatial resolution achieved by the aforementioned IFS surveys (i.e. MaGNA, SAMI, CALIFA) in mapping the physical properties of nearby galaxies. This spatial sampling rate is unhampered by atmospheric turbulence because the telescope is floating on top. The infrared (IR) spectroscopy on *HST* is enabled by the WFC3 grism elements. During observation, light from the science target is dispersed along a certain spatial axis pertinent to the telescope's roll angle *without any slits*. As a consequence, source morphology along the light dispersion direction is convolved onto the wavelength axis, causing the morphological broadening effect (van Dokkum et al., 2011). As shown in Figure 1.4, using some state-of-the-art data reduction techniques, I have been able to extract the appropriate 2D spectral information of my targets in spite of the heavy blending of neighboring objects and morphological broadening effect, to facilitate subsequent spatially resolved analysis.

The gravitational lensing phenomenon further improves the spatial resolution by roughly  $\sqrt{\mu}$ , where  $\mu$  is the lensing magnification factor. Thus by targeting cosmic-noon galaxies in the background and gravitationally lensed by foreground clusters of galaxies with the *HST* WFC3/IR grism elements, I exploit the lensing boost of *HST*'s resolving power to achieve sub-kpc scale spatial sampling of high- $z$  galaxies. Therefore I compile a statistically significant sample of star-forming galaxies at cosmic noon, whose spatial distribution of key physical properties are mapped out *precisely*. These properties include stellar mass ( $M_*$ ), star-formation rate (SFR), gas-phase metal-

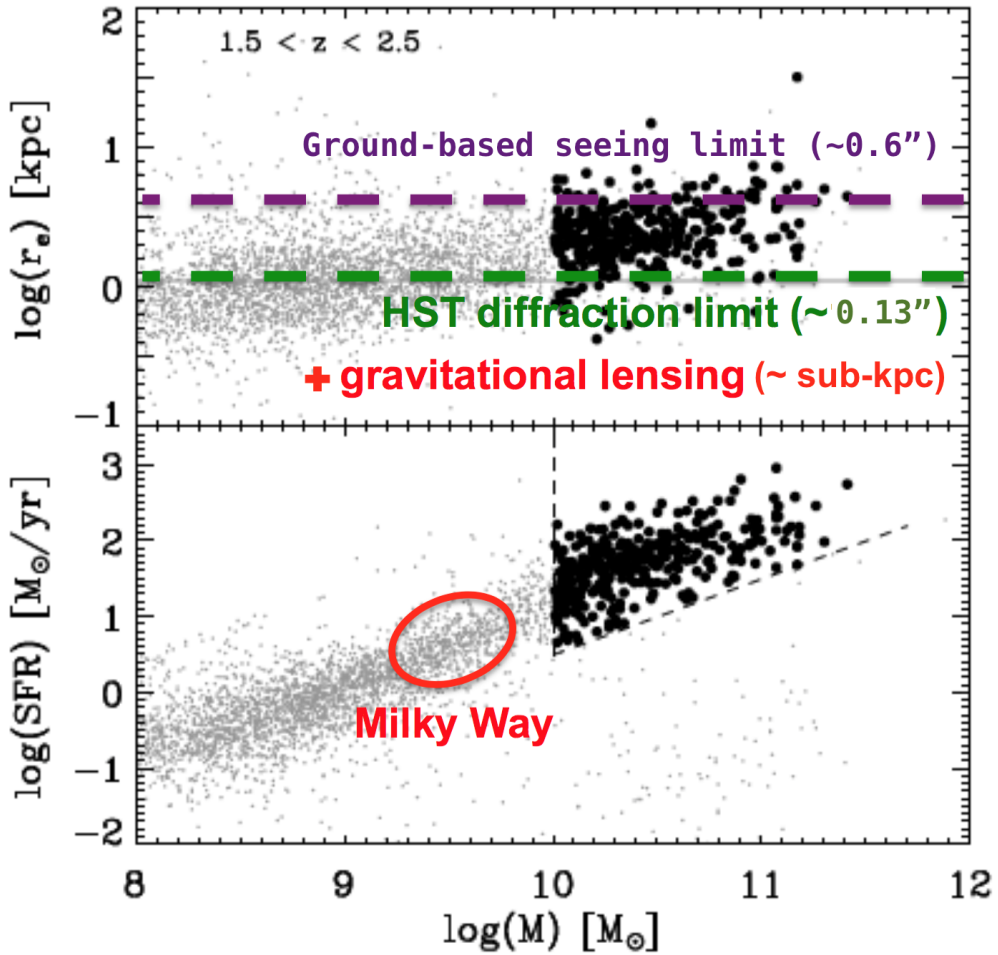


Figure 1.3 The relationship among the effective radius, star-formation rate and stellar mass for galaxies at  $z \sim 2$  covered by the CANDELS survey. The region where MW progenitors reside according to abundance matching is denoted by a red circle. The spatial resolution from natural seeing, native HST, and with gravitational lensing magnification combined are marked by the horizontal lines. We see that the only feasible approach to unambiguously resolve the MW progenitors is through the synergy of HST diffraction limit and lensing magnification. Figure credit: Wuyts et al. (2012b).

licity<sup>1</sup>, dust extinction, stellar population age, total gas mass, etc. This sample of galaxies has been shown to provide key insights into the effects of gas flows and feedback on the cycling of baryons at the cosmic noon.

### 1.3 Dissertation Overview

The content of my dissertation is briefly described as follows.

Chapter 2 is adapted from my first-author paper published as Wang et al. (2015), ApJ, 811, 29, DOI: 10.1088/0004-637X/811/1/29, and is reproduced with permission from the AAS. It presents a strong and weak lensing reconstruction of the massive cluster Abell 2744, the first cluster for which deep Hubble Frontier Fields (*HFF*) images and spectroscopy from the Grism Lens-Amplified Survey from Space (*GLASS*) are available. By performing a targeted search for emission lines in multiply imaged sources using the *GLASS* spectra, I obtain five high-confidence spectroscopic redshifts and two tentative ones. I confirm one strongly lensed system by detecting the same emission lines in all three multiple images. I also search for additional line emitters blindly and use the full *GLASS* spectroscopic catalog to test reliability of photometric redshifts for faint line emitters. I see a reasonable agreement between our photometric and spectroscopic redshift measurements, when including nebular emission in photometric redshift estimations. I introduce a stringent procedure to identify only secure multiple image sets based on colors, morphology, and spectroscopy. By combining 7 multiple image systems with secure spectroscopic redshifts (at 5 distinct redshift planes) with 18 multiple image systems with secure photometric redshifts, I reconstruct the gravitational potential of the cluster pixellated on an adaptive grid, using a total of 72 images. The resulting mass map is compared with a stellar mass map obtained from the deep *Spitzer* Frontier Fields data to study the relative distribution of stars and dark matter in the cluster. I find that the stellar to total mass ratio varies substantially across the cluster field, suggesting that stars do not trace exactly the total mass in this interacting system.

Chapter 3 is adapted from my first-author paper published as Wang et al. (2017), ApJ, 837,

---

<sup>1</sup>Throughout this dissertation I refer to the relative abundance of oxygen to hydrogen in the interstellar medium as gas-phase metallicity, or just metallicity for simplicity.

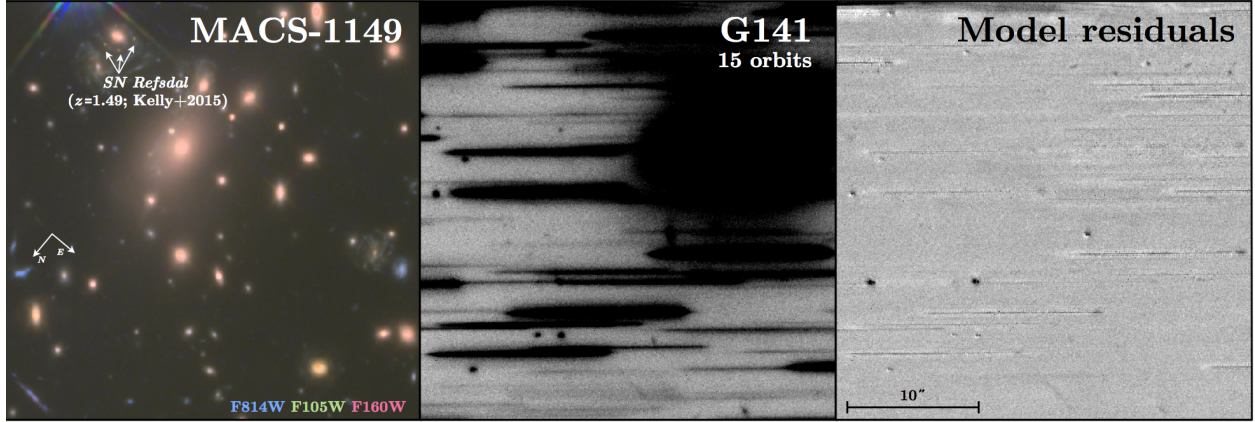


Figure 1.4 State-of-the-art data reduction techniques for *HST* WFC3/IR slitless spectroscopy are developed and adopted throughout my dissertation work. *Left*: the color-composite image of the galaxy cluster MACS1149.6+2223, where the first multiply imaged supernova (i.e. SN Refsdal) is discovered, as marked by the white arrows (Kelly et al., 2015b). *Middle*: the discovery of SN Refsdal triggers an *HST* follow-up grism program (Proposal ID 14041, P.I. Kelly) exposing the center of MACS1149.6+2223 with 30 orbits of WFC3/G141 split equally into 2 position angles. The obtained grism exposure from one of them is shown here. The analysis of these data constitutes a significant part in my dissertation work (see Chapter 3). *Right*: Due to the slitless nature of *HST* grism spectroscopy, severe blending takes place for neighboring objects along the light dispersion direction (see the middle panel). The data reduction techniques used throughout my dissertation work (see Chapter 4 for more details) properly account for this neighbour contamination and construct 2D spectral models for all sources within the WFC3 field of view (FoV). These spectral models are refined iteratively until a convergence point where the residual in the grism exposures after subtracting the fitted continuum models becomes negligible, which is shown here.

Figure credit: Gabe Brammer.

89, DOI: 10.3847/1538-4357/aa603c, and is reproduced with permission from the AAS. I combine the deep *HST* grism spectroscopy from both *GLASS* and the SN Refsdal follow-up program (see Figure 1.4) with a new Bayesian method to derive maps of gas-phase metallicity for 10 star-forming galaxies at high redshift ( $1.2 \lesssim z \lesssim 2.3$ ). Exploiting lensing magnification by the foreground cluster MACS1149.6+2223, I reach sub-kpc spatial resolution and push the limit of stellar mass associated with such high-z spatially resolved measurements below  $10^8 M_\odot$  for the first time. My maps exhibit diverse morphologies, indicative of various effects such as efficient radial mixing from tidal torques, rapid accretion of low-metallicity gas, and other physical processes that can affect the gas and metallicity distributions in individual galaxies. Based upon an exhaustive sample of all existing sub-kpc resolution metallicity gradient measurements at high  $z$ , I find that predictions given by analytical chemical evolution models assuming a relatively extended star-formation profile in the early disk-formation phase can explain the majority of observed metallicity gradients, without involving galactic feedback or radial outflows. I observe a tentative correlation between stellar mass and metallicity gradients, consistent with the “downsizing” galaxy formation picture that more massive galaxies are more evolved into a later phase of disk growth, where they experience more coherent mass assembly at all radii and thus show shallower metallicity gradients. In addition to the spatially resolved analysis, I compile a sample of homogeneously cross-calibrated integrated metallicity measurements spanning three orders of magnitude in stellar mass at  $z \sim 1.8$ . We use this sample to study the mass-metallicity relation (MZR) and find that the slope of the observed MZR can rule out the momentum-driven wind model at a  $3\sigma$  confidence level.

Chapter 4 is adapted from my first-author paper currently under review, i.e., Wang et al. (2018), arXiv:1808.08800. I report the first sub-kpc spatial resolution measurements of strongly inverted gas-phase metallicity gradients in two dwarf galaxies at  $z \sim 2$ . The galaxies have stellar masses  $\sim 10^9 M_\odot$ , specific star-formation rate  $\sim 20 \text{ Gyr}^{-1}$ , and global metallicity  $12 + \log(\text{O/H}) \sim 8.1$  (1/4 solar). Their metallicity radial gradients are measured to be highly inverted, i.e.,  $0.122 \pm 0.008$  and  $0.111 \pm 0.017 \text{ dex/kpc}$ , which is hitherto unseen at such small masses in similar redshift ranges. From the HST observations of the source nebular emission and stellar continuum, I present the 2D spatial maps of star-formation rate surface density, stellar population age, and gas fraction, which show that the two galaxies are currently undergoing rapid mass assembly via disk inside-out

growth. More importantly, using a simple chemical evolution model, I find that the gas fractions for different metallicity regions cannot be explained by pure gas accretion. My spatially resolved analysis based on a more advanced gas regulator model results in a spatial map of net gaseous outflows, triggered by active central starbursts, that potentially play a significant role in shaping the spatial distribution of metallicity by effectively transporting stellar nucleosynthesis yields outwards. The relation between wind mass loading factors and stellar surface densities measured in different regions of our galaxies shows that a single type of wind mechanism, driven by either energy or momentum conservation, cannot explain the entire galaxy. These sources present a unique constraint on the effects of gas flows on the early phase of disk growth from the perspective of spatially resolved chemical evolution within individual systems.

Chapter 5 is a summary of my previous work and concludes with a prospect of my ongoing analyses.

## CHAPTER 2

# Mass Reconstruction of the Lensing Cluster Abell 2744 from HFF Imaging and GLASS Spectroscopy

### 2.1 Introduction

In the past two decades, gravitational lensing by clusters of galaxies has transitioned from an exotic curiosity to an invaluable tool for astrophysics and cosmology (e.g. Kneib & Natarajan, 2011). Clusters can act as natural telescopes, magnifying background sources so that they appear brighter and more extended to the observer (e.g. Yee et al., 1996; Pettini et al., 2002; Bradač et al., 2012; Shirazi et al., 2014; Bayliss et al., 2014). The gravitational lensing effect can also be used to reconstruct the spatial distribution of mass in the clusters themselves, thus shedding light on the physics of dark matter and structure formation (e.g. Clowe et al., 2006; Bradač et al., 2006; Sand et al., 2008; Newman et al., 2013; Sharon et al., 2014; Merten et al., 2015).

In the past two years, clusters of galaxies as tools for cosmology and astrophysics have become a major focus of a Hubble Space Telescope (*HST*) initiative. As part of the Hubble Frontier Field (HFF) program<sup>1</sup>, six clusters of galaxies and six parallel fields are being imaged to unprecedented depths in seven optical and near-infrared (NIR) bands, using the Wide Field Camera 3 (WFC3) and the Advanced Camera for Surveys (ACS) (Coe et al., 2015). Similarly to previous public campaigns in legacy fields such as the Hubble Deep Fields (Williams et al., 1996; Ferguson et al., 2000), this major *HST* campaign has triggered coordinated observations with all major facilities, ranging from Director's Discretionary time on the *Spitzer* Space Telescope to deep observations with the Chandra X-ray Telescope and many ground based facilities.

---

<sup>1</sup><http://www.stsci.edu/hst/campaigns/frontier-fields/FF-Data>

One of the major drivers of the HFF initiative is to search for magnified objects behind galaxy clusters. Accurate magnification maps are needed to determine the unlensed (intrinsic) properties of these galaxies. Fortunately, the deep images increase significantly the number of known multiply imaged systems per cluster, thus improving dramatically the fidelity of the mass models, and magnification maps. Typical CLASH<sup>2</sup>-like depth imaging of clusters (limiting magnitude  $\sim 27$  ABmag for a 5- $\sigma$  point source Postman et al., 2012a) yields a handful of multiple image systems per cluster (e.g. Johnson et al., 2014), however at the depth of the HFF we expected to find tens of multiply image systems. This was beautifully confirmed by the first papers that analyzed the HFF imaging datasets (e.g. Jauzac et al., 2014; Ishigaki et al., 2015; Laporte et al., 2015).

The spectacular increase in the quality of imaging data has not yet been matched by advances in spectroscopic redshift ( $z_{\text{spec}}$ ) determination for the multiple images. Thus, modelers often have to rely on photometric redshifts to incorporate multiple images in their analysis, or sometimes they decide to leave the source redshift as a free parameter to be inferred by the lens model itself. Whereas one of these two choices is inevitable in the absence of other data, it is also fraught with peril. Photometric redshifts can be very uncertain and prone to catastrophic errors for sources that are well beyond the spectroscopic limit, such as most of the faint arcs and arclets. Similarly, letting the mass model determine the redshift of the multiple images can potentially introduce confirmation bias in the modeling process.

Obtaining spectroscopic redshifts for as many multiple image systems as possible is thus a fundamental step if we want to improve the mass models of the HFF clusters, and thus make the most of this groundbreaking initiative. Several efforts are currently underway to secure these redshifts, including our own based on the Grism Lens Amplified Survey from Space (GLASS) data. GLASS is a large *HST* program that has just completed obtaining deep spectroscopy in the fields of ten clusters, including all six in the HFF program.

Here we present a new mass model for the galaxy cluster Abell 2744, the first cluster for which both GLASS and HFF complete datasets are available. By exploiting the exquisite imaging and spectroscopic data we carry out a rigorous selection of multiple images used to constrain the mass

---

<sup>2</sup><http://www.stsci.edu/~postman/CLASH/Home.html>

model. We use spectroscopic redshifts – including 55 new line emitters detected at high-confidence – when available to supplement the photometric redshift ( $z_{\text{phot}}$ ) calibration. We then compare the inferred two dimensional mass distribution to the distribution of stellar mass as determined from the analysis of deep *Spitzer* imaging data, indicating that the stellar to mass ratio varies substantially across the cluster, which is expected given the merging nature of this cluster.

This Chapter is organized as follows. In Section 2.2 we give an overview of the data. In Section 2.3 we describe the reduction and analysis of the GLASS data. In Section 2.4 we detail our algorithm for selection of multiple image systems. In Section 2.5 we present our mass model and study the relative distribution of stellar and total mass. In Section 2.7 we summarize our conclusions. Throughout this work we adopt a standard concordance cosmology with  $\Omega_m = 0.3$ ,  $\Omega_\Lambda = 0.7$  and  $h = 0.7$ . All magnitudes are given in the AB system (Oke, 1974).

## 2.2 Data

Being one of the most extensively studied galaxy clusters, Abell 2744 is observed on a spectrum extending from X-ray to radio bands (e.g. Kempner & David, 2004). In this Chapter, we focus on the optical and NIR imaging and spectroscopy data newly acquired with the Hubble and *Spitzer* Space Telescopes, as part of the GLASS program (2.2.1) and HFF initiative (2.2.2 and 2.2.3).

### 2.2.1 The Grism Lens-Amplified Survey from Space

The Grism Lens-Amplified Survey from Space<sup>3</sup> (GLASS, GO-13459, P.I. Treu) is observing the cores of 10 massive galaxy clusters with the *HST* WFC3 NIR grisms G102 and G141 providing an uninterrupted wavelength coverage from  $0.8\mu\text{m}$  to  $1.7\mu\text{m}$ . The slitless spectroscopy is distributed over 140 orbits of *HST* time in cycle 21. The last GLASS observations were taken in January 2015. Amongst the 10 GLASS clusters, 6 are targeted by the HFF (see Section 2.2.2) and 8 by the Cluster Lensing And Supernova survey with Hubble (CLASH; P.I. Postman, Postman et al., 2012a). Prior to each grism exposure, imaging through either F105W or F140W is obtained to

---

<sup>3</sup><http://glass.physics.ucsb.edu>

assist the extraction of the spectra and the modeling of contamination from nearby objects on the sky. The total exposure time per cluster is 10 orbits in G102 (with either F105W or F140W) and 4 in G141 with F140W. Each cluster is observed at two position angles (P.A.s) approximately 90 degrees apart to facilitate deblending and extraction of the spectra.

In concert with the NIR observations on the cluster cores the two parallel fields corresponding to the two P.A.s are observed with ACS’s F814W filter and G800L grism. Each parallel field has a total exposure time of 7 orbits. These observations map the cluster infall regions.

A key focus point of GLASS is the advancement and improvement of the lens models of the 10 surveyed clusters. This work focuses on the modeling of the first cluster in the GLASS survey with complete GLASS spectroscopy and HFF imaging as described in Section 2.3.

## 2.2.2 Hubble Frontier Fields

The Hubble Frontier Fields initiative<sup>4</sup> (HFF, P.I. Lotz) is a Director’s Discretionary Time legacy program with *HST* devoting 840 orbits of *HST* time to acquire optical ACS and NIR WFC3 imaging of six of the strongest lensing galaxy clusters on the sky; Abell 370, Abell 2744, MACSJ 2129, MACSJ 0416, MACSJ 0717, and MACSJ 1149. For a 5- $\sigma$  point source, the limiting magnitudes are roughly 29 ABmag in both the ACS/optical (F435W, F606W, F814W) and WFC3/IR filters (F105W, F125W, F140W, F160W). All six HFF clusters are included in the GLASS sample described in Section 2.2.1. The program was initiated in *HST* cycle 21 and is planned for completion in 2016. The first cluster to have complete HFF and GLASS data available is the cluster Abell 2744.

An important aspect of the HFF efforts has been the community efforts to model the lensing clusters. Prior to the start of the HFF observations five independent groups (CATS team, Sharon et al., Merten, Zitrin et al., Williams et al., and Bradac et al.) provided lens models of the HFF clusters, which have been made available online<sup>5</sup>. In the remainder of this work we will use our own models from Bradac et al., but we will make comparison with several of the other publicly

---

<sup>4</sup><http://www.stsci.edu/hst/campaigns/frontier-fields>

<sup>5</sup><http://archive.stsci.edu/prepds/frontier/lensmodels/>

available HFF lens models of Abell 2744.

### 2.2.3 *Spitzer* Frontier Fields

The *Spitzer* Frontier Fields program<sup>6</sup> (P.I. Soifer) is a Director’s Discretionary Time program that images all six strong lensing galaxy clusters targeted by the HFF in both warm IRAC channels (3.6 and 4.5  $\mu\text{m}$ ). With the addition of archival imaging from *IRAC Lensing Survey* (P.I. Egami) we reduced the data using the methodology employed by the *Spitzer UltRa Faint SURvey Program* (SURFS UP, P.I. Bradač, Bradač et al., 2014). IRAC imaging reaches  $\sim 50$  hr depth on the *primary* (Abell 2744 cluster) and *parallel* ( $\sim 6'$  to the west) fields. There are four *flanking* fields with  $\sim 25$  hr depth (two to the north and two to the south) of the primary and parallel fields. The nominal depth for a  $5\sigma$  point source can reach 26.6 ABmag at 3.6  $\mu\text{m}$  and 26.0 ABmag at 4.5  $\mu\text{m}$ , respectively. However this sensitivity might be compromised in cluster center due to blending with cluster members and the diffuse intra-cluster light (ICL).

For this work, we focus on the primary field of Abell 2744 that we have processed in a fashion very similar to that discussed in Bradač et al. (2014); Ryan et al. (2014); Huang et al. (2015). In brief, we applied additional warm-mission column pulldown and automuxstripe corrections as provided by the *Spitzer* Science Center to the corrected basic-calibrated data (cBCD) to improve image quality, particularly near bright stars. We process these files through a standard overlap correction to equalize the sky backgrounds of the individual cBCDs. We drizzle these sky-corrected cBCDs to  $0.^{\prime\prime}6 \text{ pix}^{-1}$  with a DRIZ\_FAC= 0.01 using the standard MOPEX software<sup>7</sup>. As a final note, there are  $\sim 1800$  frames (with FRAMETIME $\sim 100$  s) per output pixel in the deep regions.

## 2.3 GLASS Observation and Data Reduction

The two P.A.s of GLASS data analyzed in this study were taken on August 22 and 23 2014 (P.A. = 135) and October 24 and 25 2014 (P.A. = 233), respectively. Prior to reducing the complete

---

<sup>6</sup><http://ssc.spitzer.caltech.edu/warmmission/scheduling/approvedprograms/ddt/frontier/>

<sup>7</sup><http://irsa.ipac.caltech.edu/data/SPITZER/docs/dataanalysistools/tools/mopex/>

GLASS data each exposure was checked for elevated background from He Earth-glow (Brammer et al., 2014b) and removed, if necessary. The Abell 2744 data was favorably scheduled so only the August 23 reads were affected and thus removed by our reduction pipeline.

The resulting total exposure times for the individual grism observations are: G102\_PA135 10929 seconds, G141\_PA135 4212 seconds, G102\_PA233 10929 seconds, and G141\_PA233 4312 seconds. The corresponding exposure times for the direct GLASS imaging are: F105W\_PA135 1068 seconds, F140W\_PA135 1423 seconds, F105W\_PA233 1068 seconds, and F140W\_PA233 1423 seconds.

In Figure 2.1 we show a color composite image of Abell 2744, using the optical and NIR imaging from the HFF combined with the NIR imaging from GLASS. The red and green squares show the positions of the spectroscopic GLASS Abell 2744 field-of-views.

The GLASS observations are designed to follow the 3D-HST observing strategy (Brammer et al., 2012a). The data were processed with an updated version of the 3D-HST reduction pipeline<sup>8</sup>. Below we summarize the main steps in the reduction process of the GLASS data but refer to Brammer et al. (2012a) and Treu et al. (2015a) for further details.

The data were taken in a 4-point dither pattern identical to the one shown in Figure 3 of Brammer et al. (2012a) to optimize rejection of bad pixels and cosmic rays and improve sampling of the WFC3 point spread function. At each dither position, a combination, a direct (F105W or F140W), and a grism (G102 or G141) exposure were taken. The direct imaging is commonly taken in the filter “matching” the grism, i.e. pairs of F105W-G102 and F140W-G141. However, to accommodate searches for supernovae and the characterization of their curves in GLASS clusters, each individual visit is designed to have imaging in both filters. Hence several pairs of F140W-G102 observations exist in the GLASS data. This does not affect the reduction and extraction of the individual GLASS spectra.

The individual exposures were turned into mosaics using AstroDrizzle from the DrizzlePac (Gonzaga & et al., 2012), the replacement for MultiDrizzle (Koekemoer et al., 2003) used in earlier versions of the 3D-HST reduction pipeline. Then all exposures and visits were aligned

---

<sup>8</sup><http://code.google.com/p/threedhst/>

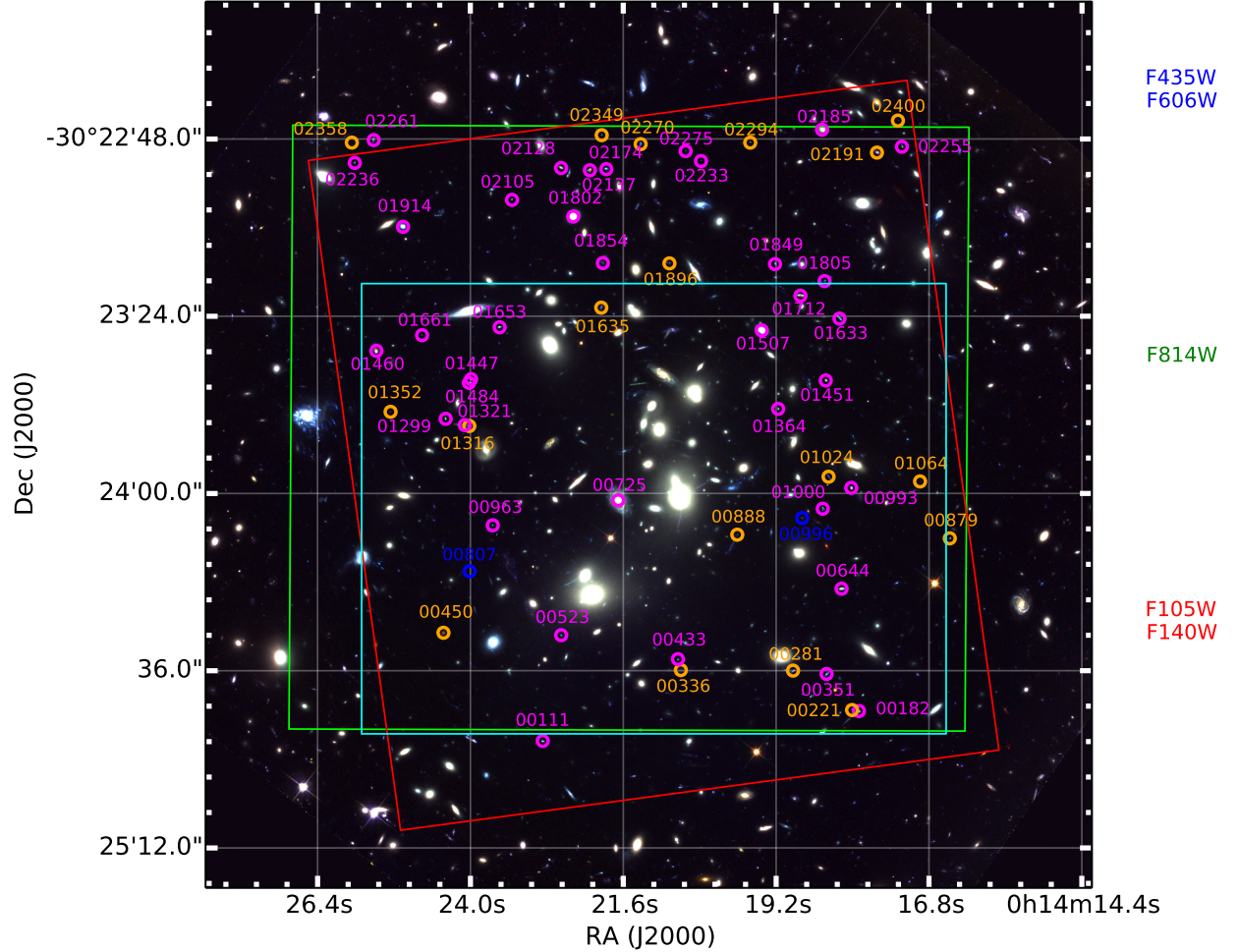


Figure 2.1 The color composite image of Abell 2744 based on the HFF and GLASS imaging. The blue, green and red channels are composed by the filters on the right. The two distinct P.A.s of the spectroscopic GLASS pointings are shown by the red (P.A.=233 degrees) and green (P.A.=135 degrees) squares. Figure 2.2 shows the grism images corresponding to these two P.A.s. The locations of the emission line objects from Table 2.2 are marked by circles, with color coding reflecting the GLASS spectroscopic redshift quality (cf. Section 2.4.2 and column “Quality” in Table 2.2; 2=blue, 3=orange, and 4=magenta). The cyan square shows the outline of Figure 2.3.

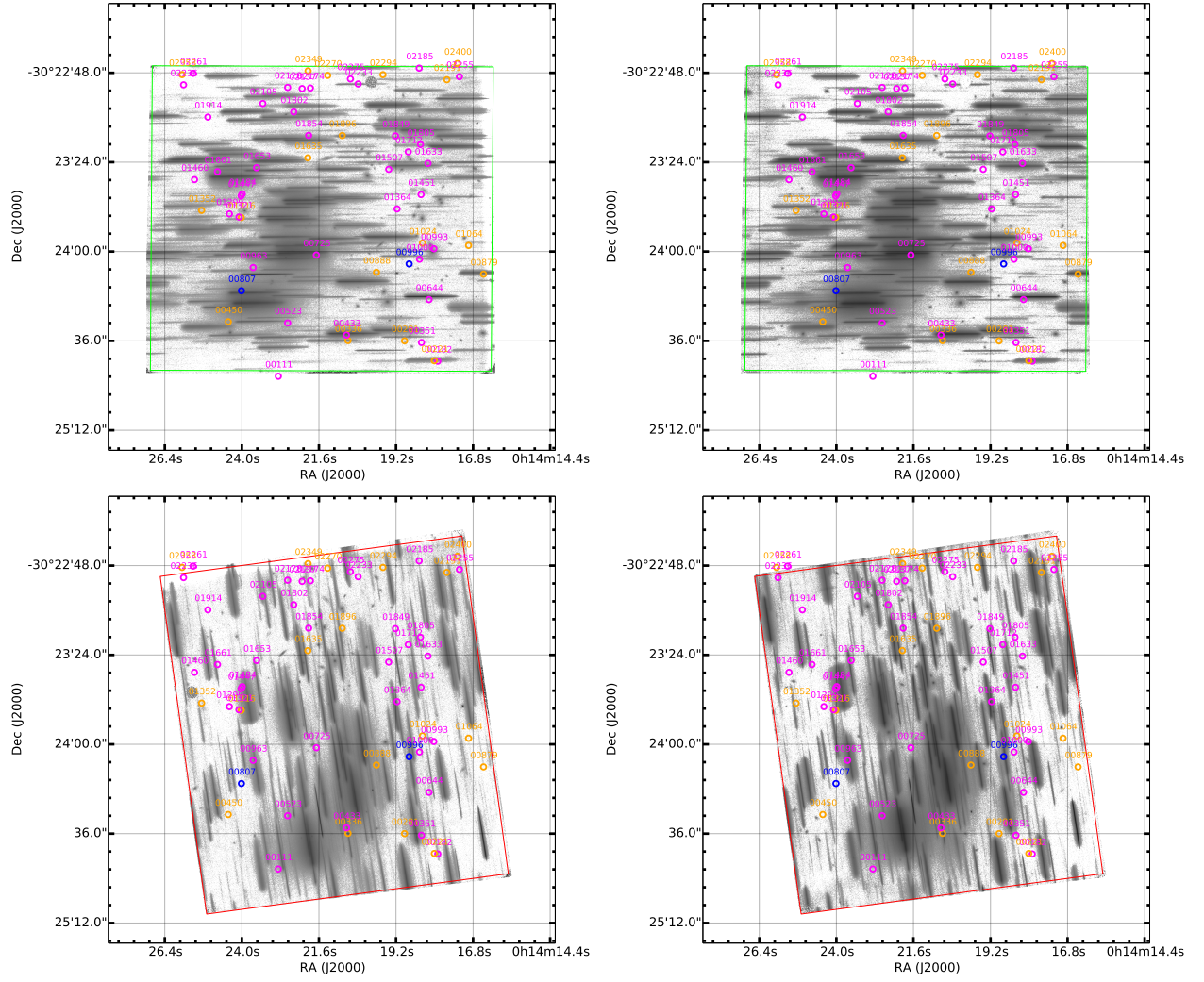


Figure 2.2 The GLASS G102 (left) and G141 (right) grism pointings of Abell 2744 at two distinct P.A.s, with field-of-view shown by the red (P.A.=233 degrees) and green (P.A.=135 degrees) squares. The circles in all panels denote the positions of the emission line objects identified in this work, with color coding following the convention adopted in Figure 2.1.

using `tweakreg`, with backgrounds subtracted from the direct images by fitting a second order polynomial to each of the source-subtracted exposures. We subtracted the backgrounds using the master sky presented by Kümmel et al. (2011) for the G102 grism, while for the G141 data the master backgrounds were developed by Brammer et al. (2012a) for 3D-HST. The individual sky-subtracted exposures were combined using a pixel scale of 0."/06 per pixel as described by Brammer et al. (2013) (~half a native WFC3 pixel) which corresponds to roughly 12Å/pixel and 22Å/pixel for the G102 and G141 grism dispersions, respectively. Figure 2.2 shows these full field-of-view mosaics of the two NIR grisms (G102 on the left and G141 on the right) at the two GLASS P.A. for Abell 2744. The individual spectra were extracted from these mosaics by predicting the position and extent of each two-dimensional spectrum according to the `SExtractor` (Bertin & Arnouts, 1996) segmentation maps from the corresponding direct images. This is done for every single object and contaminations, i.e., dispersed light from neighboring objects in the direct image, so these contaminations can be estimated and accounted for.

## 2.4 Identification of Multiple Images

In this section we describe how we identify and vet multiple image candidates using imaging (2.4.1) and spectroscopic (2.4.2 and 2.4.3) data.

### 2.4.1 Imaging Data: Identification and Photometric Redshifts

Merten et al. (2011) published the first detailed strong lensing analysis of Abell 2744 identifying a total of 34 multiple images (11 source galaxies) in imaging data pre-dating the HFF. With the addition of the much deeper HFF data, now a total of 176/56 candidate arc images/systems have been identified prior to this work (Atek et al., 2014, 2015; Zitrin et al., 2014; Richard et al., 2014; Jauzac et al., 2014; Lam et al., 2014; Ishigaki et al., 2015, see also Figure 2.3 and Table 2.1). We identify a new multiply imaged system (i.e. system 60 in Table 2.1) comprised of three images.

Despite the vast number of identifications, only a handful of multiple images have been spectroscopically confirmed; arcs 4.3 and 6.1 were spectroscopically confirmed by Richard et al. (2014),

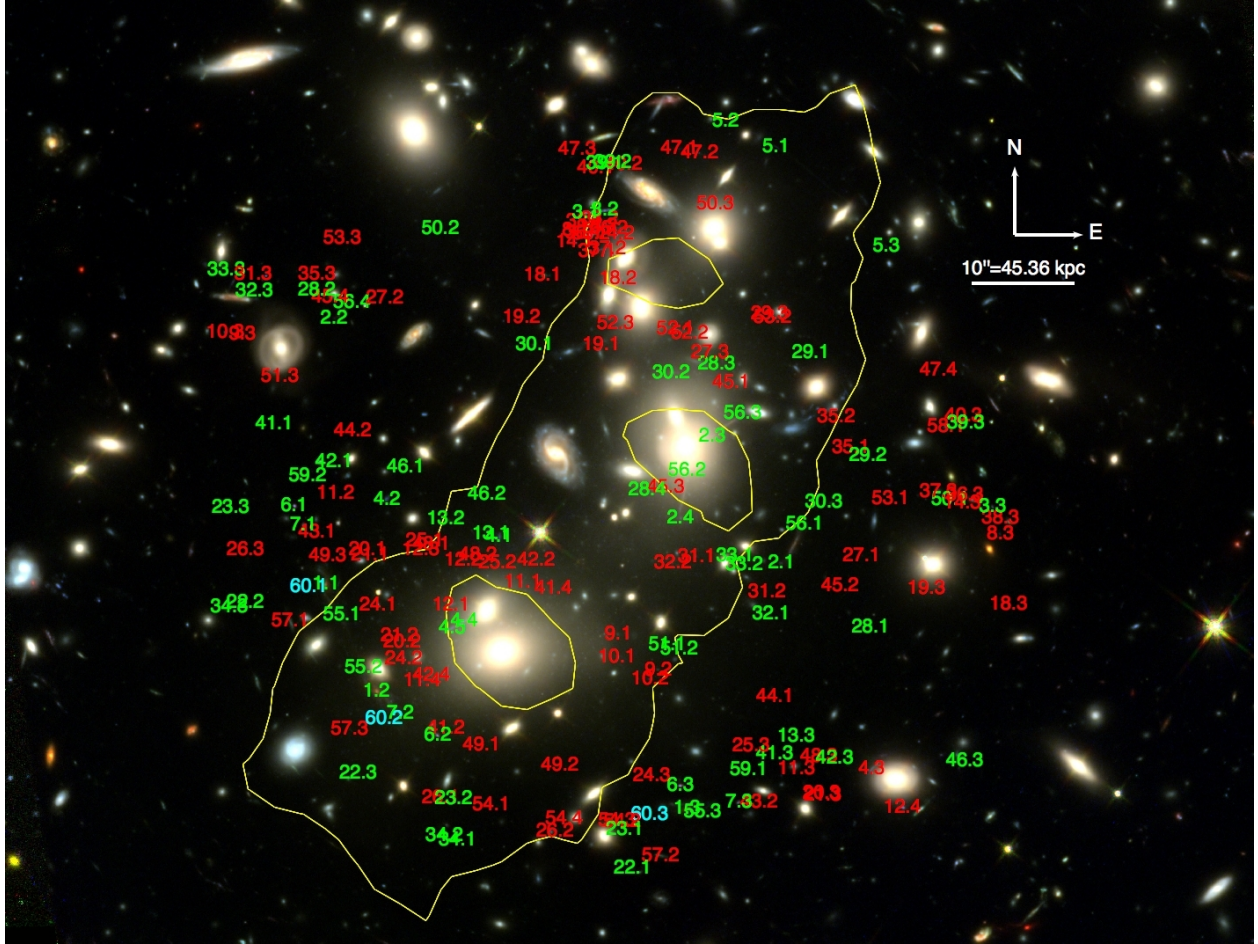


Figure 2.3 All multiple images discovered to date in Abell 2744. Green images are used in the lens model, while red images are unused for reasons discussed in Section 2.4. Cyan images belong to a new multiple image system discovered in this work. The yellow line is the critical curve from our best-fit lens model at  $z = 9$ . The RGB image is a combination of F105W, F125W and F160W.

arcs 3.1, 3.2 and 4.5 by Johnson et al. (2014), and arc 18.3 by Clément et al. (in preparation). All corresponding redshifts can be found in Table 2.1. When spectroscopy is lacking, confirming that images belong to the same source is much more difficult. Photometric redshifts alone are not adequate for confirmation. Ilbert et al. (2006) found that, within a given survey, the fraction of catastrophic errors in photometric redshift increases with faintness and redshift. Multiple images are typically faint and are necessarily at redshifts larger than the cluster redshift, which is  $z = 0.308$  for Abell 2744. The mean F140W magnitude of all images in Table 2.1 is 27.11, and the mean source redshift is  $z = 2.63$ . Photometry of sources in cluster fields is complicated due to blending with cluster members and the ICL. While we do compute photometric redshifts in order to use the multiple images in our lens model, we do not rely on them alone to test the fidelity of the images.

We instead rely on color and morphology information to determine whether images belong to the same multiple image system; to first order, multiple images of the same source have identical colors. To compute colors, photometry is done using **SExtractor** in dual-image mode. We use F160W as the detection image because it detects the largest fraction of all multiple image candidates. We then measure isophotal magnitudes and errors in all seven photometric filters. Due to difficulties in detecting many of the multiple image candidates using the default **SExtractor** settings, we adopt a more aggressive set of settings for the objects with low  $S/N$  and/or highly blended. We refer to the default **SExtractor** settings as “cold” mode and the more aggressive one as “hot” mode photometry. These are similar in spirit but not identical to those adopted by Guo et al. (2013). Even with the “hot” mode settings, we cannot detect all of the multiple image candidates, though the detected fraction is vastly increased over the “cold” mode settings. Using the seven HFF photometric filters, we compute 4 colors for each image:  $F435W - F606W$ ,  $F814W - F105W$ ,  $F125W - F140W$ , and  $F140W - F160W$ <sup>9</sup>. The colors are computed within a fixed aperture (MAG\_APER) that is 0.4'' in diameter. We compute a reduced “color- $\chi^2$ ” for each image:

$$\chi_{I\nu}^2 = \frac{1}{N-1} \sum_{i=1}^N \left( \frac{C_i - \bar{C}_i}{\sigma_i} \right)^2, \quad (2.1)$$

where  $i$  runs over the number of colors,  $N$  is the total number of colors we are able to measure,  $C_i$

---

<sup>9</sup>Note that the last two colors are not independent due to the repetition of  $F140W$ . We chose to repeat one filter to increase the number of color bins.

is the  $i$ -th color,  $\bar{C}_i$  is the inverse variance-weighted mean color of all images in the system, and  $\sigma_i$  is the uncertainty in the  $i$ -th color.

Multiple images of the same source also have predictable morphologies. In rare cases, more than one images of the same source possess a number of uniquely identifiable features. For instance, there are two such systems in Abell 2744, i.e., systems 1 and 2. The counterparts to systems 1 and 2 are systems 55 and 56, respectively. We include both counterpart systems in the lens model at the spectroscopic redshifts of systems 1 and 2 that we measure in this work. All multiple images in Table 2.1 are visually inspected. We assign each image a grade that determines the likelihood that it is part of the system to which it is assigned. We perform this grading exercise in a lens model-independent fashion; we do not make any assumptions about the location of the critical curves relative to the graded images. There are, however, configurations of multiple images that are impossible to achieve through gravitational lensing by galaxy clusters, such as three individual images (not part of an elongated arc) on the same side of, and very distant from the cluster core with no counter-images. Other information such as surface brightness and symmetry can be incorporated independently of an assumed mass distribution, and we rely on this information much more heavily in assigning the morphology grade. The grading scheme based on morphological similarity is as follows:

- 4** Image is definitely part of the system
- 3** Image is very likely part of the system
- 2** Image is potentially part of the system
- 1** Image is very unlikely part of the system
- 0** Image is definitely not part of the system

We use the color and morphology information together to determine whether to include a multiple image in our model. The joint criteria are:

$$(\chi_{I\nu}^2 < 1.5 \quad \vee \quad M > 5) \quad \wedge \quad M > 0, \quad (2.2)$$

where  $M$  is the summed morphology grade from each inspector, which ranges from 0-8. In cases where the contamination by foreground objects, clusters members or ICL is severe, we rely only on the morphology criterion,  $M > 5$ . The particular  $\chi^2_{\nu}$  threshold value of 1.5 was chosen because it is in the typical range for a good reduced chi-square test, and most of the images in spectroscopically confirmed systems are below this value.  $M > 5$  is chosen because in the least confident case that obeys this,  $M = 6$ , the modelers either both think the image is very likely part of the system ( $M = 3$ ) or one thinks the image is potentially part of the system ( $M = 2$ ), while the other is sure of it ( $M = 4$ ).

For a multiple image system to constrain the lens model, we must estimate its redshift. Having photometric redshift measurements for multiple images of the same source can provide a tighter constraint than a single measurement. Individual photometric redshifts are computed using EAZY (Brammer et al., 2008a). We then use a hierarchical Bayesian model to obtain a single redshift probability density function for each system (Dahlen et al., 2013). The mode of this probability density function will be referred to as  $z_{\text{Bayes}}$ . Only non-contaminated objects contribute to calculating  $z_{\text{Bayes}}$ . We graphically outline the procedure for measuring and including photometric redshifts as inputs to our lens model in Figure 2.4. 2/57 systems (36 and 52) are entirely contaminated, so we do not compute  $z_{\text{Bayes}}$  for those systems. 14/57 systems have  $z_{\text{Bayes}} < z_{\text{Cluster}}$ , and thereby are not included in lens modeling (a fraction of those have poorly constrained posteriors, monotonically declining from 0; they are highly uncertain and considered unreliable; we label them by assigning  $z_{\text{Bayes}} = 0.01$ ). 5/57 systems have a multi-modal or extremely broad Bayesian redshift distribution. We similarly do not include these systems in the lens modeling. For systems where only one image passed the color/morphology criteria and that image is not contaminated, we report  $z_{\text{Bayes}}$  in Table 2.1, but we do not include these systems in the modeling. We show the posterior redshift distributions for some of these cases in the Appendix. System 18 consists of a spectroscopically confirmed image (18.3), but the system as a whole does not pass all criteria required to be considered a multiple image system. Our screening rules out all the above-mentioned systems and delivers a secure set of 25/57 multiple arc systems that are used in lens modeling.

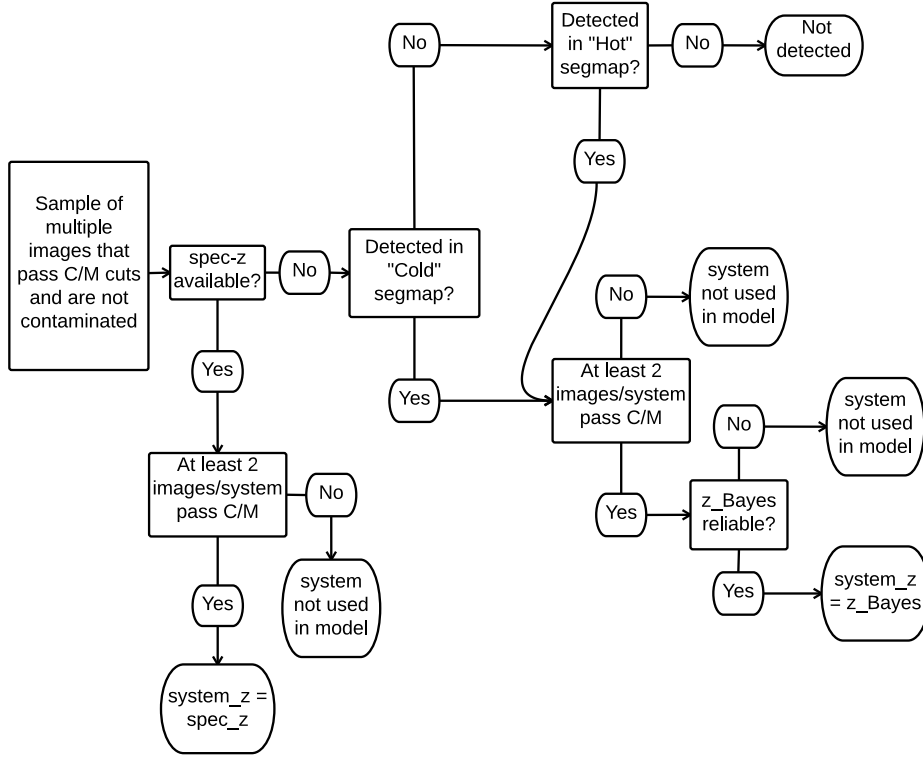


Figure 2.4 Flow chart describing our procedure for assigning photometric redshifts to multiple image systems. Two segmentation maps, a “hot” and a “cold” version, were used for source detection. The detection and deblending thresholds are set to the SExtractor defaults in the cold segmentation map. Objects detected in the cold segmentation map, typically the brighter and more isolated ones, have more accurate photometry. The hot segmentation map was created using extremely aggressive detection and deblending thresholds. It detects the majority of the remaining multiple images that are not detected in the cold version. C/M cuts refer to the color/morphology cuts used to purify the sample of multiple images.  $z_{\text{Bayes}}$  refers to the redshift obtained from combining multiple redshifts in a hierarchical Bayesian model (Dahlen et al., 2013).  $z_{\text{Bayes}}$  is considered reliable if it is larger than the redshift of Abell 2744,  $z = 0.308$ , and it is not multi-valued. See the Appendix for examples of multiple image systems that pass and fail some of the tests in this flow chart.

## 2.4.2 Targeted GLASS Spectroscopy

GLASS spectroscopy was carefully examined for a total of 179 multiply lensed arc candidates mostly seen on both P.A.s with the goal of measuring spectroscopic redshifts. Each spectrum was visually inspected by multiple investigators using the GLASS Graphic User Interfaces (GUIs) GLASS Inspection GUI (GiG) and GLASS Inspection GUI for redshifts (GiGz). The results were then combined and a preliminary list of arcs with emission lines was drafted. In the end, another round of double-check by re-running GiGz was also executed to make sure no potential emission lines were missed. Following GLASS procedure, a quality flag was given to the redshift measurement: Q=4 is secure; Q=3 is probable; Q=2 is possible; Q=1 is likely an artifact. These quality criteria take into account the signal to noise ratio of the detection, the probability that the line is a contaminant, and the identification of the feature with a specific emission line. For example, Q=4 is given for spectra where multiple emission have been robustly detected; Q=3 is given for spectra where either a single strong emission line is robustly detected and the redshift identification is supported by the photometric redshift, or when more than one feature is marginally detected; Q=2 is given for a single line detection of marginal quality. As shown in Table 2.2, new spectroscopic redshifts were obtained for 7 images in total, corresponding to 5 systems. Among them, 5 high-confidence (with quality flags 3 or 4) spectroscopic redshifts were measured for arcs 1.3, 6.1, 6.2, 6.3, 56.1. The spectra of these objects are shown in Figures 2.5–2.9. In particular for arc 6.1, our spectroscopic redshift matches that reported by Richard et al. (2014), and we provide the first spectroscopic confirmation that 6.2 and 6.3 are images of the same system.

We note that our measured redshift for arc 56.1  $z_{\text{spec}} = 1.20$  (Q=3; probable) differs significantly from that given by Johnson et al. (2014a) for arc 2.1  $z_{\text{spec}} = 2.2$  (possible), even though the two systems are likely to be physically connected. Our measurement is based on three pieces of evidence. First, we detect a spectral feature in G141 at both P.A.s (see Figure 2.9 for details) with sufficiently high signal to noise ratio to study its spectra shape. The feature is better described by a single line (identified by us as H $\alpha$  at  $z = 1.2$ ) rather than a doublet like [O III] ( $\Delta\chi^2 = 2.4$ ). Second, a line is marginally detected in one of the G102 spectra at exactly the wavelength expected for [O III]  $z = 1.2$ . Third, the wide spectral coverage of our data and the data available in the literature

rule out the possibility of the feature we see in G141 being other prominent lines such as Mg II and [O II]. Taking into account both the evidence and previous results, we assign a quality flag of Q=3 (probable).

The uncertainty on our spectroscopic redshift measurements is limited by the resolution of approximately 50Å and by uncertainties in the zero point of the wavelength calibration. By comparing multiple observations of the same object we estimate the uncertainty of our measurements to be in the order of  $\Delta z \sim 0.01$ . This is sufficient for our purposes and we will not pursue more aggressive approaches to improve the overall redshift precision (e.g. Brammer et al., 2012a).

### 2.4.3 Blind Search in GLASS Data

The targeted spectroscopy done in Section 2.4.2 could potentially miss some multiply imaged sources that are not identified photometrically. In order to increase the redshift completeness of emission line sources (both multiply and singly imaged), we also conducted a blind search within the entire grism field-of-view. As a first step, one of us (T.T.) visually inspected all the 2D grism spectroscopic data, the contamination models, and residuals after contamination for each of the 2445 objects in the prime field of Abell 2744 given by the GLASS catalog. This yielded a list of 133 candidate emission line systems that were later on inspected using the GLASS GUIs GIG and GIGz by two of us (X.W. and K.B.S.) to confirm emission line identifications and measure redshifts. In order to search for previously undiscovered multiple images we inspected each set of objects with mutually consistent redshift. None of the sets of galaxies at the same spectroscopic redshifts are consistent with being multiply lensed images of the same source. Some of them are ruled out because of their position in the sky, while others are ruled out because their colors and morphology are inconsistent with the lensing hypothesis.

Nonetheless, we compiled a list of singly imaged emission line objects, consisting of 18, 16, and 34 quality 2, 3, and 4 spectroscopic redshift measurements respectively, which are color coded in Figure 2.1. Among them, the high-confidence (with quality flag 3 or 4; orange and magenta circles in Figure 2.1) emission line identifications are also included in Table 2.2. As mentioned in Section 2.4.1, via running EAZY on the full-depth seven-filter HFF imaging data, we were able to

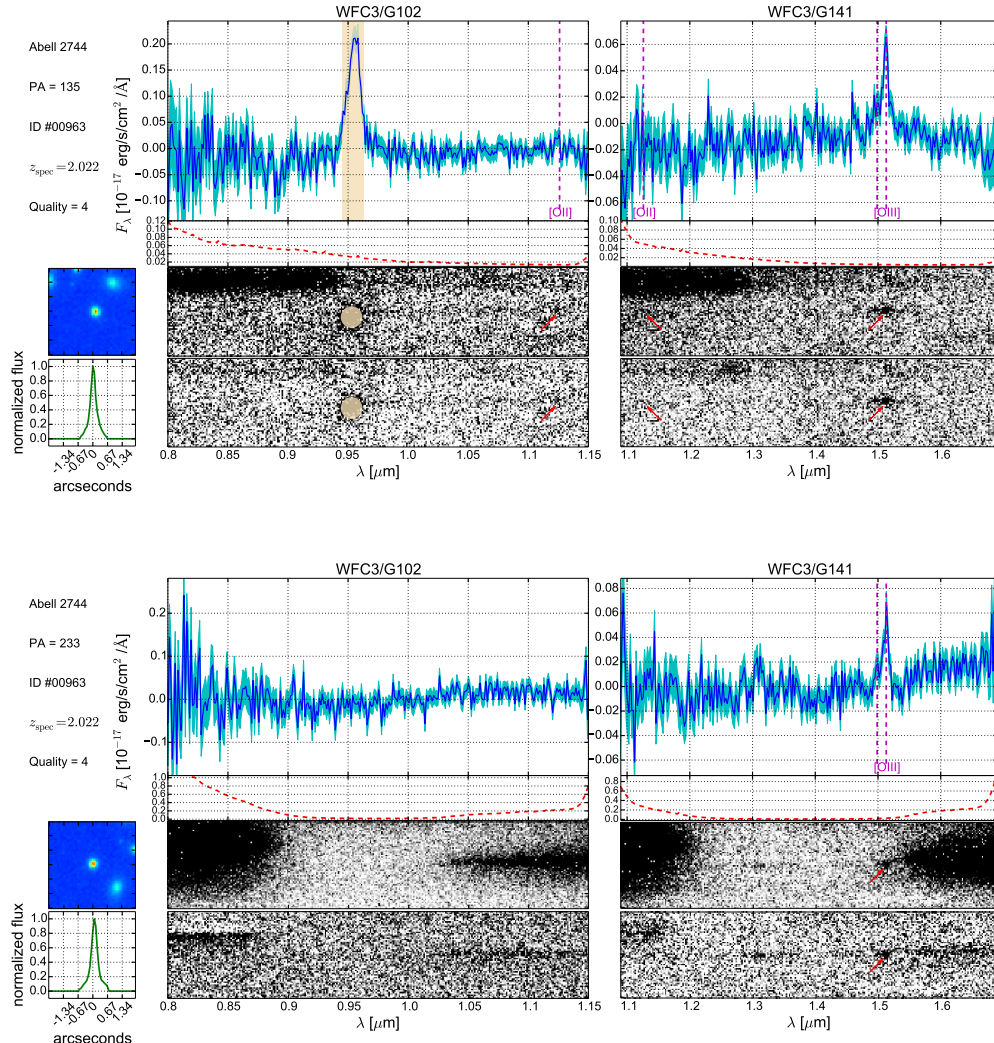


Figure 2.5 Emission line detection results on object ID #00963 (arc 6.1) at the two P.A.s displayed in the two sub-figures accordingly. In each sub-figure, the two panels on the first row show the observed 1-dimensional spectra, where the contamination subtracted flux is denoted by the blue solid line and the noise level by the cyan shaded region. The two panels on the second row give the corresponding contamination model in red dashed line. For the four panels directly underneath, the top two display the interlaced 2-dimensional spectra whereas the bottom two have contamination subtracted. In the 1- and 2-dimensional spectra, the identified emission lines are denoted by vertical dashed lines in magenta and arrows in red, respectively. The wheat colored regions cover contamination model defects. The two panels on the far left refer to the 2-dimensional postage stamp created from the HFF co-adds through drizzling (on top) and the 1-dimensional collapsed image (on bottom). Note that these two panels share the same x-axis along the grism dispersion direction. Some ancillary information can also be seen in the upper left corner in each sub-figure.

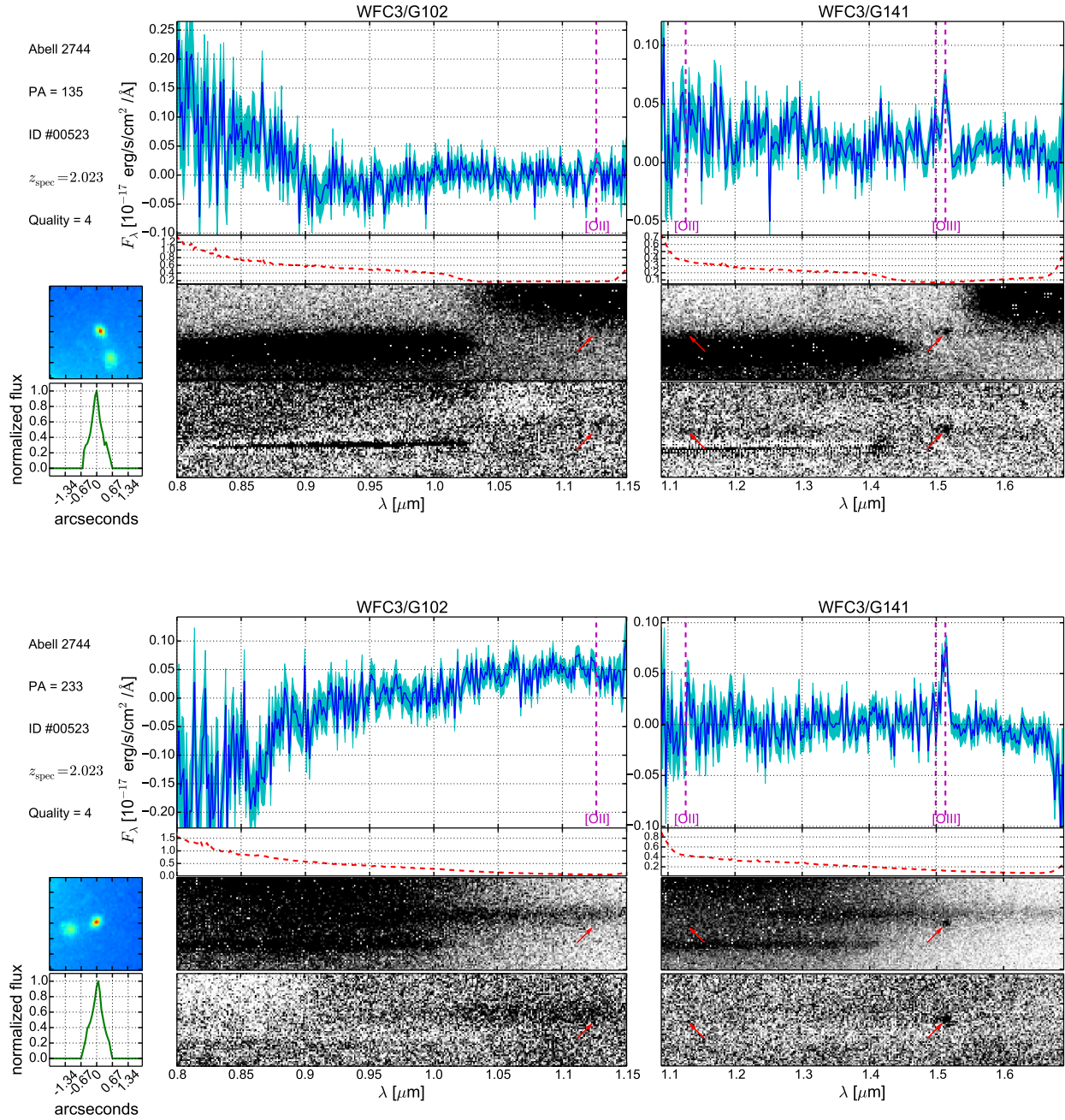


Figure 2.6 Same as Figure 2.5, except that object ID #00523 (arc 6.2) is shown.

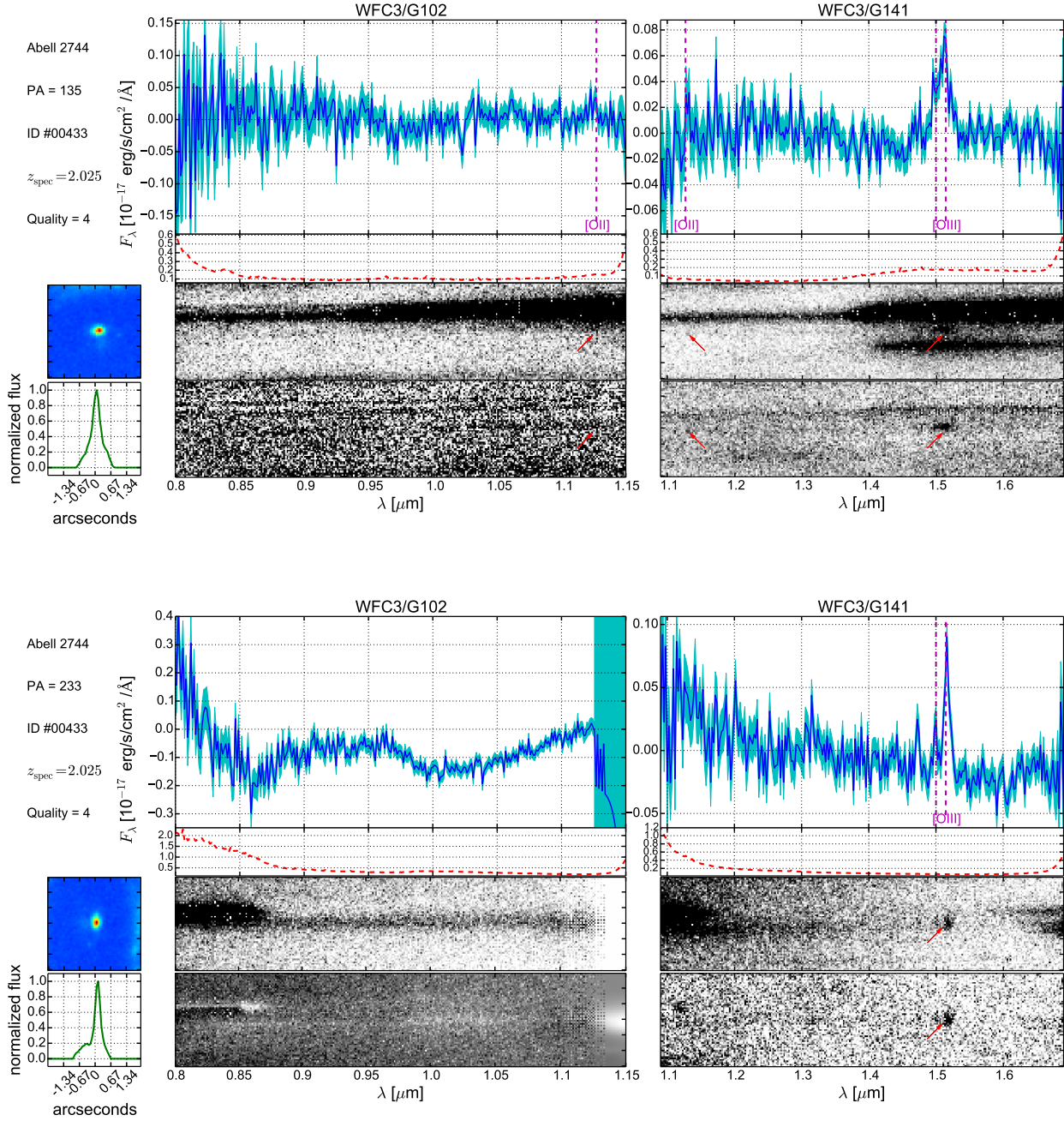


Figure 2.7 Same as Figure 2.5, except that object ID #00433 (arc 6.3) is shown. Note here WFC3/G102 at the second P.A. is cut off on the right due to grism defect.

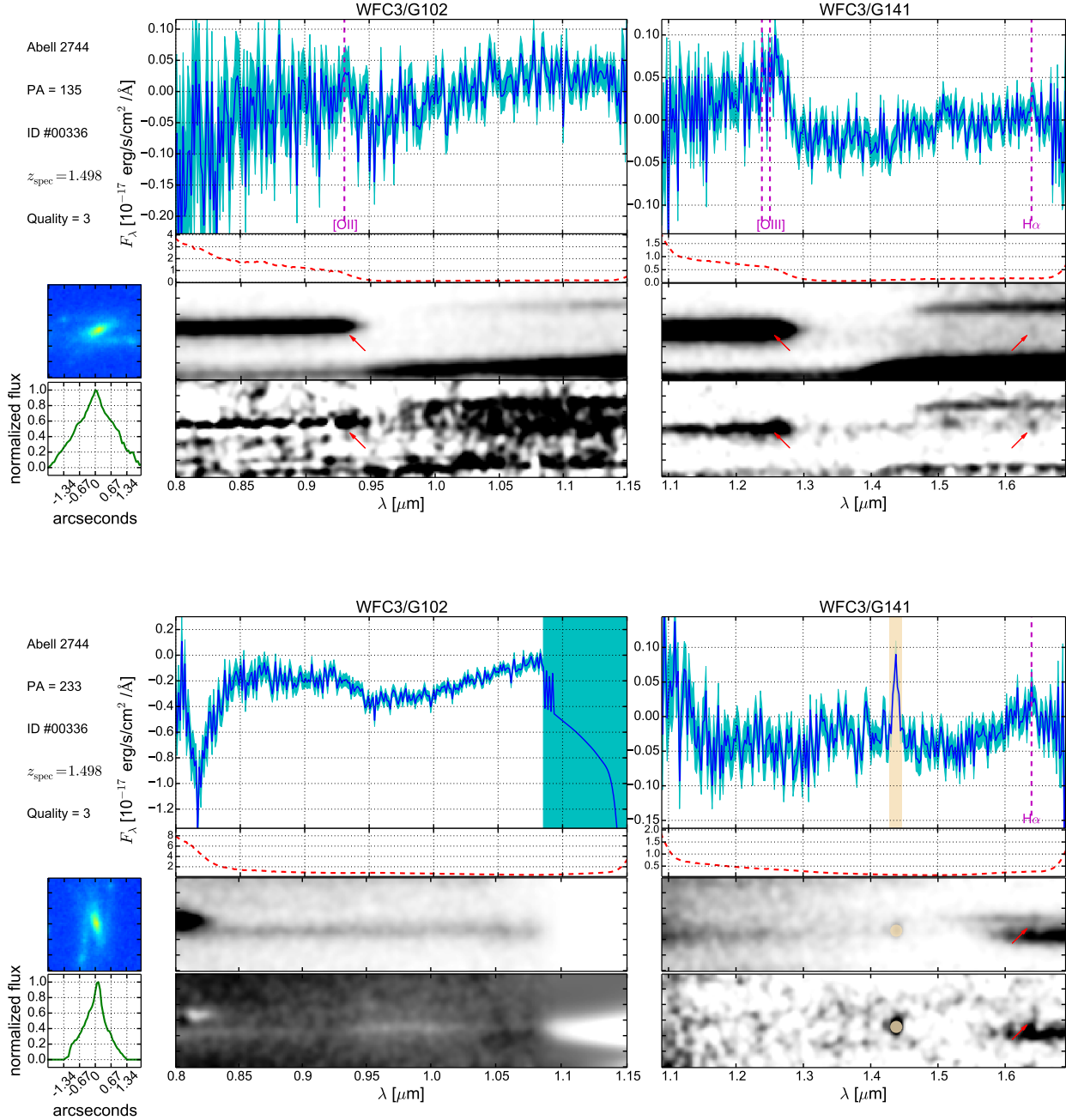


Figure 2.8 Same as Figure 2.5, except that object ID #00336 (arc 1.3) is shown. Moreover, the 2-dimensional spectra are smoothed, whilst the 1-dimensional spectral resolution remains unchanged.

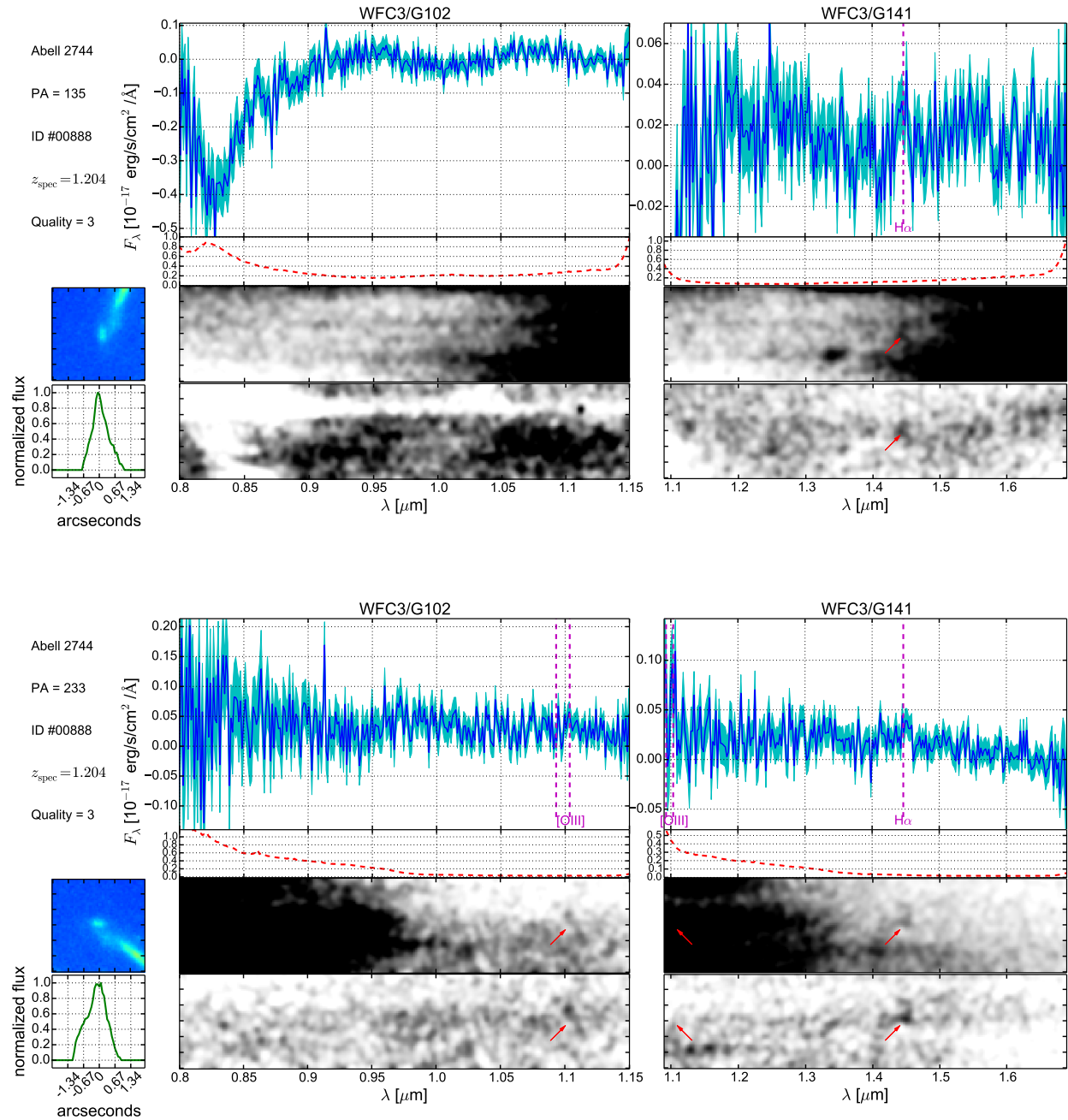


Figure 2.9 Same as Figure 2.8, except that object ID #00888 (arc 56.1) is shown.

measure photometric redshifts for those objects as well. As a result, a comparison between spectroscopic and photometric redshift measurements is possible, as displayed by Figure 2.10. We find that 25/55 photometric redshifts agree within their  $1-\sigma$  uncertainties with corresponding spectroscopic redshifts, when nebular emission lines are included in the fitting template. This suggests the presence of additional systematic errors that are likely related to the photometric redshift fitting method. In order to account for the unknown systematics, we increase the photometric redshift uncertainties for the sources used in the construction of the lens model.

We double-checked our spectroscopic redshift measurements by re-running GiGz on all the objects and also cross-checked the photometric redshift measurements through re-fitting the photometric redshifts using a different method by a subset of the authors (R.A., M.C., E.M) without knowing previous results. The general conclusions about the agreement between spectroscopic and photometric analyses remains unchanged.

## 2.5 Gravitational Lens Model

Our lens modeling method, SWUnited (Bradač et al., 2009, Bradač et al., 2005), constrains the gravitational potential within a galaxy cluster field via  $\chi^2$  minimization. It takes as input a simple initial model for the potential. A  $\chi^2$  is then calculated from strong and weak gravitational lensing data on an adaptive, pixelated grid over the potential established by the initial model. The number of grid points is increased and the  $\chi^2$  is recalculated. Once the minimum is found, and convergence is achieved, derivative lensing quantity maps, such as convergence ( $\kappa$ ), shear ( $\gamma$ ) and magnification ( $\mu$ ), are produced from the best-fit potential map. Errors in these quantities are obtained via the method described below. Maps of the convergence and magnification are shown in Figure 2.11.

A previous model of Abell 2744 using pre-HFF data was created using the same lens modeling code. The model was created as part of a call by STScI to model the HFF clusters, and it appears on the publicly accessible HFF lens modeling website as the Bradac v1 models<sup>10</sup>. The previous model was constrained using 44 total multiple images belonging to 11 distinct systems.

---

<sup>10</sup><http://www.stsci.edu/hst/campaigns/frontier-fields/Lensing-Models>

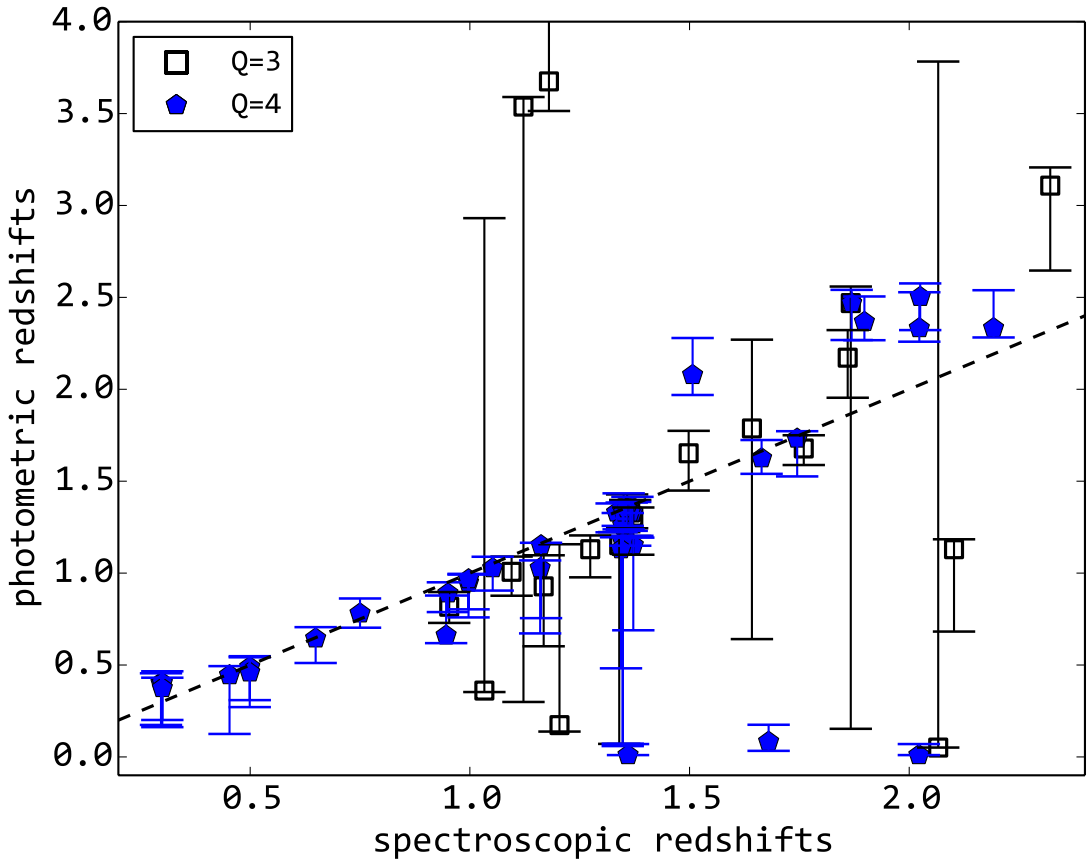


Figure 2.10 Comparison between the spectroscopic and photometric redshifts for the 55 objects with high-confidence emission lines (quality flags 3 or 4). We also show the  $1-\sigma$  error bars (enclosing 68% of the total probability) around the photometric redshifts. There is reasonably good agreement between photometric and spectroscopic redshifts, with 25 out of 55 spectroscopic redshifts within the photometric redshift error bars. This is acceptable considering that the photometric redshift uncertainties only include the random component, even though they suggest that an additional systematic uncertainty component is present. In order to account for this systematic uncertainty, for the systems used to build the lens model we added 20% in quadrature to our photometric errors.

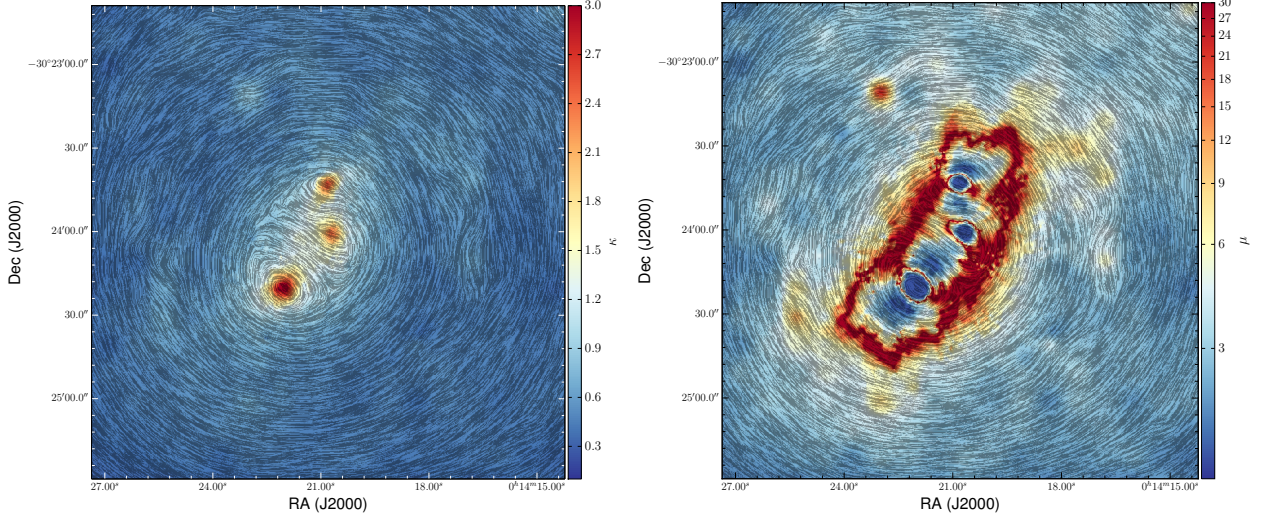


Figure 2.11 Convergence (left),  $\kappa$  and flux magnification (right),  $\mu$ , maps of Abell 2744 produced by our lens model for a source at  $z = 9$ . Maps cover  $3.5 \times 3.5$  arcmin $^2$ . In both maps, the gray stick pattern indicates the phase angle of the shear.

The weak lensing constraints were obtained by one of the modelers, Julian Merten, and distributed to all participating modeling teams. The same weak lensing constraints were used in the model that appears in this work. This model is also made available to the public on the HFF lens modeling website as the Bradac v2 model. In the v1 model, magnification uncertainties were estimated by bootstrap-resampling the weak lensing galaxies. In this work, however, we took a different approach to estimate uncertainties, one that we expect more accurately represents the true uncertainties. Because the number of multiple image systems used in this model is much larger than in the v1 model, 72 total multiple images belonging to 25 distinct systems, we bootstrap-resampled the multiple image systems that were not spectroscopically confirmed. These are the systems for which we use  $z_{\text{Bayes}}$  in the lens model. We assess the impact of photometric redshift uncertainty on the derived lensing quantities by resampling the redshift of each system lacking spectroscopic confirmation from their full  $z_{\text{Bayes}}$  posteriors<sup>11</sup>. We compare the variance in magnification due to redshift uncertainty with the variance in magnification due to bootstrap-resampling the multiple image systems, finding that the latter is dominant. We nonetheless propagate both sources of error

<sup>11</sup>We exclude values of the redshift  $z < z_{\text{cluster}} + 0.1$  when resampling from the  $z_{\text{Bayes}}$  posteriors because they are unphysical.

when reporting the errors on all derived lensing quantities in this work.

As a test of the improvement of the lens model with the addition of the new multiple image constraints from the HFF data, we calculate the magnification of SN HFF14Tom, a Type Ia Supernova (SN Ia) at  $z = 1.35$  discovered in the primary cluster field of Abell 2744 (Rodney et al., 2015). We compare the magnification predicted by our lens model with the magnification calculated directly from a comparison with other SNe Ia at similar redshifts,  $\mu = 2.03 \pm 0.29$  (Rodney et al., 2015). The magnification predicted by the v1 model, using pre-HFF data was  $\mu_{\text{best}} = 3.15$ , with  $\mu_{\text{median}} = 2.45^{+0.19}_{-0.16}$  (68% confidence). The new model presented in this work, v2, predicts a consistent magnification of  $\mu_{\text{best}} = 2.23$ , with  $\mu_{\text{median}} = 2.24^{+0.07}_{-0.08}$  (68% confidence). The improved lensing constraints significantly improve the accuracy as well as the precision according to this test. We note that while we were not blind to the magnification of the supernova predicted by Rodney et al. (2015) when producing the v2 lens model, we did not use the magnification as an input to our model.

### 2.5.1 Comparison with Previous Work

Three teams (Jauzac et al., 2014, Lam et al., 2014 and Ishigaki et al., 2015) have published models of Abell 2744 using new multiple image constraints identified in the HFF imaging data. Of these teams, currently only the lens models produced by Ishigaki et al., 2015 (GLAFIC) are publicly available through the Mikulski Archive for Space Telescopes (MAST<sup>12</sup>). We compare our models to theirs as well as the Sharon v2 models, which include updated spectroscopic measurements of multiple images identified before the HFF data were obtained (Johnson et al., 2014). Finally, we also compare our model with several updates of the CATS(v1) models (Jauzac et al. 2015, private communication). The CATS(v2) models are presented by Jauzac et al. (2014) and use a much larger number of multiple images than we include in our lens model. CATS(v2.1) employs the same set of multiple images as CATS(v2), but makes use of the spectroscopic redshifts obtained in this work. CATS(v2.2) uses the same set of multiple image constraints used in our model. We compare the surface mass density profiles (Figure 2.12) and cumulative magnified source plane

---

<sup>12</sup><http://archive.stsci.edu/prepds/frontier/lensmodels/>

areas (Figure 2.13) predicted by all models described above. The surface mass density profiles agree quite well at radii where multiple image constraints are plentiful. However, the models begin to differ rapidly near the boundaries of the constrained area. Our model disagrees with the CATS models most severely. It is interesting to note that the three CATS models agree internally extremely well, despite CATS(v2.2) using the same set of multiple images used in this work, a considerably different set than the one used in CATS(v2) and CATS(v2.1). The significant difference between our model and the CATS models may be due to differences in the modeling techniques or the fact that our method uses additional constraints (weak lensing). Weak lensing constraints have a stronger impact on the model at radii beyond where multiple images are observed. In contrast, there is excellent agreement among the models in the inferred magnified source plane area. Thus, even though there may be small but significant differences in the specific details of each reconstructions, by and large the total integrated properties are very similar.

We also note that our model supersedes the model obtained by members of our team as part of the initial HFF modeling effort based on pre-HFF data. The uncertainties in this current version of the model are smaller, consistent with the fact that we have increased the number of strong lensing constraints.

We also compare our method of estimating redshifts of multiple image systems with the one used by the CATS team (Richard et al., 2014, Jauzac et al., 2014). In Figure 2.14,  $z_{\text{Bayes}}$  is the redshift obtained from hierarchical Bayesian modeling of the photometric redshifts obtained in this work.  $z_{\text{model}}$  is the redshift obtained by Jauzac et al. (2014) by minimizing their analytical model uncertainty while leaving the redshift as a free parameter. It is important to check this procedure independently since leaving  $z_{\text{model}}$  as a free parameter or predicting additional multiple images that belong to the same system could in principle lead to confirmation bias. Overall, we find good agreement between  $z_{\text{Bayes}}$  and  $z_{\text{model}}$ , within the admittedly large uncertainties on  $z_{\text{Bayes}}$ . There are only two new systems with spectroscopic redshifts available to compare with  $z_{\text{model}}$ , and they are both inconsistent at  $> 5\sigma$ . This may be due to small number statistics or perhaps an indication that the uncertainties on  $z_{\text{model}}$  are underestimated. More spectroscopic redshifts are needed to perform this test in a more stringent manner.

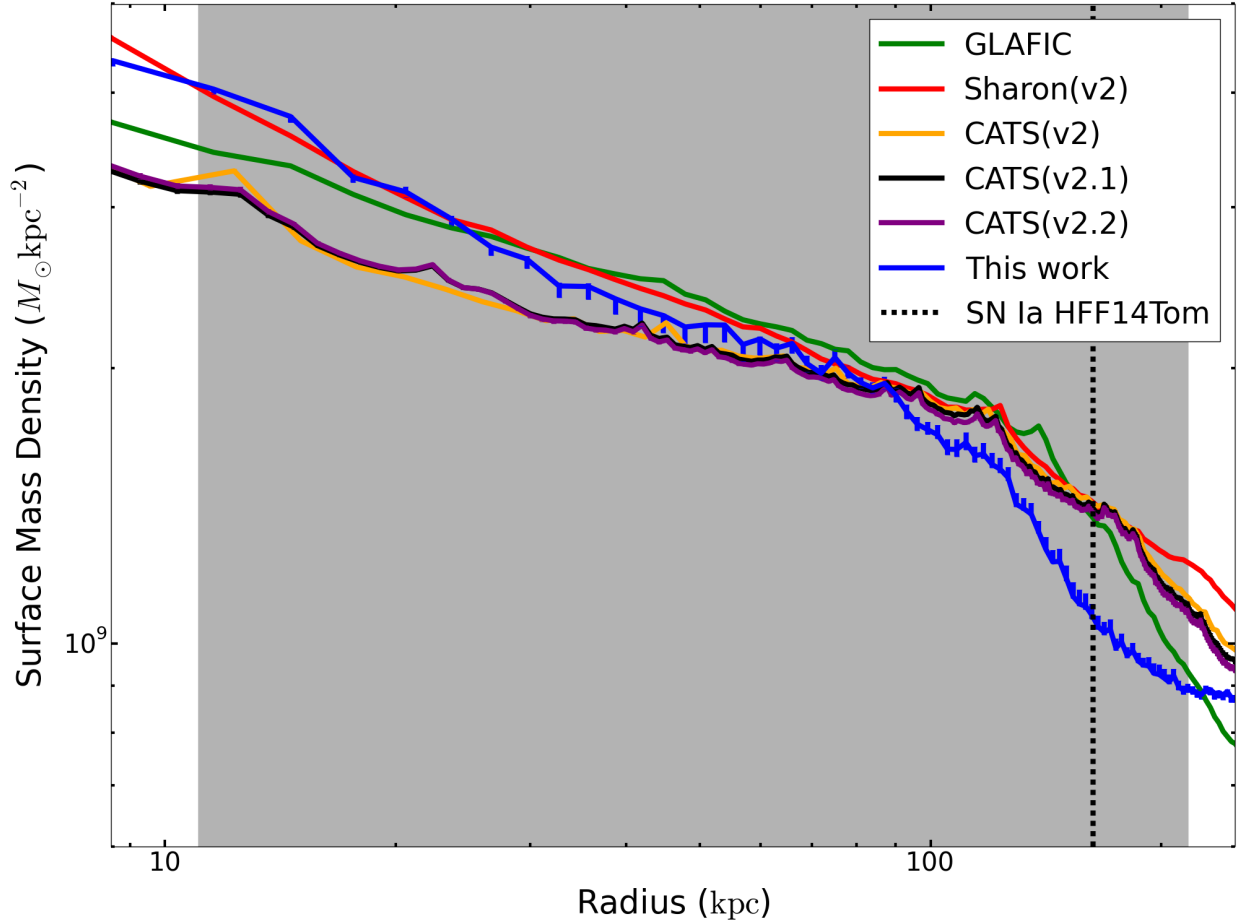


Figure 2.12 Surface mass density profile for the lens model obtained in this work compared to several recently published lens models of Abell 2744. The Sharon v2 model is presented by Johnson et al. (2014), the GLAFIC model by Ishigaki et al. (2015), the CATS(v2) model in Jauzac et al. (2014), and the CATS(v2.1) and CATS(v2.2) models by Jauzac et al. (2015, private communication). The shaded gray region indicates the radii over which multiple image constraints are available. The models agree best within this region, and they begin to significantly disagree at radii  $\gtrsim 200\text{kpc}$ . The radius is measured from the center of the BCG. Error bars shown for our model represent 68% confidence. Gaussian 1- $\sigma$  error bars are included on all three CATS models, but are almost entirely too small to discern.

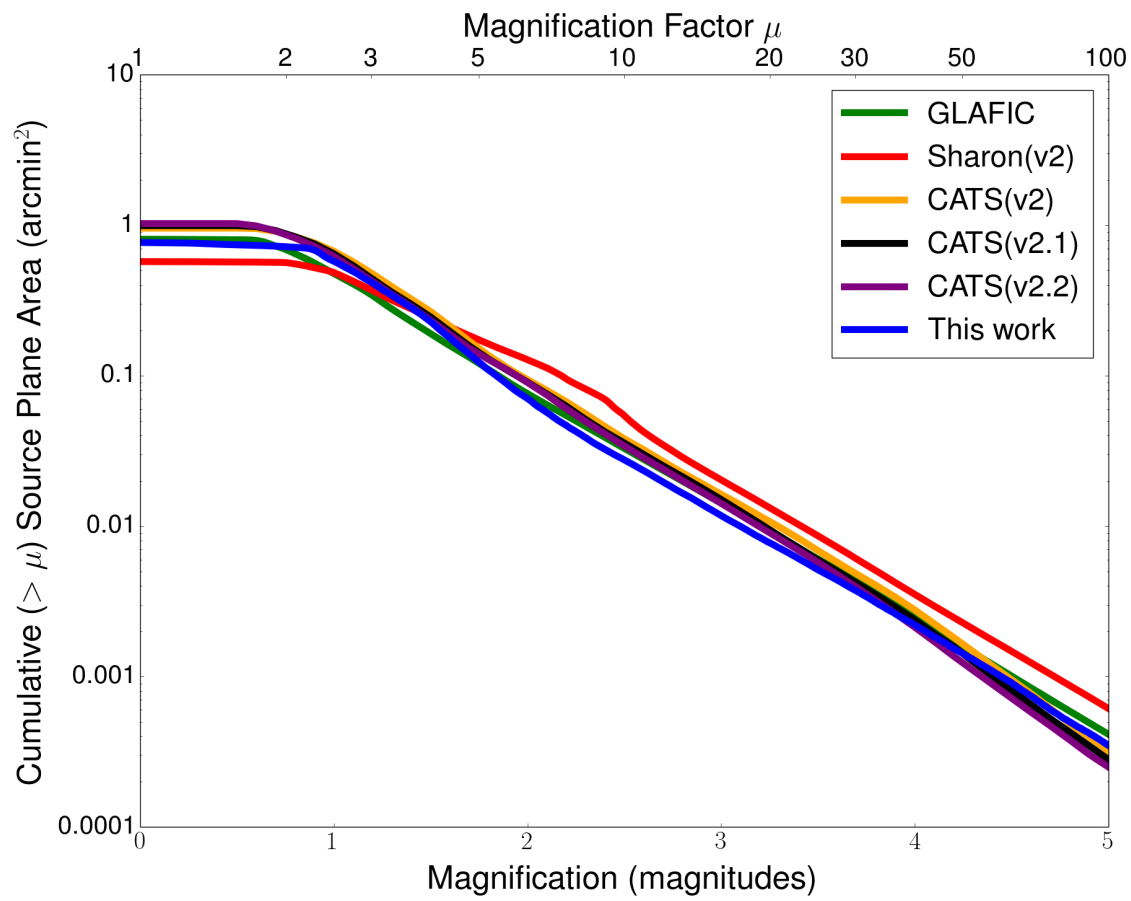


Figure 2.13 Cumulative source plane area versus magnification at  $z = 9$ . The models used in this comparison are the same as those described in Figure 2.12.

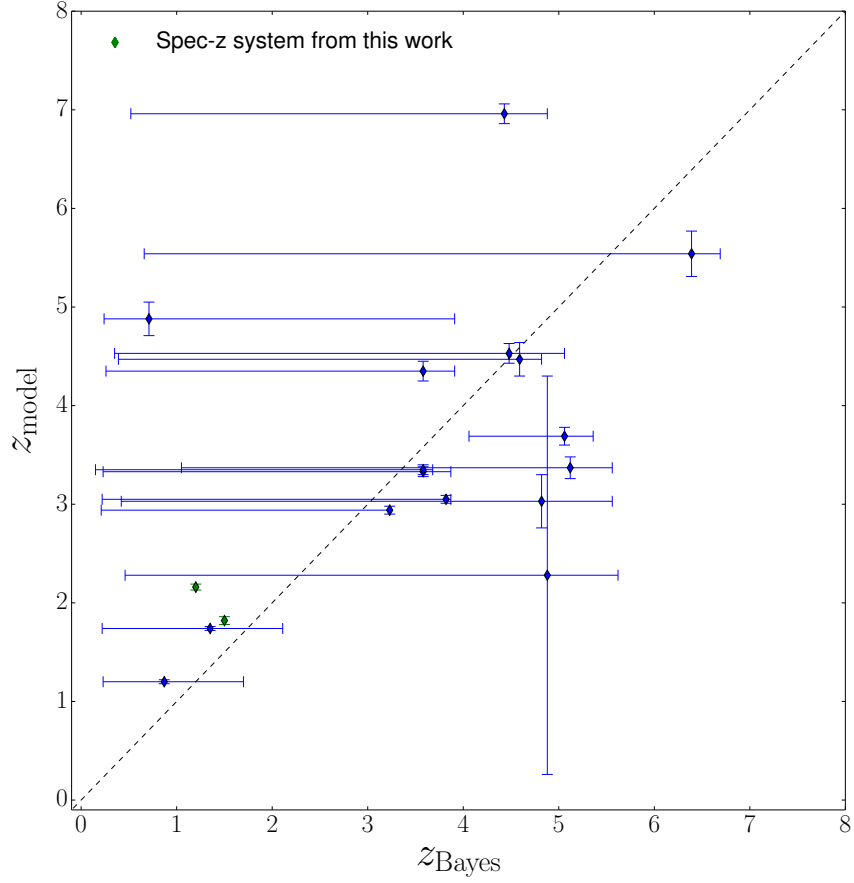


Figure 2.14 Comparison of the redshifts determined in this work ( $z_{\text{Bayes}}$ ) versus the model-predicted redshifts given by Jauzac et al. (2014) for all multiple image systems used in the lens model. Note that the previously confirmed spectroscopic systems are left out of this comparison because  $z_{\text{model}}$  were not calculated. Two systems (green) are spectroscopically confirmed in this work for the first time and are included in the comparison. For these two objects, we use the new spectroscopic redshift on the horizontal axis in place of  $z_{\text{Bayes}}$ . The  $z_{\text{model}}$  values are in significant disagreement with the spectroscopic values for these two systems.  $z_{\text{Bayes}}$  represents the peak of a statistical combination of all available photometric redshift probability density functions (Dahlen et al., 2013). The vertical error bars reflect  $1-\sigma$  Gaussian error on  $z_{\text{model}}$ , and the horizontal error bars show the 68% credible interval for  $z_{\text{Bayes}}$ . 12/16 systems are consistent at 68% confidence level.

## 2.6 The Spatial Distribution of Stellar and Dark Matter

### 2.6.1 Stellar Mass Map

The *Spitzer* IRAC 3.6  $\mu\text{m}$  image samples close to rest-frame  $K$ -band for the cluster, so we use the 3.6  $\mu\text{m}$  fluxes from cluster members to approximate the cluster stellar mass distribution. We first selected the red sequence cluster members brighter than the 25th mag in F814W from the color-magnitude and color-color diagrams following the procedure described in Richard et al. (2014). We also cross-matched the selected cluster members with the spectroscopic redshift catalog given by Owers et al. (2011) to ensure that we included all the cluster members confirmed with spectroscopy. We selected a total of 190 bright cluster members for their stellar mass distribution.

To create an image with 3.6  $\mu\text{m}$  flux from cluster members only, we first created a mask with value 1 for pixels that belong to cluster members in the F160W image and 0 otherwise. We then convolved the mask with the 3.6  $\mu\text{m}$  PSF to match the IRAC angular resolution, set the pixels below 10% of the peak value to zero, and resample the mask onto the IRAC pixel grid. We obtained the 3.6  $\mu\text{m}$  map of cluster members by setting all IRAC pixels not belonging to cluster members to zero and smoothed the final surface brightness map with a two-pixel wide Gaussian kernel.

The IRAC surface brightness map was transformed into a surface mass density map by transforming the 3.6  $\mu\text{m}$  flux into K-band luminosity and then by multiplying by stellar mass to light ratio derived by Bell & de Jong (2001) using the so-called “diet”-Salpeter stellar initial mass function (IMF). The resulting stellar mass map is shown in the left panel of Figure 2.15.

The main source of uncertainty on the stellar mass density is the unknown initial mass function. For example, if one were to adopt a Salpeter (1955) IMF – as suggested by studies of massive early-type galaxies, the stellar mass density would increase by a factor of 1.55.

### 2.6.2 Stellar to Total Mass Ratio

We obtain the stellar to total mass ratio map by dividing the stellar surface mass density map obtained from photometry by the total surface mass density map obtained from gravitational lensing. This is shown in the right panel of Figure 2.15. We note that resolution effects are non-trivial to

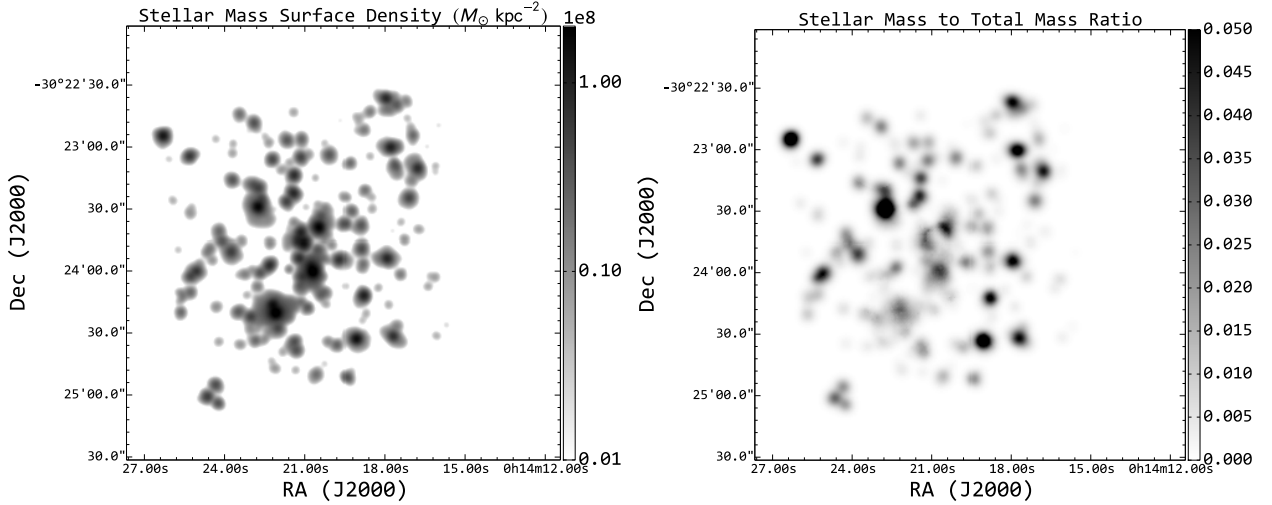


Figure 2.15 Stellar mass surface density (left) and stellar to total mass ratio (right) distributions of Abell 2744. Stellar mass surface density is in the unit of  $M_{\odot} \text{ kpc}^{-2}$ .

take into account, since the resolution of the lensing map depends on the density of local sources and the amount of regularization. Thus, the map should be interpreted keeping in mind this caveat. Interestingly the stellar to total mass ratio varies significantly across the cluster. Many but not all the massive ellipticals seem to reach values of 0.05 or more, which are typical of the central regions of isolated massive galaxies (e.g. Gavazzi et al., 2007). However, the ratio appears to be significantly lower in the center of the cluster and in the south-east quadrant. In future work, we plan to compare the observed map with those obtained from numerical simulations by taking into account the effects of finite resolution in the observed mass and light maps, in order to test whether the spread in stellar to total mass ratio is reproduced. Furthermore, we plan to carry out a systematic comparison with mass reconstructions where mass is assumed to follow light up to a scale factor (Zitrin et al., 2009). At face value our result is inconsistent with this assumption for a merging cluster like Abell 2744. However, uncertainties on both models and resolution effects must be taken into account in order to evaluate the significance of this apparent violation. Thus, this result should be considered as preliminary until confirmed by a more detailed analysis.

## 2.7 Conclusions

We have used spectroscopic data from the GLASS survey in combination with ultra-deep imaging data from the HFF program to construct a strong gravitational lens model for the cluster Abell 2744. In an effort to obtain a precise and accurate mass model we carried out a systematic search for spectroscopic redshifts of multiple images and we applied a rigorous algorithm to select only secure multiple image systems amongst the dozens that have been proposed in the literature. The lensing mass map is then combined with a stellar mass map derived from IRAC photometry to study the relative spatial distribution of luminous and dark matter. Our main results can be summarized as follows:

1. We have measured spectroscopic redshifts for 5 multiple image systems (quality flag 4 and 3, i.e. secure and probable). We have also confirmed spectroscopically that images 6.1, 6.2, 6.3 belong to the same source. The spectroscopically confirmed images are used to constrain the gravitational lens model. We also obtain 2 tentative redshifts, which are not used to constrain the mass model, but could potentially be confirmed by future work.
2. From the GLASS data we derive an extensive redshift catalog of faint emission line systems which we use to test photometric and lensing determinations of redshift. Generally speaking, the measurements agree within the  $1-\sigma$  uncertainties, when nebular emission lines are included in the fitting template. In addition, we compare photometric redshifts with redshifts determined by Jauzac et al. (2014), based on their gravitational lens model and find an agreement within the large uncertainties of the former. For the two systems with new spectroscopic redshifts we find a significant difference with respect to model redshifts. This may be due to small number statistics or to the model redshifts uncertainties being underestimated. More spectroscopic redshifts are needed to make a more stringent test.
3. Our rigorous selection algorithm identifies a total of 25/72 multiple arc systems/images as secure out of a sample of 57/179 candidate multiple arc systems/images, compiled from the literature and from our own work. Most systems are rejected either on the basis of inconsistent morphology or inconsistent spectral energy distribution between the candidate

multiple images, or because of insufficient evidence that they belong to the same source.

4. The derived mass model is found to be very precise, as measured by bootstrap- and redshift-resampling the set of multiple images used as input. Furthermore, we tested how well our model reproduces the magnification of the background SN Ia Tomas (Rodney et al., 2015). The SN Ia was not used as a constraint to the model and yet its magnification is consistent ( $2.03 \pm 0.29$  for the supernova vs  $2.23_{-0.07}^{+0.08}$  from our mass model).
5. Abell 2744 is confirmed to be an excellent gravitational telescope, with a source plane area of  $\sim 0.7$  arcminute square being magnified by a factor of 2.
6. We construct a stellar surface mass density map and the stellar to total mass ratio by selecting the light associated with red sequence cluster galaxies and using the total mass density map obtained from strong lensing. Albeit with significant uncertainties, we find that the stellar to mass ratio varies significantly across the cluster, tentatively suggesting that stellar mass does not trace total mass in this interacting system.

Table 2.1. Multiply lensed arc systems identified in the Abell 2744 field

ID <sub>arc</sub> <sup>1</sup>	R.A. (deg.)	Dec. (deg.)	F140W (mag)	z <sub>spec</sub>	z <sub>Bayes</sub> <sup>2</sup>	Quality			Pass Flag	Magnification <sup>4</sup>	
						z <sub>Bayes</sub> <sup>3</sup>	Color- $\chi^2$	Morphology			
1.1 J 3.597540	-30.403920	22.16		1.70 [1.08-2.01]	0.487	8	0	1	1	3.88 [4.04-5.26]	
1.2 J 3.595960	-30.406820	22.24			3.079	8	0		1	3.81 [3.63-4.64]	
1.3 G 3.586210	-30.409990	22.92	1.50		2.572	8	0		1	3.73 [3.52-4.66]	
2.1 J 3.583250	-30.403350	24.87	1.20	0.01	0.892	8	0	1	1	7.34 [7.49-9.18]	
2.2 <sup>5</sup> J 3.597290	-30.396720	...			...	8	0		1	2.53 [2.45-2.59]	
2.3 J 3.585420	-30.399990	27.46			1.702	8	1		1	14.84 [9.88-17.08]	
2.4 J 3.586420	-30.402130	26.34			0.696	8	1		1	4.08 [4.22-4.66]	
3.1 T 3.589380	-30.393870	24.28	3.98	4.06 [3.82-4.38]	0.830	8	0	1	1	16.59 [10.17-23.33]	
3.2 T 3.588790	-30.393800	24.74	3.98		0.681	8	0		1	17.86 [9.74-23.48]	
3.3 J 3.576620	-30.401810	26.26			1.323	6	0		1	2.94 [2.87-3.02]	
4.1 J 3.592120	-30.402630	25.33		3.45 [3.21-6.47]	1.806	8	0	1	1	12.35 [16.57-77.81]	
4.2 J 3.595630	-30.401620	24.97			3.395	8	0		1	6.52 [6.17-8.85]	
4.3 R 3.580420	-30.408920	26.56	3.58		16.563	5	1		0	3.39 [3.12-3.53]	
4.4 J 3.593210	-30.404910	25.86			2.044	8	1		1	12.65 [11.09-23.70]	
4.5 T 3.593580	-30.405110	25.87	3.58		8.688	8	1		1	9.50 [6.94-13.66]	
5.1 J 3.583420	-30.392070	27.68		3.58 [3.31-4.14]	1	0.102	8	0	1	1	162.55 [21.87-330.20]
5.2 J 3.585000	-30.391380	26.96				0.291	8	0		1	19.39 [13.00-65.20]
5.3 J 3.579960	-30.394760	29.51				0.075	7	0		1	9.25 [8.90-14.88]
6.1 R,G 3.598540	-30.401800	24.86	2.02	0.01	0.435	8	0	1	1	3.89 [3.60-4.74]	
6.2 G 3.594040	-30.408010	24.66	2.02		0.966	8	0		1	1.75 [1.86-2.09]	
6.3 G 3.586420	-30.409370	24.29	2.02		0.326	7	0		1	5.32 [5.08-6.09]	
7.1 J 3.598250	-30.402320	24.98		3.27 [1.96-3.45]	1	0.626	8	0	1	1	6.31 [5.38-7.74]
7.2 J 3.595210	-30.407420	23.14				1.347	7	0		1	1.55 [1.62-2.06]
7.3 J 3.584580	-30.409810	25.12				0.385	8	0		1	5.50 [4.43-6.88]
8.1 J 3.589710	-30.394340	26.61		3.54 [2.10-9.44]	0	0.333	8	1	0	0	...
8.2 J 3.588830	-30.394220	27.97				0.536	8	1		0	...
8.3 J 3.576380	-30.402560	27.63				0.249	6	0		0	...
9.1 J 3.588380	-30.405270	27.11		0.01	0	1.424	8	1	0	0	...
9.2 J 3.587120	-30.406240	27.00				1.172	8	0		0	...
9.3 J 3.600170	-30.397150	26.16				1.154	5	0		0	...
10.1 J 3.588420	-30.405880	26.51		0.01	0	1.541	8	1	0	0	...
10.2 J 3.587380	-30.406480	26.76				1.183	8	0		0	...
10.3 J 3.600710	-30.397100	26.07				2.154	6	0		0	...

Table 2.1 (cont'd)

ID <sub>arc</sub> <sup>1</sup>	R.A. (deg.)	Dec. (deg.)	F140W (mag)	$z_{\text{spec}}$	$z_{\text{Bayes}}^2$	Quality			Pass Flag	Magnification <sup>4</sup>
						$z_{\text{Bayes}}^3$	Color- $\chi^2$	Morphology	Contaminated?	
11.1 J	3.591380	-30.403860	27.53		0.20	0	2.195	7	1	0 0 ...
11.2 J	3.597250	-30.401450	27.11				3.443	7	0	0 ...
11.3 J	3.582790	-30.408910	23.91				3.077	6	0	0 ...
11.4 J	3.594540	-30.406540	27.31				7.762	6	1	0 ...
12.1 J	3.593630	-30.404470	26.23		0.01	0	1.335	7	1	0 0 ...
12.2 J	3.593250	-30.403260	27.54				0.535	8	0	0 ...
12.3 J	3.594580	-30.402990	27.12				0.705	8	0	0 ...
12.4 J	3.579460	-30.409950	24.64				0.596	6	1	0 ...
13.1 J	3.592370	-30.402560	25.86	1.35 [0.94-5.77]	1	1	1.143	8	1	1 18.40 [15.27-194.08]
13.2 J	3.593790	-30.402160	25.84				0.698	8	0	1 11.75 [5.64-72.96]
13.3 J	3.582790	-30.408040	27.46				0.931	5	0	1 3.27 [3.19-4.00]
14.1 J	3.589750	-30.394640	26.79		0.01	0	0.359	8	0	0 0 ...
14.2 J	3.588460	-30.394440	27.04				1.199	8	1	0 ...
14.3 J	3.577580	-30.401710	26.86				1.408	5	0	0 ...
18.1 J	3.590750	-30.395560	24.85	5.30 [3.31-9.16]	0	0	0.619	8	0	0 0 ...
18.2 J	3.588380	-30.395640	27.72				0.553	6	1	0 ...
18.3 C	3.576130	-30.404470	26.50	5.66			2.959	5	0	0 ...
19.1 J	3.588920	-30.397440	...		0.01	0	...	7	1	0 0 ...
19.2 J	3.591420	-30.396690	28.16				2.114	5	0	0 ...
19.3 J	3.578710	-30.404040	25.34				2.039	5	1	0 ...
20.1 J	3.596250	-30.402970	27.50		0.01	0	0.116	7	0	0 0 ...
20.2 J	3.595170	-30.405470	28.07				0.427	7	1	0 ...
20.3 J	3.582000	-30.409570	28.18				0.798	6	0	0 ...
21.1 J	3.596170	-30.403120	28.74		0.01	0	0.284	7	0	0 0 ...
21.2 J	3.595250	-30.405320	29.66				0.435	7	1	0 ...
21.3 J	3.58196	-30.409620	28.18				1.157	6	0	0 ...
22.1 J	3.587920	-30.411610	27.54	5.12 [4.61-5.72]	1	1	0.287	7	0	1 1 5.88 [5.81-9.29]
22.2 J	3.600080	-30.404420	27.48				0.145	7	0	1 5.17 [4.89-6.26]
22.3 J	3.596540	-30.409030	27.28				0.235	7	0	1 5.63 [4.38-5.98]
23.1 J	3.588170	-30.410550	27.61	5.06 [4.65-5.44]	1	1	0.102	7	0	1 1 5.64 [3.86-9.06]
23.2 J	3.593540	-30.409720	26.79				0.046	7	0	1 3.92 [3.15-5.02]
23.3 J	3.600540	-30.401840	27.38				0.225	6	0	1 3.31 [3.09-3.95]
24.1 J	3.595920	-30.404480	26.02	0.87 [0.71-6.05]	0	0	0.942	8	0	0 0 ...

Table 2.1 (cont'd)

ID <sub>arc</sub> <sup>1</sup>	R.A. (deg.)	Dec. (deg.)	F140W (mag)	$z_{\text{spec}}$	$z_{\text{Bayes}}^2$	Quality			Pass Flag	Magnification <sup>4</sup>
						$z_{\text{Bayes}}^3$	Color- $\chi^2$	Morphology		
24.2 J	3.595120	-30.405930	26.52		2.487	8	1		0	...
24.3 J	3.587330	-30.409100	26.91		1.489	6	0		0	...
25.1 J	3.594460	-30.402740	27.23	0.01	0	3.212	6	0	0	0
25.2 J	3.592170	-30.403330	27.38		1.070	6	1		0	...
25.3 J	3.584210	-30.408290	29.13		1.662	6	0		0	...
26.1 J	3.593960	-30.409690	28.28	0.20	0	3.172	5	0	0	0
26.2 J	3.590370	-30.410590	24.95		0.809	5	1		0	...
26.3 J	3.600080	-30.402970	27.74		0.291	5	0		0	...
27.1 J	3.580750	-30.403150	28.95	0.01	0	0.431	5	0	0	...
27.2 J	3.595710	-30.396170	28.54		0.317	5	0		0	...
27.3 J	3.585500	-30.397650	...		...	5	1		0	...
28.1 J	3.580460	-30.405070	27.20	6.39 [3.68-7.44]	1	0.957	7	0	1	1 4.88 [4.29-5.11]
28.2 J	3.597830	-30.395960	27.38			1.667	7	0	1	3.14 [3.13-3.42]
28.3 J	3.585290	-30.397970	27.22			0.610	6	1	1	2.86 [2.89-4.13]
28.4 J	3.587460	-30.401370	27.36			0.181	6	1	1	3.24 [2.99-4.32]
29.1 J	3.582330	-30.397640	29.30	4.82 [1.82-6.98]	1	0.394	5	0	1	1 47.33 [19.69-103.88]
29.2 J	3.580540	-30.400430	28.97			0.193	5	0	1	1 7.87 [6.10-8.44]
29.3 J	3.583630	-30.396600	30.58			2.121	4	1	0	1 20.38 [21.25-50.53]
30.1 J	3.591000	-30.397440	25.77	0.87 [0.75-6.47]	1	1.513	8	0	1	1 8.21 [4.77-10.53]
30.2 J	3.586710	-30.398190	26.41			3.772	6	1	1	1 4.52 [4.22-4.77]
30.3 J	3.581920	-30.401700	25.81			0.914	8	0	1	1 4.07 [4.16-8.70]
31.1 J	3.585920	-30.403170	28.91	11.90	0	0.507	8	1	0	0
31.2 J	3.583710	-30.404120	28.63			0.398	8	1	0	...
31.3 J	3.599830	-30.395520	...			...	3	0	0	...
32.1 J	3.583580	-30.404720	27.70	0.71 [0.99-6.51]	1	0.769	5	0	1	1 3.22 [2.71-3.30]
32.2 J	3.586670	-30.403350	27.43			0.893	5	1	0	1 29.09 [16.59-26.21]
32.3 J	3.599790	-30.395980	26.78			0.640	4	0	1	1 1.66 [1.65-1.71]
33.1 J	3.584710	-30.403150	28.72	4.43 [3.12-5.54]	1	2.351	7	1	1	1 667.25 [61.64-609.99]
33.2 J	3.584420	-30.403390	27.91			0.356	5	0	1	1 16.15 [20.27-214.71]
33.3 J	3.600670	-30.395420	28.63			0.664	7	0	1	1 2.39 [2.40-2.53]
34.1 J	3.593420	-30.410840	27.69	3.82 [1.03-4.33]	1	1.898	8	0	1	1 74.50 [9.39-37.41]
34.2 J	3.593830	-30.410720	27.84			1.135	5	0	1	1 66.45 [11.48-40.75]
34.3 J	3.600580	-30.404530	26.91			0.215	6	0	1	1 4.26 [3.98-5.10]

Table 2.1 (cont'd)

ID <sub>arc</sub> <sup>1</sup>	R.A. (deg.)	Dec. (deg.)	F140W (mag)	$z_{\text{spec}}$	$z_{\text{Bayes}}^2$	Quality			Pass Flag		Magnification <sup>4</sup>
						$z_{\text{Bayes}}^3$	Color- $\chi^2$	Morphology	Contaminated?	System	Image
35.1 J 3.581080	-30.400210	27.00	0.01	0	0.307	7	0	0	0	0	...
35.2 J 3.581540	-30.399390	26.33			0.773	7	0		0	0	...
35.3 J 3.597830	-30.395540	27.05			2.534	6	0		0	0	...
36.1 J 3.589460	-30.394410	29.50	0.01	...	4.101	8	1	0	0	0	...
36.2 J 3.588670	-30.394300	28.60			2.210	8	1		0	0	...
36.3 J 3.577500	-30.401500	28.28			1.193	6	1		0	0	...
37.1 J 3.589040	-30.394910	27.15	0.01	...	5.976	7	1	0	0	0	...
37.2 J 3.588710	-30.394850	...			...	7	1		0	0	...
37.3 J 3.578330	-30.401400	25.38			2.109	5	0		0	0	...
38.1 J 3.589420	-30.394110	29.12	0.78 [0.99-5.63]	0	0.243	6	0	0	0	0	...
38.2 J 3.588960	-30.394040	28.39			0.336	6	0		0	0	...
38.3 J 3.576380	-30.402130	28.17			1.254	4	0		0	0	...
39.1 J 3.588790	-30.392530	27.61	3.58 [0.80-4.10]	1	1.154	7	0	1	1	1	12.03 [9.80-35.06]
39.2 J 3.588540	-30.392510	27.13			1.355	7	0		1	53873.97 [21.17-147.82]	
39.3 J 3.577460	-30.399560	25.49			0.231	2	0		1	4.38 [3.79-5.90]	
40.1 J 3.589080	-30.392660	28.23	3.77 [2.94-6.14]	0	0.427	7	0	0	0	0	...
40.2 J 3.588210	-30.392550	29.01			0.850	7	0		0	0	...
40.3 J 3.577540	-30.399370	28.53			0.014	5	0		0	0	...
41.1 J 3.599170	-30.399580	28.45	4.48 [2.24-6.23]	1	1.133	4	0	1	1	1	3.36 [3.24-3.79]
41.2 J 3.593790	-30.407820	29.78			1.485	4	1		0	1	1.48 [1.42-1.60]
41.3 J 3.583460	-30.408500	28.40			0.437	4	0		1	5.73 [4.78-7.22]	
41.4 J 3.590420	-30.404040	28.90			0.270	4	1		0	2.07 [1.75-2.07]	
42.1 J 3.597290	-30.400610	28.56	3.58 [1.31-6.51]	1	1.162	5	0	1	1	1	4.64 [4.35-5.92]
42.2 J 3.590960	-30.403260	28.69			0.796	5	1		0	1	1.64 [1.55-1.66]
42.3 J 3.581580	-30.408630	28.54			0.359	5	0		1	3.51 [3.59-5.39]	
42.4 J 3.594250	-30.406390	28.58			3.629	5	1		0	1.72 [1.67-2.03]	
43.1 J 3.597830	-30.402500	27.35	3.72 [1.68-6.98]	0	0.156	5	0	0	0	0	...
43.2 J 3.583960	-30.409820	27.22			0.147	5	0		0	0	...
44.1 J 3.583460	-30.406970	27.75	0.24	0	0.069	4	0	0	0	0	...
44.2 J 3.596710	-30.399760	27.96			0.090	4	0		0	0	...
45.1 J 3.584830	-30.398470	28.12	2.99 [1.77-9.07]	0	0.311	7	1	0	0	0	...
45.2 J 3.581420	-30.403950	27.09			2.834	6	0		0	0	...
45.3 J 3.586880	-30.401290	26.34			3.243	5	1		0	0	...

Table 2.1 (cont'd)

ID <sub>arc</sub> <sup>1</sup>	R.A. (deg.)	Dec. (deg.)	F140W (mag)	$z_{\text{spec}}$	$z_{\text{Bayes}}^2$	Quality			Pass Flag	Magnification <sup>4</sup>		
						$z_{\text{Bayes}}^3$	Color- $\chi^2$	Morphology				
45.4 J	3.597420	-30.396150	...			...	4	1	0	...		
46.1 Z	3.595040	-30.400750	27.53	10.00 <sup>6</sup>	8.76 [3.40-9.30]	0.780	7	0	1	1	7.58 [6.30-8.67]	
46.2 Z	3.592500	-30.401490	27.89			0.059	7	0		1	15.03 [9.21-15.25]	
46.3 Z	3.577500	-30.408700	29.68			1.565	6	0		1	2.68 [2.67-2.71]	
47.1 J	3.586460	-30.392130	29.38		3.58 [1.96-8.93]	0	1.843	2	0	0	0	...
47.2 J	3.585830	-30.392240	27.39				1.952	2	0		0	...
47.3 J	3.589670	-30.392140	28.90				0.423	1	0		0	...
47.4 J	3.578330	-30.398130	29.45				3.755	1	0		0	...
48.1 J	3.594250	-30.402840	27.06		1.50 [1.45-8.37]	0	0.320	4	0	0	0	...
48.2 J	3.592790	-30.403130	28.14				0.969	4	1		0	...
48.3 J	3.582080	-30.408580	...				...	4	0		0	...
49.1 J	3.592670	-30.408270	29.25		0.04	0	0.637	4	1	0	0	...
49.2 J	3.590210	-30.408810	...				...	5	0		0	...
49.3 J	3.597500	-30.403140	28.24				0.101	5	0		0	...
50.1 J	3.577960	-30.401620	28.23		4.59 [1.12-5.91]	1	0.422	6	0	1	1	4.01 [3.61-4.09]
50.2 J	3.593960	-30.394300	28.14				0.440	6	0		1	4.07 [4.18-5.19]
50.3 J	3.585330	-30.393630	26.11				0.674	4	1		0	1.93 [1.83-2.05]
51.1 J	3.586830	-30.405550	28.70		4.88 [1.91-6.61]	1	0.364	7	0	1	1	50.72 [26.92-369.66]
51.2 J	3.586460	-30.405670	29.04				0.462	6	0		1	170.12 [35.98-623.76]
51.3 J	3.599000	-30.398300	...				...	4	1		0	2.96 [2.73-3.51]
52.1 J	3.586580	-30.397010	25.30		0.01	...	0.002	6	1	0	0	...
52.2 J	3.586130	-30.397130	...				...	6	1		0	...
52.3 J	3.588460	-30.396860	29.05				0.689	3	1		0	...
53.1 J	3.579830	-30.401590	28.35		1.60 [1.64-8.46]	0	0.000	7	0	0	0	...
53.2 J	3.583540	-30.396700	...				...	7	1		0	...
53.3 J	3.597040	-30.394550	...				...	1	0		0	...
54.1 J	3.592370	-30.409890	27.59		6.69 [1.59-8.56]	0	0.294	7	0	0	0	...
54.2 J	3.588250	-30.410340	...				...	7	1		0	...
54.3 J	3.588420	-30.410320	27.25				0.289	7	1		0	...
54.4 J	3.590080	-30.410270	...				...	7	1		0	...
55.1 L	3.597042	-30.404746	25.57	1.50	0.03		1.777	8	0	1	1	12.63 [10.24-24.00]
55.2 L	3.596371	-30.406161	25.84				1.463	8	1		1	10.28 [4.69-9.87]
55.3 L	3.585726	-30.410085	27.14				1.417	8	0		1	3.50 [3.07-3.45]

Table 2.1 (cont'd)

ID <sub>arc</sub> <sup>1</sup>	R.A. (deg.)	Dec. (deg.)	F140W (mag)	$z_{\text{spec}}$	$z_{\text{Bayes}}^2$	Quality	Pass Flag			Magnification <sup>4</sup>	
							$z_{\text{Bayes}}^3$	Color- $\chi^2$	Morphology		
									Contaminated?	System Image	
56.1 G	3.582526	-30.402290	25.52	1.20	2.61 [1.08-6.09]	1.934	8	0	1	1	5.54 [4.09-7.62]
56.2 L	3.596728	-30.396298	26.88			2.895	8	0		1	2.52 [2.53-2.61]
56.3 L	3.584467	-30.399292	26.52			4.941	8	1		1	10.39 [9.14-11.08]
56.4 L	3.586219	-30.400850	24.28			4.457	8	1		1	4.04 [3.57-4.56]
57.1 I	3.598676	-30.40491	24.59	1.05 [0.71-2.70]	0	0.490	0	0	0	0	...
57.2 I	3.587053	-30.41126	24.98			0.733	0	0		0	...
57.3 I	3.596818	-30.40783	27.40			0.494	0	1		0	...
58.1 I	3.578090	-30.39964	25.04	0.01	0	7.221	4	0	0	0	...
58.2 I	3.589237	-30.39444	24.18			3.590	4	0		0	...
59.1 I	3.584284	-30.40893	26.84	4.27 [1.45-6.56]	1	0.037	1	0	1	1	8.12 [4.82-9.31]
59.2 I	3.598125	-30.40098	27.61			0.108	1	0		1	5.15 [3.47-6.64]
60.1 G	3.5980768	-30.403991	27.39	0.07	0	2.501	8	0	0	0	...
60.2 G	3.5957195	-30.40755	27.27			0.763	8	1		0	...
60.3 G	3.587391	-30.410149	27.37			1.588	8	0		0	...

Note. — Objects for which F140W magnitudes are not reported are not detected by SExtractor. Contaminated objects are only required to fulfill the morphology criterion,  $M > 5$ , but they are not used to compute  $z_{\text{Bayes}}$ . Arc images with pass flag = 1 fulfill Color+Morphology+Contamination criteria &  $z_{\text{Bayes}} > z_{\text{cluster}}$  &  $z_{\text{Bayes}}$  single-valued. Note that arc systems 1 and 55 have the same physical origin and therefore have the same  $z_{\text{spec}}$  through our identification of arc 1.3 (object ID #336). So do systems 2 and 56, for which  $z_{\text{spec}}$  is measured through arc 56.1 (object ID #888). Systems 15, 16, and 17 are not included in the table or the lens model because they belong to northern subclumps with  $> 1$  arcminute separation from the cluster center shown in Fig. 2.3. The coordinates of these systems can be found in Richard et al. (2014).

<sup>1</sup>G = this work, J = (Jauzac et al., 2014), T = (Johnson et al., 2014), R = (Richard et al., 2014), C = (Clément et al. in preparation), Z = (Zitrin et al., 2014), L = (Lam et al., 2014), I = (Ishigaki et al., 2015). References correspond to most recent quote in the literature. System 60 is identified in this work for the first time.

<sup>2</sup>Redshift obtained from hierarchical Bayesian modeling. The values outside of the brackets are the mode of the combined posterior probability distribution. For systems that fulfill the selection criteria and do not have a spectroscopic redshift, this is the redshift assigned to the system in the lens model. Uncertainties represent the 68% credible region. Note that  $z_{\text{Bayes}} = 0.01$  is assigned if the posterior distribution of photometric redshift declines monotonically from 0, and is thus considered highly uncertain.

<sup>3</sup>Quality 0 indicates that  $z_{\text{Bayes}}$  is unreliable due to  $z_{\text{Bayes}} < z_{\text{cluster}}$  and/or there exists strong multi-modality in the posterior probability distribution of photometric redshift and/or only one image was used to compute  $z_{\text{Bayes}}$ . Quality 1 indicates that  $z_{\text{Bayes}}$  is secure.

<sup>4</sup>Best-fit magnification and 68% confidence limits derived from resampling the multiple image systems themselves and their photometric redshifts from the combined posterior distributions.

<sup>5</sup>Due to the use of a fixed SExtractor detection image at F160W, 2.2 was not detected with even the most aggressive SExtractor detection settings, i.e. the “hot” mode settings. Upon visual inspection in other HST bands, however, the object is clearly separated and unmistakably belongs to system 2.

<sup>6</sup>The redshift of this system comes from the geometric constraint by Zitrin et al. (2014).

Table 2.2. Emission line detection results on multiply and singly lensed sources

ID <sub>Glass</sub>	ID <sub>arc</sub>	R.A. (deg.)	Dec. (deg.)	F140W (mag)	$z_{\text{phot}}$	$z_{\text{spec}}$	Quality	P.A. (deg.)	N <sub>lines</sub>	Line(s)	Line Flux ( $10^{-17} \text{ erg s}^{-1} \text{ cm}^{-2}$ )	Magnification <sup>1</sup>	
00336	1.3	3.586232335	-30.409968879	22.92±0.01	$3.54^{+0.05}_{-3.24}$	1.50	3	135	3	[OII] [OIII] H $\alpha$	$4.1 \pm 1.0 \quad 10.4 \pm 0.9 \quad 1.5 \pm 0.5$	3.74 [3.63-4.22]	
00433	6.3	3.586426870	-30.409349590	24.29±0.02	$1.79^{+0.48}_{-1.15}$	2.02	4	233	1	H $\alpha$	$0.3 \pm 0.5$		
00523	6.2	3.594060460	-30.407997680	24.66±0.02	$0.05^{+3.73}_{-0.01}$	2.02	4	135	2	[OII] [OIII]	$0.4 \pm 1.0 \quad 10.1 \pm 0.7$	5.32 [5.08-6.09]	
49	00807	22.2	3.600055342	-30.404393062	27.18±0.15	$1.65^{+0.12}_{-0.20}$	4.84	2	233	1	[OII] [OIII]	$7.0 \pm 0.6$	
00888	56.1	3.582540997	-30.402326944	24.07±0.04	$0.17^{+0.98}_{-0.03}$	1.20	3	135	1	MgII	$2.4 \pm 1.1 \quad 5.3 \pm 0.6$	1.75 [1.86-2.09]	
00963	6.1	3.598536690	-30.401796690	24.86±0.02	$2.14^{+0.17}_{-0.18}$	2.02	4	233	1	MgII	$0.7 \pm 0.4$	5.10 [4.83-6.16]	
00996	37.3	3.578300682	-30.401388115	25.18±0.04	$1.60^{+0.14}_{-0.09}$	1.14	2	135	2	[OIII] H $\alpha$	$1.8 \pm 0.6$	6.40 [5.87-7.84]	
00111	...	3.595269940	-30.413962810	23.22±0.01	$0.78^{+0.08}_{-0.08}$	0.75	4	233	1	H $\alpha$	$0.9 \pm 0.6 \quad 3.3 \pm 0.6$		
00182	...	3.574583680	-30.412278150	22.83±0.01	$1.15^{+0.04}_{-0.46}$	1.37	4	135	3	[OII] [OIII] H $\alpha$	$5.4 \pm 1.2 \quad 4.8 \pm 0.8 \quad 7.9 \pm 0.5$	2.21 [2.21-2.34]	
								233	1	[OIII]	$11.4 \pm 0.9$		
									None	None		2.68 [2.51-2.81]	
								135	...	...	...	2.18 [2.05-2.19]	
								233	1	H $\alpha$	$8.7 \pm 0.9$		

Table 2.2 (cont'd)

ID <sub>GASS</sub>	ID <sub>arc</sub>	R.A. (deg.)	Dec. (deg.)	F140W (mag)	$z_{\text{phot}}$	$z_{\text{spec}}$	Quality	P.A. (deg.)	N <sub>lines</sub>	Line(s)	Line Flux ( $10^{-17} \text{ erg s}^{-1} \text{ cm}^{-2}$ )	Magnification <sup>l</sup>	
00221	...	3.575032820	-30.412223240	24.05±0.02	$1.31^{+0.05}_{-0.21}$	1.37	3	135	2	[OIII] H $\alpha$	$8.7 \pm 1.1$ 4.4±0.5	2.23 [2.22-2.38]	
00281	...	3.578893880	-30.409998270	22.77±0.01	$1.13^{+0.08}_{-0.15}$	1.27	3	233	1	[OIII]	11.8±1.2		
00351	...	3.576698590	-30.410185030	22.90±0.01	$1.62^{+0.10}_{-0.08}$	1.66	4	135	2	[OIII] H $\alpha$	$8.9 \pm 1.0$ 2.9±0.6	2.06 [2.07-2.26]	
00450	...	3.601762350	-30.407861940	22.16±0.01	$2.50^{+0.07}_{-0.18}$	1.10	3	233	2	[OIII] H $\alpha$	$8.1 \pm 1.0$ 0.9±0.5		
50	00644	...	3.575720740	-30.405377810	21.70±0.01	$1.01^{+0.08}_{-0.13}$	0.65	4	135	1	H $\alpha$	10.0±0.7	2.93 [2.97-3.30]
	00725	...	3.590332930	-30.400389630	18.43±0.01	$2.33^{+0.19}_{-0.07}$	0.50	4	233	1	H $\alpha$	7.0±0.7	
	00879	...	3.568643290	-30.402533060	23.95±0.01	$0.65^{+0.06}_{-0.13}$	1.03	3	135	1	H $\alpha$	11.1±0.4	1.56 [1.56-1.61]
	00993	...	3.575088880	-30.3996687000	21.82±0.01	$0.49^{+0.06}_{-0.22}$	1.74	4	233	1	H $\alpha$	16.1±0.8	
	01000	...	3.576954590	-30.400863030	23.70±0.01	$0.36^{+2.57}_{-0.01}$	1.33	4	135	2	[OIII] H $\alpha$	$12.5 \pm 1.1$ 5.1±0.5	2.53 [2.50-2.75]

Table 2.2 (cont'd)

ID <sub>Glass</sub>	ID <sub>arc</sub>	R.A. (deg.)	Dec. (deg.)	F140W (mag)	$z_{\text{phot}}$	$z_{\text{spec}}$	Quality	P.A. (deg.)	N <sub>lines</sub>	Line(s)	Line Flux ( $10^{-17} \text{ erg s}^{-1} \text{ cm}^{-2}$ )	Magnification	
01024	...	3.576571150	-30.399058380	23.43±0.02	0.01 <sub>-0.01</sub> <sup>+0.06</sup>	1.87	3	135	1	[OIII]	2.7±0.6	2.80 [2.78-2.97]	
01064	...	3.570589220	-30.399321550	24.93±0.07	1.73 <sub>-0.21</sub> <sup>+0.04</sup>	1.17	3	233	1	[OIII]	7.7±0.6		
01299	...	3.601617480	-30.395788330	23.33±0.01	1.33 <sub>-0.11</sub> <sup>+0.05</sup>	0.95	4	135	2	[OIII] H $\alpha$	1.1±0.6 1.0±0.5	2.43 [2.41-2.53]	
51	01316	...	3.600071860	-30.396194440	22.98±0.01	2.47 <sub>-2.32</sub> <sup>+0.09</sup>	0.95	3	233	2	[OIII] H $\alpha$	4.3±0.8 4.6±0.7	1.75 [1.74-1.91]
	01321	...	3.600368590	-30.396140420	22.51±0.01	0.93 <sub>-0.33</sub> <sup>+0.17</sup>	0.95	4	135	0	None	13.9±0.9 5.8±0.6	
	01352	...	3.605220170	-30.395395410	23.80±0.01	0.89 <sub>-0.10</sub> <sup>+0.06</sup>	1.18	3	233	1	H $\alpha$	4.6±0.6	1.86 [1.82-1.90]
	01364	...	3.579866430	-30.395231500	23.90±0.01	0.82 <sub>-0.09</sub> <sup>+0.08</sup>	0.45	4	135	1	H $\alpha$	8.9±0.7	1.87 [1.81-1.90]
	01447	...	3.600090790	-30.393760160	22.53±0.01	0.66 <sub>-0.04</sub> <sup>+0.22</sup>	1.35	4	135	3	[OII] [OIII] H $\alpha$	9.0±1.2 12.6±1.1 11.8±0.6	1.90 [1.89-2.09]
01451	...	3.576754780	-30.393626570	22.87±0.01	3.67 <sub>-0.16</sub> <sup>+2.12</sup>	1.37	4	135	3	[OII] [OIII] H $\alpha$	6.6±1.0 7.6±0.8 5.2±0.5		
								233	3	[OII] [OIII] H $\alpha$	7.4±1.1 10.7±0.8 7.0±0.5	3.11 [2.88-3.17]	
								233	3	[OII] [OIII] H $\alpha$	8.1±1.2 17.3±0.9 9.4±0.5		

Table 2.2 (cont'd)

ID <sub>GLASS</sub>	ID <sub>arc</sub>	R.A. (deg.)	Dec. (deg.)	F140W (mag)	$z_{\text{phot}}$	$z_{\text{spec}}$	Quality	P.A. (deg.)	N <sub>lines</sub>	Line(s)	Line Flux ( $10^{-17}$ erg s <sup>-1</sup> cm <sup>-2</sup> )	Magnification <sup>1</sup>
01460	...	3.606143820	-30.391952720	20.94±0.01	0.45 <sup>+0.05</sup> <sub>-0.32</sub>	2.10	4	135	1	[OIII]	12.5±1.3	1.93 [1.91-2.67]
01484	...	3.599948240	-30.393553790	23.18±0.01	1.17 <sup>+0.08</sup> <sub>-1.10</sub>	1.35	4	135	1	[OIII]	23.8±0.7	
01507	...	3.580947550	-30.390801210	19.20±0.01	1.33 <sup>+0.08</sup> <sub>-0.13</sub>	0.30	4	135	3	[OII] [OIII] H $\alpha$	9.6±1.2 19.6±0.9 13.5±0.5	1.87 [1.87-2.08]
01633	...	3.575857490	-30.390134740	22.74±0.01	1.13 <sup>+0.05</sup> <sub>-0.45</sub>	1.16	4	135	1	[OIII] H $\alpha$	10.0±1.3 26.2±1.1 12.3±0.5	
01635	...	3.591438810	-30.389519210	23.06±0.01	1.26 <sup>+0.07</sup> <sub>-1.20</sub>	1.36	3	135	1	H $\alpha$	75.2±1.4	
01653	...	3.598087370	-30.390624110	22.97±0.01	0.40 <sup>+0.05</sup> <sub>-0.23</sub>	1.00	4	233	1	H $\alpha$	76.5±2.0	
01661	...	3.603158470	-30.391072110	25.49±0.04	1.15 <sup>+0.01</sup> <sub>-0.40</sub>	2.19	4	233	2	[OIII] H $\alpha$	10.3±0.5 5.2±0.5	2.81 [2.54-2.71]
01712	...	3.578412620	-30.388848560	21.44±0.01	1.33 <sup>+0.07</sup> <sub>-0.13</sub>	1.16	4	233	1	H $\alpha$	9.8±0.6 8.7±0.6	
01802	...	3.593272850	-30.384377640	18.65±0.01	0.95 <sup>+0.05</sup> <sub>-0.14</sub>	0.30	4	135	1	H $\alpha$	12.7±0.7 8.3±0.6	1.87 [1.86-1.97]
...	...	...	...	...	...	...	...	135	1	[OIII]	2.8±0.5	2.19 [2.07-2.27]
...	...	...	...	...	...	...	...	233	1	[OIII]	3.0±0.5	
...	...	...	...	...	...	...	...	135	1	H $\alpha$	34.3±0.8	
...	...	...	...	...	...	...	...	233	1	H $\alpha$	14.2±1.1	
...	...	...	...	...	...	...	...	135	1	H $\alpha$	102.4±1.3	
...	...	...	...	...	...	...	...	233	1	H $\alpha$	112.4±1.4	

Table 2.2 (cont'd)

IDGLASS	ID <sub>arc</sub>	R.A. (deg.)	Dec. (deg.)	F140W (mag)	$z_{\text{phot}}$	$z_{\text{spec}}$	Quality	P.A. (deg.)	N <sub>lines</sub>	Line(s)	Line Flux ( $10^{-17} \text{ erg s}^{-1} \text{ cm}^{-2}$ )	Magnification <sup>1</sup>
01805	...	3.576834160	-30.388022630	24.56±0.02	$2.33^{+0.21}_{-0.05}$	1.36	4	135	2	[OIII] H $\alpha$	$4.5 \pm 0.8 \text{ } 2.9 \pm 0.5$	3.04 [2.81-3.04]
01849	...	3.580075540	-30.387061960	23.66±0.01	$1.03^{+0.04}_{-0.35}$	1.05	4	233	3	[OIII] [OII] H $\alpha$	$2.6 \pm 1.0 \text{ } 5.1 \pm 0.8 \text{ } 2.1 \pm 0.5$	2.92 [2.77-3.00]
01854	...	3.591335080	-30.387003820	23.65±0.02	$0.40^{+0.06}_{-0.20}$	1.36	4	233	2	[OIII] H $\alpha$	$6.9 \pm 0.7 \text{ } 6.4 \pm 0.6$	
53	01896	3.586980110	-30.387019390	24.88±0.02	$0.01^{+0.06}_{-0.01}$	1.86	3	135	2	[OIII] H $\alpha$	$2.9 \pm 0.8 \text{ } 1.7 \pm 0.5$	2.19 [2.06-2.20]
								233	2	[OIII] H $\alpha$	$1.9 \pm 0.8 \text{ } 2.3 \pm 0.5$	
01914	...	3.604404830	-30.384953900	20.81±0.01	$1.03^{+0.06}_{-0.12}$	0.30	4	135	1	[OIII]	$1.7 \pm 0.5$	3.31 [2.85-3.20]
								233	2	MgII [OIII]	$0.4 \pm 3.0 \text{ } 4.7 \pm 0.7$	
02105	...	3.597276410	-30.383435900	24.43±0.02	$1.33^{+0.06}_{-0.18}$	1.35	4	135	1	H $\alpha$	$14.5 \pm 1.1$	...
								233	1	H $\alpha$	$21.6 \pm 1.2$	
02128	...	3.594060590	-30.381637580	22.03±0.01	$2.17^{+0.15}_{-0.22}$	1.00	4	135	2	[OIII] H $\alpha$	$6.6 \pm 0.8 \text{ } 1.8 \pm 0.5$	2.13 [2.10-2.17]
								233	2	[OIII] H $\alpha$	$3.5 \pm 0.8 \text{ } 2.3 \pm 0.5$	
02137	...	3.592183020	-30.381766970	21.87±0.01	$0.38^{+0.06}_{-0.21}$	1.34	4	135	2	[OIII] H $\alpha$	$6.8 \pm 0.5 \text{ } 7.1 \pm 0.6$	1.98 [1.95-2.00]
								233	2	[OIII] H $\alpha$	$4.4 \pm 0.6 \text{ } 7.4 \pm 0.6$	
02174	...	3.591108650	-30.381705040	22.94±0.01	$1.33^{+0.10}_{-0.09}$	1.90	4	135	1	[OIII]	$17.4 \pm 0.5$	2.33 [2.28-2.37]
								233	1	[OIII]	$23.3 \pm 0.8$	2.73 [2.66-2.78]

Table 2.2 (cont'd)

ID <sub>GLASS</sub>	ID <sub>arc</sub>	R.A. (deg.)	Dec. (deg.)	F140W (mag)	$z_{\text{phot}}$	$z_{\text{spec}}$	Quality	P.A. (deg.)	N <sub>lines</sub>	Line(s)	Line Flux ( $10^{-17} \text{erg s}^{-1} \text{cm}^{-2}$ )	Magnification <sup>l</sup>	
02185	...	3.577000440	-30.379478020	19.94±0.01	$0.97^{+0.03}_{-0.21}$	0.50	4	135	...	...	...	1.42 [1.41-1.43]	
02191	...	3.573407710	-30.380770410	21.76±0.01	$1.13^{+0.07}_{-0.65}$	1.76	3	135	2	[OIII] [OII]	$7.0 \pm 0.5 \ 10.0 \pm 0.7$	2.46 [2.37-2.47]	
02233	...	3.584913910	-30.381249090	25.71±0.08	$2.37^{+0.14}_{-0.10}$	0.91	4	233	2	[OIII] [OII]	$12.9 \pm 0.9 \ 8.2 \pm 0.5$		
54	02236	...	3.607558590	-30.381347470	24.36±0.02	$0.46^{+0.08}_{-0.15}$	1.36	4	135	1	[OIII]	$1.4 \pm 0.6$	1.83 [1.78-1.83]
	02255	...	3.571779860	-30.380436770	23.82±0.01	$1.68^{+0.07}_{-0.09}$	1.68	4	233	1	[OIII]	$0.2 \pm 0.6$	
	02261	...	3.606322260	-30.380060610	22.73±0.02	$2.08^{+0.20}_{-0.11}$	1.34	4	135	2	[OIII] [OII]	$3.1 \pm 0.6$	1.79 [1.81-1.92]
	02270	...	3.588863100	-30.380291140	23.50±0.01	$1.35^{+0.03}_{-0.12}$	1.36	3	233	2	[OIII] [OII]	$2.8 \pm 0.6 \ 12.5 \pm 0.9$	2.49 [2.43-2.50]
	02275	...	3.585920460	-30.380684720	25.16±0.03	$0.08^{+0.09}_{-0.05}$	1.87	4	233	2	[OIII] [OII]	$3.2 \pm 0.7 \ 14.1 \pm 0.7$	
02294	...	3.581696660	-30.380207990	24.31±0.02	$1.15^{+0.07}_{-0.08}$	2.32	3	135	0	None	None	1.7±0.7 5.7±0.7	2.61 [2.50-2.61]

Table 2.2 (cont'd)

ID <sub>Glass</sub>	ID <sub>arc</sub>	R.A. (deg.)	Dec. (deg.)	F140W (mag)	$z_{\text{phot}}$	$z_{\text{spec}}$	Quality	P.A. (deg.)	N <sub>lines</sub>	Line(s)	Line Flux ( $10^{-17} \text{erg s}^{-1} \text{cm}^{-2}$ )	Magnification <sup>1</sup>
02349	...	3.591408500	-30.379785150	24.29±0.02	$1.35^{+0.07}_{-0.11}$	1.12	3	135	1	H $\alpha$	2.8±0.5	2.16 [2.13-2.18]
02358	...	3.607749030	-30.380202320	25.60±0.12	$2.47^{+0.07}_{-0.20}$	1.64	3	233	1	H $\alpha$	4.9±0.5	
55								135	0	None	None	1.83 [1.84-1.96]
02400	...	3.572036460	-30.378964260	25.82±0.05	$3.11^{+0.10}_{-0.46}$	2.07	3	233	2	[OII] [OIII]	$0.6\pm0.6$ $6.6\pm0.7$	
								135	...	...	...	
								233	3	MgII [OIII] [OIII]	$1.2\pm1.4$ $0.6\pm0.9$ $11.7\pm0.7$	2.59 [2.52-2.60]

Note. — The first part of this table consists of emission line identifications for the arcs of quality levels 4, 3, and 2, whereas the second part is comprised of only high-confidence (quality 3 or 4) emission line objects newly discovered during the blind search procedure, as described in Section 2.4.3. The uncertainty ranges and error bars quoted here all represent  $1-\sigma$  confidence level.

<sup>1</sup>Magnifications of multiply-lensed objects are calculated assuming redshift  $z_{\text{spec}}$ , which was only used in the lens model for quality > 2 objects.

# CHAPTER 3

## Sub-kiloparsec Resolution Gas-phase Metallicity Maps at Cosmic Noon behind the Hubble Frontier Fields cluster **MACS1149.6+2223**

### 3.1 Introduction

Galaxies are complex ecosystems, particularly at the peak epoch of cosmic star formation, corresponding to the redshift range of  $z \sim 1-3$ , also known as the “cosmic noon” (see Madau & Dickinson, 2014, for a recent review). During this approximately 4 Gyr, the Hubble sequence gradually breaks down and the predominant morphology of galaxies transforms from irregular systems at high redshifts to symmetric disks and bulges at low redshifts (Mortlock et al., 2013). This complexity is to a large extent induced by the interplay between the process of star formation, and the diverse aspects of baryonic cycling, e.g., galactic feedback, gas inflows/outflows, and major/minor mergers (Davé et al., 2011b; Martin et al., 2012). The effect of environment surrounding galaxies can further complicate the spatial distribution of star formation, as recently revealed by Vulcani et al. (2015); ?. Measurements of gas-phase metallicity, i.e., the chemical abundances of elements heavier than hydrogen and helium in the interstellar medium (ISM), are a powerful means to shed light on this complexity, because the metal enrichment history is strongly tied to the mass assembly history in galaxy evolution (Davé et al., 2011a; Lu et al., 2015b). Since detailed elemental abundances are not directly measurable at extragalactic distances, the relative oxygen abundance in ionized gaseous nebulae, i.e.,  $12 + \log(\text{O}/\text{H})$ , is often chosen as the observational proxy of metallicity.

For over a decade, a tight correlation between metallicity and galaxy stellar mass ( $M_*$ ), i.e., the mass-metallicity relation (MZR), has been quantitatively established, from the vast database

of local galaxies observed by the Sloan Digital Sky Survey (Tremonti et al., 2004; Zahid et al., 2012a; Andrews & Martini, 2013). This relation has been further extended to high redshifts, using deep near infrared (IR) spectroscopy facilitated by large ground-based and space-based telescopes (Erb et al., 2006; Maiolino et al., 2008; Zahid et al., 2011; Henry et al., 2013b; Steidel et al., 2014; Sanders et al., 2015; Guo et al., 2016). The measurements of the MZR as a function of redshift can cast useful constraints on various galaxy evolution models, since the slope of the MZR is sensitive to the properties of outflows, such as the mass loading factor and the outflow speed (see, e.g., Davé et al., 2012; Lu et al., 2015a). This slope can also be explained by variations of star-formation efficiency and gas mass fraction in galaxies with different stellar masses (see, e.g., Baldry et al., 2008; Zahid et al., 2014). The normalization of the MZR can shed light upon the stellar chemical yield across cosmic time (Finlator & Davé, 2008). Mannucci et al. (2010) first suggested that there exists a so-called fundamental metallicity relation (FMR) in the 3D parameter space spanned by  $M_*$ , star-formation rate (SFR), and metallicity, such that the MZR is merely a 2D projection of this more fundamental 3D manifold (see also Hunt et al., 2016). This 3D scaling relation shows a tight scatter ( $\sim 0.05$  dex) in metallicity and is speculated to not evolve with  $z$ . In this context, the apparent redshift evolution of the MZR normalization originates primarily from sampling the FMR in terms of galaxies with different SFR. This concept of the FMR is in accord with the gas regulator model proposed by Lilly et al. (2013), even though mergers can also play a subtle role in shaping the form of the FMR by increasing the scatter (Michel-Dansac et al., 2008). However, at high redshifts, the validity of the FMR is still under investigation (see, e.g., Sanders et al., 2015; Wuyts et al., 2014).

Spatially resolved chemical information provides a more powerful diagnostic tool about galaxy baryonic assembly than integrated metallicity measurements, especially at high redshifts. Because for non-interacting galaxies, their metallicity radial gradients are found to be highly sensitive to the properties of gas, i.e., the surface density, the existence of inflows/outflows, and the kinematic structure (Cresci et al., 2010; Jones et al., 2013; Sanchez et al., 2014; Troncoso et al., 2014). In the past few years, metallicity radial gradients, measured from spectroscopic data acquired by ground-based instruments with natural seeing ( $\gtrsim 0.^{\prime\prime}6$ ), have been reported at high redshifts (Queyrel et al., 2012; Troncoso et al., 2014; Stott et al., 2014). In particular, a large mass-selected sample of

galaxies at  $0.7 \lesssim z \lesssim 2.7$  were observed with spatially resolved gas kinematics and star formation, using the K-band Multi Object Spectrograph (*KMOS*) on the Very Large Telescope (*VLT*) (i.e., the *KMOS*<sup>3D</sup> survey, Wisnioski et al., 2015). As a result, ? measured metallicity gradients for 180 star-forming galaxies in three redshift intervals (i.e. [0.8, 1.0], [1.3, 1.7], and [2.0, 2.6]), and found that the majority of the metallicity gradients are flat and no statistical significant correlations between metallicity gradients, and stellar, kinematic, and structural properties of the galaxy.

However, seeing-limited measurements typically have insufficient resolution to resolve the inner structure of galaxies at  $z \gtrsim 1$ , and the inferred metallicity gradient can be potentially biased. For example, Yuan et al. (2013) showed that coarse spatial sampling ( $\geq 1$  kpc) can result in artificially flat metallicity gradients, inferring that sufficiently high spatial resolution, i.e., *sub-kpc* scale (corresponding to an angular resolution of  $< 0.^{\circ}2\text{--}0.^{\circ}3$ ), is crucial in yielding precise information of how metals are distributed spatially in extragalactic HII regions. Only a few metallicity gradient measurements meet this requirement, including a sample of 9 H $\alpha$ -selected galaxies at  $z \in [0.84, 2.23]$  (the majority at  $z \sim 1.45$ ), observed with the adaptive optics (AO) assisted integral field unit (IFU) spectrograph *SINFONI* onboard the *VLT* (Swinbank et al., 2012). Even higher resolution can be attained through the combination of diffraction-limited data and gravitational lensing as shown by Jones et al. (2010, 2013); Yuan et al. (2011), targeting strongly lensed galaxies with the laser guide star AO aided IFU spectrograph *OSIRIS* at the *Keck* telescope. Following this approach, Leethochawalit et al. (2016) recently analyzed a sample of 11 lensed galaxies (3 at  $z \sim 1.45$  and the rest at  $z \gtrsim 2$ ), deriving maps of both metallicity and emission line (EL) kinematics. Although a great amount of effort has been invested in enlarging the sample size of high- $z$  metallicity gradients obtained with sub-kpc scale spatial resolution, the current sample consists of only  $\lesssim 30$  such gradients and is still statistically insufficient to explore trends with stellar mass and redshift.

In order to enlarge the sample of sub-kpc resolution measurements, we recently demonstrated that such metallicity maps can be derived using space-based data (Jones et al., 2015b). We measured a flat metallicity gradient in a multiply lensed interacting system at  $z = 1.85$ , using diffraction-limited Hubble Space Telescope (*HST*) grism data, and confirmed that flat metallicity gradients can be caused by gravitational interactions in merging systems.

The main goal of the work presented here is to collect a uniformly analyzed large sample of high- $z$  metallicity maps obtained with sub-kpc spatial resolution. To meet our goal, we improve upon the methodology proposed in our pilot paper (Jones et al., 2015b), in particular via developing a novel Bayesian method to imply metallicity from multiple EL diagnostics simultaneously. We apply our advanced analysis to ultra-deep grism data of the massive galaxy cluster MACS1149.6+2223, thus exploiting the powerful synergy of *HST* diffraction-limited spectroscopy and lensing magnification.

The outline of this Chapter is as follows. In Section 3.2, we introduce the spectroscopic observations used in this work and the selection of our metallicity gradient sample. The photometric data and galaxy cluster lens models are briefed in Section 3.3. We then present our entire analysis process in Section 3.4, and show our results in terms of global demographics and spatially resolved analysis in Sections 3.5 and 3.6, respectively. Finally, Section 4.4 will conclude and discuss our study. The concordance cosmological model ( $\Omega_m = 0.3$ ,  $\Omega_\Lambda = 0.7$ ,  $H_0 = 70 \text{ km s}^{-1} \text{ Mpc}^{-1}$ ) and the AB magnitude system (Oke & Gunn, 1983) are used throughout. Without specific number showing the wavelength, the names of forbidden lines are simplified as [O II]  $\lambda\lambda 3726, 3729 := [\text{O II}]$ , [O III]  $\lambda 5008 := [\text{O III}]$ , [N II]  $\lambda 6585 := [\text{N II}]$ , [S II]  $\lambda\lambda 6718, 6732 := [\text{S II}]^1$ .

## 3.2 Spectroscopic Data and Sample Selection

In Section 3.2.1, we summarize our *HST* grism observations, data quality, and data reduction. Our sample selection criteria are then described in Section 3.2.2. We also carried out some ground-based integral field unit (IFU) observations on part of our sample, which are presented in Appendix 4.A.

Table 3.1. Properties of the grism spectroscopic data used in this work

	PA <sup>a</sup> (deg.)	Grism	Exposure Time (s)	Program	Time of completion
032	G102	8723	<i>GLASS</i>	Feburary 2014	
	G141	4412	<i>GLASS</i>		
111	G141	36088	SN Refsdal follow-up	December 2014	
119	G141	36088	SN Refsdal follow-up	January 2015	
125	G102	8623	<i>GLASS</i>	November 2014	
	G141	4412	<i>GLASS</i>		

Note. — Here we only include the grism observations targetted on the prime field of Abell 370.

<sup>a</sup>The position angle shown here corresponds to the “PA\_V3” value reported in the WFC3/IR image headers. The position angle of the dispersion axis of the grism spectra is given by  $\text{PA}_{\text{disp}} \approx \text{PA}_V3 - 45$ .

### 3.2.1 Hubble Space Telescope Grism Spectroscopy

#### 3.2.1.1 The Grism Lens-Amplified Survey from Space

The Grism Lens-Amplified Survey from Space<sup>2</sup> (*GLASS*; Proposal ID 13459; P.I. Treu, Schmidt et al., 2014; Treu et al., 2015b) is an *HST* cycle 21 large general observing (GO) program. *GLASS* observed 10 massive galaxy clusters with the Wide Field Camera 3 Infrared (WFC3/IR) grisms (G102 and G141; 10 and 4 orbits per cluster, respectively) targeted at their centers and the Advanced Camera for Survey (ACS) Optical grism (G800L) at their infall regions. The exposure on each cluster core is split into two nearly orthogonal position angles (PAs), in order to disentangle contamination from neighboring objects. Data acquisition was completed in January 2015. Here we focus on the grism data targeted on the center of MACS1149.6+2223 taken in February 2014 (PA=032°) and November 2014 (PA=125°), marked by blue squares in Figure 3.1 (also see Table 3.1). *GLASS* provides ~10% of the G141 exposures used in this work, and 100% of the G102

<sup>1</sup>The wavelength values are taken from <http://classic.sdss.org/dr7/algorithms/linetable.html>

<sup>2</sup><http://glass.astro.ucla.edu>

exposures. Details on *GLASS* data reduction can be found in Schmidt et al. (2014); Treu et al. (2015b).

Shallow images through filters F105W or F140W were taken to aid the alignment and extraction of grism spectra. The imaging exposures are combined with the exposures obtained by the Hubble Frontier Fields (*HFF*) initiative and other programs to produce the deep stacks, released as part of the *HFF* program (see Section 3.3 for more details).

### 3.2.1.2 The Supernova Refsdal Follow-up Program with *HST* G141

The majority of the G141 exposures used in this work (30 orbits) were taken as part of the follow-up *HST* GO/DDT campaign (Proposal ID 14041, P.I. Kelly, Brammer et al. in prep.) of the first multiply imaged supernova, SN Refsdal (Kelly et al., 2015b). Two pointings (shown by the red squares in Figure 3.1) were exposed between December 2014 and January 2015 with 8 degrees apart (i.e. at PA=111°, and 119° respectively, as shown in Table 3.1), in order to optimize the spectroscopy of SN Refsdal. The analysis of the spectra of SN Refsdal, which showed that it was SN 1987A-like, is described by Kelly et al. (2015c).

### 3.2.1.3 Grism Data Reduction

The combined grism dataset was reduced following the procedure of the 3D-*HST* survey (Brammer et al., 2012b; Momcheva et al., 2016). An updated 3D-*HST* pipeline<sup>3</sup> was employed to reduce the images and spectra. The ASTRODRIZZLE software from the DRIZZLEPAC package and `tweakreg` were used to align and combine individual grism exposures, subtracting the sky images provided by Brammer et al. (2012b). The time-varying sky background due to helium glow (at 10,830 Å) in the Earth exosphere was also accounted for according to Brammer et al. (2014a). After these initial steps, the mosaics were co-added through interlacing onto a grid of 0.065 resolution, Nyquist sampling the point spread function (PSF) full width half maximum (FWHM). The average spectral resolution is  $R \sim 210$  and  $R \sim 130$  for G102 and G141, respectively. The average pixel scale after interlacing is 12 Å and 22 Å respectively for G102 and G141.

---

<sup>3</sup><http://code.google.com/p/threedhst/>

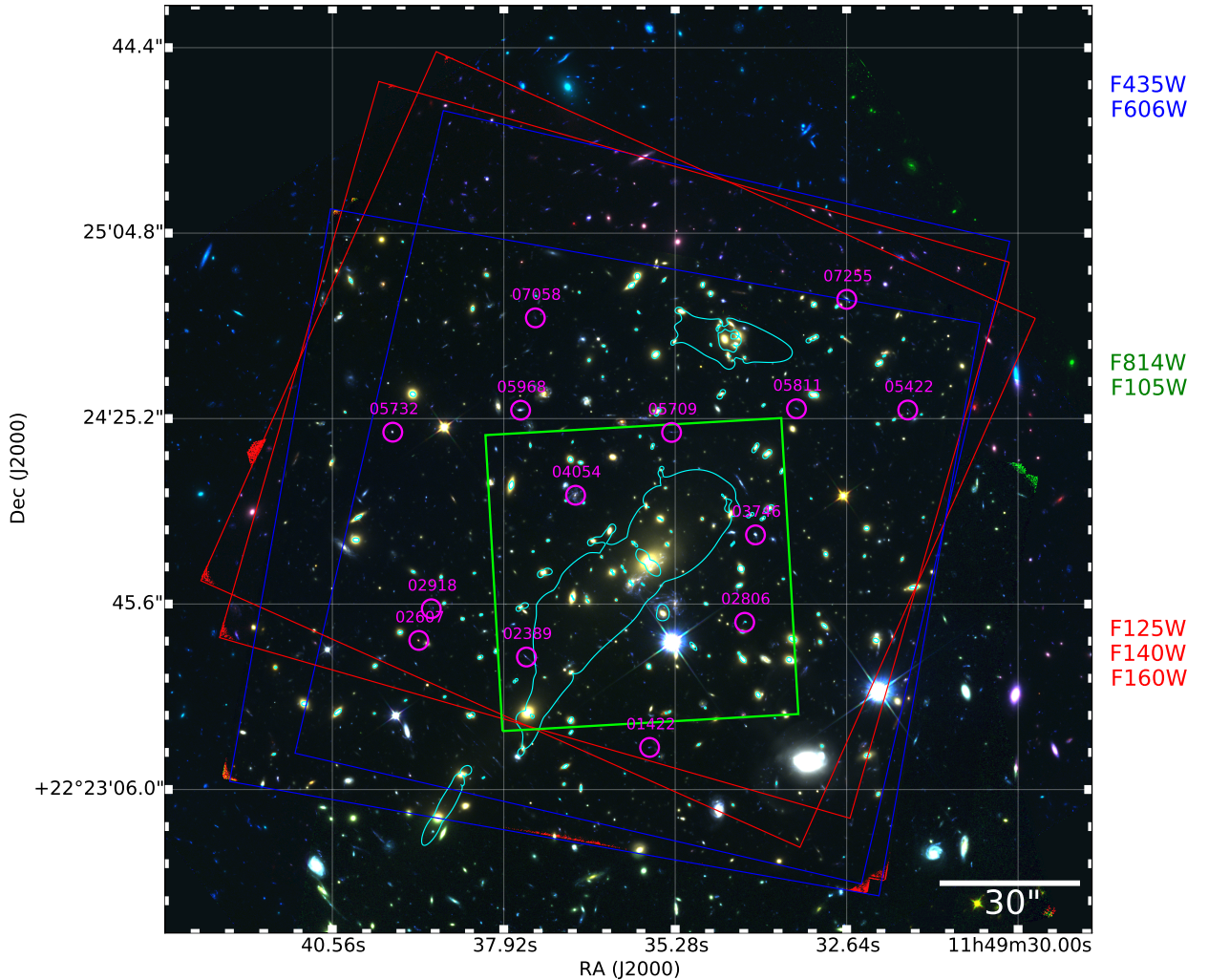


Figure 3.1 Color composite image of MACS1149.6+2223 from the full-depth 7-filter *HFF* photometry. The blue, green, and red channels are comprised of the *HST* broad-band filters shown on the right. The blue, red and green squares mark the footprints of *GLASS*, the Refsdal follow-up, and *MUSE* programs utilized in this work. The cyan contours are the critical curves at  $z = 1.8$  predicted by the GLAFIC version 3 lens model. The critical curves denote the regions where lensing magnification reaches infinity. Thus the closer proximity between the object and the critical curve at the object's redshift indicates higher magnification that the object has. The magenta circles show the positions of our metallicity gradient sample.  $3 \times 3$  arcsec $^2$  zoom-in postage stamps around these positions are shown in Figure 3.2.

We used the co-added  $H_{160}$ -band mosaics as the detection image, on which SExtractor was run. An object catalog was generated and a corresponding segmentation map was created for each object, determining which spatial pixels (spaxels) belong to this object. Thus for a source registered in the catalog and falling within the WFC3 grism field-of-view (FoV), we extracted its spectra from grism mosaics through adding up the dispersed flux for all spaxels within an area defined by the segmentation image of this source, after flat-field correction and background subtraction. The “fluxcube” model from the AXE package (Kümmel et al., 2009) was employed to generate the 2D models of stellar spectrum, based upon the spatial profile of the source, the color information from direct image mosaics (if available), and the grism calibration configurations. For sources of interest, this model serves as the continuum model which we re-scaled and subtracted from the observed 2D spectra (see Section 3.4.3 for more details) in order to obtain pure EL maps. At the same time, if the object is a bright contaminating neighbour, this 2D model also functions as spectral contamination, which is subtracted before the continuum removal.

The data used in this work contain a total of 34 orbits of G141 and 10 orbits of G102, reaching a  $1-\sigma$  flux limit (uncorrected for lensing magnification) of  $3.5(1.2)\times 10^{-18}$  erg s $^{-1}$  cm $^{-2}$  over the wavelength range of G102(G141), calculated from Schmidt et al. (2016). Our data provide an uninterrupted wavelength coverage in the range of 0.8-1.7  $\mu$ m and make this particular field one of the deepest fields probed by *HST* spectroscopy to date.

### 3.2.2 Sample Selection

Table 3.2. Global demographic properties of the metallicity gradient sample analyzed in this work

ID	R.A. [deg.]	Dec. [deg.]	$z_{\text{spec}}$	$\mu^{\text{a}}$	$H_{160}$ magnitude [ABmag]	SED fitting		EL diagnostics		
						$\log(M_* / M_\odot)$	$A_V^{\text{S}^{\text{c}}}$	$12 + \log(\text{O}/\text{H})$	SFR [ $M_\odot/\text{yr}$ ]	$A_V^{\text{N}^{\text{c}}}$
01422	177.398643	22.387499	2.28	2.35 [2.09, 2.26]	24.46	$9.29^{+0.07}_{-0.01}$	< 0.01	$8.26^{+0.11}_{-0.13}$	$15.10^{+16.76}_{-7.11}$	< 1.07
02389	177.406546	22.392860	1.89	43.25 [37.47, 50.28]	23.29	$8.43^{+0.06}_{-0.07}$	< 0.01	$7.88^{+0.16}_{-0.15}$	< 6.37	$1.36^{+0.69}_{-0.82}$
02607 <sup>d</sup>	177.413454	22.393843	1.86	3.01 [2.79, 2.98]	22.63	$10.25^{+0.06}_{-0.10}$	$1.70^{+0.42}_{-0.18}$	$7.70^{+0.13}_{-0.11}$	> 36.51	$2.26^{+0.31}_{-0.58}$
02806	177.392541	22.394921	1.50	4.82 [3.11, 3.51]	23.35	$8.72^{+0.19}_{-0.01}$	$0.50^{+0.01}_{-0.01}$	$7.96^{+0.15}_{-0.16}$	$1.96^{+1.37}_{-0.13}$	< 0.18
02918	177.412652	22.395723	1.78	2.95 [2.72, 2.91]	25.22	$8.37^{+0.15}_{-0.08}$	$0.10^{+0.34}_{-0.10}$	$8.42^{+0.11}_{-0.14}$	< 70.32	$1.25^{+0.72}_{-0.80}$
03746	177.391848	22.400105	1.25	3.78 [3.56, 3.83]	22.48	$8.81^{+0.03}_{-0.01}$	< 0.01	$8.11^{+0.10}_{-0.11}$	$10.95^{+1.61}_{-0.58}$	< 0.17
04054	177.403393	22.402456	1.49	3.39 [3.04, 3.28]	21.27	$9.64^{+0.05}_{-0.01}$	$1.10^{+0.01}_{-0.01}$	$8.70^{+0.09}_{-0.11}$	$16.99^{+5.71}_{-2.80}$	$0.72^{+0.23}_{-0.23}$
05422	177.382077	22.407510	1.97	3.63 [3.11, 4.41]	25.05	$8.45^{+0.15}_{-0.46}$	$0.00^{+0.56}_{-0.01}$	$7.56^{+0.16}_{-0.12}$	< 38.18	< 1.85
05709	177.397234	22.406181	1.68	7.10 [6.74, 7.53]	25.44	$7.90^{+0.02}_{-0.03}$	< 0.01	$8.21^{+0.13}_{-0.21}$	< 17.97	< 1.18
05732	177.415126	22.406195	1.68	1.56 [1.51, 1.61]	23.45	$9.09^{+0.01}_{-0.01}$	< 0.01	$8.41^{+0.10}_{-0.12}$	< 84.70	< 1.31
05811	177.389220	22.407583	2.31	7.50 [6.88, 9.34]	23.79	$8.85^{+0.11}_{-0.10}$	< 0.01	$8.16^{+0.14}_{-0.21}$	$4.94^{+3.13}_{-2.47}$	< 0.74
05968	177.406922	22.407499	1.48	1.84 [1.78, 1.96]	22.24	$9.34^{+0.02}_{-0.03}$	$0.60^{+0.20}_{-0.01}$	$8.47^{+0.07}_{-0.08}$	$27.95^{+4.70}_{-4.41}$	$0.23^{+0.15}_{-0.13}$
07058	177.405976	22.412977	1.79	2.13 [1.97, 3.01]	24.28	$8.74^{+0.17}_{-0.15}$	$0.00^{+0.12}_{-0.01}$	$8.38^{+0.13}_{-0.19}$	< 44.99	< 1.85
07255	177.385990	22.414074	1.27	2.34 [2.31, 2.99]	22.47	$9.36^{+0.01}_{-0.21}$	$0.30^{+0.21}_{-0.01}$	$8.38^{+0.08}_{-0.08}$	$8.73^{+3.53}_{-3.10}$	< 0.79

Note. — The error bars and upper/lower limits shown in the columns of SED fitting and EL diagnostics correspond to  $1-\sigma$  confidence ranges. Note that the errors on the SED fitting results do not include any systematic uncertainties associated with the Bruzual & Charlot (2003) stellar population models.

<sup>a</sup>Best-fit magnification values and  $1-\sigma$  confidence intervals. Except for galaxy ID 02389, the magnification results are from the GIAFIC version 3 model, calculated by the *HFF* interactive online magnification calculator available at <https://archive.stsci.edu/prepds/frontier/lensmodels/webtool/magnif.html>. For galaxy ID 02389, we use the SHARON & JOHNSON version 3 model instead to compute the magnification results and correct for lensing magnification.

<sup>b</sup>Values presented here are corrected for lensing magnification.

<sup>c</sup>The superscripts of ‘‘S’’ and ‘‘N’’ refer to the stellar and nebular V-band dust extinction in units of magnitude, respectively.

<sup>d</sup>The EL diagnostic result on this source is not trustworthy, since it is classified as an AGN candidate (see Sect. 3.5).

The selection of our metallicity gradient sample is based upon the master redshift catalog for MACS1149.6+2223<sup>4</sup>, published by the *GLASS* collaboration. As described by Treu et al. (2016), redshifts were determined by combining spectroscopic information from *GLASS* and the SN Refsdal follow-up *HST* grism programs, ground-based *MUSE* observations and Keck *DEIMOS* data.

For the purpose of this study, we compiled an exhaustive list of spatially extended sources with secure spectroscopic redshift measurements in the range of  $z \in [1.2, 2.3]$ , showing strong ELs (primarily [O III] and H $\beta$ ) in the 2D grism spectra. The reason this redshift range is selected is that we require high signal-to-noise ratio (SNR) detections of [O III], H $\beta$  and [O II] ELs in the spectral region where grism sensitivity and throughput do not drop significantly, in order to deliver reliable metallicity estimates from well-calibrated EL diagnostics<sup>5</sup>. The selection results in a sample of 14 galaxies. The positions of these 14 galaxies relative to the cluster are denoted by the magenta circles in Figure 3.1, while the postage stamp images of these galaxy are shown in Figure 3.2. The full sample is also listed in Table 4.1. In particular, one source in our sample, i.e., galaxy ID 04054, is one of the multiple images of SN Refsdal’s host galaxy (see Figure 3.3 for its appearances from various perspectives). A steep metallicity gradient ( $-0.16 \pm 0.02$  dex/kpc) has been previously measured on another multiple image of this spiral galaxy (Yuan et al., 2011). Our work is the first metallicity gradient measurement on this particular image, which is least distorted/contaminated by foreground cluster members. We also take advantage of a more precise lens model of both the entire cluster and the SN Refsdal host, from the extensive lens modeling effort summarized by Treu et al. (2016).

### 3.3 Photometry and Lens Models from the *HFF*

The Hubble Frontier Fields initiative<sup>6</sup> (*HFF*; P.I. Lotz, Lotz et al., 2016) is an ongoing multi-cycle treasury program enabled by an *HST* director’s discretionary time allocation. *HFF* targets

---

<sup>4</sup>available at <https://archive.stsci.edu/prepds/glass/>

<sup>5</sup>The H $\alpha$  EL is only accessible in sources at  $z \leq 1.5$  in our sample. The *GLASS* spectra of an exemplary galaxy whose H $\alpha$  is covered are displayed in Appendix 3.2.

<sup>6</sup><http://www.stsci.edu/hst/campaigns/frontier-fields>

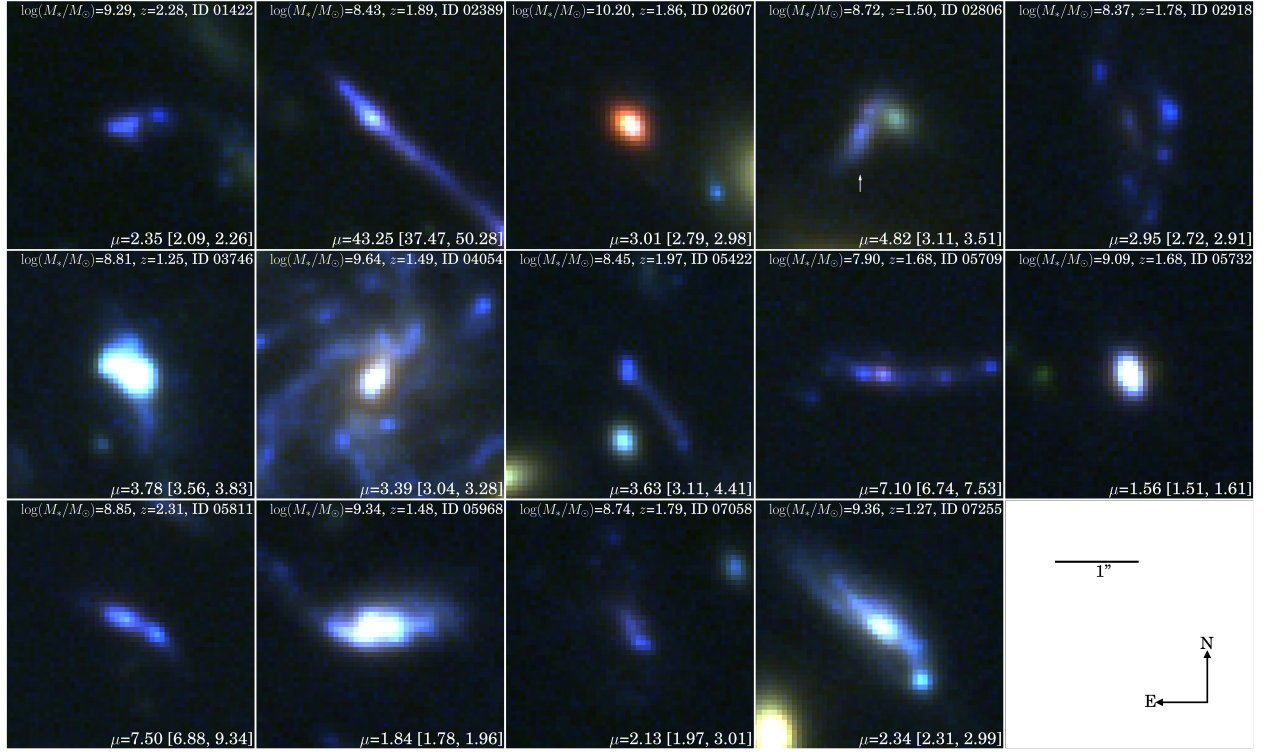


Figure 3.2 Zoom-in color composite stamps of our metallicity gradient sample, cut out from the full FoV image shown in Figure 3.1. In each stamp, we also show the spectroscopic redshift, stellar mass and lensing magnification (best-fit value followed by  $1-\sigma$  confidence interval) of the galaxy. In the panel of ID 02806, we use the white arrow to point to our galaxy of interest (ID 02806). All stamps are on the same spatial scale. The  $1''$  scale bar and north-east compass are shown in the lower right corner.

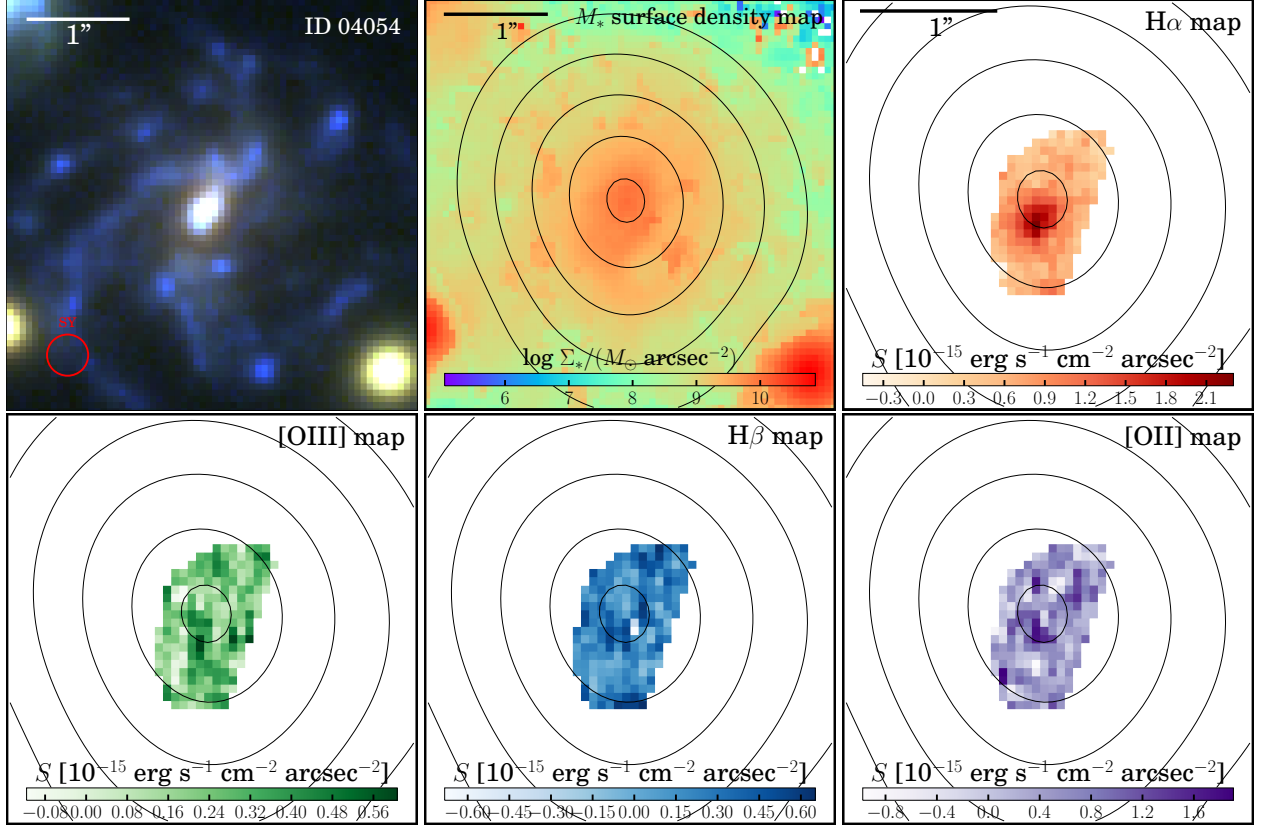


Figure 3.3 Multi-perspective view of the SN Refsdal host galaxy multiple image 1.3, i.e., ID 04054 in our metallicity gradient sample. *Upper left:* zoom-in color composite stamp cut out from Figure 3.1, where the estimated site of the un-observed past appearance of SN Refsdal is denoted by the red circle. *Upper middle:* stellar mass surface density map for this galaxy, where the source plane de-projected galactocentric radius contours are overlaid, in 2 kpc intervals, starting from 1 kpc. *Upper right:* H $\alpha$  surface brightness map combined from the *HST* grism exposures at all PAs from the *GLASS* and Refsdal follow-up programs. The black contours again show the de-projected galactocentric radii in the same fashion presented in the stellar mass surface density map in the upper middle panel. *Lower rows:* combined surface brightness maps of [O III], H $\beta$ , and [O II], presented in the same fashion as in the H $\alpha$  emission line map in the upper right panel.

the cores (prime fields) and infall regions (parallel fields) of six massive galaxy clusters, reaching an ultra-faint intrinsic magnitude of 30-33, made possible by the synergy of diffraction limited photometry and lensing magnification. The large wavelength coverage, uninterrupted from  $B_{435}$  to  $H_{160}$  passbands, is crucial for photometric redshift determinations and stellar population synthesis.

Besides the deep image mosaics, the *HFF* collaboration also provides the community with cluster lens models<sup>7</sup>. Several groups of scientists were invited prior to the beginning of the campaign to provide independent models depicting the total mass distribution of the six *HFF* clusters, using a number of distinct techniques. As data accumulate and more multiply imaged systems are identified, the lens models are continuously improved. For our cluster of interest, MACS1149.6+2223, the most up-to-date publicly available model is the GLAFIC version 3 model, constructed using a simply parametrized method proposed by Oguri (2010). For an in-depth description of the various modeling techniques, their advantages and limitations, we refer to Treu et al. (2016); Meneghetti et al. (2016).

In this work, we need lens models to trace the observed metallicity maps back to the source plane. Following our previous work (Jones et al., 2015b), we experiment with several publicly available models to find the ones that give the reconstruction of our target sources the highest fidelity (judging by how well the source plane morphologies of multiply imaged sources match each other). Based upon the SN Refsdal test (see also Kelly et al. (2015a)), the GLAFIC version 3 model (Kawamata et al., 2015), the GRILLO model (Grillo et al., 2016), and the SHARON & JOHNSON version 3 model were the most accurate ones, so we considered those three. As an illustration, the GLAFIC version 3 critical curves at  $z = 1.8$ , the median redshift of our metallicity gradient sample, are overlaid in cyan in Figure 3.1.

The most highly magnified source in our sample is galaxy ID 02389, one of the folded arcs which straddle the critical curve. For that particular source, we used as our default the SHARON & JOHNSON version 3 model, updated from the earlier versions presented in Johnson et al. (2014b); Sharon & Johnson (2015). The SHARON & JOHNSON version 3 model leads to a more precise reconstruction of the source plane morphology of galaxy ID 02389. We also tested that switching

---

<sup>7</sup><http://archive.stsci.edu/prepds/frontier/lensmodels/>

entirely from the GLAFIC version 3 model to the SHARON & JOHNSON version 3 model does not affect our measurements significantly, as also pointed out by Leethochawalit et al. (2016). The lensing magnification results from the considered lens models are given in Table 4.1.

## 3.4 Analysis Procedures

Here we describe the stellar population synthesis analysis of our sample in Section 3.4.1, and source plane morphology reconstruction in Section 3.4.2. The entire steps necessary for extracting EL maps from 2D grism spectra combined from different PAs are detailed in Section 3.4.3. Our new Bayesian method to jointly infer metallicity, nebular dust extinction, and SFR from a simultaneous use of multiple strong ELs is presented in Section 3.4.4.

### 3.4.1 Spectral Energy Distribution Fitting

The full-depth 7-filter *HFF* photometry was fitted with the template spectra from Bruzual & Charlot (2003) using the stellar population synthesis code FAST (Kriek et al., 2009b), in order to derive global estimates of stellar mass ( $M_*$ ) and the dust extinction of stellar continuum ( $A_V^S$ ) for each source in our sample. We take a grid of stellar population parameters that include: exponentially declining star formation histories with  $e$ -folding times ranging from 10 Myr to 10 Gyr, stellar ages ranging from 5 Myr to the age of the universe at the observed redshift, and  $A_V^S=0\text{--}4$  magnitudes for a Calzetti et al. (2000) dust extinction law. We assume the Chabrier (2003) initial mass function (IMF) and fix the stellar metallicity to solar. Table 4.1 lists the best-fit  $M_*$  values, corrected for lensing magnification. Although the adopted solar metallicity is higher than the typical gas-phase abundances we infer for the sample, this has little effect on the derived stellar mass. Fixing the stellar metallicity to 1/5 solar (i.e.  $Z = 0.004$  or  $12 + \log(\text{O/H}) = 8.0$ , corresponding to the sample median) reduces the best-fit  $M_*$  by only  $\sim 0.03$  dex.

### 3.4.2 Source Plane Morphology

Measurements of metallicity gradients require knowledge of the galaxy center, major axis orientation, and inclination or axis ratio. We derive these quantities from spatially resolved maps of the stellar mass surface density following the methodology described in Jones et al. (2015b). Briefly, we smooth the *HFF* photometric images to a common point spread function of  $0.^{\prime\prime}2$  FWHM and fit the spectral energy distribution (SED) of each spaxel using the same procedure described in Section 3.4.1. The resulting  $M_*$  maps in the image plane are shown in Figures 3.3 and 3.4. We reconstruct the  $M_*$  maps in the source plane using the adopted lens models and determine the centroid, axis ratio, inclination and major axis orientation from a 2D elliptical Gaussian fit to the  $M_*$  distribution. This allows us to measure the galactocentric radius at each point, assuming that contours of  $M_*$  surface density correspond to constant de-projected radius (following Jones et al., 2015b).

Since the following analysis is mostly done with the robust image plane data, we reconstruct the derived radius maps in the image plane. The contours of constant source-plane galactocentric radius for each galaxy in our sample are shown in Figures 3.3 and 3.4. Note that these contours are distorted from ellipses ascribed to the shear of gravitational lensing. For nearly half of our sample where we have seeing-limited IFU data described in Appendix 4.A, we verify that for galaxies with significant rotation support (e.g. IDs 05709 and 05968), the morphological major axis agrees at  $2\sigma$  with the pseudo-slit that maximizes velocity shear according to our kinematic analysis.

### 3.4.3 Emission Line Maps from Grism Spectra

The broad grism wavelength coverage provides spatially resolved maps of multiple ELs, such as [O II], H $\gamma$ , H $\beta$ , [O III], H $\alpha$  +[N II], and [S II]. The integrated fluxes of these ELs for our sample of galaxies are presented in Appendix 3.2. To obtain pure EL maps, we first use the AXE continuum models described in Section 3.2 to subtract contaminating flux from neighboring sources. The continuum model for the target object is scaled to match the locally observed levels, and then subtracted. We check that the flux residual in regions near the ELs of interest follow a normal distribution with zero mean.

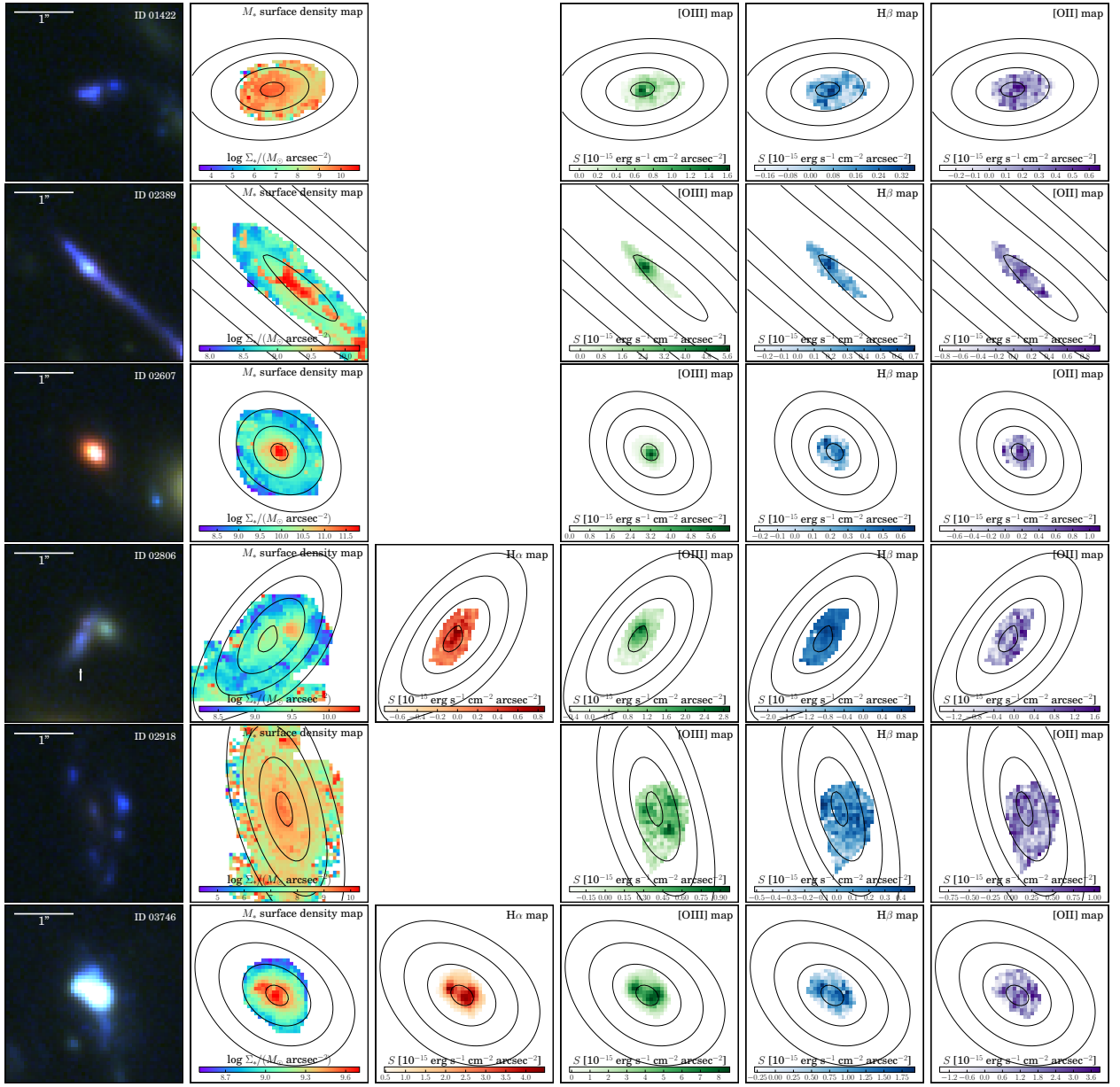


Figure 3.4 Multi-perspective view of our metallicity gradient sample except for the SN Refsdal host which is shown in Figure 3.3. In each row, we show the zoom-in color composite stamp (the same as that in Figure 3.2), the stellar mass surface density map, the combined surface brightness maps of H $\alpha$  (if available given object redshift), [O III], H $\beta$ , [O II] for each object. The black contours overlaid represent the source plane de-projected galactocentric radii in 2 kpc interval, starting from 1 kpc. The spatial extent and orientation of the stamps for each object have been fixed. The typical surface brightness 1- $\sigma$  uncertainty in these combined EL maps is  $2 \times 10^{-16} \text{ erg s}^{-1} \text{ cm}^{-2} \text{ arcsec}^{-2}$ .

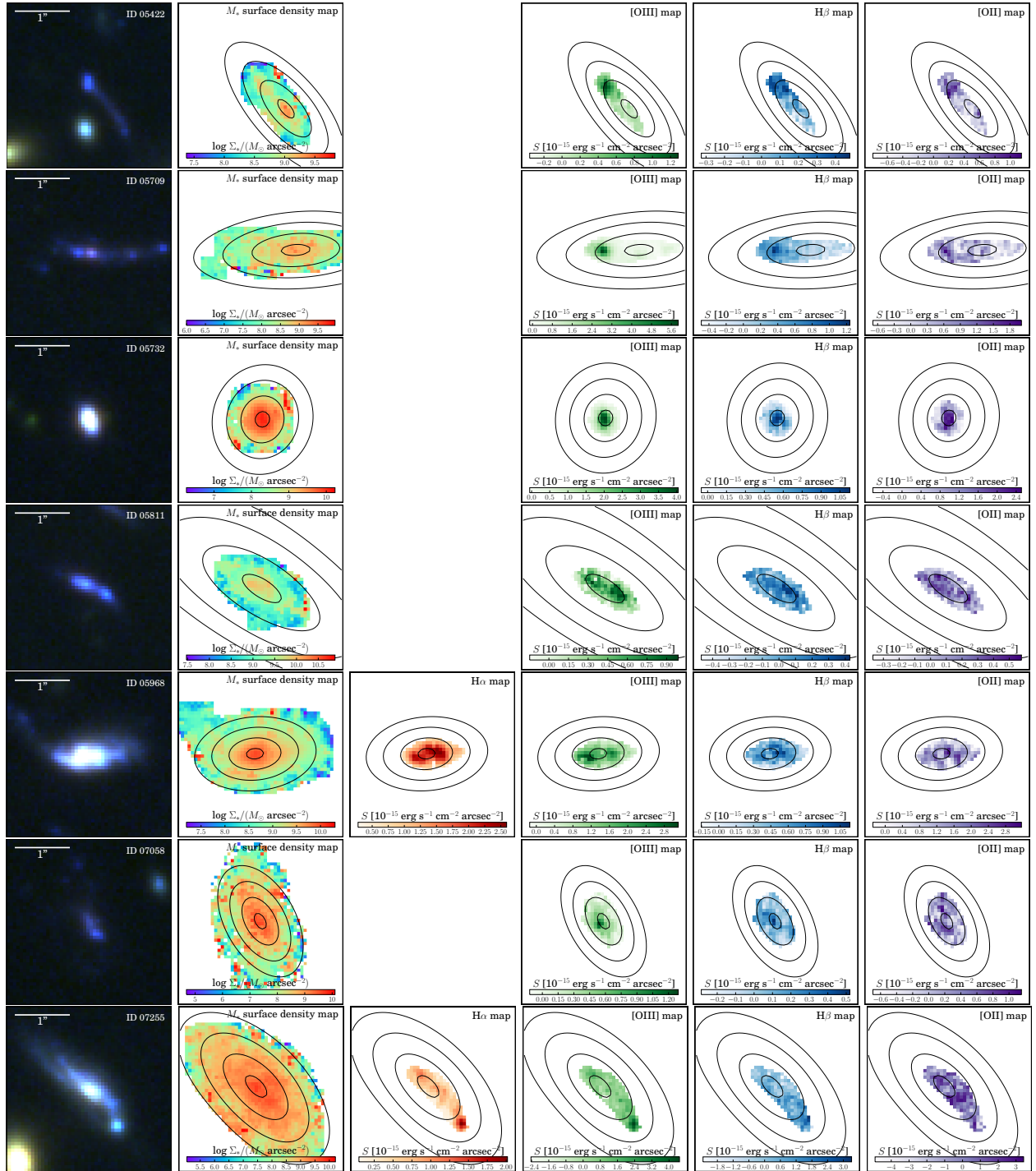


Figure 3.4 (cont.)

Due to the limited spectral resolution of *HST* WFC3/IR grisms, H $\beta$  and the [O III]  $\lambda\lambda$ 4960,5008 doublets are partially blended in the spatially extended sources. We adopt a direct de-blending technique to separate these emission lines following the procedure used in Jones et al. (2015b). First, an isophotal contour is measured from the co-added *HST*  $H_{160}$ -band postage stamp, typically at the level of  $\sim$ 10 percent of the peak flux received from the source. We then apply this contour to the 2D grism spectra at the observed wavelengths corresponding to [O III]  $\lambda\lambda$ 4960,5008 and H $\beta$ , maximizing the flux given grism redshift uncertainty ( $\sim$ 0.01). We use the theoretical [O III]  $\lambda\lambda$ 4960,5008 doublet flux ratio (i.e. [O III]  $\lambda$ 5008/[O III]  $\lambda$ 4960=2.98, calculated by Storey & Zeippen (2000)) to subtract the flux contribution of [O III]  $\lambda$ 4960 corresponding to the region where [O III]  $\lambda$ 5008 is unblended. We iterate this procedure to remove the [O III]  $\lambda$ 4960 emission completely, resulting in pure maps of H $\beta$  and [O III]  $\lambda$ 5008.

Note that this direct de-blending will be compromised if the source is so extended that its [O III]  $\lambda$ 5008 and H $\beta$  are blended. In practice, we fine-tune the isophotal contour level to avoid this contamination. As a result, no cases in our sample have problem with our direct de-blending method, and the resulting pure [O III]  $\lambda$ 5008 and H $\beta$  maps are uncontaminated.

In the case of H $\alpha$  and [N II], the emission lines are separated by less than the grism spectral resolution. Therefore we cannot use the direct technique to de-blend H $\alpha$  and [N II] emission, and instead treat the [N II]/H $\alpha$  ratio as an unknown parameter in Section 3.4.4.

After obtaining pure EL maps, we rotate the maps from each PA to the same orientation and then combine the data, in order to utilize the full depth of the grism exposures. We note that EL maps must first be extracted from grism spectra at each PA before being combined, in order to account for the different rotation and spectral resolution. There are in total six different PA-grism combinations as given in Table 3.1. At certain redshifts, ELs are visible in the overlapping region between the two grisms at  $\lambda \in [1.08, 1.15]$   $\mu$ m resulting in up to six individual maps of the same EL. We use the data taken at PA=119° as a reference, as this minimizes errors arising from rotating the various PAs into alignment. We first apply a small vertical offset to each EL map to account for the slight tilt of the spectral trace (i.e. known offset between the dispersion direction and the x-axis of extracted spectra; Brammer et al. 2012b). Next, we apply a small horizontal shift to correct for uncertainties in the wavelength calibration and redshift. Finally we rotate each EL map to align

Table 3.3. Sampling parameters and their prior information.

Set	Parameter	Symbol (Unit)	Prior
Vanilla	gas-phase metallicity	$12 + \log(\text{O/H})$	flat: [7.0, 9.3]
	nebular dust extinction	$A_V^N$	flat: [0, 4]
	de-reddened $\text{H}\beta$ flux	$f_{\text{H}\beta} (10^{-17} \text{erg s}^{-1} \text{cm}^{-2})$	Jeffrey's: [0, 100]
Extended	[N II] to $\text{H}\alpha$ flux ratio	[N II]/ $\text{H}\alpha$	Jeffrey's: [0, 0.5]
Derived	star-formation rate	SFR ( $M_\odot/\text{yr}$ )	—

Note. — Most constraints presented in this work are obtained under the “Vanilla” parameter set with the extended parameter fixed as [N II]/ $\text{H}\alpha$  = 0.05.

it with the reference orientation at PA=119°. The best values of these three alignment parameters are found by maximizing the normalized cross-correlation coefficient (NCCF) in order to achieve optimal alignment of multiple PAs:

$$\text{NCCF} = \frac{1}{n} \sum_{x,y} \frac{(S_{\text{ref}}(x,y) - \langle S_{\text{ref}} \rangle)(S_{\text{PA}}(x,y) - \langle S_{\text{PA}} \rangle)}{\sigma_{S_{\text{ref}}} \sigma_{S_{\text{PA}}}}. \quad (3.1)$$

Here  $S$  is the surface brightness profile for a specific EL,  $S_{\text{ref}}$  corresponds to the reference alignment stamp adopted as the PA=119° data, and  $n$  is the number of spaxels in the surface brightness profile.  $\langle S \rangle$  and  $\sigma_S$  represent the average and standard deviation of the surface brightness, respectively.

Once the data from each PA are aligned, we vet the EL maps from each PA-grism combination and reject those which show significant contamination-subtraction residuals or grism reduction defects. We combine the remaining maps of a given EL using an inverse variance weighted average in order to properly account for the different exposure times and noise levels. The final combined maps of each EL for each galaxy are shown in Figures 3.3 and 3.4.

### 3.4.4 Line-flux-based Bayesian Inference of Metallicity

Generally speaking, two methods exist in deriving gas-phase oxygen abundance in star-forming galaxies at high redshifts. “Direct” determinations based on electron temperature measurements,

which require high SNR detections of auroral lines (e.g. [O III]  $\lambda$ 4364), are still extremely challenging beyond the local universe (see Sanders et al., 2016, for a rare example). We therefore rely on the calibrations of strong collisionally excited EL flux ratios to estimate metallicities.

One of the most popular strong EL diagnostics is the flux ratio of [N II]/H $\alpha$  calibrated by Pettini & Pagel (2004). However, a large offset (0.2-0.4 dex) between the loci of high- $z$  and present-day star-forming galaxies in the Baldwin-Phillips-Terlevich (BPT, Baldwin et al., 1981) diagram has recently been discovered, indicating that extending the locally calibrated [N II]/H $\alpha$  to high- $z$  can be problematic (Shapley et al., 2015; Sanders et al., 2015). The interpretation of this offset is still the topic of much debate. It has been interpreted as the existence of a fundamental relation between nitrogen-oxygen abundance ratio and  $M_*$  (Masters et al., 2016), a systematic dependence of strong EL properties with respect to Balmer line luminosity (Cowie et al., 2016), a combination of harder ionizing radiation and higher ionization states of the ISM gas at high redshifts. (Steidel et al., 2014; ?), or an enhancement of nitrogen abundance in hot HII regions (Pilyugin et al., 2010). Fortunately, the alpha-element BPT diagrams show no offset with  $z$  (Shapley et al., 2015; Sanders et al., 2015), and therefore the diagnostics based upon those ELs are more reliable.

In this work we adopt the calibrations of Maiolino et al. (2008, M08), including the flux ratios of [O III]/H $\beta$ , [O II]/H $\beta$ , [N II]/H $\alpha$ . Given the potential systematics related to nitrogen ELs, we do not use the [N II]/H $\alpha$  calibration of M08. M08 fit the relation between these EL ratios and gas-phase oxygen abundance based upon “direct” measurements (from [O III]  $\lambda$ 4364) for  $12 + \log(\text{O/H}) < 8.3$ , and photoionization model results for higher metallicities. This provides a continuous framework valid over the wide range  $12 + \log(\text{O/H}) \in (7.1, 9.2)$ . We note that although there are alternative calibrations of metallicity available in the literature and the applicability of these recipes is currently a hotly debated topic (see, e.g., Blanc et al., 2015; Dopita et al., 2013). Here we are primarily interested in relative metallicity measurements. Even though the absolute measurements of metallicity may change if we used a different calibration, the gradients and morphological features in the maps should be more robust to changes in the calibration. We will restrict our comparisons with other samples to only include studies assuming the M08 calibrations.

Unlike previous work in which calibrated relations are applied to various EL flux ratios (see, e.g., Pérez-Montero, 2014; Bianco et al., 2015), we design a Bayesian statistical approach which

uses directly the individual EL fluxes as input, such that the information from one EL is only used once. Our approach presents several advantages over those based on line flux ratios. First, it properly accounts for flux uncertainties for lines that are weak or undetected. Second, multiple lines can be taken into consideration without the risk of double counting any information.

Our approach simultaneously infers gas-phase metallicity ( $12 + \log(\text{O/H})$ ), nebular dust extinction ( $A_V^N$ ), and expected de-reddened  $\text{H}\beta$  flux in units of  $10^{-17} \text{ erg s}^{-1} \text{ cm}^{-2}$ . Details of the prior assumptions applied to these parameters are explained in Table 3.3. For values of these three parameters we can compute the expected line fluxes, and compare with measured values to compute the likelihood and then the posterior probability. The  $\chi^2$  statistic in our inference procedure is calculated as

$$\chi^2 = \sum_i \frac{(f_{\text{EL}_i} - R_i \cdot f_{\text{H}\beta})^2}{(\sigma_{\text{EL}_i})^2 + (f_{\text{H}\beta})^2 \cdot (\sigma_{R_i})^2}. \quad (3.2)$$

Here  $\text{EL}_i$  denotes the set of emission lines [ $\text{O II}$ ],  $\text{H}\gamma$ ,  $\text{H}\beta$ , [ $\text{O III}$ ],  $\text{H}\alpha$ , and [ $\text{S II}$ ].  $f_{\text{EL}_i}$  and  $\sigma_{\text{EL}_i}$  represent the observed de-reddened  $\text{EL}_i$  flux and its uncertainty given a value of  $A_V^N$ . We adopt the Cardelli et al. (1989) galactic extinction curve with  $R_V = 3.1$ .  $R_i$  is the dust-corrected flux ratio between  $\text{EL}_i$  and  $\text{H}\beta$ , with  $\sigma_{R_i}$  being the associated intrinsic scatter. Note that the content of  $R_i$  varies depending on the corresponding  $\text{EL}_i$  in the following ways.

- For  $\text{EL}_i \in \{\text{H}\alpha, \text{H}\gamma\}$ ,  $R_i$  corresponds to the Balmer decrement. We use the intrinsic Balmer ratios of  $\text{H}\alpha/\text{H}\beta = 2.86$  and  $\text{H}\gamma/\text{H}\beta = 0.47$ , appropriate for case B recombination and fiducial  $\text{HII}$  region conditions (see, e.g., Hummer & Storey, 1987). We set  $\sigma_{R_i} = 0$ , assuming the intrinsic Balmer ratios are fixed with no scatter. These ratios are proxies of the nebular dust extinction  $A_V^N$ .
- For  $\text{EL}_i \in \{[\text{O II}], [\text{O III}]\}$ ,  $R_i$  and  $\sigma_{R_i}$  are taken from the M08 calibrations. These ratios are diagnostics of the oxygen abundance  $12 + \log(\text{O/H})$ .
- For  $\text{EL}_i = [\text{S II}]$ , we compute the values of  $R_i$  and  $\sigma_{R_i}$  using the Balmer ratio of  $\text{H}\alpha/\text{H}\beta$  and our new calibration of the ratio  $[\text{S II}]/\text{H}\alpha$ , derived following Jones et al. (2015a). Jones et al. (2015a) used the same data as the low-metallicity calibrations of M08. Although M08 do not provide any calibrations for  $[\text{S II}]$ , we expect our calibration to be self-consistent and reliable for  $12 + \log(\text{O/H}) \lesssim 8.4$ .  $[\text{S II}]/\text{H}\alpha$  is primarily useful as a diagnostic to differentiate between the upper and lower branches of the  $[\text{O III}]/\text{H}\beta$  calibration. This is valuable because  $[\text{N II}]$  is not directly

measured and [O II] is typically low signal-to-noise in the lower redshift galaxies for which [S II] is available, due to decreasing grism throughput at  $\lambda < 0.9 \mu\text{m}$ .

- For  $\text{EL}_i = \text{H}\beta$ ,  $R_i = 1$  with  $\sigma_{R_i} = 0$ . This is just comparing the observed and expected  $\text{H}\beta$  flux, corrected for dust extinction.

These EL flux ratios can be computed given a value of  $12 + \log(\text{O/H})$ , using a universal polynomial functional form, i.e.,  $\log R = \sum_{i=0}^5 c_i \cdot x^i$ , where  $x = 12 + \log(\text{O/H}) - 8.69$ . We summarize the coefficients ( $c_i$ ) for each ratio diagnostic used in our statistical inference in Table 3.4.

In addition, the [N II]/ $\text{H}\alpha$  ratio is included as an additional parameter for galaxies at  $z \lesssim 1.5$  where these lines are observed. However we do not attempt to determine [N II]/ $\text{H}\alpha$  using the M08 calibrations, as locally-calibrated diagnostics tend to underestimate the [N II]/ $\text{H}\alpha$  ratio in high- $z$  galaxies whereas oxygen and other  $\alpha$ -element line ratios remain constant with redshift (Steidel et al., 2014; Shapley et al., 2015; Jones et al., 2015a). Instead we either leave this parameter free (“extended” priors), or fixed to [N II]/ $\text{H}\alpha = 0.05$  (“vanilla” priors). The vanilla value is typical of galaxies with similar  $z$  and oxygen EL ratios as our sample. Fixing the value of [N II]/ $\text{H}\alpha$  provides faster convergence and does not significantly affect the inferred metallicity. We therefore report constraints for the “vanilla” parameter set. For galaxy ID 04054, the SN Refsdal host galaxy, we fix its [N II]/ $\text{H}\alpha$  to be 0.11, as measured by Yuan et al. (2011).

We use the Markov Chain Monte Carlo sampler EMCEE (Foreman-Mackey et al., 2013) to explore the parameter space, setting the number of walkers to 100 with 5,000 iterations for each walker, and a burnin of 2,000. The autocorrelation times are computed for each parameter and are used to make sure chains have converged. An example constraint result for the SN Refsdal host galaxy’s global EL fluxes is shown in Figure 3.5. While this work is primarily concerned with gas-phase metallicities, our method simultaneously provides constraints on  $A_V^{\text{N}}$  and SFR which can be compared to the results of SED fitting. We then calculate the lensing-corrected de-reddened  $\text{H}\alpha$  luminosity from  $f_{\text{H}\beta}$  (assuming the fiducial Balmer ratio) and the magnification estimate of the source. Then the instantaneous SFR can be derived, via the commonly-used calibration of Kennicutt (1998a); Moustakas et al. (2010), i.e.,

$$\text{SFR} = 4.6 \times 10^{-42} \frac{L(\text{H}\alpha)}{\text{erg/s}} \quad [\text{M}_{\odot}/\text{yr}], \quad (3.3)$$

Table 3.4. Coefficients for the EL flux ratio diagnostics used in our Bayesian inference.

$R$	$c_0$	$c_1$	$c_2$	$c_3$	$c_4$	$c_5$
$H\alpha/H\beta$	0.4564	...	...	...	...	...
$H\gamma/H\beta$	-0.3279	...	...	...	...	...
$[O\text{ III}]/H\beta$	0.1549	-1.5031	-0.9790	-0.0297	...	...
$[O\text{ II}]/H\beta$	0.5603	0.0450	-1.8017	-1.8434	-0.6549	...
$[S\text{ II}]/H\alpha$	-0.5457	0.4573	-0.8227	-0.0284	0.5940	0.3426

Note. — The value of EL flux ratio is calculated by the polynomial functional form, i.e.,  $\log R = \sum_{i=0}^5 c_i \cdot x^i$ , where  $x = 12 + \log(\text{O/H}) - 8.69$ . The ratio of  $[S\text{ II}]/H\alpha$  is calibrated by the work of Jones et al. (2015a), and the Balmer line ratios correspond to the Balmer decrement, whereas the ratios between oxygen lines and  $H\beta$  are from M08.

valid for a Chabrier (2003) IMF. This SFR estimate does not rely on any assumptions about star-formation history, and thus is a more direct measure of ongoing star formation than values given by SED fitting.

We apply this inference procedure to both galaxy-integrated line fluxes (to be discussed in Section 3.5) as well as individual spaxels in the EL maps (which will lead to metallicity gradient measurements described in Section 3.6).

### 3.5 Global Demographic Properties

Based upon the Bayesian analysis, we obtain the global measurements of gas-phase metallicity, nebular dust extinction, and SFR, for all sources in our sample, as shown in Table 4.1. First, we check for the presence of any active galactic nucleus (AGN) contamination in our sample. Because not all galaxies in our sample reside in the redshift range where all BPT lines are available, we resort to the mass-excitation diagram showing the  $[O\text{ III}]/H\beta$  flux ratio as a function of  $M_*$ , first proposed by Juneau et al. (2011) to differentiate star-forming galaxies and AGNs in local Sloan Digital Sky Survey (SDSS) observations. Juneau et al. (2014) further revised the demarcation

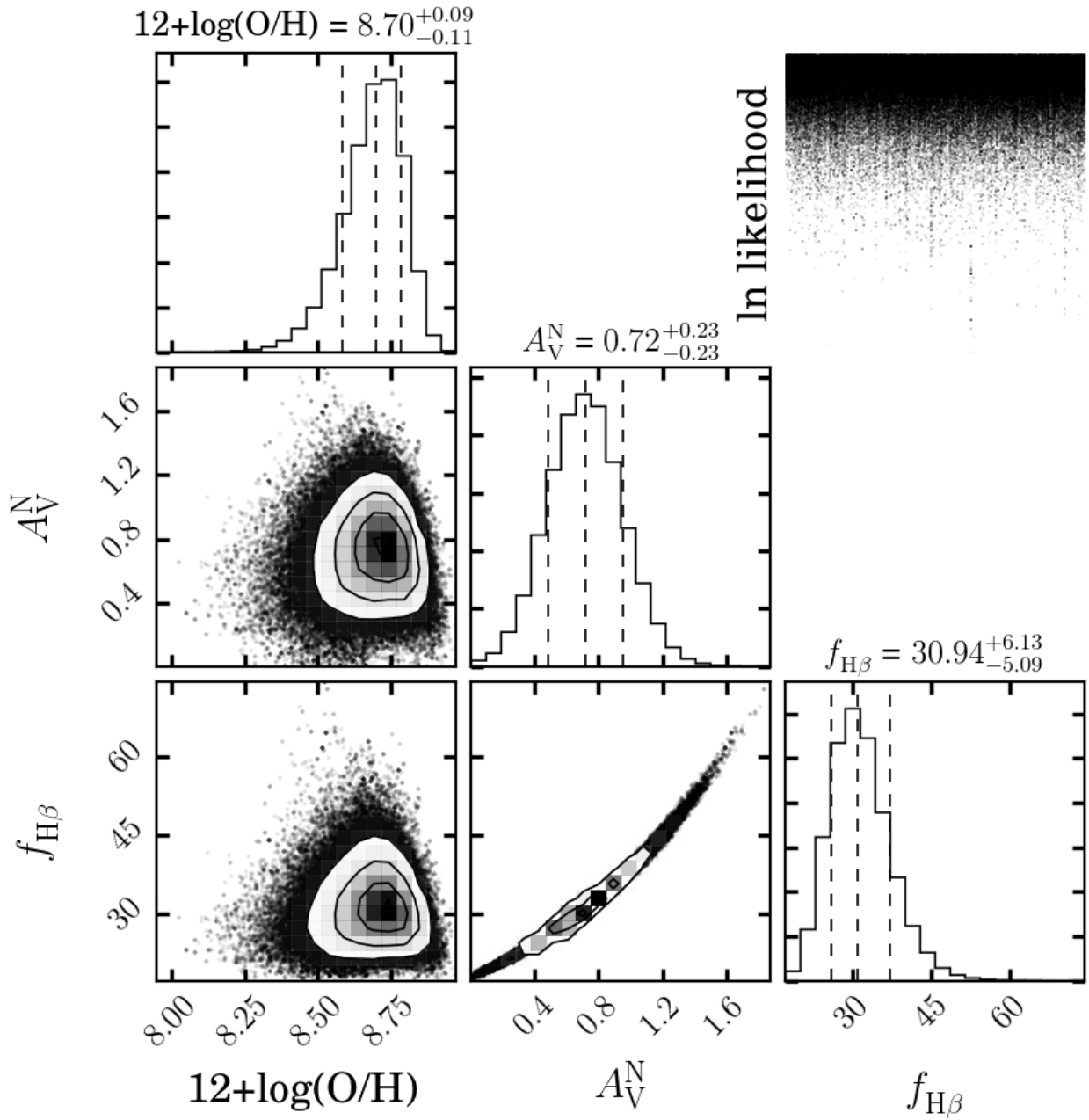


Figure 3.5 The marginalized 1D and 2D constraints on  $(12 + \log(\text{O/H}))$ ,  $A_V^N$ , and  $f_{H\beta}$ ), which are drawn from the integrated line fluxes of the Refsdal host galaxy (ID 04054), after all grism exposures are combined. The values on top of each column are the medians with  $1-\sigma$  uncertainties for each parameter. The plot in the upper right corner illustrates a good convergence of the sampling.

scheme by applying line luminosity evolution and selection effects to a more complete SDSS galaxy sample, and tested that this scheme agrees well with the bivariate distributions found in a number of high- $z$  galaxy samples. According to the Juneau et al. (2014) classification scheme, all but one galaxy (ID 02607) have a negligible probability of being AGN (see Figure 3.6). Recently, Coil et al. (2015) found that a +0.75 dex  $M_*$  shift in the Juneau et al. (2014) scheme is required to avoid serious AGN contamination in the *MOSDEF* galaxy sample at  $z \sim 2.3$ . We verified that galaxy 02607 can still be safely classified as an AGN candidate, even considering the Coil et al. (2015) shifted classification scheme. Because the M08 calibrations originate from HII region observations and theoretical models, not designed for AGNs, our method will not predict a reliable metallicity constraint for the AGN candidate ID 02607. We thereby exclude this source in the rest of our population analysis. For the rest of our sample, comprising 13 star-forming galaxies, the constraint on gas-phase metallicity is robust.

In Figure 3.7, we plot the measured SFR as a function of  $M_*$  for our sample. In comparison, the loci of mass-selected galaxies observed by the *KMOS*<sup>3D</sup> survey and the “star-formation main sequence” (SFMS, Whitaker et al., 2014; Speagle et al., 2014) at similar redshifts are also shown. We can see that selecting lensed galaxies based upon EL strength can probe deep into the low-mass regime at high redshifts that is currently inaccessible to mass complete surveys. As expected, our emission line selected targets probe the upper envelope of the SFMS, so that a detail comparison is non-trivial and should take into account the selection functions of each sample. The advantage of the emission line selection technique is that it is the most cost-effective way to obtain gas metallicities for stellar masses down to  $10^7 M_*$  at  $z \sim 2$ . Using the same technique, we discovered an analog of local group dwarf spheroidals (e.g., Fornax, Coleman & de Jong, 2008) at  $z = 1.85$  experiencing active star formation (with 1 dex offset from the SFMS), in our previous work (Jones et al., 2015b).

We also collect all published gas-phase metallicity measurements in emission-line galaxies in the redshift range of our sample  $1.2 \lesssim z \lesssim 2.3$ , obtained exclusively from the strong EL calibrations prescribed by M08. The reason we only select measurements based upon the M08 calibrations is that adopting different strong EL calibrations can give rise to different absolute metallicity scales offset by up to  $\sim 0.7$  dex at the high-mass end, according to the comparative study conducted by Kewley & Ellison (2008). In order to minimize the systematic uncertainty associated with EL

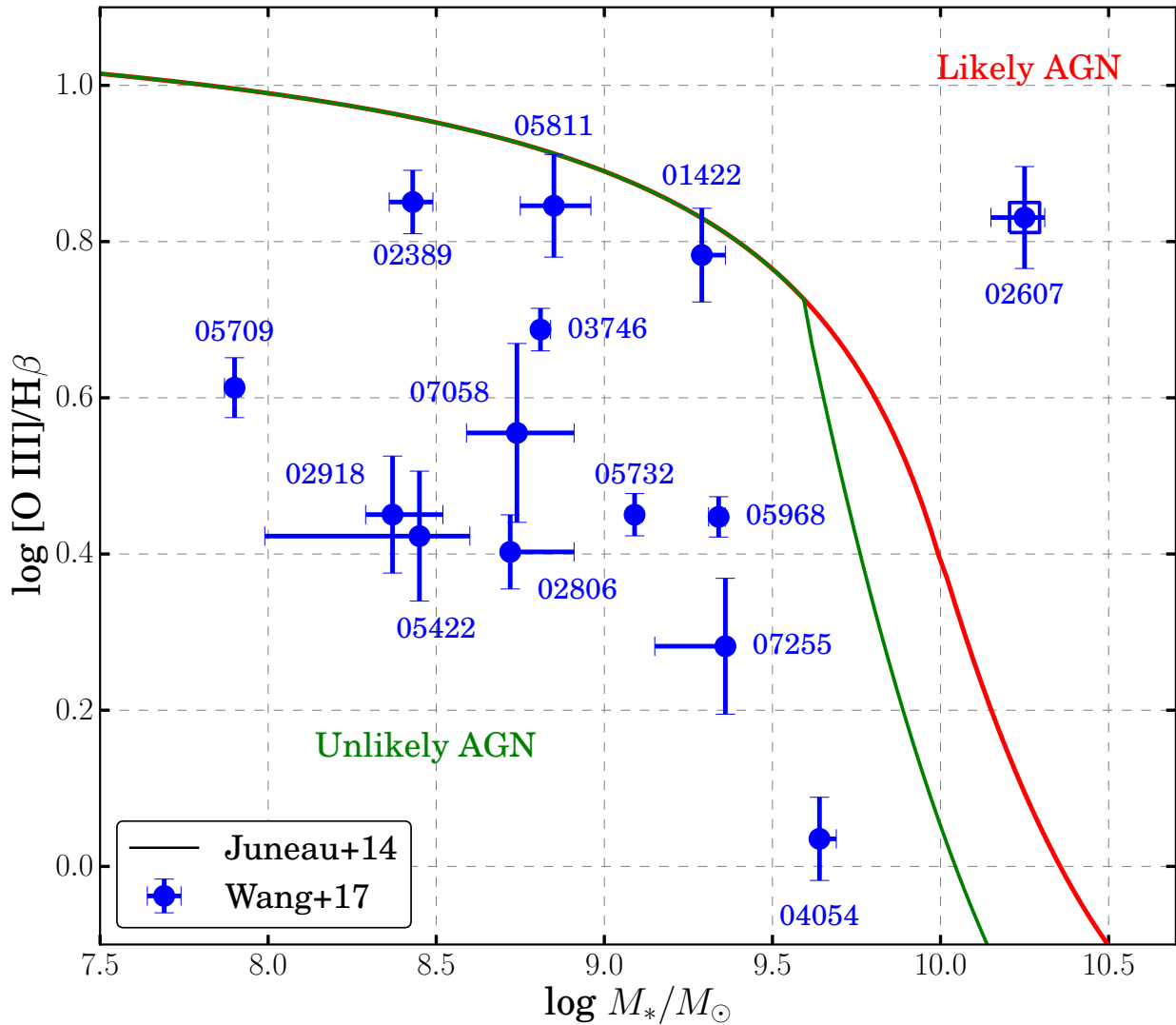


Figure 3.6 Mass excitation diagnostic diagram for our metallicity gradient sample. The curves are the demarcation lines updated by Juneau et al. (2014). The regions below the green curve have a low probability (< 10%) of being classified as AGNs, whereas galaxies located above the red curve are secure AGN candidates. In our sample, the only AGN candidate, i.e., ID 02607, is marked by a square.

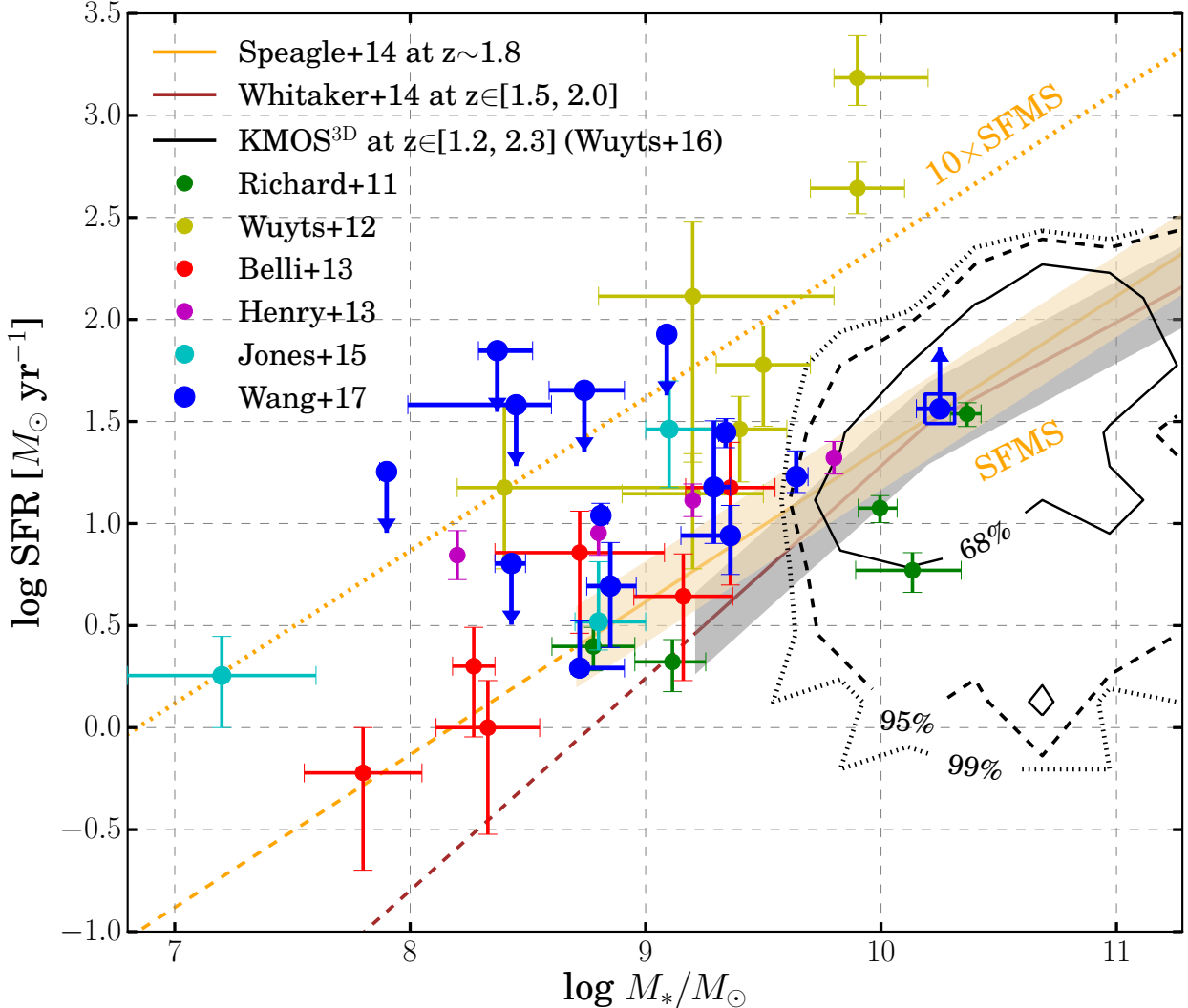


Figure 3.7 Star formation rate as a function of stellar mass for emission-line galaxies at  $z \in [1.2, 2.3]$ . Our metallicity gradient sample is marked by blue points; the literature sample is color-coded by reference according to the legend. The star-forming main sequence compiled by Speagle et al. (2014) and Whitaker et al. (2014) are represented by brown and orange lines respectively, where the dotted part is extrapolated at masses below the mass completeness limit. The shaded regions denote the typical scatter of star-forming main sequence, i.e. 0.2-0.3 dex. We also show the source density contours for the  $KMOS^{3D}$  survey at the same redshift range, where 68%, 95%, and 99% of all  $KMOS^{3D}$  galaxies at  $z \in [1.2, 2.3]$  can be found within the black solid, dashed, and dotted contours respectively. It is found that our sample is highly complementary to the  $KMOS^{3D}$  sample in terms of stellar mass.

calibrations, we thus focus on this homogeneous M08 sample alone.

As shown in Figure 3.8, the M08-based sample includes five galaxies from Richard et al. (2011), seven from Wuyts et al. (2012a), six from Belli et al. (2013), four stack measurements by Henry et al. (2013b), three interacting galaxies at  $z = 1.85$  analyzed by Jones et al. (2015b), and 13 star-forming galaxies presented in this work. In total, this sample consists of 38 independent measurements at  $1.2 \lesssim z \lesssim 2.3$ , with median redshift  $z_{\text{median}} = 1.84$ . The mutual agreement between our sample and that from the literature provides an independent confirmation that our new Bayesian method leads to constraints on gas-phase metallicity consistent with previous studies also adopting the same calibrations. With the combined sample we are able to derive the MZR at this redshift, spanning three orders of magnitude in stellar mass.

We fit the following functional form to this sample of 38 galaxies in order to derive the MZR, i.e.,

$$12 + \log(\text{O/H}) = \alpha \log(M_*/M_\odot) + \beta + N(\sigma), \quad (3.4)$$

where  $\alpha$ ,  $\beta$ , and  $\sigma$  represent the slope, the intercept and the intrinsic scatter, respectively. The Python package LINMIX<sup>8</sup> was employed to perform a Bayesian linear regression following the method proposed by Kelly (2007). The median values and  $1-\sigma$  uncertainties for these three parameters drawn from the marginalized posteriors are

$$\alpha = 0.40^{+0.07}_{-0.07}, \beta = 4.71^{+0.62}_{-0.64}, \sigma = 0.03^{+0.02}_{-0.01}. \quad (3.5)$$

The resulting MZR together with its  $1-\sigma$  confidence region is shown in Figure 3.8.

Recently, Guo et al. (2016) presented a comprehensive study of the MZR and its scatter at  $z=0.5\text{-}0.7$  from data acquired by large spectroscopic surveys in the *CANDELS* fields (Grogin et al., 2011; Koekemoer et al., 2011). Guo et al. (2016) also summarized a variety of theoretical predictions of the MZR slope (i.e.  $\alpha$ ) given by diverse approaches. The slopes predicted by the energy-driven wind ( $\alpha \sim 0.33$ ) and the momentum-driven wind ( $\alpha \sim 0.17$ ) equilibrium models proposed by Finlator & Davé (2008); Davé et al. (2012) are shown schematically in Figure 3.8. We see that our inferred slope is only marginally compatible with the prediction given by the energy-driven wind model at  $1-\sigma$  confidence level, whereas strongly disfavors the momentum-driven wind

---

<sup>8</sup>available at <https://github.com/jmeyers314/linmix>

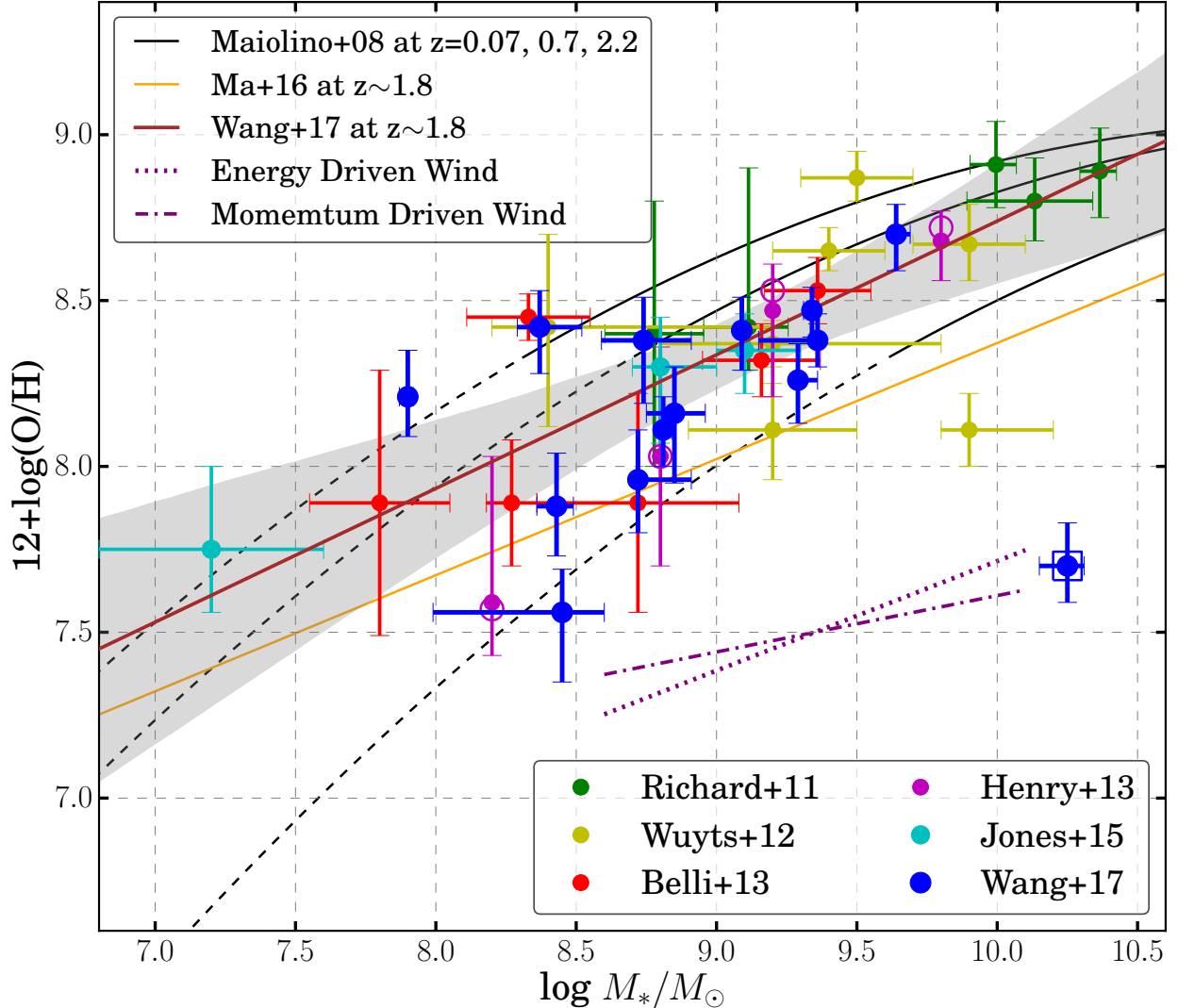


Figure 3.8 The relation between stellar mass and gas-phase oxygen abundance, from observations and simulations at  $z \sim 1.8$ . The color-coding for all the points is the same as in Figure 3.7. For the sake of consistency, all metallicity measurements are derived assuming the Maiolino et al. (2008) strong EL calibrations. The black curves represent the 2nd order polynomials fitted by Maiolino et al. (2008) to data sets at different redshifts, where dashed parts correspond to extensions beyond mass completeness limits of those data sets. The thick brown line denotes our best-fit linear relation based upon all data points except the AGN candidate (i.e. ID 02607) marked by a square. The shaded band marks the  $1-\sigma$  confidence region. For the Henry et al. (2013b) stack data points, we also show the measurements without dust correction as open circles, which are not included in the fit. The thin orange line is the prediction from the cosmological zoom-in simulations conducted by Ma et al. (2016) at the same redshift range. <sup>84</sup> The purple dotted and dash-dot lines illustrate the slopes given by the energy and momentum driven models, respectively.

model. Considering the majority of the galaxies in our sample have relatively lower masses, our result confirms the finding by Henry et al. (2013b) that momentum-driven winds cannot be the primary workhorse that shapes the MZR in the low-mass regime (below  $10^{9.5} M_{\odot}$ ) at  $z \gtrsim 1$ .

Our constrained value of  $\alpha$  is consistent at  $1-\sigma$  confidence level with that given by Ma et al. (2016), from the FIRE (Feedback in Realistic Environment) cosmological zoom-in simulations (Hopkins et al., 2014). Evaluated at  $z = z_{\text{median}}$ , their MZR reads  $12 + \log(\text{O/H}) = 0.35 \log(M_{*}/M_{\odot}) + 4.87$ . The FIRE simulations reaches a spatial resolution as high as 1-10 pc, 1-2 orders of magnitude better than that in conventional large-volume cosmological hydrodynamic simulations (e.g. Davé et al., 2013). The high spatial resolution enables a more realistic and self-consistent treatment of multiphase ISM, star formation, galactic winds and stellar feedback, than those in semi-analytic models (see Somerville & Davé, 2015, for a recent review). As a result, these zoom-in simulations are capable of reproducing many observed relations, e.g., the galaxy stellar mass functions, the evolution of cosmic SFR density and specific SFR (sSFR). The consistency between the slopes of our MZR and that by Ma et al. (2016) indicates that small-scale physical processes are important in producing the cumulative effects of galactic feedback. However, we note that there is a 0.16 dex offset in the values of the MZR intercept ( $\beta$ ). One possible cause is that the absolute metallicity scale in the M08 calibrations is offset. As shown by Kewley & Ellison (2008), the intercepts given by different metallicity calibrations can vary up to 0.7 dex. Other potential causes lie in the assumptions adopted by the Ma et al. (2016) simulations, e.g., the stellar yield is too small, the gas fractions in their simulated galaxies are too high, etc.. Nevertheless, a discrepancy of 0.1-0.2 dex is not unusual given the uncertainties in stellar yield and metallicity calibrations.

Aiming at testing the validity of the FMR using the M08-based sample at  $z \sim 1.84$  compiled in this work, we calculate the predicted values for metallicity from the measurements of  $M_{*}$  and SFR, according to Eq. (2) in Mannucci et al. (2011), who extended the FMR to masses down to  $10^{8.3} M_{\odot}$ . Figure 3.9 shows the difference between the FMR-predicted values and the actual measurements of metallicity. We find that the entire M08-based sample is consistent with the FMR given the measurement uncertainties and intrinsic scatter. The median offset for the entire sample is 0.07 dex, with median uncertainty 0.14 dex. The median offset and uncertainty for our galaxy sample analyzed in this work are  $-0.07$  dex and 0.12 dex, respectively. Among other individual datasets,

the only one that shows a marginally significant deviation from the FMR is that by Wuyts et al. (2012a), which has median offset 0.22 dex and median uncertainty 0.11 dex. We speculate that it is due to the fact that the Wuyts et al. (2012a) dataset is the only one in our compiled M08-based sample which relies solely upon the [N II]/H $\alpha$  flux ratio, which can be a biased tracer of metallicity at high redshifts (Shapley et al., 2015; Sanders et al., 2015). This result reiterates the necessity of combining multiple EL flux ratio diagnostics simultaneously in order to suppress the systematics associated with local calibrations in the accurate measurement of high- $z$  metallicity.

## 3.6 Spatially Resolved Analysis

In this section, we present and discuss in depth the new and unique results obtained from the spatially resolved analysis of our sample, beyond the reach of the conventional integrated measurements in Section 3.5. The high spatial resolution maps of gas-phase metallicity from *HST* grism spectroscopy are described in Sect 3.6.1. We make notes on individual galaxies in Section 3.6.2. The maps of EL kinematics on part of our sample are presented in Appendix 4.A.

### 3.6.1 Gas-phase Metallicity Maps at Sub-kpc Resolution

To estimate the spatial distribution of the constrained parameters we apply the analysis described in Section 3.5 to each individual spaxel in the EL maps. In Figure 4.3, we show the maps of best-fit metallicity and the corresponding conservative uncertainty (the larger side of asymmetric error bars given by the Bayesian inference) measured for galaxies in our metallicity gradient sample. We bin spaxels 2 by 2 to regain the native WFC3/IR pixel scale. In the maps, we only include spaxels with at least one EL (primarily H $\alpha$  or [O III]) detected with  $\geq 5\sigma$  significance. The metallicity gradients measured from these individual spaxels are shown in the right column of Figure 4.3. We also measure metallicity gradients using another independent method, i.e., via radial binning. The range of each radial annulus is determined by requiring its SNR  $\gtrsim 15$ . In order to avoid biasing toward low metallicities, we put the SNR threshold on H $\alpha$  whenever available (i.e.  $z \lesssim 1.5$ ) instead of on [O III], since the latter correlates tightly with  $12 + \log(\text{O/H})$ , in the lower branch of [O III]/H $\beta$ , where the majority of our sample resides. Based upon our SNR threshold criterion,

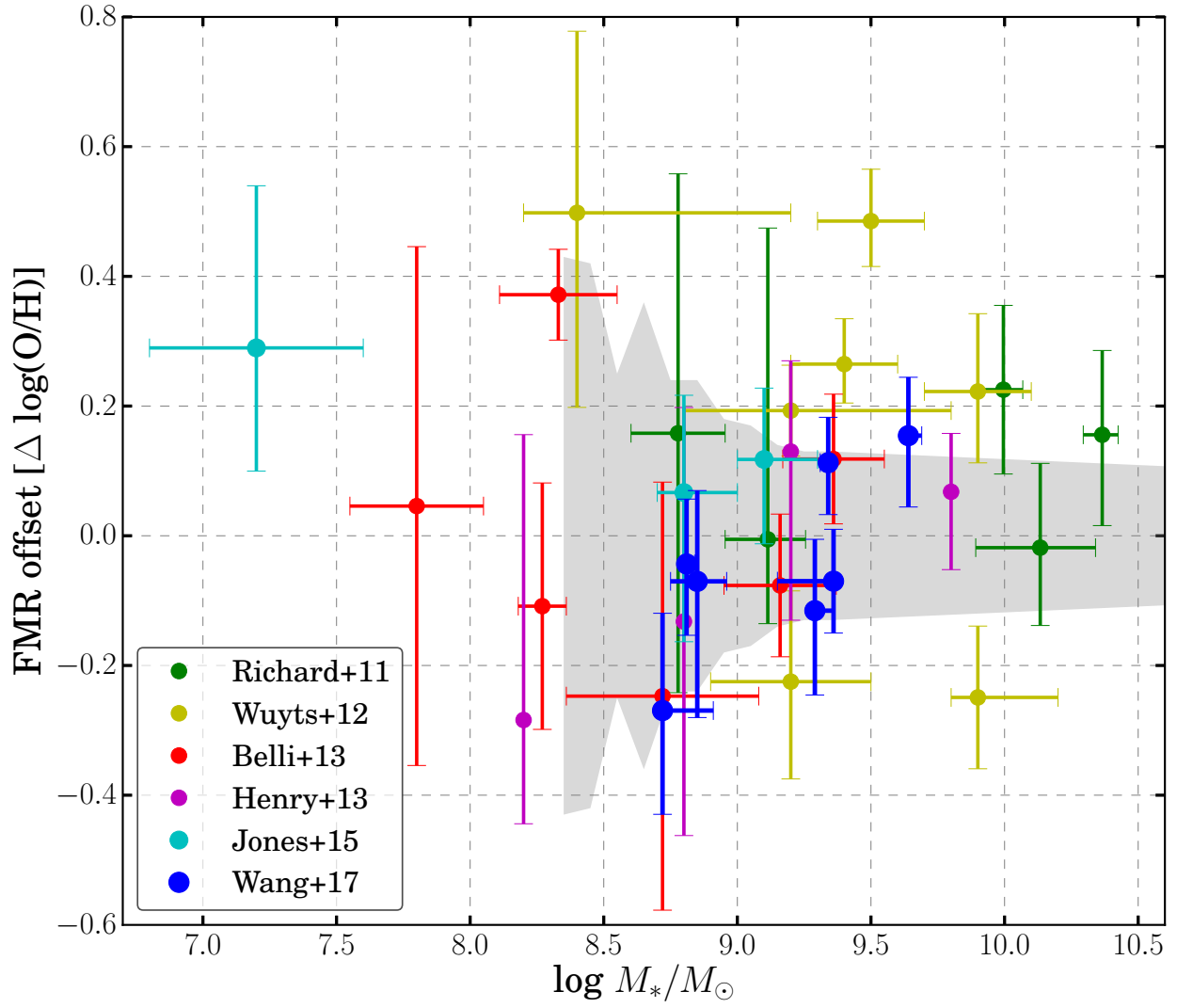


Figure 3.9 The offset from the fundamental metallicity relation first proposed by Mannucci et al. (2010) for the  $z \sim 1.8$  metallicity measurements derived assuming the Maiolino et al. (2008) calibrations. The color-coding for the points is the same as in Figure 3.7. The shaded region shows the intrinsic scatter of the FMR extended to low-mass regime given by Mannucci et al. (2011).

Table 3.5. Gas-phase metallicity gradients measured by two different methods.

ID	Metallicity gradient [dex/kpc]	
	Individual spaxel	Radial annulus
01422	0.02 ± 0.08	0.06 ± 0.04
02389	-0.07 ± 0.04	-0.13 ± 0.03
02806	-0.01 ± 0.02	0.04 ± 0.02
03746	-0.03 ± 0.03	0.04 ± 0.02
04054	-0.04 ± 0.02	-0.07 ± 0.02
05709	-0.22 ± 0.05	-0.19 ± 0.06
05732	0.06 ± 0.05	0.08 ± 0.02
05811	-0.18 ± 0.08	-0.40 ± 0.07
05968	-0.01 ± 0.02	0.02 ± 0.01
07255	-0.16 ± 0.03	-0.21 ± 0.03

three sources in our sample, IDs 02918, 05422 and 07058, do not have enough spaxels to constitute a trustworthy metallicity map, and therefore were removed from the spatially resolved analysis. So in total, we present 10 star-forming galaxies with sub-kpc resolution metallicity maps. In order to measure radial gradients, we perform Bayesian linear regressions in the same manner as described in Section 3.5. We take into account the conservative uncertainties for individual metallicity constraints in each spaxel or annulus. The resulted metallicity gradients are given in Table 3.5. We note that the metallicity maps are not always symmetric around the center of stellar mass. Therefore, while gradients are a useful statistic to describe the overall behavior and to compare with numerical simulations, they do not contain all the available information about the apparent diversity of morphologies. Thus, it is helpful to keep the 2D maps in mind while interpreting the gradients.

As a result, seven galaxies have gradients consistent with being flat at  $2\sigma$ , among which three show almost uniformly distributed metals (IDs 02806, 03746 and 05968), two have marginally positive gradients (IDs 01422 and 05732), and the other two display mildly negative gradients (IDs 02389 and 04054). Apart from these, the other three galaxies in our sample have very steep negative gradients: IDs 07255, 05709 and 05811. In particular, after the lensing magnification correction, the stellar mass of galaxy ID 05709 is estimated to be  $\sim 10^{7.9} M_\odot$ . This is for the first

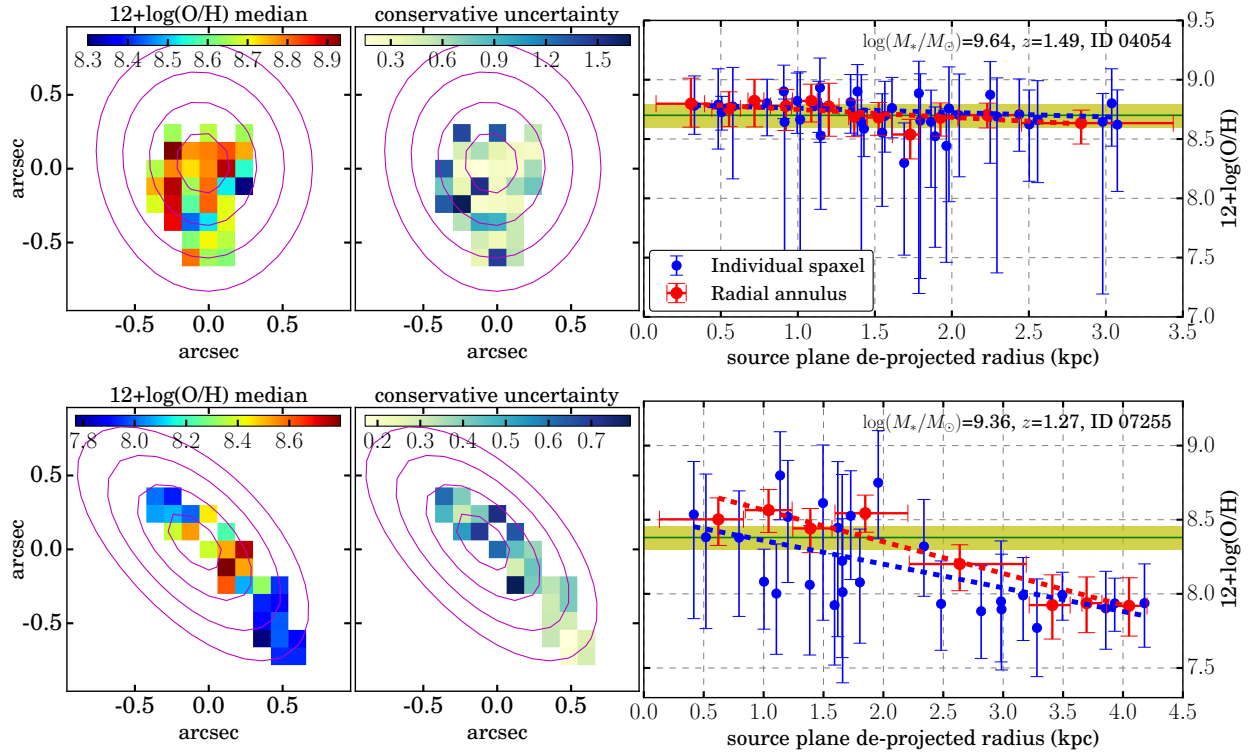


Figure 3.10 Maps of metallicity constraints (median value in the left column and conservative uncertainty — the larger side of asymmetric  $1-\sigma$  error bars — in the center column) and plots of radial metallicity gradients in the right column. Note that unlike what we show in the combined EL maps (Figures 3.3 and 3.4), here the metallicity maps are rebinned to a scale of  $0.^{\prime\prime}13$ , corresponding to the native resolution of WFC3/IR. In the maps, only spaxels with the signal-to-noise ratio of H $\alpha$  or [O III] larger than 5 are shown. The same source plane de-projected galactocentric radii that are denoted by black contours in Figures 3.3 and 3.4 are represented by magenta contours, with the only difference being that contours are in 1 kpc intervals now. In the panels in the right column, blue and red points correspond to metallicity measurements for individual spaxels and radial annuli, respectively. The radial gradients derived based upon these measurements are shown by the dashed lines in corresponding colors. The yellow band and green horizontal line mark the global constraint on  $12 + \log(\text{O}/\text{H})$ , from integrated line fluxes.

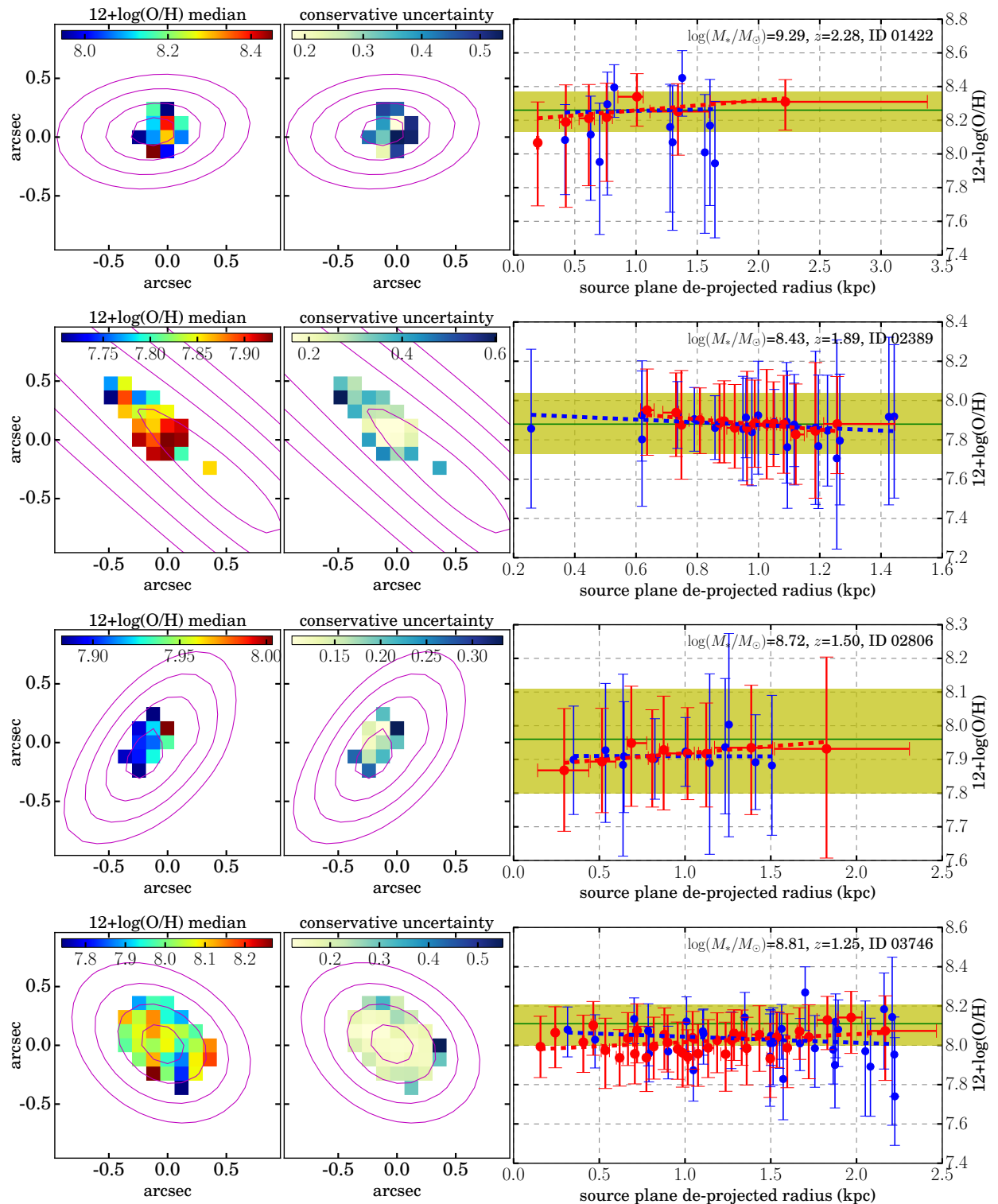


Figure 3.10 (cont.)

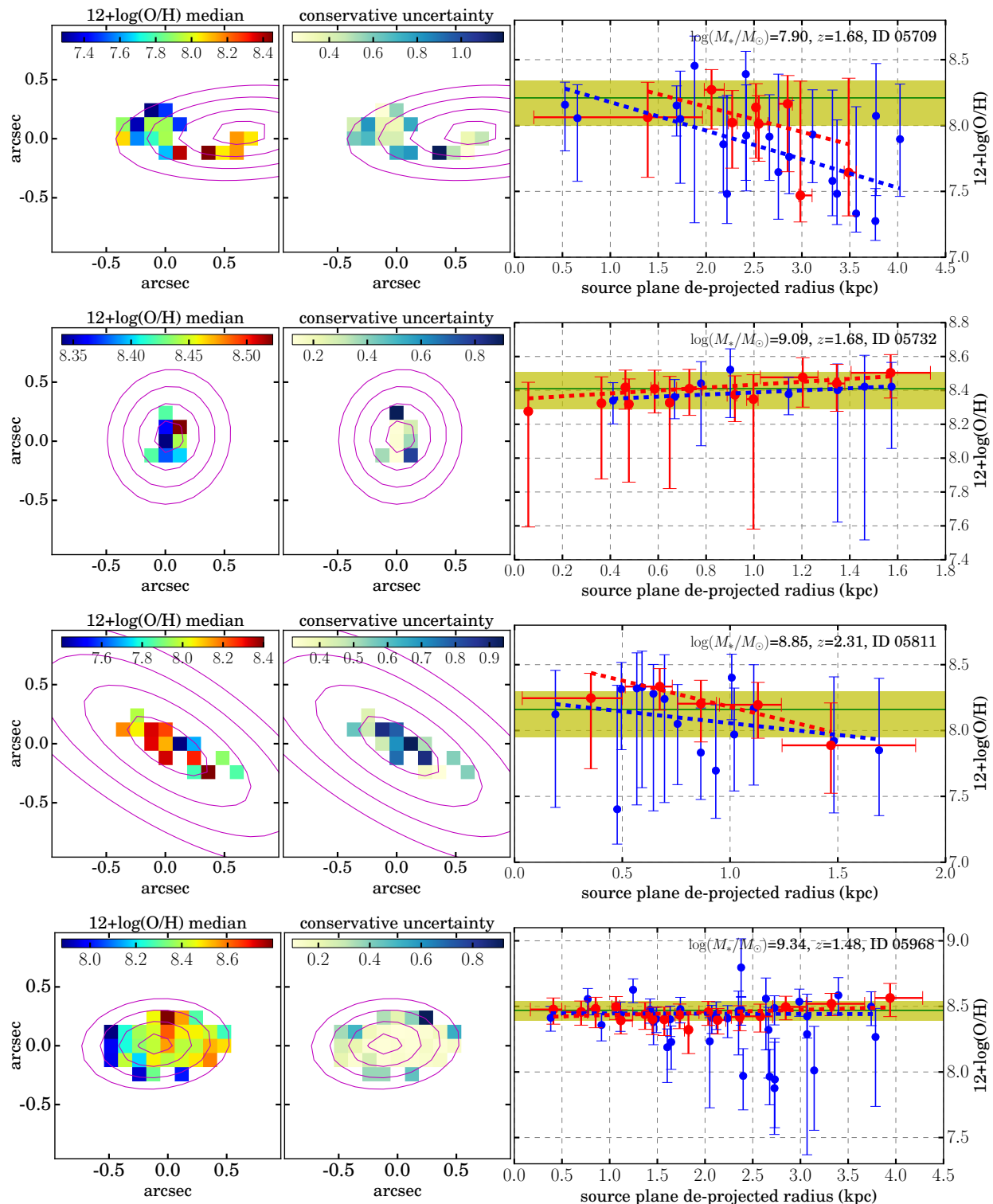


Figure 3.10 (cont.)

time sub-kpc scale spatially resolved analysis has been done on such low-mass systems at high redshifts.

In order to verify that our results are not contaminated by ionizing radiation from AGN, we examine spatially resolved BPT diagrams. This approach is only possible for sources at  $z \lesssim 1.5$ , where  $\text{H}\alpha$  is detectable. Furthermore, due to the low spectral resolution of *HST* grisms, we slightly modify the BPT diagram to plot flux ratio of  $[\text{O III}]/\text{H}\beta$  as a function of  $[\text{S II}]/\text{H}\alpha + [\text{N II}]$ , using the “vanilla” value for  $[\text{N II}]/\text{H}\alpha$ . As Figure 3.11 shows, we do not identify any strong correlation between source plane galactocentric radius and deviation from the  $\text{HII}$  region loci, suggesting that there is no AGNs hidden in the center of these galaxies. Moreover, the integrated EL fluxes of all three galaxies lie in close proximity to the extreme starburst model prescribed by Kewley et al. (2006b), which confirms our working assumption that AGN contributions are negligible for our sample, except in one case (i.e. ID 02607, see Figure 3.6).

We also test our metallicity estimates using the pure empirical EL calibrations based on a large sample of “direct” metallicity determinations in SDSS local  $\text{HII}$  regions recently published by Curti et al. (2016), in replacement of the M08 hybrid EL calibrations. It is found out that our results on integrated metallicities and metallicity gradients of the galaxies in our sample remain unaffected.

The radial range where metallicity gradients are measured is critical since  $\text{HII}$  regions at far outer/inner regions of galaxies are found to show significantly elevated/truncated oxygen abundances (see e.g. Sanchez et al., 2014). A reasonable radial range for metallicity gradient measurements is believed to be between the disk effective radius (Freeman, 1970; Sanchez et al., 2014) and the optical radius (Mollá & Díaz, 2005; Mollá et al., 2016c), i.e., roughly twice the size of disk effective radius. We verified that all our metallicity gradients are derived in this radial range, which enhances the significance of the comparative studies (of our measurements at least) presented in Sections 3.6.1.1 and 3.6.1.2.

### 3.6.1.1 Cosmic Evolution of Metallicity Gradients

We plot the evolution of metallicity gradient across cosmic time in Figure 3.12. Here we include all existing high- $z$  gradient measurements obtained with sufficiently high spatial sampling, i.e.

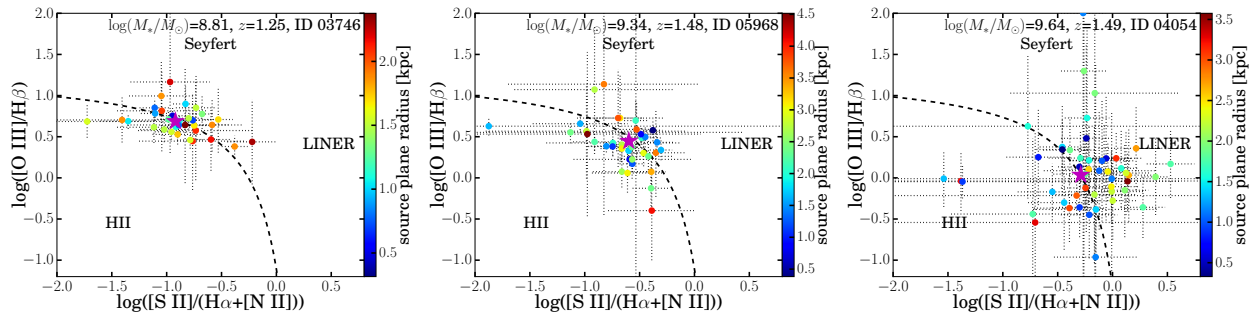


Figure 3.11 Spatially resolved BPT diagrams for three representative sources in our metallicity gradient sample. The points in each panel correspond to spaxels in the combined EL maps for each source, color coded by the source plane de-projected galactocentric radius. Note that similar to what we show in Figure 4.3, all spaxels represented by colored points here are rebinned to recover the native WFC3/IR pixel scale ( $0.^{\prime\prime}13$ ). The magenta star denotes the position where the entire galaxy would lie, calculated from integrated EL fluxes, with the length of the error bar comparable to the size of the symbol. The dashed curve is adapted from the extreme starburst scenario given by Kewley et al. (2006b), assuming the “vanilla” value for  $[\text{N II}]/\text{H}\alpha$ . Given the  $1-\sigma$  uncertainties, all the spaxels are broadly consistent with being HII regions.

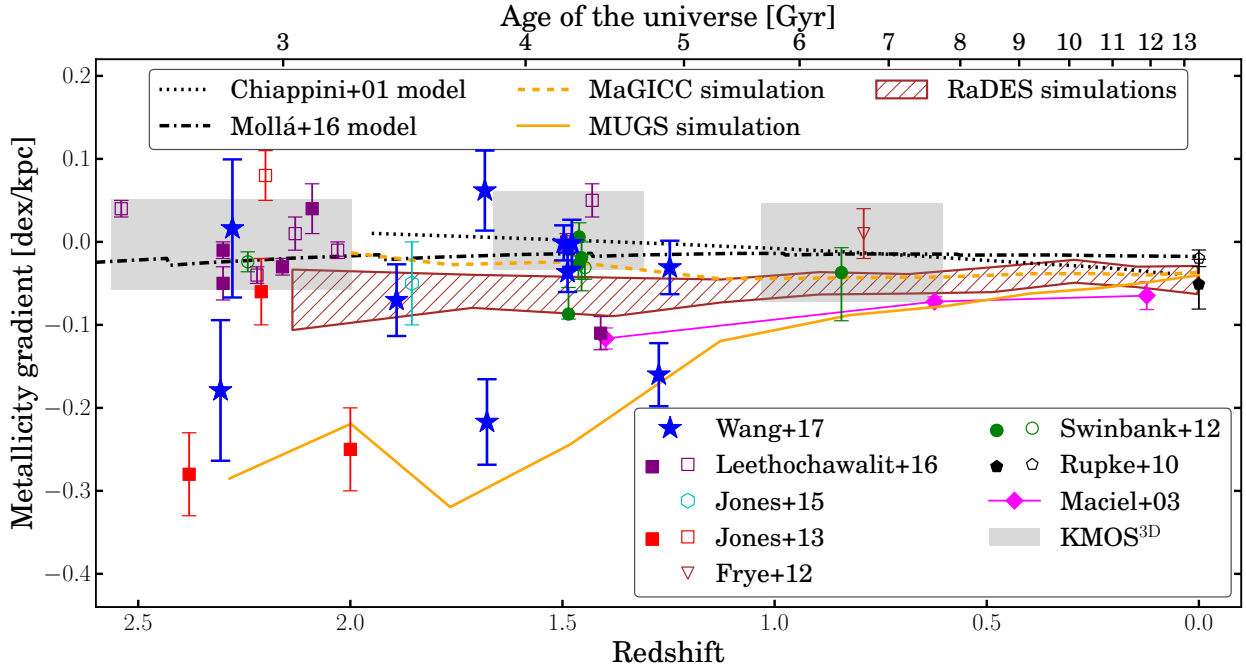


Figure 3.12 Evolution of metallicity gradients with redshift. The blue stars represent the metallicity gradients measured in this work, and the cyan hexagon is from our previous work (Jones et al., 2015b). We include all the high- $z$  metallicity gradient measurements with sub-kpc resolution in the current literature: lensed galaxies analyzed by Frye et al. (2012), Jones et al. (2013), and Leethochawalit et al. (2016), non-lensed galaxies observed with AO (Swinbank et al., 2012). The spread of the  $KMOS^{3D}$  measurements obtained with seeing-limited conditions (?) is marked as grey shaded regions. We also show the averages of local metallicity gradients (Rupke et al., 2010), and the trend of the Milky Way gradient evolution based upon planetary nebula estimates (Maciel et al., 2003). Except for the blue stars, hollow and filled symbols correspond to interacting/merging and isolated systems, respectively. In addition, the predictions from different analytical chemical evolution models and numerical simulations are also shown as comparisons to the observational results (see Section 3.6.1 for more details).

finer than kpc resolution in the source plane. Together with the 10 new metallicity gradient measurements from the individual spaxel method presented here, in Figure 3.12, we show one highly magnified galaxy of an interacting triple at  $z=1.85$  analyzed in our previous work (Jones et al., 2015b). We also include 11 measurements by Leethochawalit et al. (2016) (5 isolated and 6 merging), 4 by Jones et al. (2013) (3 isolated and 1 merging), 1 sub- $L_*$  post-merger at  $z \sim 1$  by Frye et al. (2012), and 7 data points from Swinbank et al. (2012) (5 isolated and 2 interacting). The scatter of these high-resolution gradient measurements is  $\sim 0.12$  dex and  $\sim 0.22$  dex at  $z \sim 1.5$  and  $z \sim 2.3$  respectively. The spread of recent gradient measurements from the seeing-limited  $KMOS^{3D}$  survey is also overlaid in Figure 3.12. Note that the PSF FWHM given by the median seeing of their observations is  $0.^{\prime\prime}6$ , which results in a 5 kpc resolution at  $z \sim 2$ , twice the size of the half-light radius of an  $L_*$  galaxy at this redshift. We thus only focus on interpreting the sub-kpc resolution gradient measurements, in order to avoid possible biases toward null values associated poor spatial sampling (see, e.g., Yuan et al., 2013). Although corrected for beam smearing, the  $KMOS^{3D}$  gradient measurements still display small scatter than that of the high resolution results. When possible, we also divide each data set in terms of sources being isolated or kinematically disturbed (i.e. undergoing merging). In part of our sample, signatures of post-merger tidal remnants can be clearly identified, which strongly indicates that gravitational interaction plays a key role in shaping the spatial distribution of metals in these galaxies (IDs 02806, 03746, and 05968).

In order to compare theoretical predictions with observations, we incorporate into Figure 3.12 the predictions for the metallicity gradient cosmic evolution from canonical chemical evolution models (CEMs) based upon the “inside-out” disk growth paradigm given by Chiappini et al. (2001, C01) and Mollá et al. (2016a,b, M16). C01 constructed a two-phase accretion model for galaxy formation. The first infall period corresponds to the formation of the dark matter halo and the thick disk, with an exponentially declining infall rate at a fixed  $e$ -folding time scale ( $\sim 1$  Gyr). In this phase, the infall of pristine gas is rapid and isotropic, giving birth to a relatively extended profile of star formation. The thin disk is formed in the second phase, where gas is preferentially accreted to the periphery of the disk, with the  $e$ -folding time scale proportional to galactocentric radius (vis-á-vis the “inside-out” growth). The foundation of M16 is Mollá & Díaz (2005), who proposed their prescription by treating the ISM as a multiphase mixture of hot diffuse gas and cold

condensing molecular clouds, and calibrating against different star-formation efficiencies. Popular nucleosynthesis prescriptions for type Ia/II SNe and AGB stars are employed by both to construct the yields of dominant isotopes (e.g. H, He, C, N, O, Fe). Improving over what is done in the Mollá & Díaz (2005) multiphase CEMs, M16 adopted newly calibrated gas infall rates from Mollá et al. (2016c) and a variety of different prescriptions for H<sub>i</sub>-to-H<sub>2</sub> conversion, with the best being the ASC technique (Ascasibar et al. in prep). We thus show this model solution in the black dash-dot curve. As shown in Figure 3.12, the majority of the high- $z$  measurements are generally compatible with both model predictions, with the M16 model showing better consistency, largely ascribed to its more accurate assumptions of ISM structure and more realistic treatment of star formation. Note that these chemical evolution models do not take galactic feedback or radial gas flows into account. So without the consideration of strong physical mechanisms that stir and mix up the enriched gas with relatively unenriched ambient ISM, conventional analytical models are still able to match the metallicity gradients observed at high redshifts.

In addition to the predictions from these analytical models, we also compare our measurements with results from numerical simulations. First, we show the fiducial representative (i.e. the realization g15784) of the McMaster Unbiased Galaxy Simulations (MUGS, Stinson et al., 2010) using the gravitational N-body and SPH code GASOLINE. This simulation employed the “conventional” feedback scheme, i.e. depositing  $\sim$ 10-40% kinetic energy from SN explosions into heating ambient ISM. Furthermore, it adopted a high star-formation threshold (gas particle density  $>1\text{ cm}^{-3}$ ), which makes star forming activities highly concentrated in the galaxy center at early stages of disk formation. As a result, a steep gradient (i.e.  $\gtrsim -0.2\text{ dex/kpc}$ ) is persisting at  $z > 1$  and then significantly flattens with time. Although greatly offset from most of the measurements (and other theoretical predictions) as seen in Figure 3.12, this particular evolutionary track is actually quite consistent with some of the observed steep gradients (galaxies 07255, 05709, 05811 in our analysis). In comparison, the same galaxy (g15784) is re-simulated with an enhanced feedback prescription of sub-grid physics as part of the Making Galaxies In a Cosmological Context (MaG-ICC, Stinson et al., 2013) program. A factor of 2.5 difference in the energy output rate from SN feedback diverges the evolutionary track of metallicity gradients given by the MUGS and MaG-ICC simulations, making the evolution of the MaGICC gradient less dramatic and more similar to

the M16 model solution. This demonstrates that amplifying the feedback strength can significantly flatten the metallicity gradients in early star-forming galaxies (Gibson et al., 2013). This is actually adopted by some recent studies (Leethochawalit et al., 2016; ?) to explain their metallicity gradient measurements, which are also shown in Figure 3.12. However, as we have already mentioned, this is not the only explanation possible.

Lastly, in Figure 3.12, we also show another set of numerical results, from an ensemble of 19 galaxies in different environments (9 in isolated field and 10 in loose groups), simulated by the RAMSES Disk Environment Study (RaDES, Few et al., 2012) using the adaptive mesh refinement code RAMSES. Unlike what is shown for the MUGS and MaGICC simulations (i.e. just one single realization), the full range of the whole suite of RaDES simulations is marked in Figure 3.12, which provides a statistical comparison sample, although the scatter of the RaDES simulations cannot capture the scatter seen in actual measurements. Generally speaking, the evolutionary trends of the abundance gradients of RaDES galaxies lie somewhat in-between the two tracks of g15784 in MUGS and MaGICC simulations, but still quite consistent with the majority of the high- $z$  gradient measurements. Because no mass loading is assumed in the RaDES simulations, outflows do not play any role in this observed consistency. Moreover, since a lower star-formation threshold is used ( $> 0.1 \text{ cm}^{-3}$ ), which is similar to what the analytical CEMs assumed, star formation in RaDES galaxies occurs more uniformly in the early disk formation phase. This strongly suggests that having more extended star formation can also result in galaxies possessing shallower gradients, confirming the tight link between star formation profile and metallicity gradient (Pilkington et al., 2012).

### 3.6.1.2 Mass Dependence of Metallicity Gradients

In Figure 3.13, we plot metallicity gradient as a function of stellar mass for a subset of all gradient measurements shown in Figure 3.12, where reliable  $M_*$  estimates are available. Notably, in the low-mass regime of  $M_* \lesssim 10^9 M_\odot$ , all the current sub-kpc resolution metallicity gradient measurements at  $z \gtrsim 1$  are obtained from our work, and our measurements even extend to below  $10^8 M_\odot$ . This illustrates the power of combining the space-based grism spectroscopy with gravitational lensing

as a means to recover reliable metal abundance distributions in early star-forming disks in the low-mass regime. From these measurements, we can tentatively observe an intriguing correlation between  $M_*$  and metallicity gradient: more massive galaxies tend to have shallower (less negative) gradients. This is consistent with the galaxy formation “downsizing” picture (see, e.g., Brinchmann et al., 2004; Fontanot et al., 2009) such that more massive galaxies are more evolved and their metal distributions flatter since they are in a later phase of disk mass assembly where star formation occurs in a more coherent mode throughout the disk. This correlation between mass and gradient slope has also been seen in a variety of theoretical studies including the RaDES simulations (Few et al., 2012) and the multiphase CEMs by (Mollá & Díaz, 2005).

Several groups of authors have reported a characteristic oxygen abundance gradient for nearby disk galaxies, such that the normalized gradient in units of dex per scale radius is approximately invariant with galaxy global properties ( $M_*$ , morphology, etc.; e.g. Sanchez et al., 2014; Bresolin & Kennicutt, 2015; Ho et al., 2015). Consequently larger and more massive galaxies have shallower gradients in physical units (dex/kpc; e.g. Ho et al., 2015), as we tentatively see in Figure 3.13. We verify that 8/10 of our gradient measurements, if expressed in terms of disk effective radii, are consistent with the common gradient slope reported by Sanchez et al. (2014). This common normalized abundance gradient may reflect a more fundamental relation between local surface mass density and metallicity (e.g. Bresolin & Kennicutt, 2015). Both of these quantities decrease more rapidly with radius in smaller galaxies, in line with our “downsizing” picture of metallicity gradients. Downsizing is further reinforced by the evolution in the size-mass relation recovered by Van der Wel et al. (2014).

As a comparison, we include the linear fit to the low spatial resolution metallicity gradient measurements from the *KMOS<sup>3D</sup>* survey in the similar  $z$  range (see Figure 6 in ?). Since the mass completeness limit for the *KMOS<sup>3D</sup>* data set is  $\sim 10^{9.7} M_\odot$ , our analysis is highly complementary to the *KMOS<sup>3D</sup>* result in terms of  $M_*$ , albeit our metallicity gradients are measured at much higher spatial resolution. However, the *KMOS<sup>3D</sup>* fitting relation deviates systematically from the “downsizing” mass dependency of metallicity gradients and is also in conflict with some sub-kpc resolution gradient measurements obtained by Jones et al. (2013) at over 3- $\sigma$  confidence level. This can be attributed to possible biases associated with the low spatial resolution of the *KMOS<sup>3D</sup>*

observations and the small mass range of their sample.

We also show the  $2\sigma$  spread of the galaxy metallicity gradients from the FIRE cosmological zoom-in simulations (?). This suite of simulations has been used to study the MZR as we discussed in Section 3.5 (Ma et al., 2016). The simulations show a diversity of gradient behaviors at four redshift epochs ( $z=0, 0.8, 1.4, 2.0$ ). At  $z = 2$ , the scatter of their simulation results can reach 0.2 dex when radial gradients are measured in the central 2 kpc region, quite consistent with the scatter ( $\sim 0.22$  dex) seen in high-resolution gradient measurements at  $z \sim 2.3$ . However, their simulations still cannot reproduce some of the steep gradient measurements, especially some of our results in the low-mass regime. According to ?, galactic feedback from intense starburst episodes on 0.1-1 Gyr time scale can effectively flatten metallicity gradients. Hence for the galaxies measured with steep metallicity gradients, galactic feedback must be of limited influence, at least in affecting metal distribution in HII regions on such short time scale.

In short, we observe a tentative mass dependence of metallicity gradients that low-mass galaxies have steeper gradients compared with high-mass galaxies at high redshifts. A larger set of accurately measured and uniformly analyzed metallicity gradients well sampled in  $M_*$  (in the regime of  $M_* \lesssim 10^9 M_\odot$  in particular) is needed in order to fully explore the validity of the metallicity gradient “downsizing” picture and whether galactic feedback plays a crucial role in altering this picture.

### 3.6.2 Notes on Individual Galaxies

In this section, we highlight some noteworthy sources in our metallicity gradient sample. For reference, all the measurements of global properties, metallicity gradients, and kinematic decompositions in these sources are presented in Tables 4.1, 3.5, and 3.6, respectively.

**02389:** This is the most highly magnified source in our sample, with  $\mu = 43.25^{+7.03}_{-5.78}$ , given by the SHARON & JOHNSON version 3 model. It is one of two connected double images that straddle the lensing critical curve at source redshift  $z = 1.89$ , forming a highly sheared arc more than 5 arcsec. This is confirmed by the velocity shear of  $\sim 50$  km s $^{-1}$  detected in both components of the fold arc. After lensing correction, the stellar mass of this source is  $\log(M_*/M_\odot) = 8.43^{+0.06}_{-0.07}$ ,

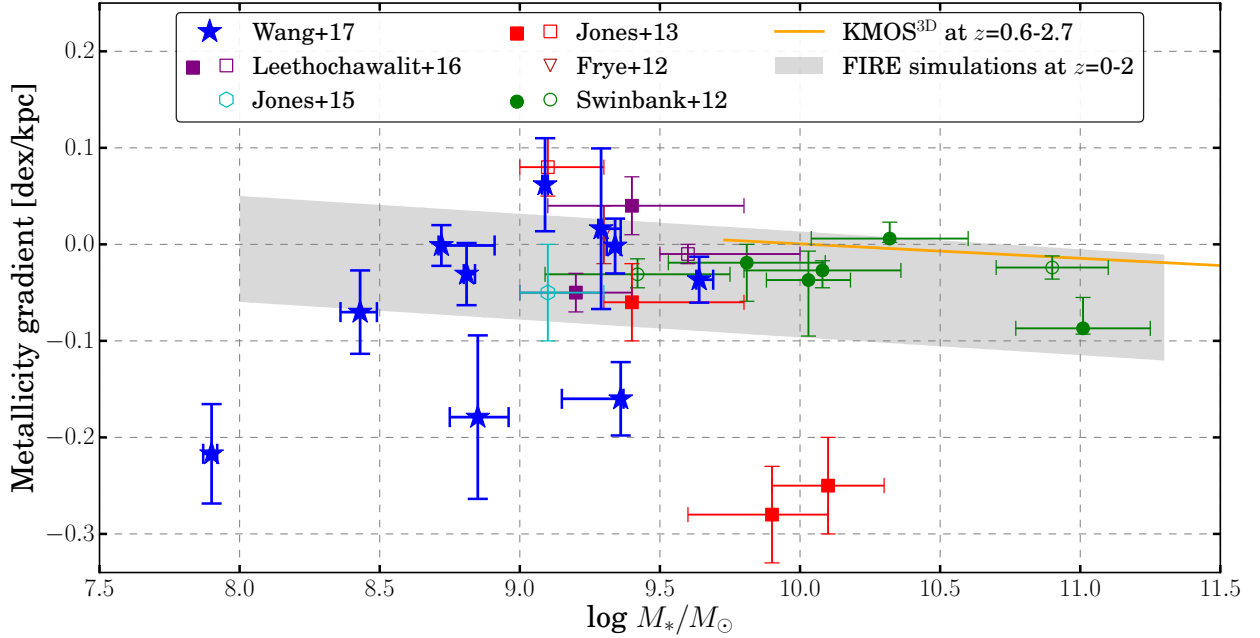


Figure 3.13 Observed metallicity gradients as a function of  $M_*$ . The color-coding of symbols is the same as in Figure 3.12. Except for the blue stars, hollow and filled symbols correspond to interacting/merging and isolated systems, respectively. Most of the Leethochawalit et al. (2016) gradient measurements do not have reliable  $M_*$  estimates due to the lack of near IR photometry. The orange line shows a simple linear fit to the metallicity gradient results at  $z=0.6-2.7$  from the  $KMOS^{3D}$  observations, only covering the stellar mass range of  $\log(M_*/M_\odot) \in [9.7, 11.5]$  (?). The  $2-\sigma$  interval of the FIRE simulation results presented by ? is shown as the shaded region. The only work to date that presents metallicity gradient measurements in the  $M_* \lesssim 10^9 M_\odot$  regime is this work, which even extends to below  $10^8 M_\odot$ .

consistent with the very low dynamical mass indicated by both the velocity shear and integrated velocity dispersion. The relatively high  $V/\sigma \gtrsim 2$  of this source shows that it is a disk galaxy. The metallicity gradient is mildly negative, i.e.,  $-0.07 \pm 0.04$ , consistent with the prediction by analytical CEMs for disk galaxies at similar redshifts.

**02806:** This is a star-forming galaxy at  $z = 1.50$  with very flat metallicity gradient of  $-0.01 \pm 0.02$ . We removed the contamination from a marginally overlapping cluster member (with greenish color in the color composite stamp shown in Figure 3.4). Note that such a process would not be possible with seeing-limited data quality. The *MUSE* observation does not spatially resolve this source well, and its [O II] emission line is detected with low SNR near the red edge of *MUSE* spectral coverage. A tentative velocity shear is seen at low significance. The faint fuzzy elongation to the south-east of this galaxy suggests a likely recent merging event, which accounts for its gradient being flat. (See sources 03746 and 05968 for more outstanding cases where post-merger features can be identified.) The global metallicity of this source ( $12 + \log(\text{O/H}) = 7.91_{-0.16}^{+0.16}$ ) is slightly lower than the average given by the MZR at similar  $M_*$ , in agreement with the study of Michel-Dansac et al. (2008) suggesting that the infall of low-metallicity gas during mergers reduces the average metallicity.

**03746:** This is an intense starburst galaxy with  $\text{SFR} = 10.95_{-0.58}^{+1.61} M_\odot/\text{yr}$  at  $z = 1.25$ , as revealed by the BPT diagram in Figure 3.11. It also displays a flat metallicity gradient of  $-0.03 \pm 0.03$ . Moreover the EL maps of this source show highly clumpy star-forming regions, which do not have direct correspondence in the broad-band photometry. The *MUSE* observation gives a velocity shear of  $\sim 20 \text{ km s}^{-1}$ , and an integrated dispersion of  $\sim 60 \text{ km s}^{-1}$ , which suggests that this system is dispersion dominated ( $V/\sigma < 1$ ). There is an extended feature southward to the source center, which is probably a tidal remnant, consistent with this source being in a recent post-merger phase. Besides, given the irregularities seen in the central region of the  $M_*$  map, this system is still long before dynamical relaxation, and we likely capture this merger system almost right after the coalescence. Therefore we conclude that the flat metallicity gradient recovered in this system is from tidal interactions. See galaxy 05968 below for an even more outstanding post-merger case.

**04054:** This is one of the multiple images of the SN Refsdal host galaxy, a highly magnified almost face-on spiral at  $z = 1.49$ . It is labeled as image 1.3 by Treu et al. (2016)<sup>9</sup>. Our global demographic analysis yields the following measurements:  $\log(M_*/M_\odot) = 9.64_{-0.01}^{+0.05}$ ,  $\text{SFR} = 16.99_{-2.80}^{+5.71} M_\odot/\text{yr}$ ,  $12 + \log(\text{O/H}) = 8.70_{-0.11}^{+0.09}$ . Compared with the previous analysis of this galaxy (Livermore et al., 2015; Rawle et al., 2016, not necessarily the same image though), our work benefits from a more complete wavelength coverage of imaging data (from  $B_{435}$  to  $H_{160}$  bands) at a greater depth. In particular, we used the most updated lens model, optimized specifically for this spiral galaxy (Treu et al., 2016), giving a reliable estimate of the magnification. Rawle et al. (2016) measured  $\text{SFR} \sim 5 M_\odot/\text{yr}$  on image 1.1 of the SN Refsdal host from *Herschel* IR photometry. However their value is derived assuming a magnification factor of  $\mu = 23.0$ , given by an older lens model for MACS1149.6+2223 (Smith et al., 2009). If the magnification value of  $\mu = 8.14$  given by the latest GLAFIC model is adopted instead, their measurement yields  $\text{SFR} \sim 14$ , comparable to our SFR measurement. As a result, our measurements are fairly consistent with the star-formation main sequence, the MZR and the FMR at similar redshifts. Given the high  $M_*$  and  $12 + \log(\text{O/H})$ , this galaxy is significantly evolved by  $z \sim 1.5$  and with the still relatively high SFR, it will likely turn into a galaxy more massive than our Milky Way at  $z = 0$ . According to the kinematic map derived from the *MUSE* spectroscopy of the [O II] EL doublet, we obtain the velocity shear to be  $\sim 110 \text{ km s}^{-1}$  (see also Figure 8 in Grillo et al. (2016)) and the integrated dispersion  $\sim 60 \text{ km s}^{-1}$ , in good agreement with Livermore et al. (2015) who found  $2v_{2.2} = 118 \pm 6 \text{ km s}^{-1}$ , and local (spatially resolved) velocity dispersion of  $50 \pm 10 \text{ km s}^{-1}$ , based upon adaptive optics data.

The measured metallicity gradient for the SN Refsdal host based upon our analysis of image 1.3 is  $-0.04 \pm 0.02$  from the individual spaxel method, and  $-0.07 \pm 0.02$  from the radial annulus method. This measurement is very close to the usual abundance gradient of local spirals, including our Milky Way, measured from either HII regions or planetary nebulae (Smartt & Rolleston, 1997; van Zee et al., 1998; Henry et al., 2004; Esteban et al., 2015). It is worth noting that our measurement is not as steep as the previous result reported by Yuan et al. (2011), i.e.  $-0.16 \pm 0.02$ , measured from the AO assisted *OSIRIS* IFU observation of image 1.1 of the SN Refsdal host, assuming the Pettini

---

<sup>9</sup>It is located at the minimum of its lensing time delay surface, any intrinsic variabilities in the source are observed first in this image. Unfortunately in the case of SN Refsdal, its image is estimated to appear  $\sim 12$  years ago, long before the deployment of WFC3.

& Pagel (2004)  $[\text{N II}]/\text{H}\alpha$  empirical calibration. After the discovery of SN Refsdal, Kelly et al. (2015c) obtained a 1-hr *MOSFIRE* spectra on the nuclear region and the SN explosion site in image 1.1, and measured  $12 + \log(\text{O/H}) = 8.6 \pm 0.1$  and  $12 + \log(\text{O/H}) = 8.3 \pm 0.1$ , respectively, using the same  $[\text{N II}]/\text{H}\alpha$  calibration. The spatial offset between these two measurements in terms of galactocentric radius is  $8.2 \pm 0.5$  kpc, given by the GLAFIC model. As a result, the recent *MOSFIRE* observations indicate a gradient being  $-0.04 \pm 0.02$ , highly consistent with our measurements.

Moreover, we obtain a robust constraint on the nebular dust extinction, i.e.,  $A_V^N = 0.72_{-0.23}^{+0.23}$ . Compared with the stellar dust extinction retrieved from SED fitting, i.e.,  $A_V^S = 1.10_{-0.01}^{+0.01}$ , we see that in this galaxy, the dust reddening of the ionized gas in HII regions is less severe than that of the stellar continuum (see another source, i.e. ID 05968, from which the same conclusion is drawn). This is different from what has been assumed previously: the color excess of nebular ELs is larger than that of the stellar continuum, i.e.,  $E_N(B - V) = (0.44 \pm 0.03)E_N(B - V)$  (Calzetti et al., 2000). Recently, Reddy et al. (2015) conducted a systematic study of dust reddening using the early observations from the *MOSDEF* survey and found that only 7% of their sample is consistent with  $E_N(B - V) \gtrsim E_S(B - V)/0.44$ . They also discovered that as sSFR (derived from Balmer EL luminosities) increases,  $E_N(B - V)$  diverges more significantly from  $E_S(B - V)$ , with a scatter of  $\sim 0.3\text{-}0.4$  dex at  $\text{sSFR} \sim 3 \times 10^{-9} \text{ yr}^{-1}$ , which can account for the difference we see in the total dust attenuation ( $A_V$ ) of the line and continuum emissions of this galaxy.

**05709:** This galaxy has the lowest stellar mass in our metallicity gradient sample ( $\log(M_*/M_\odot) = 7.90_{-0.03}^{+0.02}$ ) after lensing correction<sup>10</sup>. This is for the first time any diffraction-limited metallicity gradient analysis and seeing-limited gas kinematics measurement have been achieved in star-forming galaxies with such small  $M_*$  at the cosmic noon. This galaxy shows a steep metallicity gradient, i.e.  $-0.22 \pm 0.05$ . The velocity shear is measured to be  $\sim 25 \text{ km s}^{-1}$ , with integrated dispersion being  $\sim 20 \text{ km s}^{-1}$ . The inferred low dynamical mass is consistent with the result from SED fitting mentioned above. In light of the kinematic result  $V/\sigma \gtrsim 1$ , this galaxy is probably a clumpy thick disk. More interestingly, observed from a multi-perspective point of view (see Figure 3.4), this galaxy shows a clumpy star-forming region at the periphery of its disk (having a distance of 3-4

---

<sup>10</sup>The magnification value we used in correcting for lensing is  $7.10_{-0.36}^{+0.43}$ , given by the GLAFIC model. The magnification value given by the SHARON & JOHNSON model is similar, i.e.,  $8.43_{-0.60}^{+0.73}$ .

kpc to the mass center), which has a tremendous amount of line emission, yet very little stellar mass, and has low gas-phase metallicity. Also see galaxy ID 07255 for a more dramatic case.

**05968:** With a tidal tail more appreciably shown to the north-east, and almost perpendicular to the galactic plane, this galaxy (at  $z = 1.48$ ) is safely classified as a post-merger. However note that this identification would not be possible and this source would have been surely classified as a thick disk due to its symmetric morphology and kinematic properties, without the ultra deep *HFF* imaging data. Compared with the  $M_*$  and EL maps of ID 03746, the  $M_*$  map of this galaxy is more smooth and EL maps less clumpy, which indicates that merging has taken place longer before than in source ID 03746. Still the star formation is high, i.e.  $\text{SFR} = 27.95^{+4.70}_{-4.41} M_\odot/\text{yr}$ . The global metallicity ( $12 + \log(\text{O/H}) = 8.47^{+0.07}_{-0.08}$ ) and stellar mass ( $\log(M_*/M_\odot) = 9.34^{+0.02}_{-0.03}$ ) are quite comparable to the MZR at similar redshifts. The metallicity gradient, as expected for systems which have experienced recent mergers (see e.g. Kewley et al., 2010), is constrained to be robustly flat ( $-0.01 \pm 0.02$ ). The EL kinematic analysis yields a velocity shear of  $\sim 120 \text{ km s}^{-1}$ , and an integrated dispersion being  $\sim 75 \text{ km s}^{-1}$ . The velocity field appears typical of intermediate-mass disk galaxies at this redshift, which infers that this post-merger system has been significantly relaxed and regained at least some of the rotation support. This is also one of the few cases where robust constraints on nebular dust extinction can be derived, i.e.  $A_V^N = 0.23^{+0.15}_{-0.13}$ , which is less than the dust extinction of stellar continuum obtained from SED fitting  $A_V^S = 0.60^{+0.20}_{-0.01}$ , as already seen in the case of ID 04054.

**07255:** This galaxy is highly consistent with the SFMS at  $z = 1.27$  formulated by Speagle et al. (2014), with  $\log(M_*/M_\odot) = 9.36^{+0.01}_{-0.21}$  and  $\text{SFR} = 8.73^{+3.53}_{-3.10} M_\odot/\text{yr}$ . By  $z = 0$ , it will turn into a sub-Milky Way-sized galaxy according to Behroozi et al. (2013). Its slightly lower than average metallicity of  $12 + \log(\text{O/H}) = 8.38^{+0.08}_{-0.08}$  can be a result of low-metallicity gas inflow, following the popular interpretation of the FMR at high  $z$ . This hypothesis would also explain its slightly enhanced SFR. In the metallicity map the inflow can be identified with a bright star-forming clump in the lower right corner, which consists of very little  $M_*$ , but is dominating in the EL maps, similar to the case of galaxy 05709 discussed above. This indicates that in this system, the metal enrichment time scale is much larger than the star-forming time scale, which is in turn much larger than the gas infall time scale. Unfortunately, at the moment we do not have EL

kinematic observation on this system.

The metallicity gradient for this galaxy is constrained to be very steep, i.e.  $-0.16 \pm 0.03$  using the individual spaxel method, and  $-0.21 \pm 0.03$  from the radial annulus method. We also dissected this galaxy to separate the star-forming clump from the bulk part and re-do the analysis. It is found that the HII regions closely related to the clump (with at least 2.5 kpc distance to the galaxy mass center) have significantly lower metallicity and provide more than one third of the entire star formation, i.e.,  $12 + \log(\text{O/H}) = 8.04_{-0.18}^{+0.14}$ ,  $A_V^N < 0.78$ ,  $\text{SFR} = 3.05_{-1.10}^{+1.21}$ , compared with the quantities measured in the bulk of the galaxy (within 2 kpc to the mass center), i.e.,  $12 + \log(\text{O/H}) = 8.51_{-0.10}^{+0.08}$ ,  $A_V^N = 0.63_{-0.41}^{+0.59}$ ,  $\text{SFR} = 5.78_{-2.47}^{+3.41}$ . In both regions, EL H $\alpha$  is detected at a significance of  $\gtrsim 30\sigma$ . This again demonstrates that measurements of global quantities can be to some extent misleading, and the importance of detailed spatially resolved information. Cases like this galaxy should be exceedingly interesting, since their steep metallicity gradients at such high  $z$  are not predicted by current mainstream numerical simulations (equipped with strong galactic feedback) or conventional analytical CEMs. Through studying systems like this, we can also learn how gas is accreted into the inner disk, and more importantly whether the accretion happens alongside star formation or long before the gas clouds can collapse.

## 3.7 Summary and Discussion

### 3.7.1 Summary

In this Chapter, we took advantage of the deep *HST* grism spectroscopic data, acquired by the *GLASS* and SN Refsdal follow-up programs, and obtain gas-phase metallicity maps in high- $z$  star-forming galaxies. The *HST* grisms provide an un-interrupted window for observing the cosmic evolution of metallicity gradients through  $z$  from 2.3 to 1.2 (corresponding to the age of the universe from roughly 2.5 to 5.5 Gyr), including the redshift range  $1.7 < z < 2.0$ , unattainable from ground-based observations due to low atmospheric transmission. Another advantage of the HST grisms is that multiple ELs are available within a single setup and all the potential issues related to combining data with different setups and atmospheric conditions are eliminated. Our main conclusions can be

summarized as follows:

1. We presented 10 maps of gas-phase metallicity (as shown in Figure 4.3), measured at sub-kpc resolution in star-forming galaxies in the redshift range of  $1.2 \lesssim z \lesssim 2.3$ , in the prime field of MACS1149.6+2223. This field is so far one of the deepest fields exposed by *HST* spectroscopy, at a depth of 34(12) orbits of G141(G102), reaching a  $1-\sigma$  flux limit of  $1.2(3.5) \times 10^{-18}$  erg s $^{-1}$  cm $^{-2}$ , without lensing correction.
2. We developed a novel Bayesian statistical approach to jointly constrain gas-phase metallicity, nebular dust extinction, and H $\alpha$ -based dust-corrected star formation rate. In determining these quantities, our method does not rely on any assumptions about star-formation history, nor the conversion of dust reddening from stellar phase to nebular phase. Unlike the majority of previous work on deriving metallicity from strong EL calibrations, our method does not compare directly the observed EL flux ratios with the calibrated ones. Instead we work directly with EL fluxes, which effectively avoids using redundant information and circumvents possible biases in the low SNR regime.
3. The metallicity maps we obtained show a large diversity of morphologies. Some maps display disk-like shapes and have metallicity gradients consistent with those predicted by analytical chemical evolution models (i.e. IDs 04054, 01422, 02389, 05732), whereas other disk-shaped galaxies have exceedingly steep gradients (i.e. IDs 07255, 05709, 05811) and bright star-forming clumps at the periphery of their disks. These large-offset star-forming clumps, containing very little stellar mass, are estimated to have lower metallicity than the corresponding global values, which can be interpreted as an evidence for the infall of low metallicity gas enhancing star formation. We also recovered three systems with nearly uniform spatial distribution of metals (i.e. IDs 02806, 03746, 05968). In these systems, we can identify possible signatures of post-merger tidal remnants, which suggests that the observed flat gradients are likely caused by gravitational interactions.
4. Collecting all existing sub-kpc resolution metallicity gradient measurements at high redshifts, we study the cosmic evolution and mass dependence of metallicity gradients.

- We found that predictions given by analytical chemical evolution models assuming a relatively extended star-formation profile in the early phase of disk growth can reproduce the majority of observed metallicity gradients at high redshifts, without involving strong galactic feedback or radial outflows. This confirms the tight link between star formation and metal enrichment.
- We tentatively observed an correlation between stellar mass and metallicity gradient, which is in accord with the “downsizing” galaxy formation scenario that more massive galaxies are more evolved into a later phase of disk growth, where they experience more coherent mass assembly and metal enrichment, than lower mass galaxies.

A larger sample of uniformly analyzed metallicity maps well sampled in the full  $M_*$  range (especially in the low mass regime, i.e.,  $M_* \lesssim 10^9 M_\odot$ ) at high redshifts is needed to further investigate the cosmic evolution and mass dependence of metallicity gradients.

5. We also compiled a sample of 38 global metallicity measurements all derived from the Maiolino et al. (2008) EL calibrations in the current literature (including 13 galaxies presented in this work). This sample, at  $z \sim 1.8$ , spans three orders of magnitude in  $M_*$ . We measured the MZR and tested the FMR using this sample.

- The slope of the MZR constrained by this sample rules out the momentum-driven wind model by Davé et al. (2012) at  $3\sigma$  confidence level. Our MZR is consistent with the theoretical prediction given by recent cosmological zoom-in simulations, suggesting that high spatial resolution simulations are favorable in reproducing the metal enrichment history in star-forming galaxies.
- Given the intrinsic scatter and measurement uncertainties, we do not see any significant offset from the FMR except the subsample of Wuyts et al. (2012a). This discrepancy is likely due to the fact that the Wuyts et al. (2012a) dataset is the only subsample which relies exclusively on [N II]/H $\alpha$  to estimate metallicity. We therefore advocate to avoid nitrogen lines when estimating gas-phase metallicity in high- $z$  HII regions.

### 3.7.2 Interpretation of Flat/stEEP Metallicity Gradients at High Redshifts

We now turn to the interpretation of our observed metallicity gradients and maps. Apart from the flattening of metallicity gradients through natural evolution of galaxies that brings the abundances of any elements in the ISM asymptotically to the average stellar yields at the end of the evolution everywhere in the galaxy, there are four physical mechanisms on relatively short timescale that could significantly flatten a star-forming galaxy’s *pre-existing* negative metallicity gradient (not exclusively in high- $z$  scenarios):

- Efficient radial mixing by tidal effects from gravitational interactions, as seen in galaxy IDs 02806, 03746, and 05968 in our sample and the triply imaged arc 4 in our previous work (Jones et al., 2015b).
- Rapid recycling of metal-enriched material by enhanced galactic feedback, as seen in the results of the MaGICC numerical simulations for example.
- Turbulence mixing driven by thermal instability as elucidated by Yang & Krumholz (2012).
- Funnelling of cold streams of low metallicity gas directly into the galaxy center, as suggested by Dekel et al. (2009b)<sup>11</sup>

Besides *pre-existing* negative gradients being flattened by these processes, galaxies can also inherit a broadly flat metallicity gradient from relatively extended star-formation profile in the early disk-formation phase and coherent mass assembly for the disk growth. Because there is strong evidence that the mass assembly for Milky Way progenitors takes place uniformly at all radii, maintaining almost the same  $M_*$  profile from  $z \sim 2.5$  to  $z \sim 1$  (van Dokkum et al., 2013; Morishita et al., 2015). However the uncertainties associated with current measurements are still insufficient to distinguish numerical simulations with enhanced feedback prescriptions from conventional analytical CEMs assuming more uniform star formation (see Figure 3.12).

One perhaps obvious but nevertheless important caveat common to most galaxy evolution work is that we only have access to *cross-sectional* data, i.e., observations of different objects at one specific epoch. Therefore any interpretations of plots like Figure 3.12, which try to tie these data

---

<sup>11</sup>This mechanism is invoked to explain the inverted gradients (lower abundances in the inner disk regions) seen in some of the AMAZE/LSD observations (Cresci et al., 2010). But we note in their observations, the near-IR integral field spectrometer *SINFONI* was used in seeing-limited mode.

with *longitudinal* theories (describing the evolution of one specific object), should be made with caution.

Perhaps an even more intriguing interpretation of Figure 3.12, which is robust against the aforementioned caveat, is that there exist some really steep metallicity gradients at high  $z$ , such as our galaxy IDs 07255, 05709, and 05811. Based upon current measurements, the occurrence rate of high- $z$  metallicity gradients more negative than  $-0.1 \text{ dex/kpc}$  is 5/34. We can derive the following constraints on the physical processes that can contribute to these steep metallicity gradients observed beyond the local universe:

- galactic feedback (including supernova explosions and stellar winds) must be of limited influence (via being confined for instance),
- star-formation efficiency is low, or at least lower than their local analogs (in simulations, this can be achieved by having a higher star-formation threshold or less concentrated molecular gas, as shown by the MUGS runs),
- star formation at early times is highly centrally concentrated, and the mass assembly of the inner regions is much faster than that of the outer regions,
- alternatively, steep gradients are the result of low-metallicity gas falling onto the outskirts of their disks, implying that the dynamic time scale is much shorter than the star-forming time scale, which is much shorter than the metal enrichment time scale, as seen in our galaxy 07255.

We need larger samples with robust measurements in order to more accurately quantify the occurrence rate of these steep metallicity gradients in high- $z$  star-forming disks. The existence of a distinct population of galaxies with steep metallicity gradients, if confirmed by future observations constraining their abundance, is a powerful test of galaxy formation models, because this is not predicted by most current theoretical models. Hence, these galaxies with steep metallicity gradients should be the prime targets for new numerical predictions: future *JWST* observations will constrain their properties in great detail, allowing discriminating tests of current theories.

Furthermore, most current numerical simulations are aimed at reproducing present-day Milky Way analogs, surrounded by a dark matter halo with Virial mass  $\sim 10^{12} M_{\odot}$ . It would be useful to have large samples of simulated sub- $L_*$  galaxies ( $M_*$  below  $5 \times 10^9 M_{\odot}$  at  $z \sim 2$ ) in order to investigate how metals are recycled in these less massive systems and provide a more suitable

comparison to our metallicity gradient measurements at high  $z$ . With improvements on both the observational and theoretical sides, we will be able to answer why in these high- $z$  star-forming disk galaxies, the metallicity gradients can be established so early and why they are so steep compared with those found in local analogs.

### 3.A Emission line kinematics from ground-based IFU observations

When available, we use ground based spectroscopic IFU data to investigate the 2D kinematics of the sources for which we obtain metallicity maps from the *HST* grism data. A first set of ground-based data were obtained in 2015 with the instrument *MUSE* on the *VLT*, taken as part of the Director’s Discretionary Time program 294.A-5032 (P.I. Grillo) aimed at assisting with the modeling of SN Refsdal. The *MUSE* pointing is denoted by the green square in Figure 3.1. The observations, data reduction, first results, and applications to the host galaxy of Refsdal and mass modeling of the cluster are described by Grillo et al. (2016); Karman et al. (2016). Five objects in our metallicity gradient sample fall within the *MUSE* pointing, with one on the edge of the FoV. Hence four maps showing complete kinematic structures can be extracted for sources IDs 02389, 02806, 03746, and 04054. A second set of ground based observations were obtained with the instrument *KMOS* also on the *VLT*, as part of our *GLASS* follow-up *KMOS* Large Program 196.A-0778 (P.I. Fontana). Two objects (IDs 05709 and 05968) in our sample were targeted with the deployable IFUs, using the YJ grating. The observations, data reduction, and first results from this program are described by ?. Thanks to lensing magnification, we push for the first time the mass limit of EL kinematic analyses to below  $10^8 M_\odot$  (see Table 3.6).

Kinematic information is valuable for interpreting metallicity gradients and their evolution. We derive gas-phase kinematics for the aforementioned galaxies, by fitting the strongest available emission feature. This is typically C III]  $\lambda\lambda 1907, 1909$ , [O II], or [O III]  $\lambda\lambda 4960, 5008$ . We fit each doublet as a sum of two Gaussian components with equal velocity dispersion ( $\sigma$ ) and redshift, plus a constant continuum level. The fits are weighted by the inverse-variance spectrum estimated from sky regions in the data cubes. Best-fit values for the spatially integrated spectra are given in Table 3.6. The intrinsic velocity dispersion  $\sigma_{\text{int}}$  is calculated by subtracting the instrument

Table 3.6. Measured velocity dispersions using ground-based IFU data.

ID	$\log(M_*/M_\odot)$	Instrument	Emission feature	$\sigma_{\text{obs}}^{\text{b}}(\text{km s}^{-1})$	$\sigma_{\text{int}}^{\text{c}}(\text{km s}^{-1})$
02389	$8.43^{+0.06}_{-0.07}$	<i>MUSE</i>	C III]	$63 \pm 4$	$19^{+11}_{-19}$
02806	$8.72^{+0.19}_{-0.01}$	<i>MUSE</i>	[O II]	$42 \pm 3$	$24 \pm 5$
03746	$8.81^{+0.03}_{-0.01}$	<i>MUSE</i>	[O II]	$74 \pm 9$	$63^{+10}_{-11}$
04054	$9.64^{+0.05}_{-0.01}$	<i>MUSE</i>	[O II]	$68 \pm 6$	$59 \pm 7$
05709	$7.90^{+0.02}_{-0.03}$	<i>KMOS</i>	[O III]	$41 \pm 7$	$17^{+13}_{-17}$
05968	$9.34^{+0.02}_{-0.03}$	<i>KMOS</i>	[O III]	$85 \pm 6$	$76 \pm 7$

<sup>a</sup>Values taken from Table 4.1.

<sup>b</sup>Not corrected for instrument resolution

<sup>c</sup>Corrected intrinsic velocity dispersion

resolution (determined from sky ELs) in quadrature from the observed best-fit velocity dispersion  $\sigma_{\text{obs}}$ . For C III] and [O II] we determine the best-fit doublet ratio of the integrated spectra, while the [O III] doublet ratio is fixed to its intrinsic atomic value. For individual spaxels, we fix the doublet ratios to their integrated values in order to avoid spurious fits. We also spatially smooth each data cube with a 3-pixel (0."6) kernel to improve SNR in the diffuse extended regions. We attempt to fit every spaxel in the smoothed data cube surrounding each object. Bad fits are rejected on the basis of low SNR and unrealistic values (typically requiring  $20 \text{ km s}^{-1} < \sigma_{\text{obs}} < 200 \text{ km s}^{-1}$ , and velocities within  $200 \text{ km s}^{-1}$  of the integrated systemic value). Figure 4.8 shows velocity fields of each source from all spaxels with acceptable EL fits. We discuss the kinematics of individual galaxies in the context of their metallicity gradients and other properties in Section 3.6.2. For purposes of this discussion, we estimate velocity shear  $V_{\text{shear}}$  as the total change in velocity across the kinematic major axis of each source shown in Figure 4.8. Estimates of  $V/\sigma$  in the text refer to  $V_{\text{shear}}$ . This quantity serves as a useful proxy for the gas orbital velocity:  $V_{\text{shear}} = 2V_{\text{max}} \sin i$ , i.e., twice the observed maximum orbital velocity (not corrected for inclination).

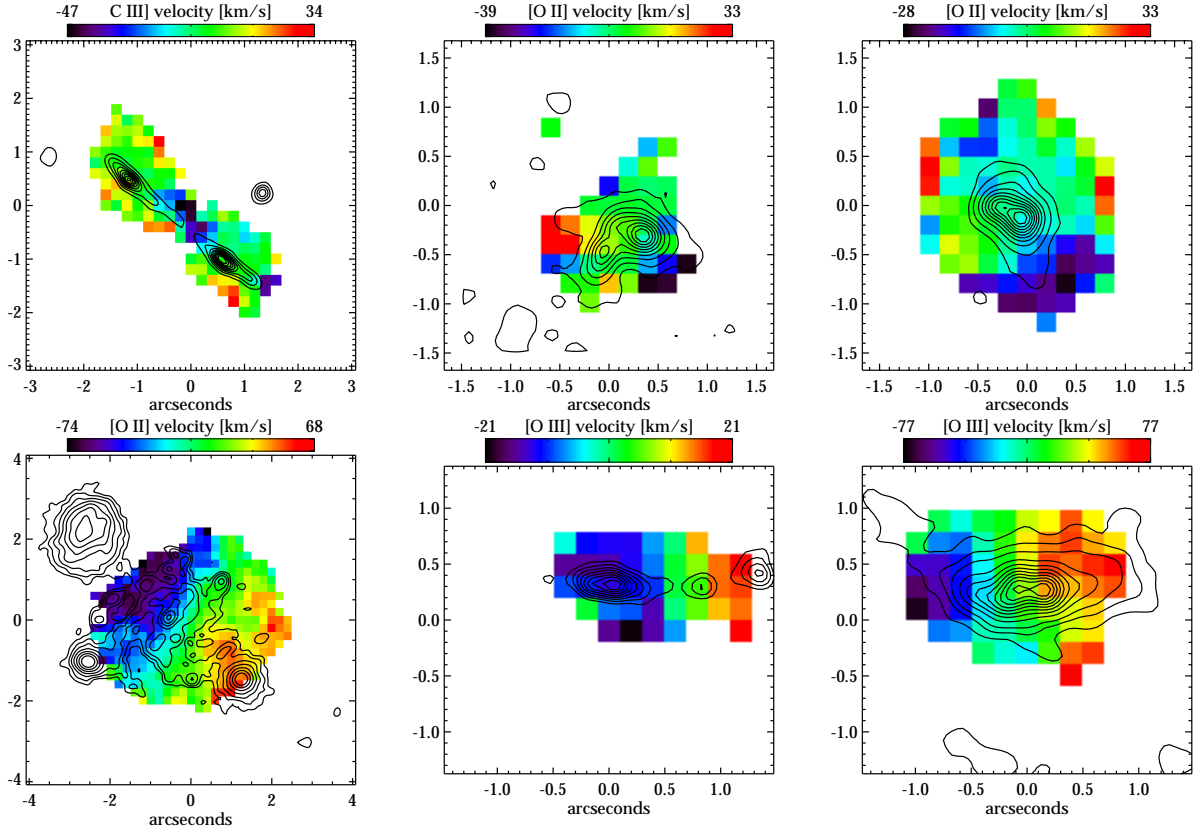


Figure 3.14 Velocity fields derived from integral field spectra. *Top row*: IDs 02389, 02806, 03746 (left to right) observed with *MUSE*. *Bottom row*: ID 04054 observed with *MUSE* (see also Figure 8 in Grillo et al. (2016)) and IDs 05709, 05968 (left to right) observed with *KMOS*. In all cases, the color scale shows EL velocity centroids in each spaxel, with contours showing *HST/ACS I*<sub>814</sub> band continuum. The kinematics map for galaxy 05709 (shown in the lower middle panel) is the first one to date presented for star-forming galaxies with  $M_* \lesssim 10^8 M_\odot$  at  $z \gtrsim 1$ .

Table 3.7. Measured emission line fluxes

ID	$z_{\text{spec}}$	$f_{[\text{S II}]}$	$f_{\text{H}\alpha}$	$f_{[\text{O III}]}$	$f_{\text{H}\beta}$	$f_{\text{H}\gamma}$	$f_{[\text{O II}]}$
01422	2.28	...	...	$18.08 \pm 0.60$	$2.98 \pm 0.61$	$3.60 \pm 0.86$	$8.70 \pm 1.18$
02389	1.89	...	...	$53.24 \pm 0.66$	$7.51 \pm 0.70$	$3.65 \pm 1.25$	$4.65 \pm 2.03$
02607	1.86	...	...	$37.86 \pm 0.65$	$5.59 \pm 0.83$	$< 1.68$	$4.23 \pm 1.94$
02806	1.50	$7.00 \pm 2.39$	$12.75 \pm 0.78$	$30.21 \pm 1.17$	$11.95 \pm 1.22$	$9.29 \pm 2.69$	$5.17 \pm 4.08$
02918	1.78	...	...	$22.96 \pm 1.26$	$8.14 \pm 1.33$	$2.18 \pm 1.70$	$14.71 \pm 3.79$
03746	1.25	$11.69 \pm 0.77$	$97.29 \pm 0.81$	$170.40 \pm 1.39$	$35.00 \pm 2.18$	$14.93 \pm 3.29$	$49.40 \pm 8.37$
04054	1.49	$29.38 \pm 3.14$	$57.26 \pm 1.06$	$17.96 \pm 1.45$	$16.56 \pm 1.53$	$< 5.16$	$34.08 \pm 5.10$
05422	1.97	...	...	$10.79 \pm 0.71$	$4.08 \pm 0.73$	$3.91 \pm 0.88$	$1.82 \pm 1.63$
05709	1.68	...	...	$54.03 \pm 1.06$	$13.17 \pm 1.13$	$8.59 \pm 1.60$	$18.69 \pm 3.54$
05732	1.68	...	...	$35.12 \pm 0.71$	$12.45 \pm 0.73$	$6.57 \pm 1.07$	$22.92 \pm 2.88$
05811	2.31	...	...	$21.09 \pm 0.61$	$3.01 \pm 0.64$	$7.71 \pm 0.93$	$7.31 \pm 1.25$
05968	1.48	$17.19 \pm 1.36$	$68.13 \pm 0.81$	$59.08 \pm 1.09$	$21.08 \pm 1.19$	$21.36 \pm 3.10$	$55.99 \pm 3.95$
07058	1.79	...	...	$12.87 \pm 0.96$	$3.59 \pm 0.91$	$3.96 \pm 1.25$	$8.73 \pm 2.77$
07255 <sup>a</sup>	1.27	$11.70 \pm 1.21$	$37.19 \pm 0.92$	$41.81 \pm 2.59$	$21.85 \pm 4.16$	...	$11.84 \pm 9.28$

Note. — The fluxes are observed values in unit of  $10^{-17} \text{erg s}^{-1} \text{cm}^{-2}$ , not accounted for dust extinction nor lensing magnification. The flux error bars denote  $1-\sigma$  measurement uncertainties. The  $2-\sigma$  upper limit is given for undetected lines. Only sources at  $z \leq 1.5$  have H $\alpha$  and [S II] line flux measurements due to the grism spectral coverage.

<sup>a</sup>The missing of H $\gamma$  flux for this source is due to grism defect.

### 3.2 Emission line flux measurements from *HST* grisms

After a careful selection, we compiled a list of sources most promising for the spatially resolved spectroscopic analysis in the redshift range of  $z \in [1.2, 2.3]$ . For instance, we show the *GLASS* spectra of two of these sources (one at  $z \leq 1.5$  with H $\alpha$  covered and the other at  $z \geq 1.5$  without H $\alpha$ ) in Figures 3.15 and 3.16. The SN Refsdal follow-up exposures, albeit only covering G141, have better SNRs compared with the spectra shown here by a factor of  $\sqrt{15/2}$  at each PA. Combining all the available grism exposures, we measured the EL fluxes on all our sources and presented the measurements in Table 3.7.

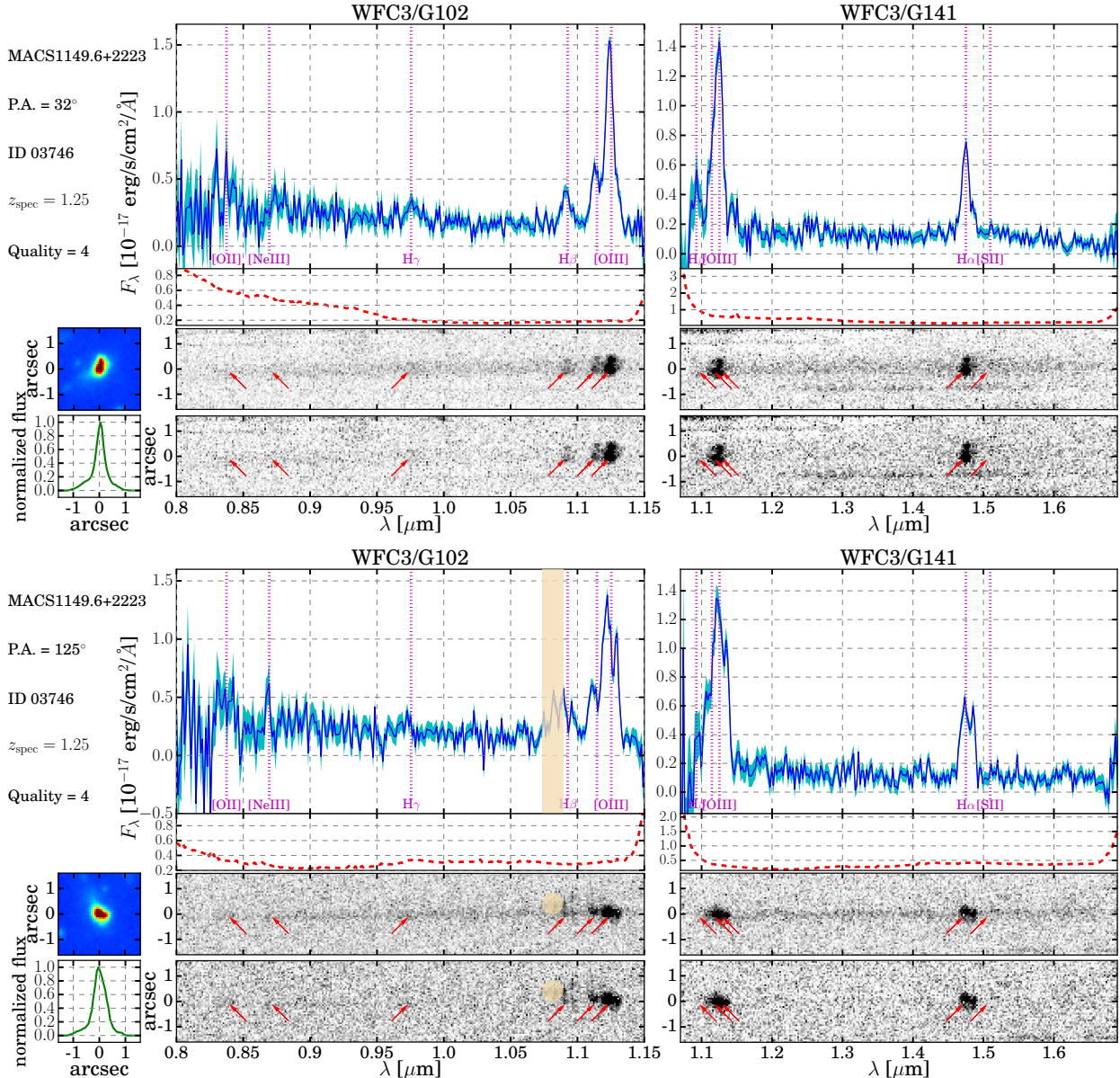


Figure 3.15 The *HST* grism spectra for one exemplary source in our sample, ID 03746, seen at the two *GLASS* PAs displayed in the two sub-figures respectively. The H $\alpha$  EL of this galaxy is covered by G141 because of its redshift  $z = 1.25$ . In each sub-figure, the two small square panels on the left refer to the 2D postage stamp (top) and the 1D collapsed image (bottom). The 2D postage stamp is created from the *HFF*  $H_{160}$ -band co-adds. The eight panels in the middle and right rows show, from top to bottom, the contamination subtracted 1D spectra (where flux is represented by the blue solid line and the noise level by the cyan shaded band), the 1D contamination model in red dashed line, the contamination subtracted 2D spectra and the 2D spectra having source continuum further removed. In the 1D and 2D spectra, the locations of emission lines are highlighted by vertical dotted lines in magenta and arrows in red, respectively, and the wheat colored patches cover contamination model defects.

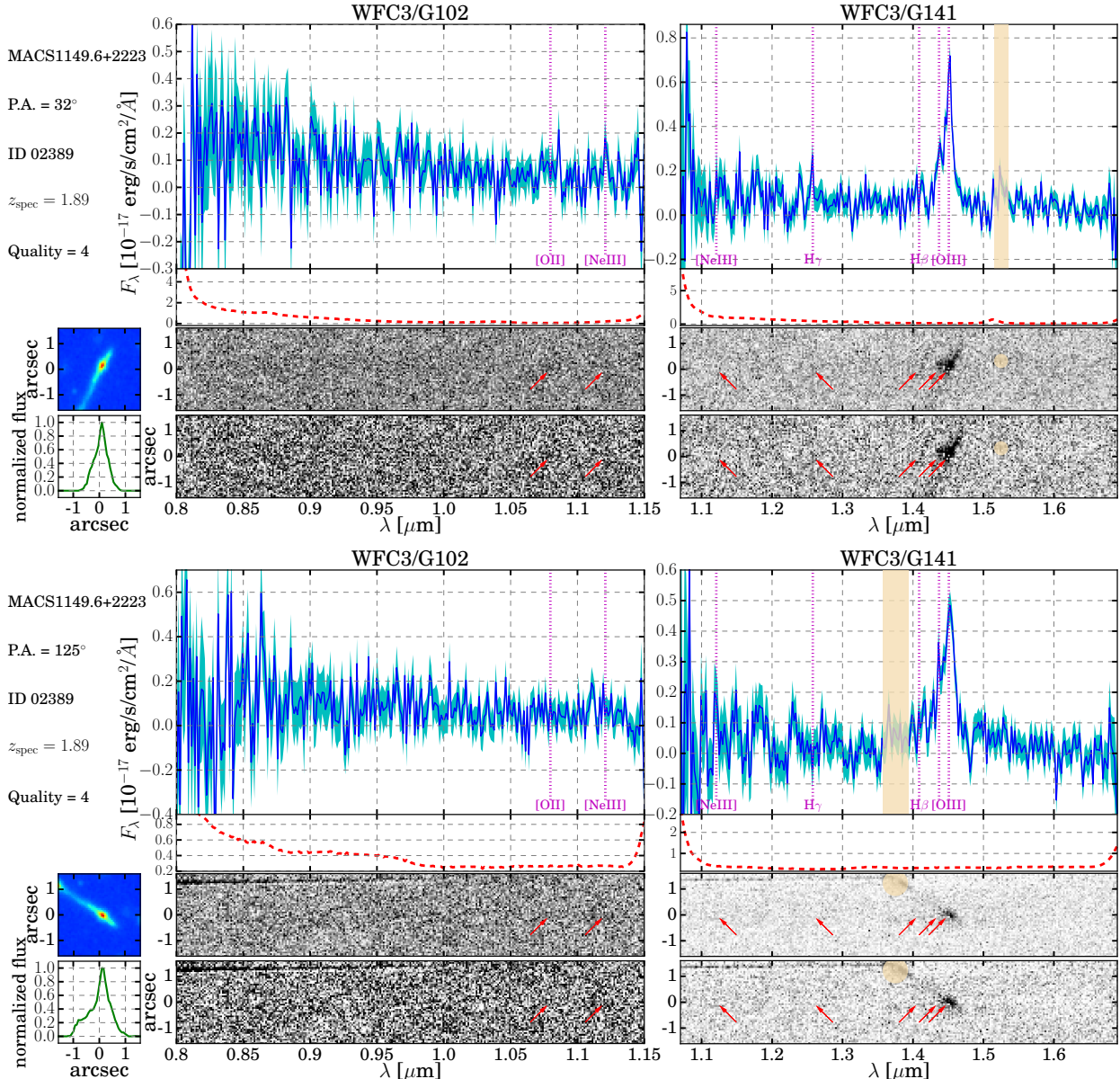


Figure 3.16 Same as Figure 3.15, except that source ID 02389 is shown. The H $\alpha$  EL of this galaxy has shifted out of the grism coverage because of its redshift  $z = 1.89$ .

# CHAPTER 4

## Discovery of Strongly Inverted Metallicity Gradients in Dwarf Galaxies at $z \sim 2$

### 4.1 Introduction

Galaxy formation models require inflows and outflows of gas to regulate star formation (Finlator & Davé, 2008; Recchi et al., 2008; Bouche et al., 2010; Davé et al., 2012; Dayal et al., 2013; Dekel et al., 2013; Lilly et al., 2013; Dekel & Mandelker, 2014; Peng & Maiolino, 2014; Pipino et al., 2014), yet this “baryon cycle” is not quantitatively understood. The interstellar medium (ISM) oxygen abundance (i.e. metallicity) and its spatial distribution is fortunately a key observational probe of this process (Tremonti et al., 2004; Erb et al., 2006; Maiolino et al., 2008; Bresolin et al., 2009; Mannucci et al., 2010, 2011; Zahid et al., 2011; Yates et al., 2012; Zahid et al., 2012b; Henry et al., 2013a; Jones et al., 2013; Sanchez et al., 2014; Zahid et al., 2014; Bresolin & Kennicutt, 2015; Ho et al., 2015; Sanders et al., 2015; Strom et al., 2016). “Inside-out” galaxy growth implies that initially steep radial gradients of metallicity flatten at later times (higher masses) as disks grow larger, yet other scenarios suggest metallicities are initially well mixed by strong galactic feedback, and then locked into negative gradients as winds lose the power to disrupt massive gas disks (Prantzos & Boissier, 2000; Hou et al., 2000; Mollá & Díaz, 2005; Kobayashi & Nakasato, 2011; Few et al., 2012; Pilkington et al., 2012; Gibson et al., 2013; Ma et al., 2017). What is common between these scenarios is that none of them predict the existence of a steep positive (i.e. inverted) radial gradient such that metallicity increases with galacto-centric radius.

However, there is growing evidence of such phenomenon in both the local and distant Universe (Cresci et al., 2010; Queyrel et al., 2012; Stott et al., 2014; Troncoso et al., 2014; Sanchez et al., 2014; Pérez-Montero et al., 2016; Wuyts et al., 2016; Belfiore et al., 2017; Carton et al., 2018).

The key reason for local galaxies possessing inverted gradients is gas re-distribution by tidal force in strongly interacting systems (Kewley et al., 2006a, 2010; Rupke et al., 2010; Rich et al., 2012; Torrey et al., 2012). At high redshifts, inverted gradients are often attributed to the inflows of metal-poor gas from the filaments of cosmic web, infalling directly onto galaxy centers, diluting central metallicities and hence creating positive gradients (Cresci et al., 2010; Mott et al., 2013). Given most of the high- $z$  observations are conducted from the ground with natural seeing, the targets are usually super- $L_*$  galaxies with stellar mass ( $M_*$ )  $\gtrsim 10^{10} M_\odot$  (see e.g., Troncoso et al., 2014).

These high- $z$  inverted gradients are in concert with the “cold-mode” gas accretion which has long been recognized to play a crucial role in galaxies getting their baryonic mass supply (Birnboim & Dekel, 2003; Kereš et al., 2005; Dekel & Birnboim, 2006; Dekel et al., 2009b; Kereš et al., 2009). Instead of being shock-heated to dark matter (DM) halo virial temperature ( $\sim 10^6$ K for a  $M_h \sim 10^{12} M_\odot$  halo) and then radiate away the thermal energy to condense and form stars (vis-á-vis “hot-mode” accretion), gas streams can remain relatively cold ( $< 10^5$ K) while being steadily accreted onto galaxy disks<sup>1</sup>. This cold accretion dominates the growth of galaxies forming in low-mass halos irrespective of redshifts since a hot permeating halo of virialized gas can only manifest in halos above  $2\text{-}3 \times 10^{11} M_\odot$ , at  $z \lesssim 2$  (Birnboim & Dekel, 2003; Kereš et al., 2005).

A question thus arises: if cold-mode gas accretion dominates in low-mass systems (with  $M_*$  less than a few  $10^{10} M_\odot$ ) and is thought to lead to inverted gradients under the condition that the incoming gas streams are centrally directed, can we observe this phenomenon in dwarf galaxies (with  $M_* \lesssim 10^9$ ) at high redshifts? The answer is not straightforward since the effect of ejective feedback (e.g. galactic winds driven by supernovae) is more pronounced in lower mass galaxies, given their shallower gravitational potential wells and higher specific star-formation rate (sSFR) (see e.g. Hopkins et al., 2014; Vogelsberger et al., 2014). On one hand, galactic winds can bring about kinematic turbulence that prevents a smooth accretion of filamentary gas streams directly onto galaxy center, resulting in rapid formation of in-situ clumps (Dekel et al., 2009a). On the other hand, metal-enriched outflows triggered by these powerful winds can help remove stellar nucleosynthe-

---

<sup>1</sup>Note however that cold-mode accretion does not necessarily enforce that gas has to reach galaxy center first given the large dynamic range of the scales of galaxy disks ( $\sim$ kpc) and cosmic web ( $\sim$ Mpc).

sis yields from galaxy center (Tremonti et al., 2004; Erb et al., 2006). Therefore the existence of strongly inverted gradients in dwarf galaxies at high redshifts, if any, presents a sensitive test of the relative strength of feedback-induced radial gas flows, in the early phase of the disk mass assembly process. There have not been any attempts to investigate such existence, primarily due to the small sizes of these dwarf galaxies and sub-kiloparsec (sub-kpc) spatial resolution required to yield accurate gradient measurements (Yuan et al., 2013). In this work, we present the first effort to secure two robustly measured inverted metallicity gradients in  $z \sim 2$  star-forming dwarf galaxies from the Hubble Space Telescope (*HST*) near-infrared (NIR) grism slitless spectroscopy, aided with galaxy cluster lensing magnification. The details of data and sample galaxies are presented in Section 4.2. We describe our analysis methods alongside main results in Section 4.3, and conclude in Section 4.4. Throughout this Chapter, a flat  $\Lambda$ CDM cosmology is assumed.

## 4.2 Data and Galaxy Sample

The two galaxies with exceptional inverted gradients are selected from a comprehensive study of  $\sim 300$  galaxies with metallicity measurements at  $1.2 \lesssim z \lesssim 2.3$  (Wang et al. 2017; Wang et al. in prep.). Before we discuss the two systems in detail in Section 4.2.4, we give for convenience a brief summary of the spectroscopic data (Section 4.2.1), a concise description of the data reduction procedure (Section 4.2.2), and the ancillary imaging used in this work (Section 4.2.3).

### 4.2.1 *HST* Grism Slitless Spectroscopy

We use the diffraction-limited spatially resolved slitless spectroscopy, obtained using the *HST* wide-field camera 3 (WFC3) NIR grisms (G102 and G141), acquired by the Grism Lens-Amplified Survey from Space (*GLASS*, Schmidt et al., 2014; Treu et al., 2015b). *GLASS* observes the distant Universe through 10 massive galaxy clusters as natural telescopes, exposing 10 orbits of G102 (0.8-1.15 $\mu$ m,  $R \sim 210$ ) and 4 orbits of G141 (1.1-1.7 $\mu$ m,  $R \sim 130$ ) per sightline. This amounts to a sum of  $\sim 22$  kiloseconds of G102 and  $\sim 9$  kiloseconds of G141, as well as  $\sim 7$  kiloseconds of F140W+F105W direct imaging for astrometric alignment and wavelength/flux calibrations per field. These exposures distributed over two separate pointings per cluster with nearly orthogonal

orientations, designed to help disentangle spectral contamination from neighboring objects. So for each source, two sets of G102+G141 spectrum are obtained, covering an uninterrupted wavelength range of  $0.8\text{--}1.7\mu\text{m}$  with almost unchanging sensitivity, reaching a  $1\sigma$  surface brightness of  $3 \times 10^{-16}\text{ erg s}^{-1}\text{ cm}^{-2}\text{ arcsec}^{-2}$  across the entire spectral range. The *GLASS* collaboration has made the catalogs of their redshift identifications in the 10 fields, based on visual inspections of emission line (EL) features, publicly available at <https://archive.stsci.edu/prepds/glass/>.

#### 4.2.2 Grism Data Reduction

To explore the chemical properties of galaxies at the peak epoch of cosmic chemical enrichment, we select from these catalogs, a parent sample consisting of  $\sim 300$  galaxies with secure redshifts (i.e. redshift quality  $\geq 3$  in the publicly available catalogs as described by Treu et al. (2015b)) in the range of  $1.2 \lesssim z \lesssim 2.3$ . This range is chosen for the detection of multiple nebular ELs<sup>2</sup> — in particular the Balmer lines, [O III], and [O II] — enabling the metallicity measurements, as in our earlier work (Jones et al., 2015b; Wang et al., 2017). The *GLASS* data for these  $\sim 300$  galaxies are reduced using the Grism Redshift and Line analysis (GRZILI<sup>3</sup>; G. Brammer et al. in prep) software. GRZILI presents an end-to-end processing of the paired grism and direct exposures. The procedure includes five steps: 1) pre-processing of the raw grism exposures, 2) full field-of-view (FoV) grism model construction, 3) 1D/2D spectrum extraction, and 4) solving for best-fit redshift from spectral template fitting (see Appendix 4.B for more details), 5) refining full FoV grism model and extractions of source 1D/2D spectrum and EL stamps. In step 1), the pre-processing consists of hot-pixel/persistence masking, cosmic ray flagging, flat fielding, astrometric alignment, sky background subtraction, and extraction of visit-level source catalogs and segmentation maps. In step 5), the EL stamps are drizzled onto a grid with a pixel scale of  $0.^{\prime\prime}06$ , Nyquist sampling the WFC3 point spread function (PSF). We apply an additional step on the GRZILI output products to obtain pure 2D maps of [O III]  $\lambda 5008$  and H $\beta$ , clean from the partial contamination of [O III]  $\lambda 4960$ , due to the limited grism spectral resolution and extended source morphology. Our procedure properly

---

<sup>2</sup>The names of the forbidden lines are simplified as usual, if presented without wavelength numbers: [O III]  $\lambda 5008 :=$  [O III], [O II]  $\lambda\lambda 3726, 3729 :=$  [O II].

<sup>3</sup><https://github.com/gbrammer/grizli/>

combines EL maps at multiple orientations, preserving angular resolution and accounting for EL blending.

#### 4.2.3 *HST* Imaging: Estimating $M_*$ from SED Fitting

In addition to the deep NIR spectroscopy, there exists a wealth of ancillary imaging data with equally high spatial resolution on the 10 *GLASS* fields, which encompass all 6 Hubble Frontier Field (*HFF*, Lotz et al., 2016) clusters and 4 from the Cluster Lensing And Supernova Survey with Hubble (*CLASH*, Postman et al., 2012b). These broad-band photometry, covering observed wavelengths of  $\sim$ 0.4-1.7  $\mu$ m, can help constrain stellar population properties (especially  $M_*$ ) of our selected  $\sim$ 300 galaxies at sufficient confidence. We use the images sampled with 0. $''$ 06 pixel size, and apply kernel convolutions to match the angular resolution of all images to that of the F160W filter. We subtract contamination from intracluster light using established procedures (Morishita et al., 2016). Since our targets have rest-frame optical ELs with high equivalent widths (EWs), we subtract EL contributions from the broad-band photometry to obtain the stellar continuum flux. We then fit the spectral energy distribution (SED) with the Bruzual & Charlot (2003) (BC03) stellar population synthesis models using the software FAST (Kriek et al., 2009a). We assume a Chabrier (2003) initial mass function (IMF), constant star formation history, stellar dust attenuation in the range  $A_V^S=0\text{-}4$  with a Calzetti et al. (2000) extinction curve, and age ranging from 5 Myr to the Hubble time at the redshifts of our targets. Stellar metallicity is fixed to 1/5 solar and we verify that this assumption affects the results by no more than  $<0.05$  dex on  $M_*$ .

#### 4.2.4 Two Dwarf Galaxies with Strongly Inverted Metallicity Gradients

Out of the parent sample of  $\sim$ 300 galaxies, we are able to secure accurate (i.e. at sub-kpc resolution) radial metallicity gradients on 81 sources with suitable spatial extent and high signal-to-noise ratio (SNR) nebular emission. These extended sources typically have half-light radii  $R_{50} \gtrsim 0. $''$ 15$ . In a range of  $7 \lesssim \log(M_*/M_\odot) \lesssim 10$  given by the analyses in Section 4.2.3, our sample probes much lower  $M_*$  than other surveys of spatially resolved line emission at similar redshifts (Wuyts et al., 2016; Förster Schreiber et al., 2018), thanks to the enhanced resolution from lensing magni-

fication, and high sensitivity of the *HST* NIR grisms. We have previously described the properties of 10 galaxies in our sample from the cluster MACS1149.6+2223 (Wang et al., 2017); results for the full sample are in preparation.

In most cases, we find that metallicity gradients are approximately flat (i.e. consistent with zero given the typical  $\sigma = 0.03 \text{ dex kpc}^{-1}$ ) or slightly negative. A minority (10/81) of our sample shows positive (i.e. “inverted”) gradients, which are of interest as they pose a challenge to standard galactic chemical evolution models (e.g., Mollá & Díaz, 2005; Mollá et al., 2018). We have selected the two best examples with strongly inverted gradients for further study in this Chapter. The two sources are ID03751 ( $z = 1.96$ ,  $M_* = 1.12 \times 10^9 M_\odot$ ) in the prime field of Abell 370, and ID01203 ( $z = 1.65$ ,  $M_* = 2.55 \times 10^9 M_\odot$ ) in the prime field of MACS0744.9+3927.

Table 4.1 presents their properties. Figure 4.1 shows the color-composite *HST* images of these two galaxies and their 2D spatially resolved maps of the nebular ELs. Remarkably, they have  $M_*$  considerably lower — by one order of magnitude — than those of previous positive gradients measured at similar redshifts (see e.g., Cresci et al., 2010; Queyrel et al., 2012; Stott et al., 2014; Troncoso et al., 2014). To complement the low dispersion grism spectra, we have obtained adaptive optics (AO) assisted kinematic data on our sources using ground-based integral-field unit (IFU) spectrograph when available. The observation of source ID01203 is presented in Appendix 4.A. The full data analysis is presented in Hirtenstein et al. (2018) in detail.

### 4.3 Methods and Results

In this section, we describe our key methods used to derive radial metallicity gradients (Section 4.3.1), 2D maps of SFR, average stellar population age, and gas fraction (Section 4.3.2), as well as spatial distributions of net gaseous outflow rate and mass loading factor (Section 4.3.3). The main results are presented alongside the corresponding methods.

Table 4.1. Measured quantities of the two dwarf galaxies

ID	03751	01203
cluster	Abell 370	MACS0744.9+3927
R.A. (deg.)	39.977361	116.197585
Decl. (deg.)	-1.591636	39.456698
$z_{\text{spec}}$	1.96	1.65
$\mu^{\text{a}}$	$6.35^{+0.40}_{-0.58}$	$2.25^{+0.04}_{-0.03}$
Observed emission line fluxes		
$f_{[\text{O III}]} [10^{-17} \text{erg s}^{-1} \text{cm}^{-2}]$	$111.41 \pm 0.84$	$117.66 \pm 1.17$
$f_{\text{H}\beta} [10^{-17} \text{erg s}^{-1} \text{cm}^{-2}]$	$17.68 \pm 0.68$	$17.46 \pm 1.06$
$f_{[\text{O II}]} [10^{-17} \text{erg s}^{-1} \text{cm}^{-2}]$	$29.57 \pm 0.51$	$34.00 \pm 0.96$
$f_{\text{H}\gamma} [10^{-17} \text{erg s}^{-1} \text{cm}^{-2}]$	$7.21 \pm 0.67$	$7.06 \pm 1.00$
Restframe equivalent widths		
$\text{EW}_{[\text{O III}]} [\text{\AA}]$	$466.22 \pm 3.52$	$797.14 \pm 7.95$
$\text{EW}_{\text{H}\beta} [\text{\AA}]$	$73.98 \pm 2.83$	$118.29 \pm 7.18$
$\text{EW}_{[\text{O II}]} [\text{\AA}]$	$79.14 \pm 1.37$	$123.91 \pm 3.50$
$\text{EW}_{\text{H}\gamma} [\text{\AA}]$	$30.18 \pm 2.82$	$25.73 \pm 3.68$
Estimated physical parameters		
$M_* [10^9 M_\odot]^{\text{b}}$	$1.12^{+0.14}_{-0.14}$	$2.55^{+0.04}_{-0.04}$
$12 + \log(\text{O/H})^{\text{c}}$	$8.08^{+0.11}_{-0.12}$	$8.10^{+0.11}_{-0.11}$
$\Delta \log(\text{O/H})/\Delta r [\text{dex/kpc}]$	$0.122 \pm 0.008$	$0.111 \pm 0.017$
$\text{SFR} [M_\odot \text{ yr}^{-1}]^{\text{b}}$	$25.39 \pm 2.19$	$48.86 \pm 3.04$
$A_V$	$0.84 \pm 0.13$	$0.90 \pm 0.16$
$t_{\text{age}} [10^7 \text{ yrs}]$	$7.93 \pm 0.88$	$3.98 \pm 0.51$
$M_{\text{gas}} [10^9 M_\odot]^{\text{b}}$	$4.07 \pm 1.27$	$23.85 \pm 7.33$
$f_{\text{gas}}^{\text{d}}$	$0.56 \pm 0.20$	$0.86 \pm 0.13$
$B/T^{\text{e}}$	$0.36 \pm 0.14$	$0.14 \pm 0.07$
$R_{\text{eff}} [\text{kpc}]^{\text{b}}$	$1.53 \pm 0.12$	$1.66 \pm 0.17$
Gas kinematics		
$\sigma [\text{km/s}]$	... f	$73 \pm 3$
$V/\sigma$	... f	$1.3 \pm 0.1$
Measurements of the gaseous outflows at the central 1kpc		
$\lambda$	$49.9 \pm 14.7$	$52.1 \pm 20.2$
$\Psi [M_\odot \text{ yr}^{-1}]$	$311.3 \pm 96.2$	$1700.9 \pm 681.9$

<sup>a</sup>The magnification estimates are obtained from the SHARON & JOHNSON version 4 model of Abell 370 (Johnson et al., 2014b) and the Zitrin PIEMD+eNFW version 2 model of MACS0744.9+3927 (Zitrin et al., 2015), for the two sources respectively.

<sup>b</sup>Values presented here are corrected for lensing magnification.

<sup>c</sup>Values represent global metallicity, inferred from integrated line fluxes.

<sup>d</sup>Here the gas fraction is calculated according to Eq. 4.3.

<sup>e</sup>In the bulge-disk decomposition, we fix the Sérsic index  $n = 4$ .

<sup>f</sup>For the cluster,  $V/\sigma = 1.3$ ; for the dwarf,  $V/\sigma = 1.6$ .

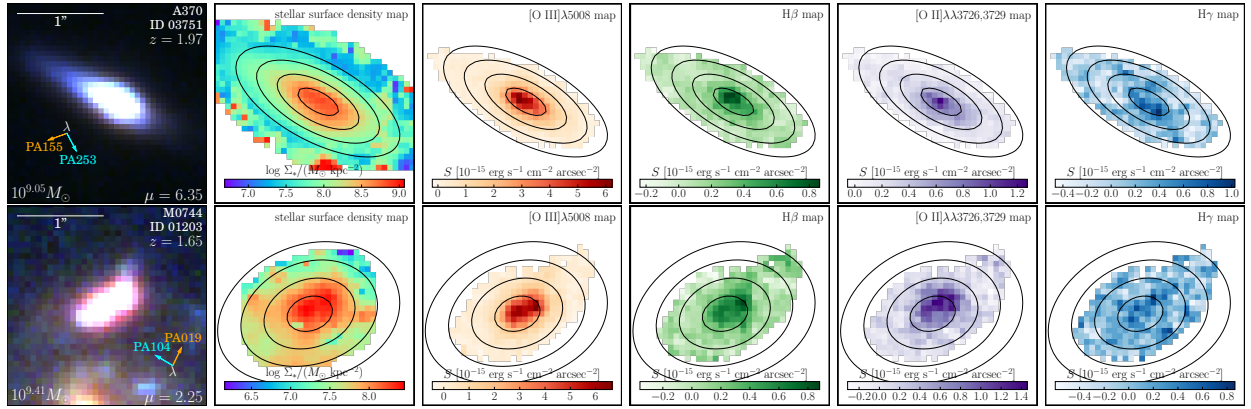


Figure 4.1 Two star-forming dwarf galaxies at  $z \sim 2$  displaying unusually strong inverted metallicity gradients, securely determined at sub-kpc spatial resolution. For each source we show, from left to right: color composite image (created from *HST* broad-band photometry), stellar surface density map (obtained from SED fitting to *HST* photometry), and surface brightness map of ELs [O III], H $\beta$ , [O II], and H $\gamma$ . The black contours overlaid represent the source plane de-projected galactocentric radii with 1 kpc interval. The two light-dispersion directions for the grism exposures are denoted by the orange and cyan arrows (see Figures 4.9 and 4.10 for the corresponding spectra). The spatial extent and orientation are unchanged for the two sources in all 2D stamps throughout. North is up and east is to the left.

### 4.3.1 Radial Metallicity Gradients

Since we infer metallicity from strong line flux ratio diagnostics, calibrated by either empirical methods, or theoretical methods, or a hybrid of both, it is essential to make sure that the line emission is not contaminated by active galactic nucleus (AGN) ionization or shock excitation. As shown in Figure 4.2, we verify that our targets have a low probability (<%10) of being classified as AGNs according to the mass-excitation diagram (Juneau et al., 2014). Their individual radial annuli also have excitation and ionization states, as revealed in their loci in the  $f_{[\text{O III}]} / f_{\text{H}\beta}$  versus  $f_{[\text{O II}]} / f_{\text{H}\beta}$  diagram and the  $\text{O}_{32}(=f_{[\text{O III}]} / f_{[\text{O II}]})$  versus  $\text{R}_{23}(=(f_{[\text{O III}]} \text{ 5008} + f_{[\text{O III}]} \text{ 4960} + f_{[\text{O II}]})) / f_{\text{H}\beta}$  diagram, compatible with HII regions (Lamareille et al., 2004; Rodrigues et al., 2012; Jones et al., 2015a). In the source ID01203 covered by our follow-up *OSIRIS* observations (see Appendix 4.A), its integrated  $f_{[\text{N II}]} / f_{\text{H}\alpha}$  ( $\lesssim 0.1$  at  $3\sigma$ ) also shows no sign of AGN or shocked gas emission.

Our measurements of radial metallicity gradients largely follow the procedures described in our previous work (Wang et al., 2017). We use a Bayesian approach to jointly infer metallicity ( $12 + \log(\text{O/H})$ ), nebular dust extinction ( $A_V^N$ ), and de-reddened  $\text{H}\beta$  flux ( $f_{\text{H}\beta}$ ). We explore the parameter space using the Markov Chain Monte Carlo sampler EMCEE (Foreman-Mackey et al., 2013). The likelihood function is given by  $L \propto \exp(-\chi^2/2)$  with

$$\chi^2 = \sum_i \frac{(f_{\text{EL}_i} - R_i \cdot f_{\text{H}\beta})^2}{(\sigma_{\text{EL}_i})^2 + (f_{\text{H}\beta})^2 \cdot (\sigma_{R_i})^2}, \quad (4.1)$$

where  $\text{EL}_i$  corresponds to each available EL: [O III],  $\text{H}\beta$ , [O II], and  $\text{H}\gamma$ .  $f_{\text{EL}_i}$  and  $\sigma_{\text{EL}_i}$  are the flux and uncertainty of  $\text{EL}_i$ .  $R_i$  is the flux ratio between  $\text{EL}_i$  and  $\text{H}\beta$ , with  $\sigma_{R_i}$  being the intrinsic scatter at fixed physical properties. In the case  $\text{EL}_i = \text{H}\gamma$ ,  $R_i$  is given by the Balmer decrement  $f_{\text{H}\gamma} / f_{\text{H}\beta} = 0.47$ . For  $\text{EL}_i \in \{\text{[O II]}, \text{[O III]}\}$ ,  $R_i$  and  $\sigma_{R_i}$  are given by the strong line metallicity diagnostics ( $f_{[\text{O III}]} / f_{\text{H}\beta}$  and  $f_{[\text{O II}]} / f_{\text{H}\beta}$ ) calibrated by Maiolino et al. (2008). The Maiolino et al. (2008) calibrations combine the direct electron temperature measurements from the Sloan Digital Sky Survey in the low-metallicity ( $12 + \log(\text{O/H}) < 8.35$ ) branch (Nagao et al., 2006) and the photoionization model predictions in the high-metallicity ( $12 + \log(\text{O/H}) > 8.35$ ) branch (Kewley & Dopita, 2002), providing a continuous and coherent recipe over a wide metallicity range. We also adopt the empirical calibrations by Curti et al. (2016) based on metallicities given by pure electron

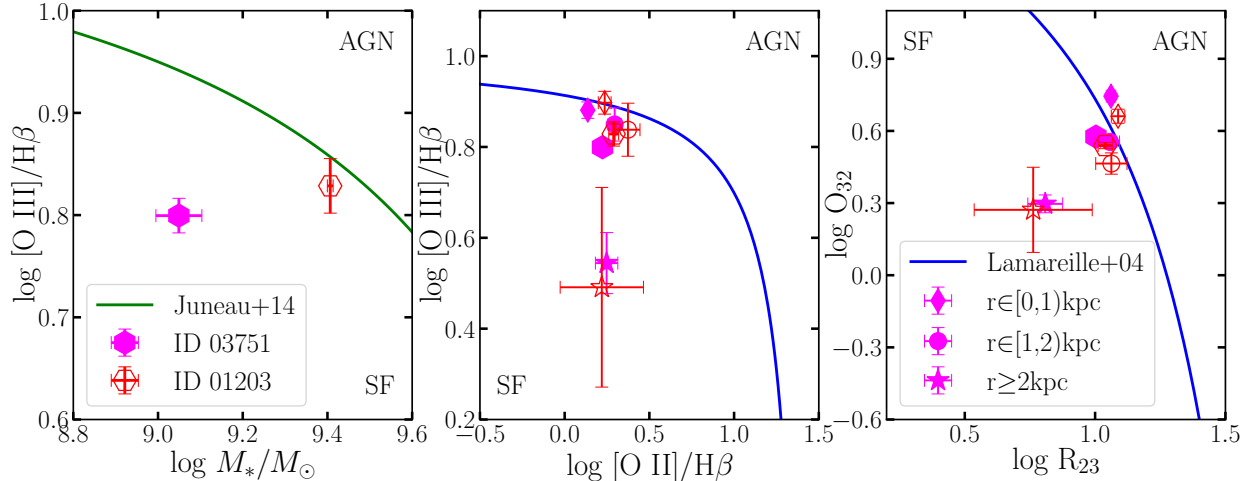


Figure 4.2 The diagnostic diagrams for our sources. On the left, we show the mass-excitation diagram with the demarcation scheme between the loci of AGNs and star-forming (SF) galaxies proposed in Juneau et al. (2014). Our galaxies can be safely classified as the latter. In the middle and right panels, we show the “blue” diagrams with the boundaries described by Lamareille et al. (2004). Following the conventions in the left panel, we use filled symbols to represent measurements for ID03751 whilst empty ones for ID01203. Furthermore, the hexagons correspond to the measurements integrated over the entire galaxies (as in the left panel), whereas the other symbols denote results obtained in different radial annuli, as explained in the legend of the right panel. Again we see that the contamination from AGN ionization is minimum for our sources, even in the central regions. The two galaxies presented in this work share similar evolutionary trends in their excitation and ionization states with respect to galacto-centric radius, in addition to the strongly inverted radial gradient in metallicity (see Figure 4.3).

temperature method, and verified that there is no significant change in our gradient measurements. The same process is applied to both galaxy-integrated fluxes and to fluxes measured at individual spatial pixels (spaxels).

To obtain the correct intrinsic de-projected distance scale for each spaxel, we conducted full source plane morphological reconstruction of our sources. We ray-trace the image of each galaxy to its source plane using up-to-date lens models for each cluster: the macroscopic model of SHARON & JOHNSON version 4 for Abell 370 (Johnson et al., 2014b), and the ZITRIN version 2 model for MACS0744.9+3927 (Zitrin et al., 2015). Other lens models are available for these clusters (e.g. Diego et al., 2016; Strait et al., 2018) and we verified that the morphology of each source is robust to the choice of model.

For each source, we fit the SED of individual spaxels using the procedures described in Section 4.2, obtaining the 2D stellar surface density ( $\Sigma_*$ ) map shown in Figure 4.1. Then we reconstruct  $\Sigma_*$  map in the source plane by de-lensing the surface densities according to the deflection field given by the macroscopic lens models. To minimize the stochasticity in stellar population synthesis (Fouesneau & Lançon, 2010; Eldridge, 2012), we make sure that the source plane resolution elements during this reconstruction contain enough stellar masses ( $\gtrsim 10^5 M_\odot$ ) to be representative of complete stellar populations. The axis ratios, inclinations, and major axis orientations are determined from an elliptical Gaussian fit. This procedure provides the intrinsic lensing-corrected morphology, and in particular, the galacto-centric radius at each point of the observed images. The radial scale as black contours in all figures is used to establish the absolute metallicity gradient slope (i.e., in units of dex per proper kpc). From the source reconstructed morphology, we measure their effective radius where the enclosed mass reaches half the total mass of the source. The measurements are represented by  $R_{\text{eff}}$  in Table 4.1.

Figure 4.3 shows the 2D maps of metallicity of our selected two dwarf galaxies at  $z \sim 2$ . Clearly, the outskirts of our galaxies display highly elevated oxygen abundance ratios. In particular, the outskirts of ID03751 are more metal enriched by  $\sim 0.4$  dex (i.e. a factor of 2.5) than its center, and more metal-rich by  $\sim 0.2$  dex than the value inferred based on the fundamental metallicity relation (FMR) given its integrated  $M_*$  Mannucci et al. (2010, 2011). Note that our metallicity measurements extend beyond the source effective radius to cover large enough dynamic range, but

not into the region where a plateau/flattening in metallicity (i.e., at  $R > 2 - 2.5R_{\text{eff}}$ , Sanchez et al., 2014; Sánchez-Menguiano et al., 2016; Mollá et al., 2018) is likely to occur, which might bias the overall gradient determination. For the first time, we are able to detect strongly inverted metallicity gradients in  $z \sim 2$  dwarf galaxies at unprecedently high confidence:  $0.122 \pm 0.008$  dex/kpc for ID03751 ( $\sim 15.2\sigma$ ), and  $0.111 \pm 0.017$  dex/kpc for ID01203 ( $\sim 6.5\sigma$ ).

The question is thus what caused these dwarf galaxies to have such strongly inverted gradients? First of all, our sources show no evidence of major mergers, supported by their regular morphology displayed in the 2D maps of  $M_*$  and EL surface brightness in Figure 4.1. For source ID01203 with *OSIRIS* data, this statement is further strengthened by the kinematic evidence of disk orderly rotation. Secondly, the fact that the outskirts of our sources show elevated metallicity as compared to the FMR expectations indicates that there are more metals in the outer regions than could be produced by the stars in those regions. This discourages any explanations involving solely low-metallicity gas inflows, not limited to those induced by mergers. In the subsequent sections, we thus gather all available pieces of observational evidence to further investigate the possible cause.

### 4.3.2 SFR, Stellar Population Age, and Gas Fraction

To understand the cause of the strongly inverted metallicity gradients seen in these dwarf galaxies, we combine their EL maps with *HST* broad-band photometry to derive 2D maps of  $M_*$ , SFR, stellar population age, and gas surface density for each galaxy. The SFR is derived from extinction-corrected Balmer emission line flux. Maps of H $\beta$  and H $\gamma$  emission are shown in Figure 4.1. The H $\beta$ /H $\gamma$  line ratio provides a measurement of nebular extinction although it is limited by the modest signal-to-noise of H $\gamma$ . We obtain more precise results from *HST* photometry, by converting  $B_{435} - I_{814}$  color maps to spatial distributions of stellar reddening  $E_S(B - V)$  (Daddi et al., 2004). Nebular reddening  $E_N(B - V)$  is then calculated following Valentino et al. (2017). The nebular reddening maps of both our galaxies show lower dust attenuation in centers than that in outskirts, consistent with the inverted metallicity gradients shown in Figure 4.3.

We calculate extinction in H $\beta$  adopting a Cardelli et al. (1989) dust extinction law (with  $R_V = 3.1$ ) and assuming Case B recombination with Balmer ratios appropriate for fiducial HII region

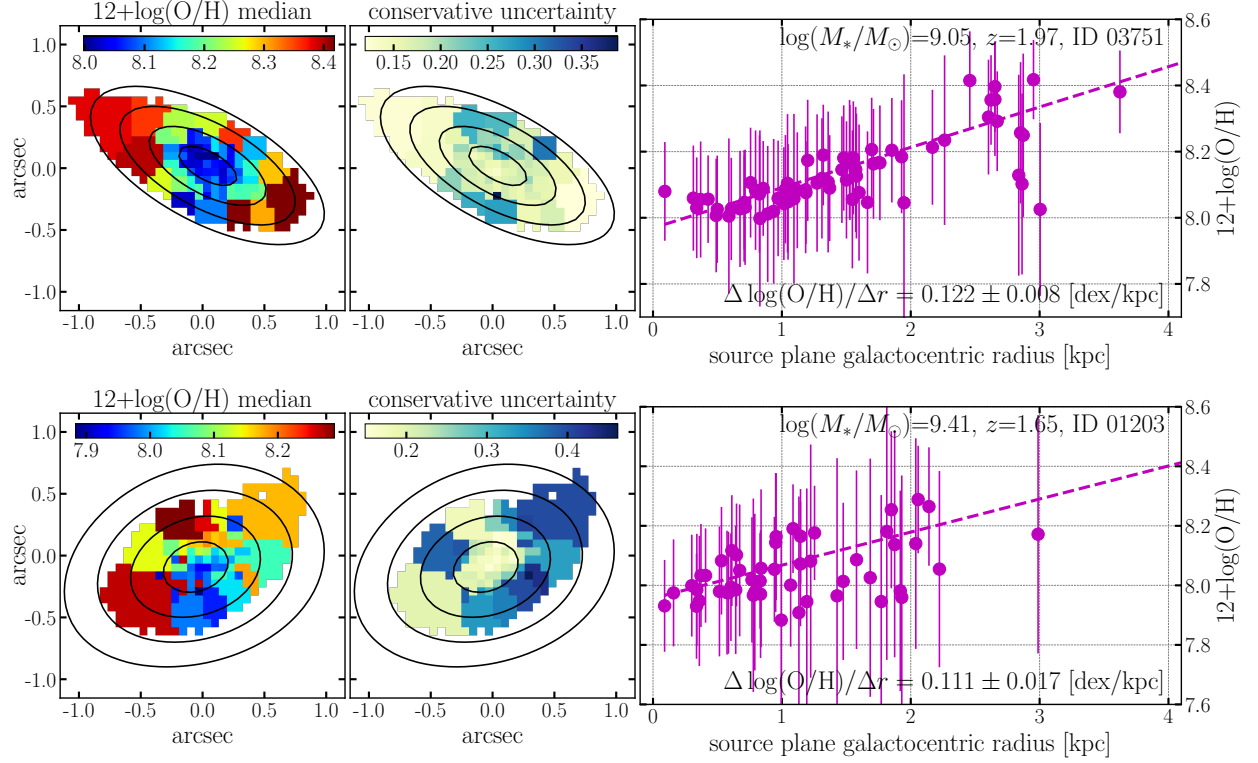


Figure 4.3 Metallicity maps and radial gradient measurements of the two galaxies. The left panels show the 2D maps of the median value estimates of metallicity, and the central panels show their conservative uncertainties (i.e. the larger side of the asymmetric  $1-\sigma$  error bars). The right panels show the corresponding radial gradients measurements. The black contours again mark the source plane de-projected galacto-centric distances as in Figure 4.1. We adopted weighted Voronoi tessellation (Cappellari & Copin, 2003; Diehl & Statler, 2006), with a SNR of 10 on [O III] for the binned metallicity maps. In the right column, these bins are plotted as individual data points. The dashed line denotes the linear regression from these points, with the measured radial slope shown at the bottom of each panel. For both galaxies, the radial gradient is strongly positive (i.e. inverted).

properties (i.e.,  $H\alpha/H\beta = 2.86$ ). Finally, we convert intrinsic  $H\alpha$  luminosity to SFR through the commonly used calibration (Kennicutt, 1998a),

$$\text{SFR} = 4.6 \times 10^{-42} \frac{L(H\alpha)}{\text{erg/s}} [M_\odot/\text{yr}], \quad (4.2)$$

appropriate for the Chabrier (2003) IMF. This provides the instantaneous star formation rate on  $\sim 10$  Myr time scales; we note that the ultraviolet continuum probed by *HST* photometry is sensitive to recent SFR over a longer time span ( $\sim 100$ -300 Myr). The short timescales probed by Balmer emission are most relevant for determining outflow physical properties, which are highly dynamic on small spatial scales, e.g., at sub-kpc level.

Next we derive average stellar age maps, using the spatial distribution of EL EW as the primary constraint. We calculate  $H\beta$  rest-frame EWs from our maps of the emission line flux and stellar continuum flux density. Stellar continuum maps are corrected for emission line contamination as described in Section 4.2. We correct for stellar Balmer absorption which we estimate to be rest-frame EW  $\sim 3$  Å in  $H\beta$  based on the derived galaxy properties (Kashino et al., 2013). Maps of  $H\beta$  EW are then converted to average stellar age using a series of STARBURST99 stellar population synthesis models (Leitherer et al., 1999; Zanella et al., 2015) assuming 1/5 solar metallicity and constant star formation history.

We also compare the age estimates given by our SED fitting (Section 4.2) and  $H\beta$  rest-frame EW using the method described above. The median values given by the former practice are systematically larger than those of the latter by  $\sim 0.5$  dex, but we note that the uncertainties by the SED fitting are usually much larger due to the absence of prominent continuum spectral age indicators, e.g.,  $D_n(4000)$  and  $H\delta_A$  (Kauffmann et al., 2003). Hence, we adopt the results from  $H\beta$  rest-frame EW as the average age for stellar populations throughout our analysis, as we consider this a more reliable estimate.

Finally, we calculate the gas fraction defined as

$$f_{\text{gas}} = \Sigma_{\text{gas}} / (\Sigma_{\text{gas}} + \Sigma_*). \quad (4.3)$$

Since we do not directly observe the bulk of interstellar gas, we instead estimate gas surface density  $\Sigma_{\text{gas}}$  by inverting the Kennicutt-Schmidt (KS) law (Schmidt, 1959; Kennicutt, 1998b), i.e.,  $\Sigma_{\text{SFR}} \propto$

$\Sigma_{\text{gas}}^N$  together with our measurements of  $\Sigma_{\text{SFR}}$  described above. We adopt the more robust extended version of the KS law developed by Shi et al. (2011, 2018) which is especially useful in low density regimes:

$$\frac{\Sigma_{\text{SFR}}}{M_{\odot}/\text{yr}/\text{kpc}^2} = 10^{-4.76} \left( \frac{\Sigma_*}{M_{\odot}/\text{pc}^2} \right)^{0.545} \left( \frac{\Sigma_{\text{gas}}}{M_{\odot}/\text{pc}^2} \right)^{1.09}. \quad (4.4)$$

This extended KS law has been tested in numerous ensembles of galaxies as well as low surface brightness regions in individual galaxies, and is shown to have relatively small scatter ( $\sim 0.3$  dex) over a large dynamic range of gas and SFR surface densities. We have combined in quadrature this systematic uncertainty of 0.3 dex in our estimates of  $\Sigma_{\text{gas}}$ .

Figure 4.4 shows the derived 2D maps of SFR, average stellar age, and gas fraction. In general, we observe centrally concentrated star formation, with the most actively star-forming regions having surface densities  $\gtrsim 10 M_{\odot}/\text{yr}/\text{kpc}$ . On average, the central regions also have older stellar populations and smaller gas fractions than the outskirts, indicating that the outer regions are still in the early stages of converting their gas into stars. These features together indicate that we are witnessing the rapid build-up of galactic disks through in-situ star formation and strongly support an inside-out mode of galaxy growth (Nelson et al., 2014; Jones et al., 2013).

As in Cresci et al. (2010), we compare our radially averaged  $f_{\text{gas}}$  and metallicity measurements against the predictions from the simple chemical evolution model developed by Erb (2008). To separate the effects of gas inflows and outflows, we compute two extreme sets of models, one being pure gas accretion (i.e. with no outflows,  $f_o = \Psi/\text{SFR} = 0$ ) and the other corresponding to the leaky box model (i.e. with no inflows,  $f_i = \Phi/\text{SFR} = 0$ ). The results are shown in Figure 4.5. We note that for the pure gas accretion scenario,  $f_{\text{gas}}$  cannot decrease beyond a certain value, i.e.,

$$f_{\text{gas}}^{\min} = 1 - \frac{1 - R}{f_i - f_o}$$

where  $f_o = 0$  and  $R$  is the instantaneous return fraction. This  $f_{\text{gas}}^{\min}$ , implicitly imposed by Eq. (11) of Erb (2008), physically indicates that galaxies cannot exhaust their gas reservoir to below a certain amount without the help of outflows, under the equilibrium condition with steady gas accretion (see Section 4.3.3 when this equilibrium assumption is relaxed). Therefore, the pure gas accretion scenario cannot explain the observed gas fractions in our source central regions (at  $\lesssim 2\text{kpc}$ )

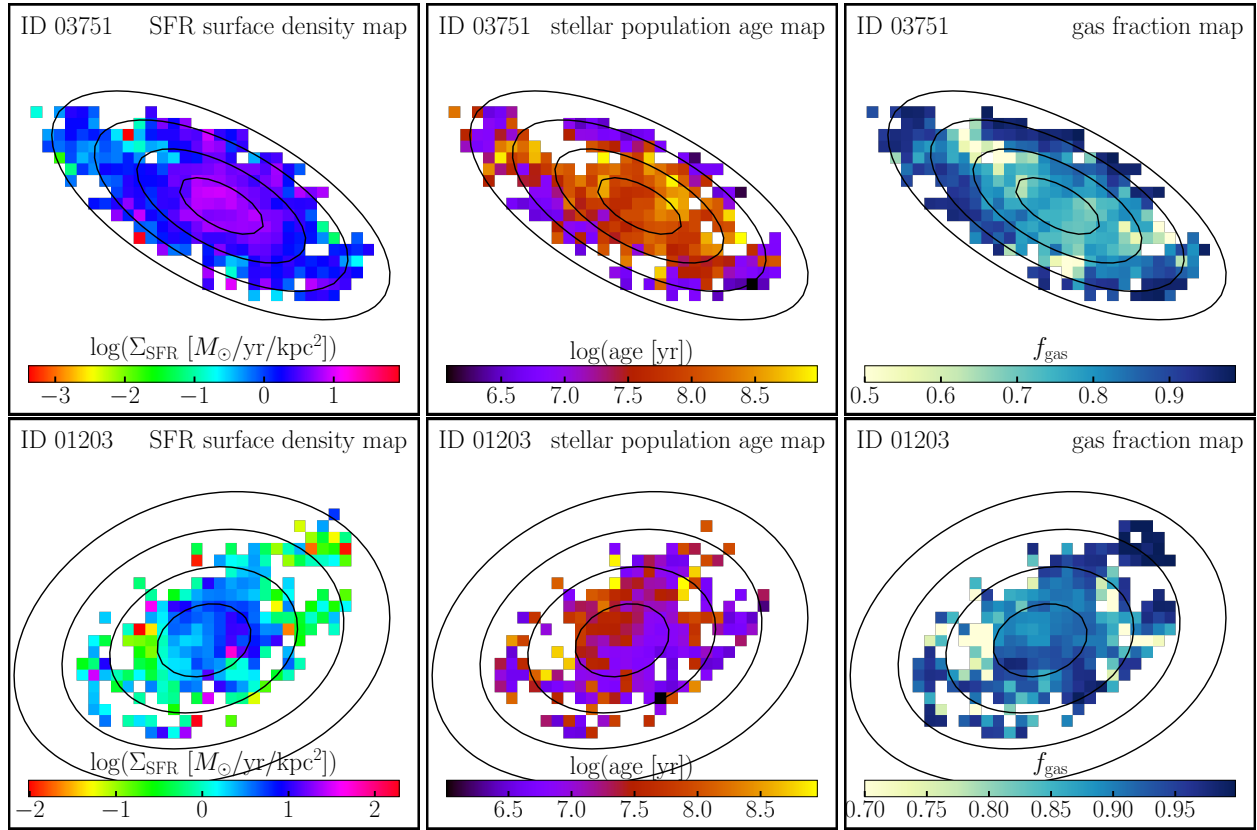


Figure 4.4 Maps of SFR surface density, average stellar population age, and gas fraction for our galaxies, derived from our spatially resolved analysis of stellar continuum and nebular emission. The spatial extent and orientation follows that in Figure 4.1. We see that for both sources compared with their outskirts, their central regions have more active star formation, older stellar population, and lower gas fraction.

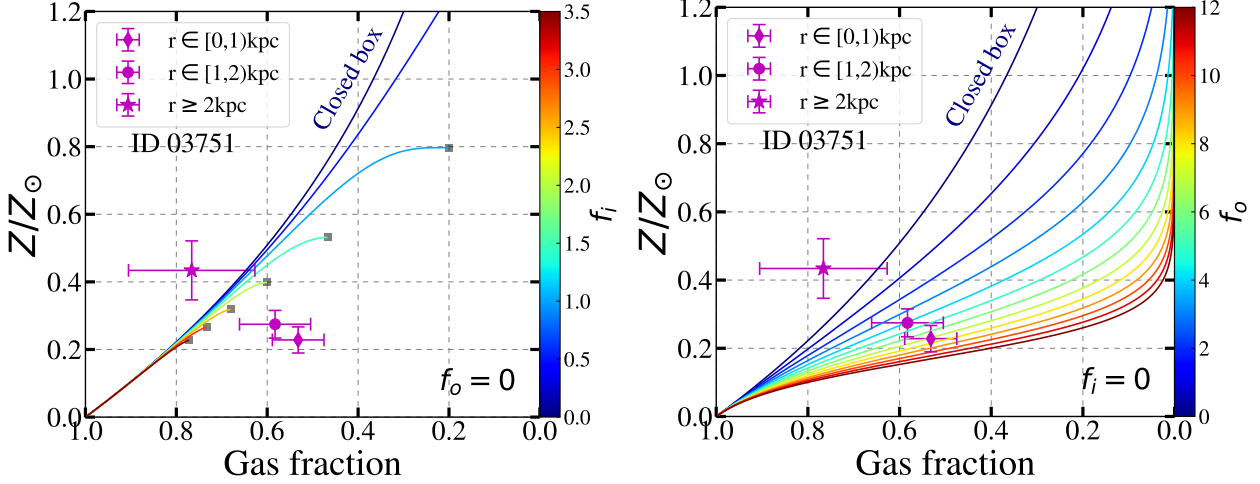


Figure 4.5 Gas fraction and metallicity estimated in different radial annuli for galaxy ID03751. The diamond, circle, and star symbols represent measurements derived at a galacto-centric radius of  $r \in [0, 1]\text{kpc}$ ,  $r \in [1, 2]\text{kpc}$ , and  $r \gtrsim 2\text{kpc}$ , respectively. We also overlay the curves calculated from a simple chemical evolution model Erb (2008) under extreme conditions, i.e., pure gas inflow ( $f_o = 0$ ; left) and pure gas outflow ( $f_i = 0$ ; right). Note that the trajectories of pure gas inflow cases cease at the grey squares for high infall rate ( $f_i \gtrsim 1$ ) conditions; any extensions from those grey squares toward low gas fraction (while fixing metallicity) are unphysical. This simple comparison shows that purely gas accretion does not suffice to explain the strong inverted gradients seen in our galaxies.

where metallicities are also lower. The leaky box model, on the other hand, provides a plausible explanation for our observation such that the outflow rate tends to increase towards galaxy center. However, we stress that in reality both gas outflows and inflows are acting together to re-distribute metallicity. This test using simple chemical evolution models just clearly shows that using gas accretions *alone* cannot explain our spatially resolved measurements.

### 4.3.3 Spatially Resolved Gaseous Outflows

The application of simple chemical evolution in Section 4.3.2 is enlightening but depends on strong assumption, such as that the azimuthal variations are negligible and galaxies live in equilibrium. In reality, these conditions might not be valid, e.g., due to rapid gas flows. To gain a more precise

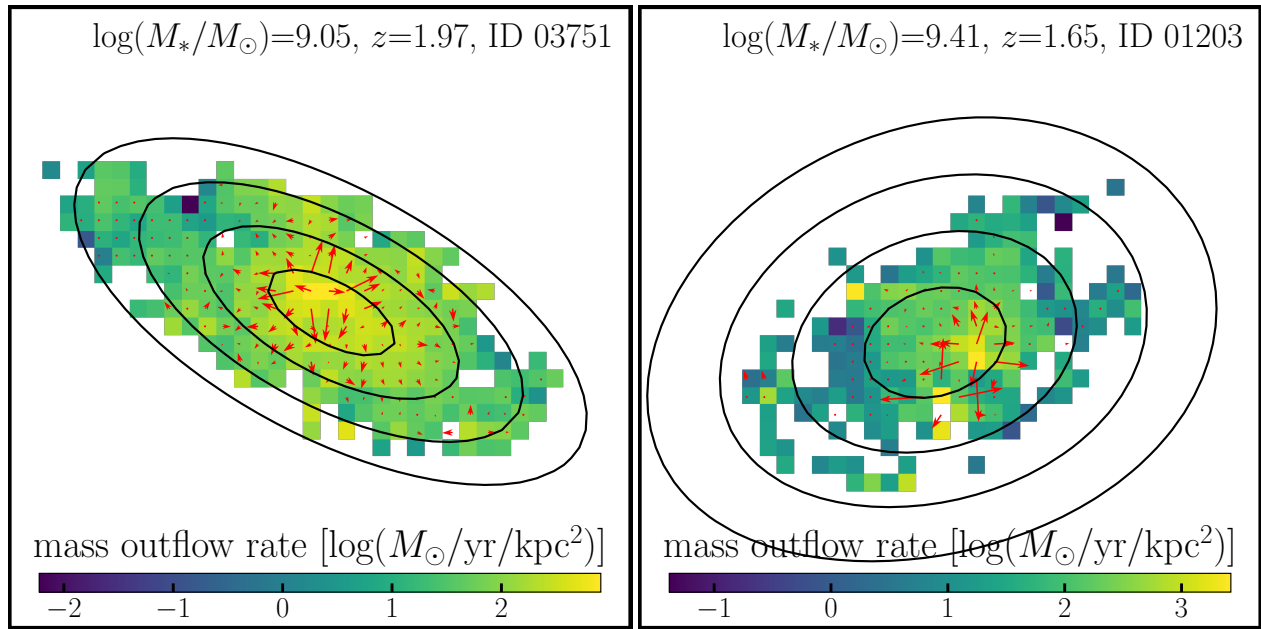


Figure 4.6 Maps of gaseous outflow rates derived from our analysis combining gas regulator models and empirical star-formation laws. The spatial extent and orientation follows that in Figure 4.1. Red arrows show the net direction and magnitude of the gaseous outflows driven by galactic winds. We argue that outflows play a key role in effectively transporting stellar nucleosynthesis yields from the inner regions of these two galaxies to their outskirts.

understanding of the physics of galactic winds and the role of gaseous outflows in shaping the observed spatial distribution of metallicity, independent of those assumptions, we can turn to a more advanced framework for galaxy chemical evolution: the gas regulator model (Lilly et al., 2013; Peng & Maiolino, 2014). This model provides an informative and coherent view of the full baryon cycle, involving the accretion of underlying DM halos, as well as the instantaneous regulation of star formation by a time-variable gas reservoir. A key feature of this model is that it does not assume that galaxies live in an equilibrium state, where the total amount of gas mass remains constant. The non-equilibrium flexibility is especially important for applying this model to spatially resolved regions within a galaxy, where gas may be transported radially from one region to another. Chemical evolution within the gas regulator model is described by the equations

$$Z_{\text{gas}} = \left[ Z_0 + y\tau_{\text{eq}}\epsilon \left( 1 - \exp\left(-\frac{t}{\tau_{\text{eq}}}\right) \right) \right] \left[ 1 - \exp\left(\frac{-t/\tau_{\text{eq}}}{1 - \exp(-t/\tau_{\text{eq}})}\right) \right], \quad (4.5)$$

$$\tau_{\text{eq}} = \frac{1}{\epsilon(1 - R + \lambda)}.$$

Here we adopt the convention of symbols itemized in Table 1 of Peng & Maiolino (2014):  $Z_{\text{gas}}$  is the mass fraction of metals in the gas reservoir (determined from the observed  $12 + \log(\text{O/H})$  as in Peeples & Shankar (2011)),  $t$  is the average stellar population age,  $\tau_{\text{eq}}$  is the time scale on which the baryon cycle reaches equilibrium,  $\epsilon$  is the star-forming efficiency (defined as  $\epsilon \equiv \text{SFR}/M_{\text{gas}} = \Sigma_{\text{SFR}}/\Sigma_{\text{gas}}$ ), and  $\lambda$  is the mass loading factor (defined in terms of the mass outflow rate  $\Psi$ , such that  $\lambda = \Psi/\text{SFR}$ <sup>4</sup>). We adopt a stellar nucleosynthesis yield  $y = 0.003$  (Dalcanton, 2007) with  $R = 0.4$  estimated from BC03 (Bruzual & Charlot, 2003) stellar population models. Finally, we assume that gas inflows are pristine ( $Z_0 = 0$ ).

For each spatial region where we have estimated the metallicity, SFR, gas surface density, and age (Figures 4.3, 4.4), we solve the above equations for the mass loading factor  $\lambda$  and subsequently calculate the mass outflow rate  $\Psi$ . The 2D distribution of  $\Psi$  is displayed in Figure 4.6. Taking the gradient field of this gaseous outflow map, we obtain the net direction of the outflowing mass flux on sub-galactic scales, projected along the line of sight, denoted by the red arrows in Figure 4.6. The results demonstrate that strong galactic winds transport mass from the center to the outskirts,

---

<sup>4</sup>Note that  $\lambda$  and  $f_o$  in Section 4.3.2 represent the same quantity but here we are solving for  $\lambda$  in a spatially resolved fashion.

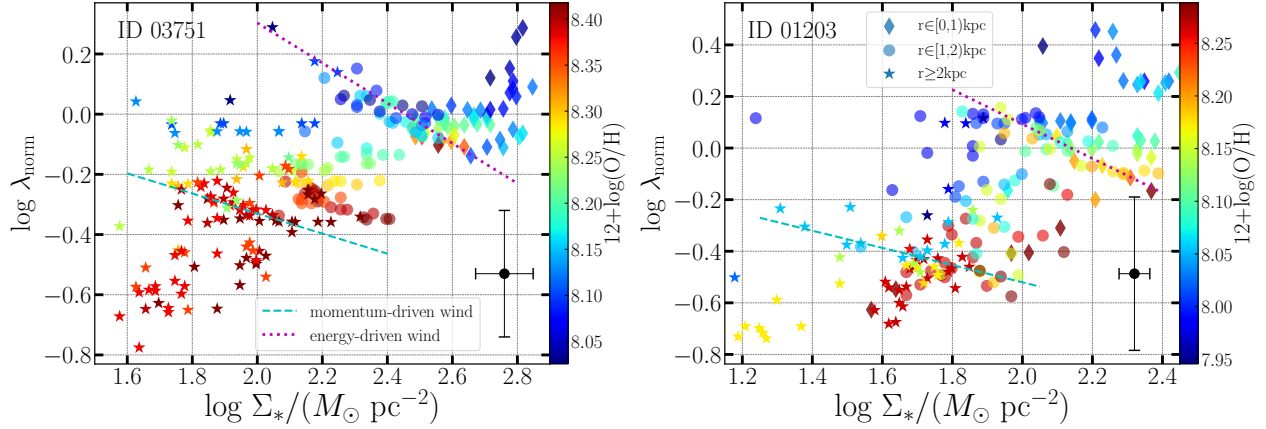


Figure 4.7 Correlation between spatially resolved mass loading factor  $\lambda$  (normalized to the value at radius 1 kpc; see Table 4.1) and stellar surface density  $\Sigma_*$ , color-coded by metallicity. As in Figure 4.4, the diamond, circle, and star symbols represent measurements derived at a galactocentric radius of  $r \in [0, 1)\text{kpc}$ ,  $r \in [1, 2)\text{kpc}$ , and  $r \gtrsim 2\text{kpc}$ , respectively. We overlay as an illustration two scaling relations that are commonly assumed to describe integrated measurements:  $\lambda \propto \Sigma_*^{-2/3}$  for an energy-driven wind model marked by magenta dotted lines, and  $\lambda \propto \Sigma_*^{-1/3}$  for a momentum-driven wind model by cyan dashed lines. Evidently, a single scaling relation is not sufficient to describe the spatially resolved data, demonstrating the need for a more sophisticated approach. The black point in the lower right corner in each panel displays the median uncertainties for these measurements.

with the net radial transport of heavy elements causing the inverted gradients observed in our targets.

The distribution of mass loading factors  $\lambda$  within each of our targets is also shown in Figure 4.7, revealing higher  $\lambda$  (and therefore a higher fraction of metals lost) in the central regions. This preferential removal of metals from the center, and subsequent deposition at larger radii, gives rise to the strong positively sloped metallicity gradients evident in Figure 4.3. The high values of  $\lambda$  have important implications for the role of feedback in galaxy formation. Most fundamentally, our results support feedback as a solution to the “over-cooling” problem in galaxy formation, by ejecting gas and preventing overly condensed baryonic regions at high redshifts (White & Rees, 1978; Dekel & Silk, 1986). Such strong outflows are also expected to suppress the formation of

stellar bulges from low angular momentum gas (Governato et al., 2010; Brook et al., 2012). This is consistent with low bulge fraction in these two galaxies measured from high resolution *HST* imaging (Table 4.1).

A key feature in the  $\lambda$  distribution is that neither of the wind modes, driven by momentum or energy conservation, can explain the behavior of the mass dependence of  $\lambda$  alone, *within* individual galaxies. Outflows are typically parameterized by either a momentum-driven (Oppenheimer & Davé, 2006, 2008) or an energy-driven (Springel & Hernquist, 2003) wind mode, both of which are physically well motivated (Murray et al., 2005). The energy-driven wind scenario assumes that outflows are launched by the thermal pressure of supernova (SN) explosions and/or winds from massive stars. A portion of this thermal energy provides the outflow kinetic energy, i.e.,  $\Psi \times v_{\text{wind}}^2 \sim \text{SFR}$ , where the wind speed  $v_{\text{wind}}$  can mimic the escape velocity from DM halo, i.e.,  $v_{\text{esc}} \sim M_h^{1/3}$  given by the virial theorem. This results in the scaling relation of  $\lambda \propto M_*^{-2/3}$ , assuming the linear correlation between the mass constituents of stellar and dark components. The energy-driven wind model is found successful in explaining the low abundance of satellite galaxies in the Milky Way (Okamoto et al., 2010). The momentum-driven wind model instead relies on the momentum injection deposited by radiation pressure from SN explosions and/or massive stars, leading to  $\Psi \times v_{\text{wind}} \sim \text{SFR}$  and  $\lambda \propto M_*^{-1/3}$ . In this scenario,  $v_{\text{wind}}$  is proportional to  $M_*$  and SFR, broadly consistent with some observational results (Martin, 2005). The transition from energy- to momentum-driven winds is typically thought to be a galaxy-wide phenomenon, resulting in the steepening of the mass-metallicity relation below  $M_* \simeq 10^{9.3} M_\odot$  at  $z \simeq 2$  (Henry et al., 2013b). However, our analysis indicates that a single mode is not sufficient to describe spatially resolved data *within* one galaxy and it is highly likely that the transition from energy- to momentum-driven winds occurs on sub-galactic scales, governed by local gas and star formation properties in addition to the global gravitational potential.

## 4.4 Summary and Discussion

We present the first robust confirmation of the existence of strongly inverted metallicity radial gradient (i.e.  $\gtrsim 0.1$  dex/kpc) in star-forming dwarf galaxies ( $M_* \lesssim 10^9 M_\odot$ ) at the peak of star

formation and chemical enrichment ( $z \sim 2$ ). Our synergy of the diffraction-limited imaging spectroscopy from *HST* NIR grisms and lensing magnification permits exquisite spatial sampling, i.e., at the scale of 50-100 pc, to securely resolve our  $z \sim 2$  galaxies with  $\gtrsim 300$  resolution elements (Figures 4.1 and 4.3) to deliver precise radial gradient measurements. To understand the physical origin of these strongly inverted gradients, we obtain high resolution 2D maps of star formation rate, characteristic stellar age (or equivalently star formation timescale), and gas fraction, from *HST* observations of source stellar continuum and nebular emission. These 2D maps show that the galactic disks of our sources are rapidly assembling stellar mass through in-situ star formation, in the early phase of inside-out growth (Figure 4.4). By comparing our observations with simple chemical evolution models, we find that gas accretion alone cannot explain these strongly inverted gradients in our galaxies (Figures 4.5).

Using a more advanced gas regulator model, we are able to calculate the spatial distribution of mass loss rates from outflows, treating each spaxel as an independent star-forming region, and thus map the macroscopic patterns of net gaseous outflows (Figure 4.6). It turns out that the mass loss rates are highest in the central regions of both galaxies, coincident with the peak star formation surface densities. A natural explanation is thus that active star formation in galaxy centers gives rise to powerful winds that transport gas and metals away from the center toward larger radii, forming “galactic fountains” (Martin et al., 2002).

Furthermore, our spatially resolved analysis of metals, SFR, and stellar populations shows that a single type of wind mechanism (either energy or momentum driven) cannot explain the entire galaxy (Figure 4.7). A primary physical parameter that has been proposed to set the transition between the two wind dynamics is the gravitational potential, often parameterized by velocity dispersion ( $\sigma$ ). There exists a critical scale  $\sigma_{\text{crit}}$  (Murray et al., 2005) such that for galaxies with  $\sigma < \sigma_{\text{crit}}$ , energy injection by SNe sets a limiting SFR above which interstellar gas is ejected in galactic winds. For galaxies with  $\sigma > \sigma_{\text{crit}}$ , momentum deposition limits the maximum SFR above which the ISM is likewise ejected. The presence of both energy- and momentum-driven wind scalings in one galaxy suggests that feedback-triggered winds are connected to physical properties on sub-galactic scales, e.g., *local* velocity dispersion ( $\sigma_{\text{local}}$ ), which is sensitive to the optical depth of gas flows, the coupling efficiency between gas clouds and dust parcels, etc.. On sub-

galactic scales, there exists a strong correlation among velocity dispersion (not necessarily  $\sigma_{\text{local}}$ ), surface density and size of molecular clouds (see Ballesteros-Paredes et al., 2011, and references therein). It appears that in our galaxies, the wind-launching mechanism transitions from energy-to momentum-driven as galacto-centric radius increases. This gives rise to a hypothesis that  $\sigma_{\text{local}}$  in our galaxies should increase from inner to outer regions. Our current kinematic data on source ID01203 have high spatial resolution (at 0.''05 plate scale) yet narrow FoV so that it is infeasible to map sub-kpc scale velocity dispersion accurately to outer regions at  $r \gtrsim 2$  kpc, where momentum-driven wind seems to take over. To test this hypothesis conclusively, more spatially resolved data taken under sufficient spatial sampling will be required to robustly derive a full 2D map of velocity dispersion out to the periphery of the galactic disk, using instruments with relatively large FoV, e.g., the *JWST* NIRSpec IFU (Kalirai, 2018).

Physically, the momentum-driven wind scaling applies to “cool” ( $T \sim 10^4$  K) ambient interstellar gas entrained in outflows, whereas the energy-driven wind is appropriate when entrained gas is shock heated to temperatures where cooling is inefficient ( $T \sim 10^6$  K). A plausible scenario for our galaxies is that feedback from an intense burst of star formation in the central regions heats the ejected gas to a highly ionized phase, while gas entrained in outflows from the outer regions remains cool. If this interpretation is correct, then we expect a distinct signature in the absorption properties of outflowing gas. Outflows from the central regions should be dominated by highly ionized species (e.g. O VI, C IV, Si IV) whereas outflows from the outer regions should have relatively more of the low ions characteristic of  $T \sim 10^4$  K gas (e.g. Fe II, Mg II, Si II). Both high and low ion species are commonly observed in outflows from star forming galaxies at  $z \simeq 2$  (Berg et al., 2018; Du et al., 2018), although their spatial distributions are not yet well known (but see James et al., 2018). Our hypothesis suggests a more central concentration of the high ions *in the specific cases* where a combination of both outflow scalings results in inverted metallicity gradients. This prediction can be directly tested with spatially resolved spectroscopy of rest-frame ultraviolet absorption lines using instruments such as *Keck*/KCWI or *VLT*/MUSE.

## 4.A Gas kinematics from *Keck OSIRIS* observations

Kinematics of HII regions are of interest both for determining whether rotating gaseous disks are present, and the overall scale of velocity dispersion which is thought to correlate with the mode of feedback. We have obtained kinematic maps from H $\alpha$  emission for source ID01203 as part of a GLASS followup campaign with the *OSIRIS* integral field spectrograph (Larkin et al., 2006) on the *Keck* I telescope. Full details of the observations and analysis are presented elsewhere (Hirtenstein et al., 2018); here we give a brief summary. Data were obtained on 2016 October 21 using the Hn5 filter, 50 milliarcsecond scale, and laser guide star AO, which provides the excellent spatial sampling needed to resolve velocity structure on the relevant  $\sim 0.^{\prime\prime}1$  scales. We obtained 3 exposures of 900 seconds each. The *OSIRIS* Data Reduction Pipeline was used to process the data, following the standard methods adopted in our previous work (Jones et al., 2013). We fit H $\alpha$  line emission in each spaxel with a Gaussian function, requiring  $\geq 5\sigma$  significance for acceptable fits. Gas rotation velocity ( $V$ ) and velocity dispersion ( $\sigma$ ) are determined from the Gaussian centroid and width. We correct velocity dispersions for the effects of instrument resolution and beam smearing by subtracting these terms in quadrature from the best-fit Gaussian dispersion. The median beam smearing correction is a 7% reduction in  $\sigma$ .

Resulting maps of  $V$  and  $\sigma$  in Figure 4.8 reveal a sheared velocity field with high local velocity dispersion ( $\gtrsim 50 \text{ km s}^{-1}$ ), common among disk galaxies at similar redshift. To quantify the degree of rotational support, we extract a 1D velocity profile along the kinematic major axis. We fit this with the circular rotation curve of an exponential disk mass profile. The disk rotation curve is in good agreement with the data, with maximum velocity  $V \sin i = 94 \pm 7 \text{ km s}^{-1}$ . Here  $i$  is the disk inclination angle relative to the line-of-sight. The pixel-averaged  $\sigma = 73 \pm 3 \text{ km s}^{-1}$  such that we derive  $V/\sigma = (1.3 \pm 0.1)/\sin i$  indicating orderly rotation in spite of a high level of ISM turbulence. This  $V/\sigma$  ratio is typical of the galaxy population harboring thick disks at similar mass and redshift (Wisnioski et al., 2015; Leethochawalit et al., 2016).

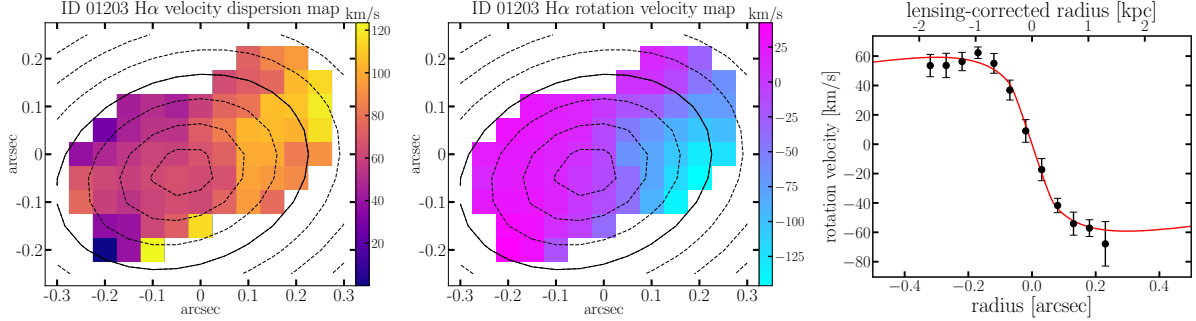


Figure 4.8 H $\alpha$  emission kinematics of ID01203 from our *OSIRIS* AO-assisted observations showing the velocity dispersion (*left*), the rotation velocity (*center*), and rotation curve extracted along the major axis (*right*). The overlaid contours in the left and center panels also represent the source plane de-projected galacto-centric radii, but in 0.25 kpc interval. To give relative scale with respect to our *HST* stamps, the 1 kpc radius contour is still in solid. The red curve in the right panel is the best-fit rotation curve for an exponential disk mass distribution, giving a maximum line-of-sight velocity  $V \sin i = 94 \pm 7$  km s $^{-1}$ . The data are in good agreement with a thick disk rotation curve despite a high level of turbulence.

## 4.B Extracting and fitting 1D and 2D *HST* grism spectra

As briefly mentioned in Section 4.2.2, we employed the Grism Redshift and Line analysis software **GRZILI** to reduce the *HST* WFC3/NIR grism data from raw exposures acquired by the *GLASS* program. Our primary goal is to obtain the spatially resolved emission line intensities after removing the contribution from source continuum. In terms of modeling the continuum spectrum, **GRZILI** first produces a simple flat (in  $F_\lambda$ ) spectral model for all sources within the WFC3 FoV with  $H_{160}$ -band magnitude brighter than 26 ABmag. The normalization is determined to match the flux in the corresponding reference image (in our cases, F105W as the reference to G102, and F140W to G141, ascribed to similar wavelength coverage). Then second-order polynomial functions are fitted to the sources whose  $H_{160}$ -band magnitude is brighter than 24 ABmag. This process is done iteratively, until a convergence point where the residual in the grism exposures after subtracting the fitted continuum models becomes negligible.

While the polynomially fitted continua serve as good enough models for contamination sub-

traction associated with neighboring objects, this polynomial functional form is clearly not physically representative of the actual SED of the underlying stellar continuum for our sources of interest. To facilitate a more accurate continuum subtraction, we further refine the source continuum model by considering primarily four template continuum spectra in a range of characteristic ages for stellar populations:

1. a low-metallicity Lyman-break galaxy (Q2343-BX418) showing very young, blue continuum (Erb et al., 2010),
2. an intermediate-age composite SED with moderate Balmer break and 4000 Å break, synthesized in Brammer et al. (2008b) following the method of Blanton & Roweis (2007),
3. a post-starburst SED showing prominent Balmer break and 4000 Å break from the UltraVISTA survey (Muzzin et al., 2013),
4. a single stellar population SED with a 13.5 Gyr age and solar metallicity (Conroy & van Dokkum, 2012).

This combination of both empirical and synthetic SED templates constitutes an optimized set appropriate for redshift fitting and continuum subtraction under our situation. As discussed in Brammer et al. (2008b), there is a trade-off between the number of templates used in SED fitting and numerical efficiency, and they find that the improvement is negligible if the number of templates is increased to above 5. For a sanity check, we also run the template fitting procedures using a more complete template library built from the Flexible Stellar Population Synthesis (FSPS) models (Conroy et al., 2009, 2010; Conroy & Gunn, 2010) and found no noticeable changes in the spectroscopic redshift determinations nor continuum subtractions.

In addition to fitting stellar continuum, we model the intrinsic nebular emission lines in 1D spectra as Gaussian functions. The amplitudes and flux ratios between most of the line species are allowed to vary (except for some certain line complexes, e.g.,  $f_{[O\ III]} 5008/f_{[O\ III]} 4960 = 3:1$ ). Given the relatively low instrument resolution of *HST* grisms, the dynamic motion of gas and stellar components leave no effect on the observed profiles (both in 1D and 2D) of line emission/absorption features. However, for spatially extended sources, the effective spectral resolution is lowered by

morphological broadening (van Dokkum et al., 2011), which usually varies with respect to the light-dispersion direction, i.e., the position angle (P.A.). We explicitly take the source morphology into account via convolving the model spectra (stellar continuum + nebular emission) with the direct image in reference frames averaged along light-dispersion directions.

As a result, in Figures 4.9 and 4.10, we show the observed and fitted grism spectra for both of our sources at separate P.A.s. Albeit slightly different in shape and slope, the red curves in 1D spectra comes from the same best-fit spectral model for each source and the difference is due to slightly varying morphological broadening. We also see that the 2D continuum-subtracted spectra are sufficiently clean, preserving only the nebular emission features that we later combined to get the spatially resolved emission line maps shown in Figure 4.1.

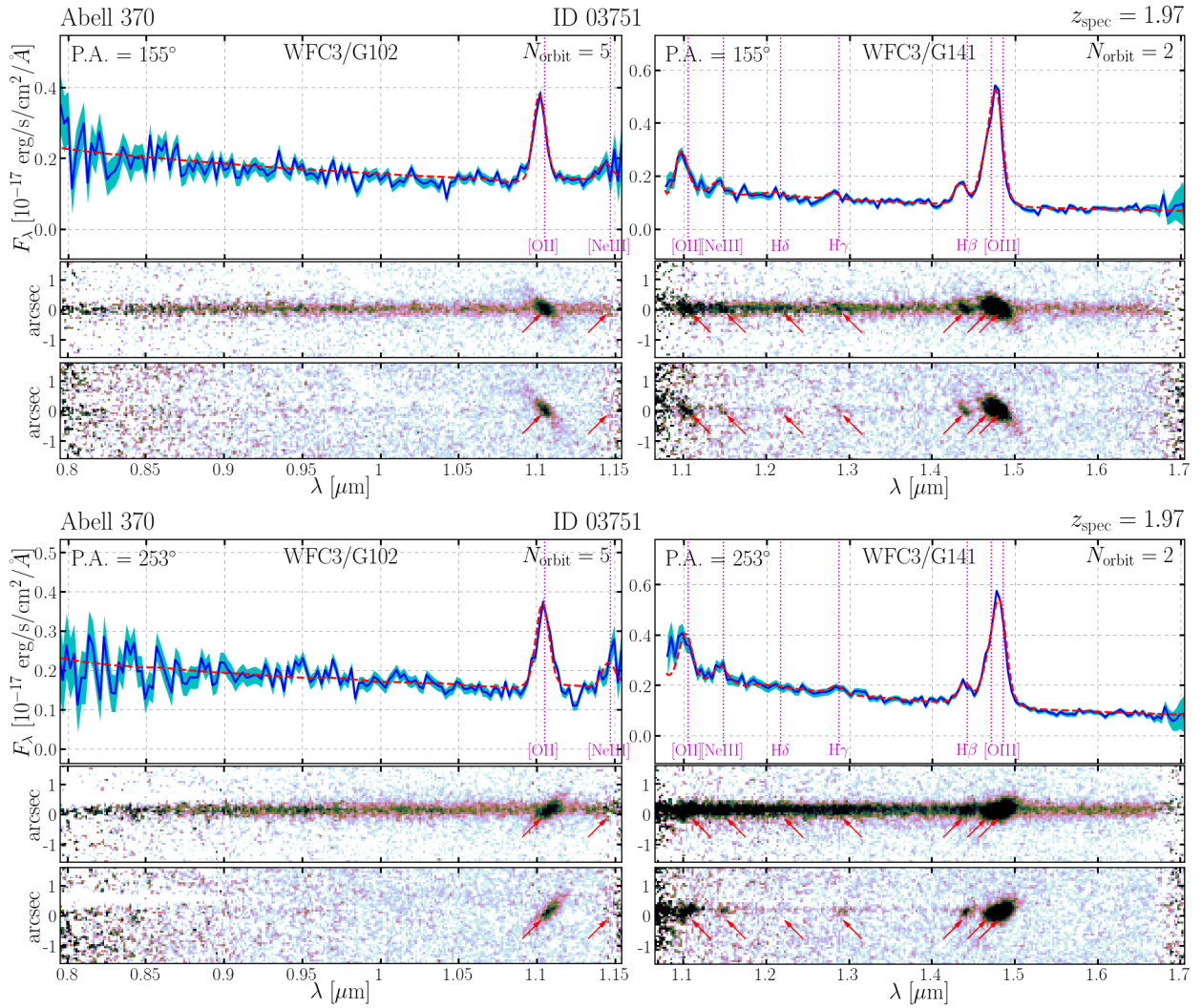


Figure 4.9 The *HST* grism spectra for source ID03751 in the field of Abell 370 taken by the *GLASS* program. The total science integration is equally distributed into two separate P.A.s, reaching 5 orbits of G102 exposures and 2 orbits of G141 exposures per P.A., shown in two sub-figures. In each sub-figure, from top to bottom, we show the optimally extracted 1D spectra and the full 2D spectra before and after source continuum subtraction, for both grism elements. On the 1D spectra, the observed flux is represented by the blue solid line with  $1-\sigma$  noise level denoted by the cyan shaded band, and the 1D model spectrum (source continuum + nebular emission) is represented by the red dashed curve. The observed locations of emission features are highlighted by vertical dotted lines in magenta and arrows in red, in 1D and 2D spectra respectively.

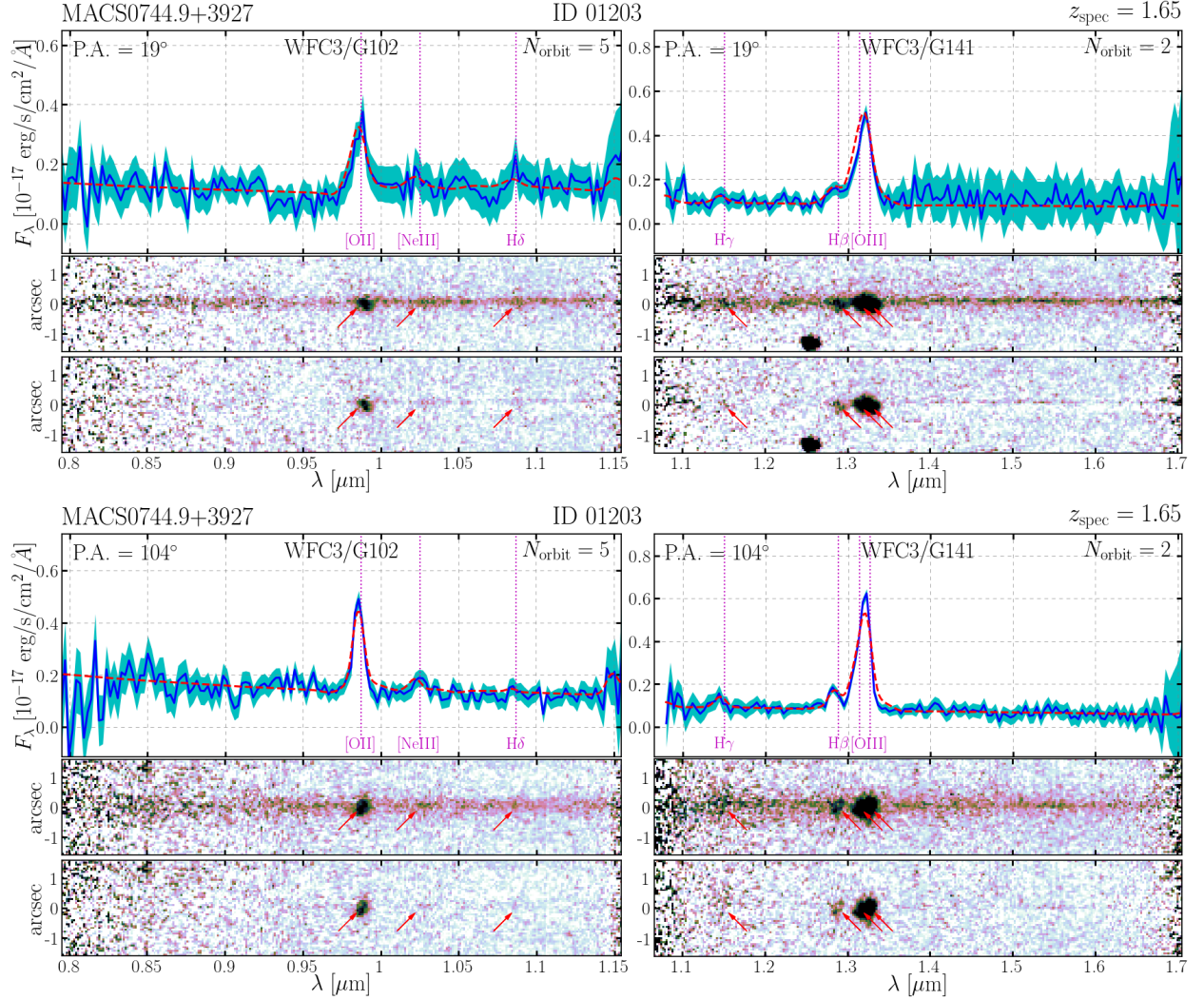


Figure 4.10 Same as Figure 4.9, except that source ID01203 in the field of MACS0744.9+3927 is shown.

## Bibliography

Abramson, L. E., Gladders, M. D., Dressler, A., Oemler, A., Poggianti, B. M., & Vulcani, B. 2016, eprint arXiv:1604.00016, 1604.00016

Aghanim, N., Akrami, Y., Ashdown, M., Aumont, J., Baccigalupi, C., Ballardini, M., Banday, A. J., Barreiro, R. B., Bartolo, N., Basak, S., Battye, R., Benabed, K., Bernard, J. P., Bersanelli, M., Bielewicz, P., Bock, J. J., Bond, J. R., Borrill, J., Bouchet, F. R., Boulanger, F., Bucher, M., Burigana, C., Butler, R. C., Calabrese, E., Cardoso, J. F., Carron, J., Challinor, A., Chiang, H. C., Chluba, J., Colombo, L. P. L., Combet, C., Contreras, D., Crill, B. P., Cuttaia, F., de Bernardis, P., de Zotti, G., Delabrouille, J., Delouis, J. M., Di Valentino, E., Diego, J. M., Dore, O., Douspis, M., Ducout, A., Dupac, X., Dusini, S., Efstathiou, G., Elsner, F., Ensslin, T. A., Eriksen, H. K., Fantaye, Y., Farhang, M., Fergusson, J., Fernandez-Cobos, R., Finelli, F., Forastieri, F., Frailis, M., Franceschi, E., Frolov, A., Galeotta, S., Galli, S., Ganga, K., Génova-Santos, R. T., Gerbino, M., Ghosh, T., Gonzalez-Nuevo, J., Gorski, K. M., Gratton, S., Gruppuso, A., Gundmundsson, J. E., Hamann, J., Handley, W., Herranz, D., Hivon, E., Huang, Z., Jaffe, A. H., Jones, W. C., Karakci, A., Keihanen, E., Keskitalo, R., Kiiveri, K., Kim, J., Kisner, T. S., Knox, L., Krachmalnicoff, N., Kunz, M., Kurki-Suonio, H., Lagache, G., Lamarre, J. M., Lasenby, A., Lattanzi, M., Lawrence, C. R., Le Jeune, M., Lemos, P., Lesgourgues, J., Levrier, F., Lewis, A., Liguori, M., Lilje, P. B., Lilley, M., Lindholm, V., Lopez-Caniego, M., Lubin, P. M., Ma, Y.-Z., Macias-Perez, J. F., Maggio, G., Maino, D., Mandolesi, N., Mangilli, A., Marcos-Caballero, A., Maris, M., Martin, P. G., Martinelli, M., Martinez-Gonzalez, E., Matarrese, S., Mauri, N., McEwen, J. D., Meinholt, P. R., Melchiorri, A., Mennella, A., Migliaccio, M., Millea, M., Mitra, S., Miville-Deschenes, M. A., Molinari, D., Montier, L., Morgante, G., Moss, A., Natoli, P., Norgaard-Nielsen, H. U., Pagano, L., Paoletti, D., Partridge, B., Patanchon, G., Peiris, H. V., Perrotta, F., Pettorino, V., Piacentini, F., Polastri, L., Polenta, G., Puget, J. L., Rachen, J. P., Reinecke, M., Remazeilles, M., Renzi, A., Rocha, G., Rosset, C., Roudier, G., Rubino-Martin, J. A., Ruiz-Granados, B., Salvati, L., Sandri, M., Savelainen, M., Scott, D., Shellard, E. P. S., Sirignano, C., Sirri, G., Spencer, L. D., Sunyaev, R., Suur-Uski, A. S., Tauber, J. A., Tavagnacco, D., Tenti, M., Toffolatti, L., Tomasi, M., Trombetti, T., Valenziano, L., Valiviita, J., Van Tent,

- B., Vibert, L., Vielva, P., Villa, F., Vittorio, N., Wandelt, B. D., Wehus, I. K., White, M., White, S. D. M., Zacchei, A., & Zonca, A. 2018, eprint arXiv:1807.06209, 1807.06209
- Andrews, B. H., & Martini, P. 2013, *The Astrophysical Journal*, 765, 140
- Atek, H., Richard, J., Kneib, J.-P., Clement, B., Egami, E., Ebeling, H., Jauzac, M., Jullo, E., Laporte, N., Limousin, M., & Natarajan, P. 2014, *ApJ*, 786, 60
- Atek, H., Richard, J., Kneib, J.-P., Jauzac, M., Schaerer, D., Clement, B., Limousin, M., Jullo, E., Natarajan, P., Egami, E., & Ebeling, H. 2015, *ApJ*, 800, 18
- Baldry, I. K., Glazebrook, K., & Driver, S. P. 2008, *Monthly Notices of the Royal Astronomical Society*, 388, 945
- Baldwin, J. A., Phillips, M. M., & Terlevich, R. 1981, *Publications of the Astronomical Society of the Pacific*, 93, 5
- Ballesteros-Paredes, J., Hartmann, L. W., Vázquez-Semadeni, E., Heitsch, F., & Zamora-Avilés, M. A. 2011, *Monthly Notices of the Royal Astronomical Society*, 411, 65
- Bayliss, M. B., Rigby, J. R., Sharon, K., Wuyts, E., Florian, M., Gladders, M. D., Johnson, T., & Oguri, M. 2014, *ApJ*, 790, 144
- Behroozi, P. S., Wechsler, R. H., & Conroy, C. 2013, *The Astrophysical Journal*, 770, 57
- Belfiore, F., Maiolino, R., Tremonti, C. A., Sanchez, S. F., Bundy, K., Bershady, M. A., Westfall, K. B., Lin, L., Drory, N., Boquien, M., Thomas, D., & Brinkmann, J. 2017, *Monthly Notices of the Royal Astronomical Society*, 469, 151
- Bell, E. F., & de Jong, R. S. 2001, *ApJ*, 550, 212
- Belli, S., Jones, T. A., Ellis, R. S., & Richard, J. 2013, *The Astrophysical Journal*, 772, 141
- Berg, D. A., Erb, D. K., Auger, M. W., Pettini, M., & Brammer, G. B. 2018, *The Astrophysical Journal*, 859, 164
- Bertin, E., & Arnouts, S. 1996, *Astronomy and Astrophysics Supplement*, 117, 393

- Bianco, F. B., Modjaz, M., Oh, S. M., Fierroz, D., Liu, Y., Kewley, L. J., & Graur, O. 2015, eprint arXiv:1505.06213, 54
- Birnboim, Y., & Dekel, A. 2003, Monthly Notices of the Royal Astronomical Society, 345, 349
- Blanc, G. A., Kewley, L. J., Vogt, F. P. A., & Dopita, M. A. 2015, The Astrophysical Journal, 798, 99
- Blanton, M. R., & Roweis, S. T. 2007, The Astronomical Journal, 133, 734
- Bouche, N., Dekel, A., Genzel, R., Genel, S., Cresci, G., Förster Schreiber, N. M., Shapiro, K. L., Davies, R. I., & Tacconi, L. J. 2010, The Astrophysical Journal, 718, 1001
- Bradač, M., Vanzella, E., Hall, N., Treu, T., Fontana, A., Gonzalez, A. H., Clowe, D., Zaritsky, D., Stiavelli, M., & Clément, B. 2012, The Astrophysical Journal Letters, 755, L7
- Bradač, M., Erben, T., Schneider, P., Hildebrandt, H., Lombardi, M., Schirmer, M., Miralles, J.-M., Clowe, D., & Schindler, S. 2005, A&A, 437, 49
- Bradač, M., Clowe, D., Gonzalez, A. H., Marshall, P., Forman, W., Jones, C., Markevitch, M., Randall, S., Schrabbach, T., & Zaritsky, D. 2006, ApJ, 652, 937
- Bradač, M., Treu, T., Applegate, D., Gonzalez, A. H., Clowe, D., Forman, W., Jones, C., Marshall, P., Schneider, P., & Zaritsky, D. 2009, ApJ, 706, 1201
- Bradač, M., Ryan, R., Casertano, S., Huang, K.-H., Lemaux, B. C., Schrabbach, T., Gonzalez, A. H., Allen, S., Cain, B., Gladders, M., Hall, N., Hildebrandt, H., Hinz, J., von der Linden, A., Lubin, L., Treu, T., & Zaritsky, D. 2014, ApJ, 785, 108
- Brammer, G. B., Pirzkal, N., McCullough, P., & MacKenty, J. W. 2014a, Space Telescope WFC Instrument Science Report
- Brammer, G. B., Pirzkal, N., McCullough, P. R., & MacKenty, J. W. 2014b, STScI IRS
- Brammer, G. B., van Dokkum, P. G., & Coppi, P. 2008a, The Astrophysical Journal, 686, 1503
- . 2008b, The Astrophysical Journal, 686, 1503

Brammer, G. B., van Dokkum, P. G., Illingworth, G. D., Bouwens, R. J., Labb  , I., Franx, M., Momcheva, I., & Oesch, P. A. 2013, *The Astrophysical Journal Letters*, 765, L2

Brammer, G. B., van Dokkum, P. G., Franx, M., Fumagalli, M., Patel, S., Rix, H.-W., Skelton, R. E., Kriek, M., Nelson, E., Schmidt, K. B., Bezanson, R., Cunha, E. D., Erb, D. K., Fan, X., Schreiber, N. F., Illingworth, G. D., Labb  , I., Leja, J., Lundgren, B., Magee, D., Marchesini, D., McCarthy, P., Momcheva, I., Muzzin, A., Quadri, R., Steidel, C. C., Tal, T., Wake, D., Whitaker, K. E., & Williams, A. 2012a, *The Astrophysical Journal Supplement*, 200, 13

Brammer, G. B., van Dokkum, P. G., Franx, M., Fumagalli, M., Patel, S. G., Rix, H.-W., Skelton, R. E., Kriek, M. T., Nelson, E. J., Schmidt, K. B., Bezanson, R., da Cunha, E., Erb, D. K., Fan, X., F  rster Schreiber, N. M., Illingworth, G. D., Labb  , I., Leja, J., Lundgren, B. F., Magee, D. K., Marchesini, D., McCarthy, P. J., Momcheva, I. G., Muzzin, A., Quadri, R. F., Steidel, C. C., Tal, T., Wake, D. A., Whitaker, K. E., & Williams, A. 2012b, *The Astrophysical Journal Supplement Series*, 200, 13

Bresolin, F., Gieren, W., Kudritzki, R.-P., Pietrzynski, G., Urbaneja, M. A., & Carraro, G. 2009, *The Astrophysical Journal*, 700, 309

Bresolin, F., & Kennicutt, R. C. J. 2015, *Monthly Notices of the Royal Astronomical Society*, 454, 3664

Brinchmann, J., Charlot, S., White, S. D. M., Tremonti, C. A., Kauffmann, G., Heckman, T. M., & Brinkmann, J. 2004, *Monthly Notices of the Royal Astronomical Society*, 351, 1151

Brook, C. B., Stinson, G. S., Gibson, B. K., Roskar, R., Wadsley, J. W., & Quinn, T. 2012, *Monthly Notices of the Royal Astronomical Society*, 419, 771

Bruzual, G., & Charlot, S. 2003, *Monthly Notices of the Royal Astronomical Society*, 344, 1000

Bundy, K., Bershady, M. A., Law, D. R., Yan, R.-B., Drory, N., MacDonald, N. K., Wake, D. A., Cherinka, B., S  nchez-Gallego, J. R., Weijmans, A.-M., Thomas, D., Tremonti, C. A., Masters, K. L., Coccato, L., Diamond-Stanic, A. M., Arag  n-Salamanca, A., Avila-Reese, V., Badenes, C., Falc  n-Barroso, J., Belfiore, F., Bizyaev, D., Blanc, G. A., Bland-Hawthorn, J., Blanton,

- M. R., Brownstein, J. R., Byler, N., Cappellari, M., Conroy, C., Dutton, A. A., Emsellem, E., Etherington, J., Frinchaboy, P. M., Fu, H., Gunn, J. E., Harding, P., Johnston, E. J., Kauffmann, G., Kinemuchi, K., Klaene, M. A., Knapen, J. H., Leauthaud, A., Li, C., Lin, L., Maiolino, R., Malanushenko, V., Malanushenko, E., Mao, S., Maraston, C., McDermid, R. M., Merrifield, M. R., Nichol, R. C., Oravetz, D., Pan, K., Parejko, J. K., Sanchez, S. F., Schlegel, D., Simmons, A. E., Steele, O., Steinmetz, M., Thanjavur, K., Thompson, B. A., Tinker, J. L., van den Bosch, R. C. E., Westfall, K. B., Wilkinson, D., Wright, S. A., Xiao, T., & Zhang, K. 2015, *The Astrophysical Journal*, 798, 7
- Calzetti, D., Armus, L., Bohlin, R. C., Kinney, A. L., Koornneef, J., & Storchi-Bergmann, T. 2000, *The Astrophysical Journal*, 533, 682
- Cappellari, M., & Copin, Y. 2003, *Monthly Notices of the Royal Astronomical Society*, 342, 345
- Cardelli, J. A., Clayton, G. C., & Mathis, J. S. 1989, *The Astronomical Journal*, 345, 245
- Carton, D., Brinchmann, J., Contini, T., Epinat, B., Finley, H., Richard, J., Patrício, V., Schaye, J., Nanayakkara, T., Weilbacher, P. M., & Wisotzki, L. 2018, *Monthly Notices of the Royal Astronomical Society*, 1805.08131
- Chabrier, G. 2003, *Publications of the Astronomical Society of the Pacific*, 115, 763
- Chiappini, C., Matteucci, F., & Romano, D. 2001, *The Astrophysical Journal*, 554, 1044
- Clowe, D., Bradač, M., Gonzalez, A. H., Markevitch, M., Randall, S. W., Jones, C., & Zaritsky, D. 2006, *ApJ*, 648, L109
- Coe, D., Bradley, L., Bradley, L. D., & Zitrin, A. 2015, *The Astrophysical Journal*, 800, 84
- Coil, A. L., Aird, J., Reddy, N. A., Shapley, A. E., Kriek, M. T., Siana, B. D., Mobasher, B., Freeman, W. R., Price, S. H., & Shvarei, I. 2015, *The Astrophysical Journal*, 801, 35
- Coleman, M. G., & de Jong, J. T. A. 2008, *The Astrophysical Journal*, 685, 933
- Conroy, C., & Gunn, J. E. 2010, *The Astrophysical Journal*, 712, 833

Conroy, C., Gunn, J. E., & White, M. 2009, *The Astrophysical Journal*, 699, 486

Conroy, C., & van Dokkum, P. G. 2012, *The Astrophysical Journal*, 747, 69

Conroy, C., White, M., & Gunn, J. E. 2010, *The Astrophysical Journal*, 708, 58

Cowie, L. L., Barger, A. J., & Songaila, A. 2016, *The Astrophysical Journal*, 817, 57

Cresci, G., Mannucci, F., Maiolino, R., Marconi, A., Gnerucci, A., & Magrini, L. 2010, *Nature*, 467, 811

Curti, M., Cresci, G., Mannucci, F., Marconi, A., Maiolino, R., & Esposito, S. 2016, eprint arXiv:1610.06939, stw2766

Daddi, E., Cimatti, A., Renzini, A., Fontana, A., Mignoli, M., Pozzetti, L., Tozzi, P., & Zamorani, G. 2004, *The Astrophysical Journal*, 617, 746

Dahlen, T., Mobasher, B., Faber, S. M., Ferguson, H. C., Barro, G., Finkelstein, S. L., Finlator, K., Fontana, A., Gruetzbauch, R., Johnson, S., Pforr, J., Salvato, M., Wiklind, T., Wuyts, S., Acquaviva, V., Dickinson, M. E., Guo, Y., Huang, J., Huang, K.-H., Newman, J. A., Bell, E. F., Conselice, C. J., Galametz, A., Gawiser, E., Giavalisco, M., Grogin, N. A., Hathi, N., Kocevski, D., Koekemoer, A. M., Koo, D. C., Lee, K.-S., McGrath, E. J., Papovich, C., Peth, M., Ryan, R., Somerville, R., Weiner, B., & Wilson, G. 2013, *The Astrophysical Journal*, 775, 93

Dalcanton, J. J. 2007, *The Astrophysical Journal*, 658, 941

Davé, R., Finlator, K., & Oppenheimer, B. D. 2011a, *Monthly Notices of the Royal Astronomical Society*, 416, 1354

—. 2012, *Monthly Notices of the Royal Astronomical Society*, 421, 98

Davé, R., Katz, N. S., Oppenheimer, B. D., Kollmeier, J. A., & Weinberg, D. H. 2013, *Monthly Notices of the Royal Astronomical Society*, 434, 2645

Davé, R., Oppenheimer, B. D., & Finlator, K. 2011b, *Monthly Notices of the Royal Astronomical Society*, 415, 11

- Davé, R., Rafieferantsoa, M. H., Thompson, R. J., & Hopkins, P. F. 2017, Monthly Notices of the Royal Astronomical Society, 467, 115
- Dayal, P., Ferrara, A., & Dunlop, J. S. 2013, Monthly Notices of the Royal Astronomical Society, 430, 2891
- Dekel, A., & Birnboim, Y. 2006, Monthly Notices of the Royal Astronomical Society, 368, 2
- Dekel, A., & Mandelker, N. 2014, Monthly Notices of the Royal Astronomical Society, 444, 2071
- Dekel, A., Sari, R., & Ceverino, D. 2009a, The Astrophysical Journal, 703, 785
- Dekel, A., & Silk, J. I. 1986, The Astrophysical Journal, 303, 39
- Dekel, A., Zolotov, A., Tweed, D., Cacciato, M., Ceverino, D., & Primack, J. R. 2013, Monthly Notices of the Royal Astronomical Society, 435, 999
- Dekel, A., Birnboim, Y., Engel, G., Freundlich, J., Goerdt, T., Mumcuoglu, M., Neistein, E., Pichon, C., Teyssier, R., & Zinger, E. 2009b, Nature, 457, 451
- Diego, J. M., Schmidt, K. B., Broadhurst, T., Lam, D., Vega-Ferrero, J., Zheng, W., Lee, S., Morishita, T., Bernstein, G. M., Lim, J., Silk, J. I., & Ford, H. C. 2016, eprint arXiv:1609.04822, 1609.04822
- Diehl, S., & Statler, T. S. 2006, Monthly Notices of the Royal Astronomical Society, 368, 497
- Dopita, M. A., Sutherland, R. S., Nicholls, D. C., Kewley, L. J., & Vogt, F. P. A. 2013, The Astrophysical Journal Supplement Series, 208, 10
- Du, X., Shapley, A. E., Reddy, N. A., Jones, T. A., Stark, D. P., Steidel, C. C., Strom, A. L., Rudie, G. C., Erb, D. K., Ellis, R. S., & Pettini, M. 2018, eprint arXiv:1803.05912, 1803.05912
- Eldridge, J. J. 2012, Monthly Notices of the Royal Astronomical Society, 422, 794
- Erb, D. K. 2008, The Astrophysical Journal, 674, 151
- Erb, D. K., Pettini, M., Shapley, A. E., Steidel, C. C., Law, D. R., & Reddy, N. A. 2010, The Astrophysical Journal, 719, 1168

- Erb, D. K., Shapley, A. E., Pettini, M., Steidel, C. C., Reddy, N. A., & Adelberger, K. L. 2006, *The Astrophysical Journal*, 644, 813
- Esteban, C., García-Rojas, J., & Pérez-Mesa, V. 2015, *Monthly Notices of the Royal Astronomical Society*, 452, 1553
- Ferguson, H. C., Dickinson, M., & Williams, R. 2000, *Annu. Rev. Astro. Astrophys.*, 38, 667
- Few, C. G., Gibson, B. K., Courty, S., Michel-Dansac, L., Brook, C. B., & Stinson, G. S. 2012, *Astronomy and Astrophysics*, 547, A63
- Finlator, K., & Davé, R. 2008, *Monthly Notices of the Royal Astronomical Society*, 385, 2181
- Fontanot, F., De Lucia, G., Monaco, P., Somerville, R. S., & Santini, P. 2009, *Monthly Notices of the Royal Astronomical Society*, 397, 1776
- Foreman-Mackey, D., Hogg, D. W., Lang, D., & Goodman, J. 2013, *Publications of the Astronomical Society of the Pacific*, 125, 306
- Förster Schreiber, N. M., Renzini, A., Mancini, C., Genzel, R., Bouche, N., Cresci, G., Hicks, E. K. S., Lilly, S. J., Peng, Y.-j., Burkert, A., Carollo, C. M., Cimatti, A., Daddi, E., Davies, R. I., Genel, S., Kurk, J. D., Lang, P., Lutz, D., Mainieri, V., McCracken, H. J., Mignoli, M., Naab, T., Oesch, P. A., Pozzetti, L., Scudeggio, M., Shapiro Griffin, K., Shapley, A. E., Sternberg, A., Tacchella, S., Tacconi, L. J., Wuyts, S., & Zamorani, G. 2018, eprint arXiv:1802.07276, 1802.07276
- Fouesneau, M., & Lançon, A. 2010, *Astronomy and Astrophysics*, 521, A22
- Freeman, K. C. 1970, *The Astrophysical Journal*, 160, 811
- Frye, B. L., Hurley, M., Bowen, D. V., Meurer, G. R., Sharon, K., Straughn, A. N., Coe, D., Broadhurst, T., & Guhathakurta, P. 2012, *The Astrophysical Journal*, 754, 17
- Gavazzi, R., Treu, T., Rhodes, J. D., Koopmans, L. V. E., Bolton, A. S., Burles, S., Massey, R. J., & Moustakas, L. A. 2007, *ApJ*, 667, 176

Gibson, B. K., Pilkington, K., Brook, C. B., Stinson, G. S., & Bailin, J. 2013, *Astronomy and Astrophysics*, 554, A47

Gonzaga, S., & et al. 2012, The DrizzlePac Handbook (STScI)

Governato, F., Brook, C. B., Mayer, L., Brooks, A., Rhee, G., Wadsley, J. W., Jonsson, P., Willman, B., Stinson, G. S., Quinn, T., & Madau, P. 2010, *Nature*, 463, 203

Green, A. W., Croom, S. M., Scott, N., Cortese, L., Medling, A. M., D'Eugenio, F., Bryant, J. J., Bland-Hawthorn, J., Allen, J. T., Sharp, R., Ho, I. T., Groves, B. A., Drinkwater, M. J., Mannerling, E., Harischandra, L., van de Sande, J., Thomas, A. D., O'Toole, S., McDermid, R. M., Vuong, M., Sealey, K., Bauer, A. E., Brough, S., Catinella, B., Cecil, G., Colless, M., Couch, W. J., Driver, S. P., Federrath, C., Foster, C., Goodwin, M., Hampton, E. J., Hopkins, A. M., Jones, D. H., Konstantopoulos, I. S., Lawrence, J. S., Leon-Saval, S. G., Liske, J., López-Sánchez, Á.-R., Lorente, N. P. F., Mould, J., Obreschkow, D., Owers, M. S., Richards, S. N., Robotham, A. S. G., Schaefer, A. L., Sweet, S. M., Taranu, D. S., Tescari, E., Tonini, C., & Zafar, T. 2018, *Monthly Notices of the Royal Astronomical Society*, 475, 716

Grillo, C., Karman, W., Suyu, S. H., Rosati, P., Balestra, I., Mercurio, A., Lombardi, M., Treu, T. L., Caminha, G. B., Halkola, A., Halkola, A., Rodney, S. A., Gavazzi, R., & Caputi, K. I. 2016, *The Astrophysical Journal*, 822, 78

Grogin, N. A., Kocevski, D. D., Faber, S. M., Ferguson, H. C., Koekemoer, A. M., Riess, A. G., Acquaviva, V., Alexander, D. M., Almaini, O., Ashby, M. L. N., Barden, M., Bell, E. F., Bournaud, F., Brown, T. M., Caputi, K. I., Casertano, S., Cassata, P., Castellano, M., Challis, P., Chary, R.-R., Cheung, E., Cirasuolo, M., Conselice, C. J., Cooray, A. R., Croton, D. J., Daddi, E., Dahlen, T., Davé, R., de Mello, D. F., Dekel, A., Dickinson, M. E., Dolch, T., Donley, J. L., Dunlop, J. S., Dutton, A. A., Elbaz, D., Fazio, G. G., Filippenko, A. V., Finkelstein, S. L., Fontana, A., Gardner, J. P., Garnavich, P. M., Gawiser, E., Giavalisco, M., Grazian, A., Guo, Y., Hathi, N. P., Häussler, B., Hopkins, P. F., Huang, J.-S., Huang, K.-H., Jha, S. W., Kartaltepe, J. S., Kirshner, R. P., Koo, D. C., Lai, K., Lee, K.-S., Li, W., Lotz, J. M., Lucas, R. A., Madau, P., McCarthy, P. J., McGrath, E. J., McIntosh, D. H., McLure, R. J., Mobasher, B., Moustakas,

L. A., Mozena, M., Nandra, K., Newman, J. A., Niemi, S.-M., Noeske, K. G., Papovich, C. J., Pentericci, L., Pope, A., Primack, J. R., Rajan, A., Ravindranath, S., Reddy, N. A., Renzini, A., Rix, H.-W., Robaina, A. R., Rodney, S. A., Rosario, D. J., Rosati, P., Salimbeni, S., Scarlata, C., Siana, B. D., Simard, L., Smidt, J., Somerville, R. S., Spinrad, H., Straughn, A. N., Strolger, L.-G., Telford, O., Teplitz, H. I., Trump, J. R., Van der Wel, A., Villforth, C., Wechsler, R. H., Weiner, B. J., Wiklind, T., Wild, V., Wilson, G., Wuyts, S., Yan, H.-J., & Yun, M. S. 2011, The Astrophysical Journal Supplement Series, 197, 35

Guo, Y., Ferguson, H. C., Giavalisco, M., Barro, G., Willner, S. P., Ashby, M. L. N., Dahlen, T., Donley, J. L., Faber, S. M., Fontana, A., Galametz, A., Grazian, A., Huang, K.-H., Kocevski, D. D., Koekemoer, A. M., Koo, D. C., McGrath, E. J., Peth, M., Salvato, M., Wuyts, S., Castellano, M., Cooray, A. R., Dickinson, M. E., Dunlop, J. S., Fazio, G. G., Gardner, J. P., Gawiser, E., Grogin, N. A., Hathi, N. P., Hsu, L.-T., Lee, K.-S., Lucas, R. A., Mobasher, B., Nandra, K., Newman, J. A., & van der Wel, A. 2013, ApJS, 207, 24

Guo, Y., Koo, D. C., Lu, Y., Forbes, J. C., Rafelski, M., Trump, J. R., Amorín, R., Barro, G., Davé, R., Faber, S. M., Hathi, N. P., Yesuf, H., Cooper, M. C., Dekel, A., Guhathakurta, P., Kirby, E. N., Pérez-González, P. G., Lin, L., Newman, J. A., Primack, J. R., Rosario, D. J., Willmer, C. N. A., & Yan, R.-B. 2016, eprint arXiv:1603.04863, 1603.04863

Henry, A. L., Martin, C. L., Finlator, K., & Dressler, A. 2013a, The Astrophysical Journal, 769, 148

Henry, A. L., Scarlata, C., Domínguez, A., Malkan, M. A., Martin, C. L., Siana, B. D., Atek, H., Bedregal, A. G., Colbert, J. W., Rafelski, M., Ross, N., Teplitz, H. I., Bunker, A. J., Dressler, A., Hathi, N., Masters, D., McCarthy, P. J., & Straughn, A. N. 2013b, The Astrophysical Journal, 776, L27

Henry, R. B. C., Kwitter, K. B., & Balick, B. 2004, The Astronomical Journal, 127, 2284

Hirtenstein, J., Jones, T. A., Wang, X., Wetzel, A. R., El-Badry, K., Hoag, A. T., Treu, T. L., Bradac, M., & Morishita, T. 2018, eprint arXiv:1811.11768, 1811.11768

Ho, I. T., Kudritzki, R.-P., Kewley, L. J., Zahid, H. J., Dopita, M. A., Bresolin, F., & Rupke, D. S. N. 2015, Monthly Notices of the Royal Astronomical Society, 448, 2030

Hopkins, P. F., Kereš, D., Onorbe, J., Faucher-Giguère, C.-A., Quataert, E., Murray, N., & Bullock, J. S. 2014, Monthly Notices of the Royal Astronomical Society, 445, 581

Hopkins, P. F., Wetzel, A. R., Kereš, D., Faucher-Giguère, C.-A., Quataert, E., Boylan-Kolchin, M., Murray, N., Hayward, C. C., Garrison-Kimmel, S., Hummels, C., Feldmann, R., Torrey, P., Ma, X., Anglés-Alcázar, D., Su, K.-Y., Orr, M., Schmitz, D., Escala, I., Sanderson, R. E., Grudic, M. Y., Hafen, Z., Kim, J.-h., Fitts, A., Bullock, J. S., Wheeler, C., Chan, T. K., Elbert, O. D., & Narananan, D. 2017, eprint arXiv:1702.06148, 1702.06148

Hou, J. L., Prantzos, N., & Boissier, S. 2000, Astronomy and Astrophysics, 362, 921

Huang, K.-H., Bradač, M., Lemaux, B. C., Ryan, Jr., R. E., Hoag, A., Castellano, M., Amorín, R., Fontana, A., Brammer, G. B., Cain, B., Lubin, L. M., Merlin, E., Schmidt, K. B., Schrabback, T., Treu, T., Gonzalez, A. H., Von Der Linden, A., & Knight, R. I. 2015, ArXiv e-prints, arXiv:1504.02099

Hummer, D. G., & Storey, P. J. 1987, Monthly Notices of the Royal Astronomical Society, 224, 801

Hunt, L., Dayal, P., Magrini, L., & Ferrara, A. 2016, eprint arXiv:1608.05417, 1608.05417

Ilbert, O., Arnouts, S., McCracken, H. J., Bolzonella, M., Bertin, E., Le Fèvre, O., Mellier, Y., Zamorani, G., Pellò, R., Iovino, A., Tresse, L., Le Brun, V., Bottini, D., Garilli, B., Maccagni, D., Picat, J. P., Scaramella, R., Scodéggi, M., Vettolani, G., Zanichelli, A., Adami, C., Bardelli, S., Cappi, A., Charlot, S., Ciliegi, P., Contini, T., Cucciati, O., Foucaud, S., Franzetti, P., Gavignaud, I., Guzzo, L., Marano, B., Marinoni, C., Mazure, A., Meneux, B., Merighi, R., Paltani, S., Pollo, A., Pozzetti, L., Radovich, M., Zucca, E., Bondi, M., Bongiorno, A., Busarello, G., de La Torre, S., Gregorini, L., Lamareille, F., Mathez, G., Merluzzi, P., Ripepi, V., Rizzo, D., & Vergani, D. 2006, A&A, 457, 841

Ishigaki, M., Kawamata, R., Ouchi, M., Oguri, M., Shimasaku, K., & Ono, Y. 2015, ApJ, 799, 12

- James, B. L., Auger, M. W., Pettini, M., Stark, D. P., Belokurov, V., & Carniani, S. 2018, Monthly Notices of the Royal Astronomical Society, 476, 1726
- Jauzac, M., Richard, J., Jullo, E., Clément, B., Limousin, M., Kneib, J.-P., Ebeling, H., Rodney, S., Natarajan, P., Atek, H., Massey, R., Eckert, D., Egami, E., & Rexroth, M. 2014, ArXiv e-prints, arXiv:1409.8663
- Johnson, T. L., Sharon, K., Bayliss, M. B., Gladders, M. D., Coe, D., & Ebeling, H. 2014, ApJ, 797, 48
- Johnson, T. L., Sharon, K., Bayliss, M. B., Gladders, M. D., Coe, D., & Ebeling, H. 2014a, The Astrophysical Journal, 797, 48
- . 2014b, The Astrophysical Journal, 797, 48
- Jones, T. A., Ellis, R. S., Jullo, E., & Richard, J. 2010, The Astrophysical Journal Letters, 725, L176
- Jones, T. A., Ellis, R. S., Richard, J., & Jullo, E. 2013, The Astrophysical Journal, 765, 48
- Jones, T. A., Martin, C. L., & Cooper, M. C. 2015a, The Astrophysical Journal, 813, 126
- Jones, T. A., Wang, X., Schmidt, K. B., Treu, T. L., Brammer, G. B., Bradac, M., Dressler, A., Henry, A. L., Malkan, M. A., Pentericci, L., & Trenti, M. 2015b, The Astronomical Journal, 149, 107
- Juneau, S., Dickinson, M. E., Alexander, D. M., & Salim, S. 2011, The Astrophysical Journal, 736, 104
- Juneau, S., Bournaud, F., Charlot, S., Daddi, E., Elbaz, D., Trump, J. R., Brinchmann, J., Dickinson, M. E., Duc, P.-A., Gobat, R., Jean-Baptiste, I., Le Floc'h, E., Lehnert, M. D., Pacifici, C., Pannella, M., & Schreiber, C. 2014, The Astrophysical Journal, 788, 88
- Kalirai, J. 2018, Contemporary Physics, 59, 251

Karman, W., Grillo, C., Balestra, I., Rosati, P., Caputi, K. I., Di Teodoro, E., Fraternali, F., Gavazzi, R., Mercurio, A., Prochaska, J. X., Rodney, S. A., & Treu, T. L. 2016, *Astronomy and Astrophysics*, 585, A27

Kashino, D., Silverman, J. D., Rodighiero, G., Renzini, A., Arimoto, N., Daddi, E., Lilly, S. J., Sanders, D. B., Kartaltepe, J., Zahid, H. J., Nagao, T., Sugiyama, N., Capak, P. L., Carollo, C. M., Chu, J., Hasinger, G., Ilbert, O., Kajisawa, M., Kewley, L. J., Koekemoer, A. M., Kovac, K., Le Fèvre, O., Masters, D., McCracken, H. J., Onodera, M., Scoville, N. Z., Strazzullo, V., Symeonidis, M., & Taniguchi, Y. 2013, *The Astrophysical Journal*, 777, L8

Kauffmann, G., Heckman, T. M., White, S. D. M., Charlot, S., Tremonti, C. A., Peng, E. W., Seibert, M., Brinkmann, J., Nichol, R. C., SubbaRao, M., & York, D. 2003, *Monthly Notices of the Royal Astronomical Society*, 341, 54

Kawamata, R., Oguri, M., Ishigaki, M., Shimasaku, K., & Ouchi, M. 2015, arXiv.org, arXiv:1510.06400

Kelly, B. C. 2007, *The Astrophysical Journal*, 665, 1489

Kelly, P. L., Rodney, S. A., Treu, T. L., Strolger, L.-G., Foley, R. J., Jha, S. W., Selsing, J., Brammer, G. B., Bradac, M., Cenko, S. B., Graham, M. L., Graur, O., Filippenko, A. V., Hjorth, J., Matheson, T., McCully, C., McCully, C., Molino, A., Nonino, M., Riess, A. G., Schmidt, K. B., Tucker, B., von der Linden, A., Weiner, B. J., & Zitrin, A. 2015a, arXiv.org, arXiv:1512.04654

Kelly, P. L., Rodney, S. A., Treu, T. L., Foley, R. J., Brammer, G. B., Schmidt, K. B., Zitrin, A., Sonnenfeld, A., Strolger, L.-G., Graur, O., Filippenko, A. V., Jha, S. W., Riess, A. G., Bradac, M., Weiner, B. J., Scolnic, D. M., Malkan, M. A., von der Linden, A., Trenti, M., Hjorth, J., Gavazzi, R., Fontana, A., Merten, J. C., McCully, C., Jones, T. A., Postman, M., Dressler, A., Patel, B., Cenko, S. B., Graham, M. L., & Tucker, B. E. 2015b, *Science*, 347, 1123

Kelly, P. L., Brammer, G. B., Selsing, J., Foley, R. J., Hjorth, J., Rodney, S. A., Christensen, L., Strolger, L.-G., Filippenko, A. V., Treu, T. L., Steidel, C. C., Strom, A. L., Riess, A. G., Zitrin, A., Schmidt, K. B., Bradac, M., Jha, S. W., Graham, M. L., McCully, C., Graur, O., Weiner, B. J., & Silverman, J. M. 2015c, arXiv.org, arXiv:1512.09093

- Kempner, J. C., & David, L. P. 2004, MNRAS, 349, 385
- Kennicutt, R. C. J. 1998a, Annual Review of Astronomy and Astrophysics, 36, 189
- . 1998b, The Astrophysical Journal, 498, 541
- Kereš, D., Katz, N. S., Fardal, M., Davé, R., & Weinberg, D. H. 2009, Monthly Notices of the Royal Astronomical Society, 395, 160
- Kereš, D., Katz, N. S., Weinberg, D. H., & Davé, R. 2005, Monthly Notices of the Royal Astronomical Society, 363, 2
- Kewley, L. J., & Dopita, M. A. 2002, The Astrophysical Journal Supplement Series, 142, 35
- Kewley, L. J., & Ellison, S. L. 2008, The Astrophysical Journal, 681, 1183
- Kewley, L. J., Geller, M. J., & Barton, E. J. 2006a, The Astronomical Journal, 131, 2004
- Kewley, L. J., Groves, B. A., Kauffmann, G., & Heckman, T. M. 2006b, Monthly Notices of the Royal Astronomical Society, 372, 961
- Kewley, L. J., Rupke, D. S. N., Zahid, H. J., Geller, M. J., & Barton, E. J. 2010, The Astrophysical Journal, 721, L48
- Kneib, J.-P., & Natarajan, P. 2011, A&A Rev., 19, 47
- Kobayashi, C., & Nakasato, N. 2011, The Astrophysical Journal, 729, 16
- Koekemoer, A. M., Fruchter, A. S., Hook, R. N., & Hack, W. 2003, The 2002 HST Calibration Workshop : Hubble after the Installation of the ACS and the NICMOS Cooling System, 337
- Koekemoer, A. M., Faber, S. M., Ferguson, H. C., Grogin, N. A., Kocevski, D. D., Koo, D. C., Lai, K., Lotz, J. M., Lucas, R. A., McGrath, E. J., Ogaz, S., Rajan, A., Riess, A. G., Rodney, S. A., Strolger, L.-G., Casertano, S., Castellano, M., Dahlen, T., Dickinson, M. E., Dolch, T., Fontana, A., Giavalisco, M., Grazian, A., Guo, Y., Hathi, N. P., Huang, K.-H., Van der Wel, A., Yan, H.-J., Acquaviva, V., Alexander, D. M., Almaini, O., Ashby, M. L. N., Barden, M., Bell, E. F., Bournaud, F., Brown, T. M., Caputi, K. I., Cassata, P., Challis, P. J., Chary, R.-R., Cheung,

E., Cirasuolo, M., Conselice, C. J., Cooray, A. R., Croton, D. J., Daddi, E., Davé, R., de Mello, D. F., de Ravel, L., Dekel, A., Donley, J. L., Dunlop, J. S., Dutton, A. A., Elbaz, D., Fazio, G. G., Filippenko, A. V., Finkelstein, S. L., Frazer, C., Gardner, J. P., Garnavich, P. M., Gawiser, E., Gruetzbauch, R., Hartley, W. G., Häussler, B., Herrington, J., Hopkins, P. F., Huang, J.-S., Jha, S. W., Johnson, A., Kartaltepe, J. S., Khostovan, A. A., Kirshner, R. P., Lani, C., Lee, K.-S., Li, W., Madau, P., McCarthy, P. J., McIntosh, D. H., McLure, R. J., McPartland, C., Mobasher, B., Moreira, H., Mortlock, A., Moustakas, L. A., Mozena, M., Nandra, K., Newman, J. A., Nielsen, J. L., Niemi, S., Noeske, K. G., Papovich, C. J., Pentericci, L., Pope, A., Primack, J. R., Ravindranath, S., Reddy, N. A., Renzini, A., Rix, H.-W., Robaina, A. R., Rosario, D. J., Rosati, P., Salimbeni, S., Scarlata, C., Siana, B. D., Simard, L., Smidt, J., Snyder, D., Somerville, R. S., Spinrad, H., Straughn, A. N., Telford, O., Teplitz, H. I., Trump, J. R., Vargas, C., Villforth, C., Wagner, C. R., Wandro, P., Wechsler, R. H., Weiner, B. J., Wiklind, T., Wild, V., Wilson, G., Wuyts, S., & Yun, M. S. 2011, *The Astrophysical Journal Supplement Series*, 197, 36

Kriek, M. T., van Dokkum, P. G., Franx, M., Illingworth, G. D., & Magee, D. K. 2009a, *The Astrophysical Journal*, 705, L71

Kriek, M. T., van Dokkum, P. G., Labb  , I., Franx, M., Illingworth, G. D., Marchesini, D., & Quadri, R. F. 2009b, *The Astrophysical Journal*, 700, 221

K  mmel, M., Kuntschner, H., Walsh, J. R., & Bushouse, H. 2011, ST-ECF Instrument Science Report WFC3-2011-01, 1

K  mmel, M., Walsh, J. R., Pirzkal, N., Kuntschner, H., & Pasquali, A. 2009, *Publications of the Astronomical Society of the Pacific*, 121, 59

Lam, D., Broadhurst, T., Diego, J. M., Lim, J., Coe, D., Ford, H. C., & Zheng, W. 2014, *ApJ*, 797, 98

Lamareille, F., Mouhcine, M., Contini, T., Lewis, I., & Maddox, S. J. 2004, *Monthly Notices of the Royal Astronomical Society*, 350, 396

Laporte, N., Streblyanska, A., Kim, S., Pell  , R., Bauer, F. E., Bina, D., Brammer, G., De Leo, M. A., Infante, L., & P  rez-Fournon, I. 2015, *A&A*, 575, A92

Larkin, J. E., Barczys, M., Krabbe, A., Adkins, S. M., Aliado, T., Amico, P., Brims, G., Campbell, R. D., Canfield, J., Gasaway, T., Honey, A., Iserlohe, C., Johnson, C. A., Kress, E., LaFreniere, D., Lyke, J. E., Magnone, K. G., Magnone, N., McElwain, M., Moon, J., Quirrenbach, A., Skulason, G., Song, I., Spencer, M., Weiss, J. L., & Wright, S. A. 2006, Society of Photo-Optical Instrumentation Engineers (SPIE) Conference Series, 6269, 62691A

Law, D. R., Yan, R.-B., Bershady, M. A., Bundy, K., Cherinka, B., Drory, N., MacDonald, N. K., Sánchez-Gallego, J. R., Wake, D. A., Weijmans, A.-M., Blanton, M. R., Klaene, M. A., Moran, S. M., Sanchez, S. F., & Zhang, K. 2015, *The Astronomical Journal*, 150, 19

Leethochawalit, N., Jones, T. A., Ellis, R. S., Stark, D. P., Richard, J., Zitrin, A., & Auger, M. W. 2016, *The Astrophysical Journal*, 820, 84

Leitherer, C., Schaerer, D., Goldader, J. D., Delgado, R. M. G., Robert, C., Kune, D. F., de Mello, D. F., Devost, D., & Heckman, T. M. 1999, *The Astrophysical Journal Supplement Series*, 123, 3

Lilly, S. J., Carollo, C. M., Pipino, A., Renzini, A., & Peng, Y.-j. 2013, *The Astrophysical Journal*, 772, 119

Livermore, R. C., Jones, T. A., Richard, J., Bower, R. G., Swinbank, A. M., Yuan, T., Edge, A. C., Ellis, R. S., Kewley, L. J., Smail, I. R., Coppin, K. E. K., & Ebeling, H. 2015, *Monthly Notices of the Royal Astronomical Society*, 450, 1812

Lotz, J. M., Koekemoer, A. M., Coe, D., Grogin, N. A., Capak, P. L., Mack, J., Anderson, J., Avila, R. J., Barker, E. A., Borncamp, D., Brammer, G. B., Durbin, M., Gunning, H., Hilbert, B., Jenkner, H., Khandrika, H., Levay, Z., Lucas, R. A., MacKenty, J. W., Ogaz, S., Porterfield, B., Reid, N., Robberto, M., Royle, P., Smith, L. J., Storrie-Lombardi, L. J., Sunnquist, B., Surace, J., Taylor, D. C., Williams, R., Bullock, J. S., Dickinson, M., Finkelstein, S. L., Natarajan, P., Richard, J., Robertson, B. E., Tumlinson, J., Zitrin, A., Flanagan, K., Sembach, K., Soifer, B. T., & Mountain, M. 2016, 1605.06567

Lu, Y., Blanc, G. A., & Benson, A. J. 2015a, *The Astrophysical Journal*, 808, 129

- Lu, Z., Mo, H., & Lu, Y. 2015b, Monthly Notices of the Royal Astronomical Society, 450, 606
- Ma, X., Hopkins, P. F., Faucher-Giguère, C.-A., Zolman, N., Muratov, A. L., Kereš, D., & Quataert, E. 2016, Monthly Notices of the Royal Astronomical Society, 456, 2140
- Ma, X., Hopkins, P. F., Feldmann, R., Torrey, P., Faucher-Giguère, C.-A., & Kereš, D. 2017, Monthly Notices of the Royal Astronomical Society, 466, 4780
- Maciel, W. J., Costa, R. D. D., & Uchida, M. M. M. 2003, Astronomy and Astrophysics, 397, 667
- Madau, P., & Dickinson, M. E. 2014, Annual Review of Astronomy and Astrophysics, 52, 415
- Maiolino, R., Nagao, T., Grazian, A., Cocchia, F., Marconi, A., Mannucci, F., Cimatti, A., Pipino, A., Ballero, S. K., Calura, F., Chiappini, C., Fontana, A., Granato, G. L., Matteucci, F., Pastorini, G., Pentericci, L., Risaliti, G., Salvati, M., & Silva, L. 2008, Astronomy and Astrophysics, 488, 463
- Mannucci, F., Cresci, G., Maiolino, R., Marconi, A., & Gnerucci, A. 2010, Monthly Notices of the Royal Astronomical Society, 408, 2115
- Mannucci, F., Salvaterra, R., & Campisi, M. A. 2011, Monthly Notices of the Royal Astronomical Society, 414, 1263
- Martin, C. L. 2005, The Astrophysical Journal, 621, 227
- Martin, C. L., Kobulnicky, H. A., & Heckman, T. M. 2002, The Astrophysical Journal, 574, 663
- Martin, C. L., Shapley, A. E., Coil, A. L., Kornei, K. A., Bundy, K., Weiner, B. J., Noeske, K. G., & Schiminovich, D. 2012, The Astrophysical Journal, 760, 127
- Masters, D., Faisst, A. L., & Capak, P. L. 2016, eprint arXiv:1605.04314, 1605.04314
- Medling, A. M., Cortese, L., Croom, S. M., Green, A. W., Groves, B. A., Hampton, E., Ho, I. T., Davies, L. J. M., Kewley, L. J., Moffett, A. J., Schaefer, A. L., Taylor, E. N., Zafar, T., Bekki, K., Bland-Hawthorn, J., Bloom, J. V., Brough, S., Bryant, J. J., Catinella, B., Cecil, G., Colless, M., Couch, W. J., Drinkwater, M. J., Driver, S. P., Federrath, C., Foster, C., Goldstein, G., Goodwin,

M., Hopkins, A. M., Lawrence, J. S., Leslie, S. K., Lewis, G. F., Lorente, N. P. F., Owers, M. S., McDermid, R. M., Richards, S. N., Sharp, R., Scott, N., Sweet, S. M., Taranu, D. S., Tescari, E., Tonini, C., van de Sande, J., Walcher, C. J., & Wright, A. 2018, Monthly Notices of the Royal Astronomical Society, 475, 5194

Meneghetti, M., Natarajan, P., Coe, D., Contini, E., De Lucia, G., Giocoli, C., Acebron, A., Borgani, S., Bradac, M., Diego, J. M., Hoag, A. T., Ishigaki, M., Johnson, T. L., Jullo, E., Kawamata, R., Lam, D., Limousin, M., Liesenborgs, J., Oguri, M., Sebesta, K., Sharon, K., Williams, L. L. R., & Zitrin, A. 2016, eprint arXiv:1606.04548, 1606.04548

Merten, J., Coe, D., Dupke, R., Massey, R., Zitrin, A., Cypriano, E. S., Okabe, N., Frye, B., Braglia, F. G., Jiménez-Teja, Y., Benítez, N., Broadhurst, T., Rhodes, J., Meneghetti, M., Moustakas, L. A., Sodré, Jr., L., Krick, J., & Bregman, J. N. 2011, MNRAS, 417, 333

Merten, J., Meneghetti, M., Postman, M., Umetsu, K., Zitrin, A., Medezinski, E., Nonino, M., Koekemoer, A., Melchior, P., Gruen, D., Moustakas, L. A., Bartelmann, M., Host, O., Donahue, M., Coe, D., Molino, A., Jouvel, S., Monna, A., Seitz, S., Czakon, N., Lemze, D., Sayers, J., Balestra, I., Rosati, P., Benítez, N., Biviano, A., Bouwens, R., Bradley, L., Broadhurst, T., Carrasco, M., Ford, H., Grillo, C., Infante, L., Kelson, D., Lahav, O., Massey, R., Moustakas, J., Rasia, E., Rhodes, J., Vega, J., & Zheng, W. 2015, ApJ, 806, 4

Michel-Dansac, L., Lambas, D. G., Alonso, M. S., & Tissera, P. B. 2008, Monthly Notices of the Royal Astronomical Society, 386, L82

Mollá, M., Cavichia, O., Costa, R. D. D., Maciel, W. J., Gibson, B. K., & Díaz, A. I. 2016a, eprint arXiv:1612.03064, 1612.03064

Mollá, M., & Díaz, A. I. 2005, Monthly Notices of the Royal Astronomical Society, 358, 521

Mollá, M., Díaz, A. I., Ascasíbar, Y., Gibson, B. K., Cavichia, O., Costa, R. D. D., & Maciel, W. J. 2016b, eprint arXiv:1612.03348, 1612.03348

Mollá, M., Díaz, A. I., Cavichia, O., Gibson, B. K., Maciel, W. J., Costa, R. D. D., Ascasíbar, Y., & Few, C. G. 2018, Monthly Notices of the Royal Astronomical Society

Mollá, M., Díaz, A. I., Gibson, B. K., Cavichia, O., & López-Sánchez, Á.-R. 2016c, Monthly Notices of the Royal Astronomical Society, 462, 1329

Momcheva, I. G., Brammer, G. B., van Dokkum, P. G., Skelton, R. E., Whitaker, K. E., Nelson, E. J., Fumagalli, M., Maseda, M. V., Leja, J., Franx, M., Rix, H.-W., Bezanson, R., da Cunha, E., Dickey, C., Dickey, C., Förster Schreiber, N. M., Illingworth, G. D., Kriek, M. T., Labbé, I., Lange, J. U., Ulf Lange, J., Lundgren, B. F., Magee, D. K., Marchesini, D., Oesch, P. A., Pacifici, C., Patel, S. G., Price, S., Price, S., Tal, T., Wake, D. A., Van der Wel, A., & Wuyts, S. 2016, The Astrophysical Journal Supplement Series, 225, 27

Morishita, T., Abramson, L. E., Treu, T. L., Schmidt, K. B., Vulcani, B., & Wang, X. 2016, eprint arXiv:1610.08503, 1610.08503

Morishita, T., Ichikawa, T., Noguchi, M., Akiyama, M., Patel, S. G., Kajisawa, M., & Obata, T. 2015, The Astrophysical Journal, 805, 34

Mortlock, A., Conselice, C. J., Hartley, W. G., Ownsworth, J. R., Lani, C., Bluck, A. F. L., Almaini, O., Duncan, K., Van der Wel, A., Koekemoer, A. M., Dekel, A., Davé, R., Ferguson, H. C., de Mello, D. F., Newman, J. A., Faber, S. M., Grogin, N. A., Kocevski, D. D., & Lai, K. 2013, Monthly Notices of the Royal Astronomical Society, 433, 1185

Mott, A., Spitoni, E., & Matteucci, F. 2013, Monthly Notices of the Royal Astronomical Society, 435, 2918

Moustakas, J., Kennicutt, R. C. J., Tremonti, C. A., Dale, D. A., Smith, J.-D. T., & Calzetti, D. 2010, The Astrophysical Journal Supplement Series, 190, 233

Murray, N., Quataert, E., & Thompson, T. A. 2005, The Astrophysical Journal, 618, 569

Muzzin, A., Marchesini, D., Stefanon, M., Franx, M., Milvang-Jensen, B., Dunlop, J. S., Fynbo, J. P. U., Brammer, G. B., Labbé, I., & van Dokkum, P. G. 2013, The Astrophysical Journal Supplement Series, 206, 8

Nagao, T., Maiolino, R., & Marconi, A. 2006, Astronomy and Astrophysics, 459, 85

- Nelson, E. J., van Dokkum, P. G., Franx, M., Brammer, G. B., Momcheva, I. G., Förster Schreiber, N. M., da Cunha, E., Tacconi, L. J., Bezanson, R., Kirkpatrick, A., Leja, J., Rix, H.-W., Skelton, R. E., Van der Wel, A., Whitaker, K. E., & Wuyts, S. 2014, *Nature*, 513, 394
- Newman, A. B., Treu, T., Ellis, R. S., & Sand, D. J. 2013, *ApJ*, 765, 25
- Oguri, M. 2010, *Publications of the Astronomical Society of Japan*, 62, 1017
- Okamoto, T., Frenk, C. S., Jenkins, A., & Theuns, T. 2010, *Monthly Notices of the Royal Astronomical Society*, 406, 208
- Oke, J. B. 1974, *ApJS*, 27, 21
- Oke, J. B., & Gunn, J. E. 1983, *Astrophysical Journal*, 266, 713
- Oppenheimer, B. D., & Davé, R. 2006, *Monthly Notices of the Royal Astronomical Society*, 373, 1265
- . 2008, *Monthly Notices of the Royal Astronomical Society*, 387, 577
- Owers, M. S., Randall, S. W., Nulsen, P. E. J., Couch, W. J., David, L. P., & Kempner, J. C. 2011, *The Astrophysical Journal*, 728, 27
- Peeples, M. S., & Shankar, F. 2011, *Monthly Notices of the Royal Astronomical Society*, 417, 2962
- Peng, Y.-j., & Maiolino, R. 2014, *Monthly Notices of the Royal Astronomical Society*, 443, 3643
- Pérez-Montero, E. 2014, *Monthly Notices of the Royal Astronomical Society*, 441, 2663
- Pérez-Montero, E., García-Benito, R., Vílchez, J. M., Sanchez, S. F., Kehrig, C., Husemann, B., Puertas, S. D., Iglesias-Páramo, J., Galbany, L., Mollá, M., Walcher, C. J., Ascasíbar, Y., Delgado, R. M. G., Marino, R. A., Masegosa, J., Pérez, E., Rosales-Ortega, F., Sánchez-Blázquez, P., Bland-Hawthorn, J., Bomans, D. J., López-Sánchez, Á.-R., Ziegler, B., & collaboration, t. C. 2016, *Astronomy and Astrophysics*, 1608.04677
- Pettini, M., & Pagel, B. E. J. 2004, *Monthly Notices of the Royal Astronomical Society*, 348, L59

Pettini, M., Rix, S. A., Steidel, C. C., Adelberger, K. L., Hunt, M. P., & Shapley, A. E. 2002, ApJ, 569, 742

Pilkington, K., Few, C. G., Gibson, B. K., Calura, F., Michel-Dansac, L., Thacker, R. J., Mollá, M., Matteucci, F., Rahimi, A., Kawata, D., Kobayashi, C., Brook, C. B., Stinson, G. S., Couchman, H. M. P., Bailin, J., & Wadsley, J. W. 2012, Astronomy and Astrophysics, 540, A56

Pillepich, A., Nelson, D., Springel, V., Pakmor, R., Torrey, P., Weinberger, R., Vogelsberger, M., Marinacci, F., Genel, S., Van der Wel, A., & Hernquist, L. 2019, eprint arXiv:1902.05553, 1902.05553

Pilyugin, L. S., Vilchez, J. M., & Thuan, T. X. 2010, The Astrophysical Journal, 720, 1738

Pipino, A., Lilly, S. J., & Carollo, C. M. 2014, Monthly Notices of the Royal Astronomical Society, 441, 1444

Postman, M., Coe, D., Benítez, N., Bradley, L., Broadhurst, T., Donahue, M., Ford, H., Graur, O., Graves, G., Jouvel, S., Koekemoer, A., Lemze, D., Medezinski, E., Molino, A., Moustakas, L., Ogaz, S., Riess, A., Rodney, S., Rosati, P., Umetsu, K., Zheng, W., Zitrin, A., Bartelmann, M., Bouwens, R., Czakon, N., Golwala, S., Host, O., Infante, L., Jha, S., Jimenez-Teja, Y., Kelson, D., Lahav, O., Lazkoz, R., Maoz, D., McCully, C., Melchior, P., Meneghetti, M., Merten, J., Moustakas, J., Nonino, M., Patel, B., Regös, E., Sayers, J., Seitz, S., & Wel, A. V. D. 2012a, The Astrophysical Journal Supplement, 199, 25

Postman, M., Coe, D., Benítez, N., Bradley, L. D., Broadhurst, T., Donahue, M., Ford, H. C., Graur, O., Graves, G. J., Jouvel, S., Koekemoer, A. M., Lemze, D., Medezinski, E., Molino, A., Moustakas, L. A., Ogaz, S., Riess, A. G., Rodney, S. A., Rosati, P., Umetsu, K., Zheng, W., Zitrin, A., Bartelmann, M., Bouwens, R. J., Czakon, N. G., Golwala, S., Host, O., Infante, L., Jha, S., Jimenez-Teja, Y., Kelson, D. D., Lahav, O., Lazkoz, R., Maoz, D., McCully, C., Melchior, P., Meneghetti, M., Merten, J. C., Moustakas, J., Nonino, M., Patel, B., Regös, E., Sayers, J., Seitz, S., & Van der Wel, A. 2012b, The Astrophysical Journal Supplement Series, 199, 25

- Prantzos, N., & Boissier, S. 2000, Monthly Notices of the Royal Astronomical Society, 313, 338
- Queyrel, J., Contini, T., Kissler-Patig, M., Epinat, B., Amram, P., Garilli, B., Le Fèvre, O., Moul-taka, J., Paioro, L., Tasca, L. A. M., Tresse, L., Vergani, D., López-Sanjuan, C., & Pérez-Montero, E. 2012, Astronomy and Astrophysics, 539, A93
- Rawle, T. D., Altieri, B., Egami, E., Pérez-González, P. G., Boone, F., Clement, B., Ivison, R. J., Richard, J., Rujopakarn, W., Valtchanov, I., Walth, G., Weiner, B. J., Blain, A. W., Dessauges-Zavadsky, M., Kneib, J.-P., Lutz, D., Rodighiero, G., Schaerer, D., & Smail, I. R. 2016, Monthly Notices of the Royal Astronomical Society, 459, 1626
- Recchi, S., Spitoni, E., Matteucci, F., & Lanfranchi, G. A. 2008, Astronomy and Astrophysics, 489, 555
- Reddy, N. A., Kriek, M. T., Shapley, A. E., Freeman, W. R., Siana, B. D., Coil, A. L., Mobasher, B., Price, S. H., Sanders, R. L., & Shvaei, I. 2015, The Astrophysical Journal, 806, 259
- Rich, J. A., Torrey, P., Kewley, L. J., Dopita, M. A., & Rupke, D. S. N. 2012, The Astrophysical Journal, 753, 5
- Richard, J., Jones, T. A., Ellis, R. S., Stark, D. P., Livermore, R. C., & Swinbank, A. M. 2011, Monthly Notices of the Royal Astronomical Society, 413, 643
- Richard, J., Jauzac, M., Limousin, M., Jullo, E., Clément, B., Ebeling, H., Kneib, J.-P., Atek, H., Natarajan, P., Egami, E., Livermore, R., & Bower, R. 2014, MNRAS, 444, 268
- Rodney, S. A., Patel, B., Scolnic, D., Foley, R. J., Molino, A., Brammer, G., Jauzac, M., Bradac, M., Coe, D., Broadhurst, T., Diego, J. M., Graur, O., Hjorth, J., Hoag, A., Jha, S. W., Johnson, T. L., Kelly, P., Lam, D., McCully, C., Medezinski, E., Meneghetti, M., Merten, J., Richard, J., Riess, A., Sharon, K., Strolger, L.-G., Treu, T., Wang, X., Williams, L. L. R., & Zitrin, A. 2015, ArXiv e-prints, arXiv:1505.06211
- Rodrigues, M., Puech, M., Hammer, F., Rothberg, B., & Flores, H. 2012, Monthly Notices of the Royal Astronomical Society, 421, 2888

Rupke, D. S. N., Kewley, L. J., & Chien, L. H. 2010, *The Astrophysical Journal*, 723, 1255

Ryan, Jr., R. E., Gonzalez, A. H., Lemaux, B. C., Bradač, M., Casertano, S., Allen, S., Cain, B., Gladders, M., Hall, N., Hildebradt, H., Hinz, J., Huang, K.-H., Lubin, L., Schrabbach, T., Stiavelli, M., Treu, T., von der Linden, A., & Zaritsky, D. 2014, *ApJ*, 786, L4

Salpeter, E. E. 1955, *ApJ*, 121, 161

Sanchez, S. F., Rosales-Ortega, F., Iglesias-Páramo, J., Mollá, M., Barrera-Ballesteros, J. K., Marino, R. A., Pérez, E., Sánchez-Blázquez, P., González Delgado, R. M., Cid Fernandes, R., de Lorenzo-Cáceres, A., Mendez-Abreu, J., Galbany, L., Falcón-Barroso, J., Miralles-Caballero, D., Husemann, B., García-Benito, R., Mast, D., Walcher, C. J., Gil de Paz, A., García-Lorenzo, B., Jungwiert, B., Vílchez, J. M., Jílková, L., Lyubenova, M., Cortijo-Ferrero, C., Díaz, A. I., Wisotzki, L., Márquez, I., Bland-Hawthorn, J., Ellis, S. C., van de Ven, G., Jahnke, K., Pápareros, P., Gomes, J. M., Mendoza, M. A., & López-Sánchez, Á.-R. 2014, *Astronomy and Astrophysics*, 563, A49

Sanchez, S. F., García-Benito, R., Zibetti, S., Walcher, C. J., Husemann, B., Mendoza, M. A., Galbany, L., Falcón-Barroso, J., Mast, D., Aceituno, J., Aguerri, J. A. L., Alves, J. F., de Amorim, A. L., Ascasíbar, Y., Barrado-Navascues, D., Barrera-Ballesteros, J. K., Bekeraitè, S., Bland-Hawthorn, J., Cano Diaz, M., Cid Fernandes, R., Cavichia, O., Cortijo, C., Dannerbauer, H., Demleitner, M., Díaz, A., Dettmar, R. J., de Lorenzo-Cáceres, A., del Olmo, A., Galazzi, A., García-Lorenzo, B., Gil de Paz, A., González Delgado, R. M., Holmes, L., Iglesias-Páramo, J., Kehrig, C., Kelz, A., Kennicutt, R. C. J., Kleemann, B., Lacerda, E. A. D., López Fernández, R., López-Sánchez, Á.-R., Lyubenova, M., Marino, R. A., Márquez, I., Mendez-Abreu, J., Mollá, M., Monreal-Ibero, A., Ortega Minakata, R., Torres-Papaqui, J. P., Pérez, E., Rosales-Ortega, F., Roth, M. M., Sánchez-Blázquez, P., Schilling, U., Spekkens, K., Vale Asari, N., van den Bosch, R. C. E., van de Ven, G., Vílchez, J. M., Wild, V., Wisotzki, L., Yildirim, A., & Ziegler, B. 2016, *Astronomy and Astrophysics*, 594, A36

Sánchez-Menguiano, L., Sanchez, S. F., Pérez, I., García-Benito, R., Husemann, B., Mast, D., Mendoza, A., Ruiz-Lara, T., Ascasíbar, Y., Bland-Hawthorn, J., Cavichia, O., Díaz, A. I.,

- Florida, E., Galbany, L., González Delgado, R. M., Kehrig, C., Marino, R. A., Márquez, I., Masegosa, J., Mendez-Abreu, J., Mollá, M., del Olmo, A., Pérez, E., Sánchez-Blázquez, P., Stanishev, V., Walcher, C. J., López-Sánchez, Á.-R., & Collaboration, C. 2016, *Astronomy and Astrophysics*, 587, A70
- Sand, D. J., Treu, T., Ellis, R. S., Smith, G. P., & Kneib, J. 2008, *ApJ*, 674, 711
- Sanders, R. L., Shapley, A. E., Kriek, M. T., Reddy, N. A., Freeman, W. R., Coil, A. L., Siana, B. D., Mobasher, B., Shavvai, I., Price, S. H., & de Groot, L. 2015, *The Astrophysical Journal*, 799, 138
- . 2016, *The Astrophysical Journal Letters*, 825, L23
- Schmidt, K. B., Treu, T. L., Brammer, G. B., Bradac, M., Wang, X., Dijkstra, M., Dressler, A., Fontana, A., Gavazzi, R., Henry, A. L., Hoag, A. T., Jones, T. A., Kelly, P. L., Malkan, M. A., Mason, C. A., Pentericci, L., Poggianti, B. M., Stiavelli, M., Trenti, M., von der Linden, A., & Vulcani, B. 2014, *The Astrophysical Journal Letters*, 782, L36
- Schmidt, K. B., Treu, T. L., Bradac, M., Vulcani, B., Huang, K.-H., Hoag, A. T., Maseda, M. V., Guaita, L., Pentericci, L., Brammer, G. B., Dijkstra, M., Dressler, A., Fontana, A., Henry, A. L., Jones, T. A., Mason, C. A., Trenti, M., & Wang, X. 2016, *The Astrophysical Journal*, 818, 38
- Schmidt, M. 1959, *The Astrophysical Journal*, 129, 243
- Shapley, A. E., Reddy, N. A., Kriek, M. T., Freeman, W. R., Sanders, R. L., Siana, B. D., Coil, A. L., Mobasher, B., Shavvai, I., Price, S. H., & de Groot, L. 2015, *The Astrophysical Journal*, 801, 88
- Sharon, K., Gladders, M. D., Rigby, J. R., Wuyts, E., Bayliss, M. B., Johnson, T. L., Florian, M. K., & Dahle, H. 2014, *ApJ*, 795, 50
- Sharon, K., & Johnson, T. L. 2015, *The Astrophysical Journal*, 800, L26
- Shi, Y., Helou, G., Yan, L., Armus, L., Wu, Y., Papovich, C. J., & Stierwalt, S. 2011, *The Astrophysical Journal*, 733, 87

Shi, Y., Yan, L., Armus, L., Gu, Q.-S., Helou, G., Qiu, K., Gwyn, S. D. J., Stierwalt, S., Fang, M., Chen, Y.-M., Zhou, L., Wu, J., Zheng, X. Z., Zhang, Z.-Y., Gao, Y., & Wang, J.-Z. 2018, 1801.00888

Shirazi, M., Vegetti, S., Nesvadba, N., Allam, S., Brinchmann, J., & Tucker, D. 2014, MNRAS, 440, 2201

Smartt, S. J., & Rolleston, W. R. J. 1997, *The Astrophysical Journal*, 481, L47

Smith, G. P., Ebeling, H., Limousin, M., Kneib, J.-P., Swinbank, A. M., Ma, C.-J., Jauzac, M., Richard, J., Jullo, E., Sand, D. J., Edge, A. C., & Smail, I. R. 2009, *The Astrophysical Journal*, 707, L163

Somerville, R. S., & Davé, R. 2015, *Annual Review of Astronomy and Astrophysics*, 53, 51

Speagle, J. S., Steinhardt, C. L., Capak, P. L., & Silverman, J. D. 2014, *The Astrophysical Journal Supplement Series*, 214, 15

Springel, V., & Hernquist, L. 2003, *Monthly Notices of the Royal Astronomical Society*, 339, 289

Steidel, C. C., Rudie, G. C., Strom, A. L., Pettini, M., Reddy, N. A., Shapley, A. E., Trainor, R. F., Erb, D. K., Turner, M. L., Konidaris, N. P., Kulas, K. R., Mace, G., Matthews, K., & McLean, I. S. 2014, *The Astrophysical Journal*, 795, 165

Stinson, G. S., Bailin, J., Couchman, H. M. P., Wadsley, J. W., Shen, S., Nickerson, S., Brook, C. B., & Quinn, T. 2010, *Monthly Notices of the Royal Astronomical Society*, 408, 812

Stinson, G. S., Brook, C. B., Macciò, A. V., Wadsley, J. W., Quinn, T. R., & Couchman, H. M. P. 2013, *Monthly Notices of the Royal Astronomical Society*, 428, 129

Storey, P. J., & Zeippen, C. J. 2000, *Monthly Notices of the Royal Astronomical Society*, 312, 813

Stott, J. P., Sobral, D., Swinbank, A. M., Smail, I. R., Bower, R. G., Best, P. N., Sharples, R. M., Geach, J. E., & Matthee, J. 2014, *Monthly Notices of the Royal Astronomical Society*, 443, 2695

- Strait, V., Bradac, M., Hoag, A. T., Huang, K.-H., Treu, T. L., Wang, X., Amorín, R., Castellano, M., Fontana, A., Lemaux, B. C., Merlin, E., Schmidt, K. B., Schrabback, T., Tomczack, A., Trenti, M., & Vulcani, B. 2018, eprint arXiv:1805.08789, 129
- Strom, A. L., Steidel, C. C., Rudie, G. C., Trainor, R. F., Pettini, M., & Reddy, N. A. 2016, eprint arXiv:1608.02587, 1608.02587
- Swinbank, A. M., Sobral, D., Smail, I. R., Geach, J. E., Best, P. N., McCarthy, I. G., Crain, R. A., & Theuns, T. 2012, Monthly Notices of the Royal Astronomical Society, 426, 935
- Torrey, P., Cox, T. J., Kewley, L. J., & Hernquist, L. 2012, The Astrophysical Journal, 746, 108
- Tremonti, C. A., Heckman, T. M., Kauffmann, G., Brinchmann, J., Charlot, S., White, S. D. M., Seibert, M., Peng, E. W., Schlegel, D. J., Uomoto, A., Fukugita, M., & Brinkmann, J. 2004, The Astrophysical Journal, 613, 898
- Treu, T., Schmidt, K. B., Bradač, M., Brammer, G. B., Dijkstra, M., Dressler, A., Fontana, A., Gavazzi, R., Henry, A., Hoag, A., Jones, T., Kelly, P. L., Malkan, M. A., Mason, C., Pentericci, L., Poggianti, B., Stiavelli, M., Trenti, M., von der Linden, A., Vulcani, B., & Wang, X. 2015a, apJ, submitted.
- Treu, T. L., Schmidt, K. B., Brammer, G. B., Vulcani, B., Wang, X., Bradac, M., Dijkstra, M., Dressler, A., Fontana, A., Gavazzi, R., Henry, A. L., Hoag, A. T., Huang, K.-H., Jones, T. A., Kelly, P. L., Malkan, M. A., Mason, C. A., Pentericci, L., Poggianti, B. M., Stiavelli, M., Trenti, M., & von der Linden, A. 2015b, The Astrophysical Journal, 812, 114
- Treu, T. L., Brammer, G. B., Diego, J. M., Grillo, C., Kelly, P. L., Oguri, M., Rodney, S. A., Rosati, P., Sharon, K., Zitrin, A., Balestra, I., Bradac, M., Broadhurst, T., Caminha, G. B., Halkola, A., Hoag, A. T., Ishigaki, M., Johnson, T. L., Halkola, A., Karman, W., Kawamata, R., Mercurio, A., Schmidt, K. B., Strolger, L.-G., Suyu, S. H., Filippenko, A. V., Foley, R. J., Jha, S. W., & Patel, B. 2016, The Astrophysical Journal, 817, 60
- Troncoso, P., Maiolino, R., Sommariva, V., Cresci, G., Mannucci, F., Marconi, A., Meneghetti,

- M., Grazian, A., Cimatti, A., Fontana, A., Nagao, T., & Pentericci, L. 2014, *Astronomy and Astrophysics*, 563, A58
- Valentino, F., Daddi, E., Silverman, J. D., Puglisi, A., Kashino, D., Renzini, A., Cimatti, A., Pozzetti, L., Rodighiero, G., Pannella, M., Gobat, R., & Zamorani, G. 2017, *Monthly Notices of the Royal Astronomical Society*, 472, 4878
- Van der Wel, A., Franx, M., van Dokkum, P. G., Skelton, R. E., Momcheva, I. G., Whitaker, K. E., Brammer, G. B., Bell, E. F., Rix, H.-W., Wuyts, S., Ferguson, H. C., Holden, B. P., Barro, G., Koekemoer, A. M., Chang, Y.-Y., McGrath, E. J., Häussler, B., Dekel, A., Behroozi, P. S., Fumagalli, M., Leja, J., Lundgren, B. F., Maseda, M. V., Nelson, E. J., Wake, D. A., Patel, S. G., Labbé, I., Faber, S. M., Grogin, N. A., & Kocevski, D. D. 2014, *The Astrophysical Journal*, 788, 28
- van Dokkum, P. G., Brammer, G. B., Fumagalli, M., Nelson, E. J., Franx, M., Rix, H.-W., Kriek, M. T., Skelton, R. E., Patel, S. G., Schmidt, K. B., Bezanson, R., Bian, F., da Cunha, E., Erb, D. K., Fan, X., Förster Schreiber, N. M., Illingworth, G. D., Labbé, I., Lundgren, B. F., Magee, D. K., Marchesini, D., McCarthy, P. J., Muzzin, A., Quadri, R. F., Steidel, C. C., Tal, T., Wake, D. A., Whitaker, K. E., & Williams, A. 2011, *The Astrophysical Journal*, 743, L15
- van Dokkum, P. G., Leja, J., Nelson, E. J., Patel, S. G., Skelton, R. E., Momcheva, I. G., Brammer, G. B., Whitaker, K. E., Lundgren, B. F., Fumagalli, M., Conroy, C., Förster Schreiber, N. M., Franx, M., Kriek, M. T., Labbé, I., Marchesini, D., Rix, H.-W., Van der Wel, A., & Wuyts, S. 2013, *The Astrophysical Journal*, 771, L35
- van Zee, L., Salzer, J. J., & Haynes, M. P. 1998, *The Astrophysical Journal*, 497, L1
- Vogelsberger, M., Genel, S., Springel, V., Torrey, P., Sijacki, D., Xu, D., Snyder, G. F., Bird, S., Nelson, D., & Hernquist, L. 2014, *Nature*, 509, 177
- Vulcani, B., Treu, T. L., Schmidt, K. B., Poggianti, B. M., Dressler, A., Fontana, A., Bradac, M., Brammer, G. B., Hoag, A. T., Huang, K.-H., Malkan, M. A., Pentericci, L., Trenti, M., von der Linden, A., Abramson, L. E., He, J., & Morris, G. 2015, *The Astrophysical Journal*, 814, 161

Wang, X., Jones, T. A., Treu, T. L., Morishita, T., Abramson, L. E., Brammer, G. B., Huang, K.-H., Malkan, M. A., Schmidt, K. B., Fontana, A., Grillo, C., Henry, A. L., Karman, W., Kelly, P. L., Mason, C. A., Mercurio, A., Rosati, P., Sharon, K., Trenti, M., & Vulcani, B. 2017, *The Astrophysical Journal*, 837, 89

Whitaker, K. E., Franx, M., Leja, J., van Dokkum, P. G., Henry, A. L., Skelton, R. E., Fumagalli, M., Momcheva, I. G., Brammer, G. B., Labb  , I., Nelson, E. J., & Rigby, J. R. 2014, *The Astrophysical Journal*, 795, 104

White, S. D. M., & Rees, M. J. 1978, *Monthly Notices of the Royal Astronomical Society*, 183, 341

Williams, R. E., Blacker, B., Dickinson, M., Dixon, W. V. D., Ferguson, H. C., Fruchter, A. S., Giavalisco, M., Gilliland, R. L., Heyer, I., Katsanis, R., Levay, Z., Lucas, R. A., McElroy, D. B., Petro, L., Postman, M., Adorf, H.-M., & Hook, R. 1996, *AJ*, 112, 1335

Wisnioski, E., F  rster Schreiber, N. M., Wuyts, S., Wuyts, E., Bandara, K., Wilman, D. J., Genzel, R., Bender, R., Davies, R., Fossati, M., Lang, P., Mendel, J. T., Beifiori, A., Brammer, G. B., Chan, J., Fabricius, M., Fudamoto, Y., Kulkarni, S., Kurk, J., Lutz, D., Nelson, E. J., Momcheva, I. G., Rosario, D., Saglia, R., Seitz, S., Tacconi, L. J., & van Dokkum, P. G. 2015, *The Astrophysical Journal*, 799, 209

Wuyts, E., Rigby, J. R., Sharon, K., & Gladders, M. D. 2012a, *The Astrophysical Journal*, 755, 73

Wuyts, E., Kurk, J., Kurk, J., F  rster Schreiber, N. M., Genzel, R., Wisnioski, E., Bandara, K., Wuyts, S., Beifiori, A., Bender, R., Brammer, G. B., Burkert, A., Buschkamp, P., Carollo, C. M., Chan, J., Davies, R., Eisenhauer, F., Eisenhauer, F., Fossati, M., Kulkarni, S. K., Lang, P., Lilly, S. J., Lutz, D., Mancini, C., Mendel, J. T., Momcheva, I. G., Naab, T., Nelson, E. J., Renzini, A., Rosario, D., Saglia, R. P., Seitz, S., Seitz, S., Sharples, R. M., Sternberg, A., Tacchella, S., Tacconi, L. J., van Dokkum, P. G., & Wilman, D. J. 2014, *The Astrophysical Journal Letters*, 789, L40

Wuyts, E., Wisnioski, E., Fossati, M., F  rster Schreiber, N. M., Genzel, R., Davies, R., Mendel, J. T., Naab, T., R  ttgers, B., Wilman, D. J., Wuyts, S., Bandara, K., Beifiori, A., Belli, S.,

- Bender, R., Brammer, G. B., Burkert, A., Chan, J., Galametz, A., Kulkarni, S. K., Lang, P., Lutz, D., Momcheva, I. G., Nelson, E. J., Rosario, D., Saglia, R. P., Seitz, S., Tacconi, L. J., Tadaki, K.-i., Übler, H., & van Dokkum, P. G. 2016, *The Astrophysical Journal*, 827, 74
- Wuyts, S., Förster Schreiber, N. M., Genzel, R., Guo, Y., Barro, G., Bell, E. F., Dekel, A., Faber, S. M., Ferguson, H. C., Giavalisco, M., Grogin, N. A., Hathi, N. P., Huang, K.-H., Kocevski, D. D., Koekemoer, A. M., Koo, D. C., Lotz, J. M., Lutz, D., McGrath, E., Newman, J. A., Rosario, D., Saintonge, A., Tacconi, L. J., Weiner, B. J., & Van der Wel, A. 2012b, *The Astrophysical Journal*, 753, 114
- Yang, C.-C., & Krumholz, M. R. 2012, *The Astrophysical Journal*, 758, 48
- Yates, R. M., Kauffmann, G., & Guo, Q. 2012, *Monthly Notices of the Royal Astronomical Society*, 422, 215
- Yee, H. K. C., Ellingson, E., Bechtold, J., Carlberg, R. G., & Cuillandre, J.-C. 1996, *AJ*, 111, 1783
- Yuan, T., Kewley, L. J., & Rich, J. A. 2013, *The Astrophysical Journal*, 767, 106
- Yuan, T., Kewley, L. J., Swinbank, A. M., Richard, J., & Livermore, R. C. 2011, *The Astrophysical Journal*, 732, L14
- Zahid, H. J., Bresolin, F., Kewley, L. J., Coil, A. L., & Davé, R. 2012a, *The Astrophysical Journal*, 750, 120
- Zahid, H. J., Dima, G. I., Kewley, L. J., Erb, D. K., & Davé, R. 2012b, *The Astrophysical Journal*, 757, 54
- Zahid, H. J., Dima, G. I., Kudritzki, R.-P., Kewley, L. J., Geller, M. J., Hwang, H. S., Silverman, J. D., & Kashino, D. 2014, *The Astrophysical Journal*, 791, 130
- Zahid, H. J., Kewley, L. J., & Bresolin, F. 2011, *The Astrophysical Journal*, 730, 137
- Zanella, A., Daddi, E., Le Floch, E., Bournaud, F., Gobat, R., Valentino, F., Strazzullo, V., Cibinel, A., Onodera, M., Perret, V., Renaud, F., & Vignali, C. 2015, *Nature*, 521, 54

Zitrin, A., Broadhurst, T., Umetsu, K., Coe, D., Benítez, N., Ascaso, B., Bradley, L., Ford, H., Jee, J., Medezinski, E., Rephaeli, Y., & Zheng, W. 2009, MNRAS, 396, 1985

Zitrin, A., Zheng, W., Broadhurst, T., Moustakas, J., Lam, D., Shu, X., Huang, X., Diego, J. M., Ford, H., Lim, J., Bauer, F. E., Infante, L., Kelson, D. D., & Molino, A. 2014, ApJ, 793, L12

Zitrin, A., Fabris, A., Merten, J. C., Melchior, P., Meneghetti, M., Koekemoer, A. M., Coe, D., Maturi, M., Bartelmann, M., Postman, M., Umetsu, K., Seidel, G., Sendra, I., Broadhurst, T., Balestra, I., Biviano, A., Grillo, C., Mercurio, A., Nonino, M., Rosati, P., Bradley, L. D., Bradley, L., Carrasco, M., Donahue, M., Ford, H. C., Frye, B. L., & Moustakas, J. 2015, The Astrophysical Journal, 801, 44